

https://dspace.org/

Aeroelastic prediction methods in supersonic flows for missile design

Meijer, Marius-Corné

2015-05-05
http://hdl.handle.net/10539/17625

Downloaded from a DSpace repository. https://dspace.org/

AEROELASTIC PREDICTION METHODS IN SUPERSONIC FLOWS FOR MISSILE DESIGN

by

Marius-Corné Meijer

A dissertation submitted to the Faculty of Engineering and the Built Environment, University of the Witwatersrand, Johannesburg, in fulfilment of the requirements for the degree of Master of Science in Engineering.

Johannesburg, 2014

Declaration

I, Marius-Corné Meijer, declare that this dissertation is my own unaided work. It is being in fulfilment of the requirements for the degree of Master of Science in Engineering to the University of the Witwatersrand, Johannesburg. It has not been submitted before for any degree or examination to any other University.

_____

Marius-Corné Meijer

_____ day of _____ 20 ___

Abstract

The prediction of aeroelastic instabilities such as flutter is important in the multi-disciplinary design and preliminary testing of missiles. Flutter prediction software varies in the fidelity of analysis, with accurate solutions being computationally expensive and involving the use of CFD.

In this dissertation, a review is given of approximate methods for supersonic aeroelastic analysis. A general formulation of piston theory is developed to encompass both classical and local piston theory, and the literature on piston theory and its application in aeroelastic analysis is reviewed.

An aeroelastic prediction method is developed for cantilevered trapezoidal plates in supersonic flows based on shock-expansion theory and local piston theory. The method is validated against 3D unsteady Euler aeroelastic computations in the Edge CFD solver and against experimental flutter data in literature.

The prediction method is shown to be suitable for computationally inexpensive aeroelastic parametric studies applicable to missile fin design.

Acknowledgements

I would like to thank my supervisor Prof. Laurent Dala for his continued support and guidance throughout this work. I am particularly grateful for the balance of freedom and advised instruction he allowed and provided in the approach to the work. His encouragement and the opportunities provided are greatly appreciated.

The financial support of this work by Armscor through the Fluxion grant is gratefully acknowledged.

I would like to thank the CSIR for the opportunity to use Edge for the computational validation of this work. Particular thanks goes to Dr. Igle Gledhill and Dr. Louw van Zyl of the CSIR for their technical insights and support in my use of Edge.

Finally, I am deeply grateful to my parents for their unwavering encouragement and support throughout my graduate studies.

Table of Contents

Declaration i
Abstract ii
Acknowledgements iii
List of Figures ix
List of Tables xix
List of Symbols and Abbreviations xxi
1 INTRODUCTION 1
1.1 Introduction 1
1.2 Review of Software for Approximate Aeroelastic Analysis 3
1.2.1 MSC NASTRAN 3
1.2.2 ZONA7 4
1.2.3 NeoCASS 4
1.2.4 NEAR Software 4
1.3 Objectives of the Dissertation 5
1.4 Outline of the Dissertation 6
2 REVIEW OF APPROXIMATE METHODS OF MODELLING OF AEROELASTICITY IN SUPERSONIC FLOWS 8
2.1 Approximate Modelling of Supersonic Aerodynamics 8
2.1.1 Shock-Expansion Theory 8
2.1.2 Slender Body Theory 11
2.1.3 Semi-Empirical Methods 13
2.1.4 Van Dyke's Unified Supersonic/Hypersonic Potential Theory 13
2.1.5 Piston Theory 15
2.1.6 Mach Box Method 19
2.1.7 Quasi-Steady Approximation to Unsteady Aerodynamics 21
2.2 Coupling of Aerodynamics and Structural Dynamics 21

2.3 Time Variance in Dynamic Systems 22
2.4 Linearity and Nonlinearity 28
2.4.1 Nonlinear effects 30
2.5 Time Integration 31
2.6 Characterization of Dynamic Aeroelastic Response 33
2.7 Aeroelastic Response at Airspeeds Below Flutter Speed 35
2.8 Experimental Data for Supersonic Flutter of Cantilevered Plates 38
2.9 Flutter Prediction Methods 40
2.9.1 Zimmerman-Weissenburger Flutter Margin 41
2.9.2 Flutter Margin for Discrete Systems 42
2.9.3 Damping Extrapolation 43
2.9.4 Envelope Function 44
2.9.5 Analytical Methods 45
3 DEVELOPMENT OF PISTON THEORY 48
3.1 Fundamental formulation 48
3.2 Cylinder conditions 52
3.2.1 Classical piston theory 52
3.2.2 Local piston theory 53
3.3 Downwash terms 58
3.3.1 Downwash terms in local piston theory 61
3.4 Third-order terms 62
3.5 Generalized Formulation 64
3.6 Physical Effects Modelled by Classical Piston Theory 65
4 DEVELOPMENT OF A FINITE ELEMENT BASED AEROELASTIC PREDICTION TOOL IN MATLAB FOR CANTILEVERED PLATES IN SUPERSONIC FLOWS 75
4.1 Geometry and Material Properties of the Analysed Cantilevered Plate 75
4.2 Structural Modelling of the Plate Using Finite Elements 76

4.3 Aerodynamic Modelling of the Plate Using Shock-Expansion Theory and Piston Theory 77

4.3.1 Shock-Expansion Contribution 78

4.3.2 Piston Theory Contribution 80

4.3.3 Total Aerodynamic Loading 81

4.4 Formulation of the Coupled Aeroelastic Equations of Motion 82

4.4.1 Full-Order Formulation with Dynamically-Nonlinear Unsteady Aerodynamic Loading 83

4.4.2 Modal Formulation with Dynamically-Nonlinear Unsteady Aerodynamic Loading 83

4.4.3 Modal Formulation with Linearized Quasi-Steady Aerodynamic Loading 84

4.5 Linearization of the Generalized Aerodynamic Forces 84

4.5.1 Linearization Procedure 84

4.5.2 Effect of the Size of the Linearization Increment 88

4.6 Solution of the Aeroelastic Equations of Motion 90

4.6.1 Implicit Time-Marching of Systems with Dynamically-Nonlinear Aerodynamic Loading 90

4.6.2 Explicit Time-Marching of Systems with Time-Linearized Aerodynamic Loading and Time-Invariant Matrices 93

4.7 Representation of System Response 94

4.7.1 Time-History of Modal Response 95

4.7.2 Phase-Plane Trajectory of Modal Response 96

4.7.3 System Eigenvalues and Parameters 96

4.7.4 Response of Individual Points on the Structure 98

5 VALIDATION OF THE AEROELASTIC PREDICTION TOOL AGAINST COMPUTATIONAL FLUID DYNAMICS 99

5.1 The Edge CFD Solver 99

5.2 Geometry and Structural Parameters of the ATM-Wing 101

5.3 Validation of the Finite Element Solver 106

5.4 Meshing of the Fluid Domain 108
5.4.1 Mesh 1 108
5.4.2 Mesh 2 112
5.4.3 Grid Independence 116
5.4.4 Mesh Deformation 119
5.5 Validation of the Aerodynamic Modelling using Shock-Expansion Theory 122
5.6 Steady Computation of the Undeformed ATM-Wing 123
5.6.1 Flow Conditions 124
5.6.2 Results 124
5.7 Transient Computation of Static Aeroelastic Deflection 130
5.7.1 Results 130
5.8 Transient Computations of Prescribed Modal Motion of the Model 137
5.8.1 Prescribed Motion of Mode 1 Only 138
5.8.2 Prescribed Motion of Mode 2 Only 139
5.8.3 Prescribed Motion of Mode 3 Only 140
5.8.4 Prescribed Motion of Mode 4 Only 141
5.9 Linearization of the Generalized Aerodynamic Forces 142
6 AEROELASTIC ANALYSIS AND FLUTTER PREDICTION OF CANTILEVERED PLATES IN SUPERSONIC FLOW 144
6.1 Free Aeroelastic Response of the ATM-Wing 144
6.1.1 Literature on the Experimentally Determined Flutter Conditions 144
6.1.2 Outline of the Computational Procedure 146
6.1.3 Analysis in Edge 148
6.1.4 Analysis in MATLAB (nonlinear) 164
6.1.5 Analysis in MATLAB (linear) 180
6.1.6 Comparison of Analysis Results 189
6.2 Flutter Envelope of the ATM-Wing 193
6.3 Flutter Prediction of the Tuovali-McCarty Models 195

6.3.1 Literature on the Experimentally Determined Flutter Conditions 195
6.3.2 Literature on Previous Computational Flutter Predictions 197
6.3.3 Outline of the Computational Procedure 201
6.3.4 Representation of the Flutter Prediction Results 202
6.3.5 Analysis in MATLAB (linear).....203
6.4 Effect of Fin Taper Ratio on the Flutter Envelope 215
7 CONCLUSIONS.....220
7.1 Work Accomplished 220
7.2 Recommendations for Future Work.....222
REFERENCES 223
APPENDICES 230
A. GEOMETRY OF THE TUOVALI AND McCARTY TEST MODELS 230
B. FINITE ELEMENT FORMULATION 232
C. SET-UP PROCEDURE FOR AEROELASTIC COMPUTATIONS IN EDGE.....251
D. FURTHER RESULTS OF THE VALIDATION OF SHOCK-EXPANSION THEORY 259
E. DEFORMED GEOMETRIES USED FOR MESH DEFORMATION COMPUTATIONS IN EDGE 267
F. FURTHER RESULTS OF THE PRESCRIBED MODAL DISPLACEMENTS 270

List of Figures

Figure 1.1: Multidisciplinary Interaction in Aerospace Design [1] 1
Figure 2.1: Definition of Nomenclature for Oblique Shock Calculations 9
Figure 2.2: Definition of Nomenclature for Prandtl-Meyer Expansion Calculations 10
Figure 2.3: Flow Turning-Angle in Quasi-Steady Shock-Expansion Theory 11
Figure 2.4: Second-Order Slender Body Theory for a Cone with Semi-Vertex Angle 5° [23] 12
Figure 2.5: Second-Order Slender Body Theory for a Cone with Semi-Vertex Angle 15° [23] 12
Figure 2.6: Surface Pressure on Wedges from Van Dyke's Unified Supersonic-Hypersonic Small-Disturbance Theory[27] 14
Figure 2.7: The Concept of the Piston in Piston Theory 15
Figure 2.8: Relationship Between Hypersonic Similarity Parameter $\boldsymbol{K = M\tau}$ *and Downwash Mach Number* 15
Figure 2.9: Pressure Coefficient on a 15° Wedge from Various Piston Theories [12] 16
Figure 2.10: Time History of Aerodynamic Loading on a NACA 0012 Airfoil from Local Piston Theory [11] 17
Figure 2.11: Flutter Speed vs α for a NACA 64A010 Airfoil from Local Piston Theory [11]. 18
Figure 2.12: Example of Mach Box Spatial Discretization [31] 20
Figure 2.13: Example of a Simple Second-Order System[39] 23
Figure 2.14: Example of Transient and Steady Responses [39] 24
Figure 2.15: Example of a Sinusoid with Variable Frequency 25
Figure 2.16: Comparison of Quasi-Steady Approximations to Unsteady Phenomena 26
Figure 2.17: Comparison of the Effect of Time-Step in Quasi-Steady Approximations 27
Figure 2.18: Example of a Nonlinear Spring 29
Figure 2.19: Limit-Cycle Oscillations of the Goland Wing [48] 34
Figure 2.20: Examples of the Phase-Plane Representation of Limit-Cycle Oscillations [44] 35
Figure 2.21: Typical Trends in the Variation of Aeroelastic System Parameters with Airspeed [50] 36
Figure 2.22: Variation of Aeroelastic System Parameters in Hypersonic Flow [1] 36

Figure 2.23: Example of the Variation in Aeroelastic System Parameters Produced by ZAERO [52] 37
Figure 2.24: A Typical Delta-Planform Cantilevered Plate in Literature 38
Figure 2.25: A Typical Untapered Cantilevered Plate in Literature 39
Figure 2.26: A Typical Tapered Cantilevered Plate in Literature 39
Figure 3.1: Definition of the Cylinder in Piston Theory 52
Figure 3.2:The Piston-Cylinder Relationship in Classical Piston Theory 55
Figure 3.3: The Piston-Cylinder Relationship in Local Piston Theory 56
Figure 3.4: Equivalence Between Piston Theory and Van Dyke's Second Order Theory 57
Figure 3.5: General Motion for a 2-Dimensional Body 58
Figure 3.6: "Steady" and "Unsteady" Motion of a Body in Piston Theory 58
Figure 3.7: Contributions to Downwash in Piston Theory 59
Figure 3.8: Contributions to the Steady Downwash Terms 66
Figure 3.9: Comparison of Mach Number Effects Between Piston Theories for a 4% Circular Arc Airfoil[11] 74
Figure 3.10: Comparison of Angle-of-Attack Effects Between Piston Theories for a 4% Circular Arc Airfoil[11] 74
Figure 4.1: Coordinate System Definition for Structural Analysis and Structural Discretization 77
Figure 4.2: Contributions to the Surface Angle to the Flow 78
Figure 4.3: Definition of Angles for Flow Turning-Angle Determination at the Leading- and Trailing-Edges 79
Figure 4.4: Linearization Step-Size Influence on Aerodynamic Stiffness Terms from SE/LPT in MATLAB 89
Figure 4.5: Comparison of the ode23t and ode45 Solvers in MATLAB 94
Figure 4.6: Example of Time-History of Modal Response for an Aeroelastic System in MATLAB 95
Figure 4.7: Example of Phase-Plane Representation of an Aeroelastic System in MATLAB . 96
Figure 4.8: Example of a Root Locus Plot for an Aeroelastic System in MATLAB 97
Figure 4.9: Example of Variation in Aeroelastic System Parameters in MATLAB 97
Figure 4.10: Example of the Response Obtained from an Individual Degree of Freedom in MATLAB 98
Figure 5.1: The Primary (solid line) and Dual (dashed line) Grids in Edge [71] 99
Figure 5.2: ATM-Wing Planform 102

Figure 5.3: ATM-Wing Profile 102
Figure 5.4: ATM-Wing, Mode 1 -- First Bending, 26.6 Hz 103
Figure 5.5: ATM-Wing, Mode 2 -- First Twist, 148.5 Hz 103
Figure 5.6: ATM-Wing, Mode 3 -- Second Bending, 195.0 Hz 103
Figure 5.7: ATM-Wing Structural Mode-Shapes 1 - 3, View from Wing-Tip 104
Figure 5.8: ATM-Wing Structural Mode-Shapes 4 - 6, View from Wing-Tip 105
Figure 5.9: Structural Mesh used for the ATM-Wing 106
Figure 5.10: Variation in MATLAB-Based Finite Element Solver Accuracy with Taper Ratio 107
Figure 5.11: Variation in MATLAB-Based Finite Element Solver Accuracy with Plate Thickness 108
Figure 5.12: Mesh 1, Domain Side View 109
Figure 5.13: Mesh 1, Domain Perspective View 110
Figure 5.14: Mesh 1, Symmetry Boundary Surface Mesh 110
Figure 5.15: Mesh 1, Wing Surface Mesh 111
Figure 5.16: Mesh 1, Volume Mesh at the Mid-Span, $\boldsymbol{y = 0.1\mathbf{m}}$ 111
Figure 5.17: Mesh 2, Domain Dimensions 113
Figure 5.18: Mesh 2, Domain Perspective View 114
Figure 5.19: Mesh 2, Symmetry Boundary Surface Mesh 114
Figure 5.20: Mesh 2, Wing Surface Mesh 115
Figure 5.21: Mesh 2, Volume Mesh at Mid-Span, $\boldsymbol{y = 0.1\mathbf{m}}$ 115
Figure 5.22: Normal Force Coefficient vs Angle-of-Attack, Undeformed ATM-Wing, Mach 3 117
Figure 5.23: Axial Force Coefficient vs Angle-of-Attack, Undeformed ATM-Wing, Mach 3 117
Figure 5.24: Pitching Moment Coefficient (LE root) vs Angle-of-Attack, Undeformed ATM-Wing, Mach 3 118
Figure 5.25: Comparison of Normal Force Coefficients, Undeformed A TM-Wing, Mach 3 118
Figure 5.26: Comparison of Pitching Moment Coefficients, Undeformed ATM-Wing, Mach 3 119
Figure 5.27: Cross-Section of the Deformed Mesh of Mode 2 of the ATM-Wing, Trailing-Edge 121
Figure 5.28: Cross-Section of the Deformed Mesh of Mode 2 of the ATM-Wing, Trailing-Edge Tip 121

Figure 5.29: Variation in the Accuracy of MATLAB-Based Shock-Expansion Normal Force Coefficient with Angle-of-Attack and Mach Number 122
Figure 5.30: Variation in the Accuracy of MATLAB-Based Shock-Expansion Pitching Moment Coefficient with Angle-of-Attack and Mach Number 123
Figure 5.31: Steady Computation for the Undeformed ATM-Wing, Normal Force Coefficient 125
Figure 5.32: Steady Computation for the Undeformed ATM-Wing, Axial Force Coefficient 126
Figure 5.33: Steady Computation for the Undeformed ATM-Wing, Pitching Moment (LE root) Coefficient 126
Figure 5.34: Steady Computation for the Undeformed ATM-Wing, Chordwise Pressure Distribution 127
Figure 5.35: Steady Computation, Undeformed ATM-Wing, Shock Front, $\boldsymbol{M = 2.51}$, $\boldsymbol{\alpha = 0.5°}$, $\boldsymbol{q = 108\ kPa}$, $\boldsymbol{y = 0.15m}$ 128
Figure 5.36: Steady Computation for the Undeformed ATM-Wing, Spanwise Normal Force Distribution 128
Figure 5.37: Steady Computation, Undeformed ATM-Wing, Planform, $\boldsymbol{M = 2.51}$, $\boldsymbol{\alpha = 0.5°}$, $\boldsymbol{q = 108\ kPa}$, $\boldsymbol{z = 0.002m}$ 129
Figure 5.38: Steady Computation, Undeformed ATM-Wing, Shock Front, $\boldsymbol{M = 2.51}$, $\boldsymbol{\alpha = 0.5°}$, $\boldsymbol{q = 108\ kPa}$, $\boldsymbol{y = 0.005m}$ 129
Figure 5.39: Determination of Steady-State Normal Force Coefficient for the Elastic ATM-Wing 131
Figure 5.40: Determination of Steady-State Axial Force Coefficient for the Elastic ATM-Wing 132
Figure 5.41: Determination of Steady-State Pitching Moment (LE root) Coefficient for the Elastic ATM-Wing 132
Figure 5.42: Determination of Steady-State Displacement for the Elastic ATM-Wing, Mode 1 133
Figure 5.43: Determination of Steady-State Displacement for the Elastic ATM-Wing, Mode 2 133
Figure 5.44: Determination of Steady-State Displacement for the Elastic ATM-Wing, Mode 3 134

Figure 5.45: Determination of Steady-State Displacement for the Elastic ATM-Wing, Mode 4 134
Figure 5.46: Determination of Steady-State GAFs for the Elastic ATM-Wing, Mode 1 135
Figure 5.47: Determination of Steady-State GAFs for the Elastic ATM-Wing, Mode 2 135
Figure 5.48: Determination of Steady-State GAFs for the Elastic ATM-Wing, Mode 3 136
Figure 5.49: Determination of Steady-State GAFs for the Elastic ATM-Wing, Mode 4 136
Figure 5.50: Aerodynamic Response of the ATM-Wing to Prescribed Step Modal Displacement, Mode 1 138
Figure 5.51: Aerodynamic Response of the ATM-Wing to Prescribed Step Modal Displacement, Mode 2 139
Figure 5.52: Aerodynamic Response of the ATM-Wing to Prescribed Step Modal Displacement, Mode 3 140
Figure 5.53: Aerodynamic Response of the ATM-Wing to Prescribed Step Modal Displacement, Mode 4 141
Figure 6.1: Planform of the Torii and Matsuzaki Wing [54].....145
Figure 6.2: Time History of Response of the Torii-Matsuzaki Flutter Test [55].....146
Figure 6.3: ATM-Wing Response Below Flutter Speed, Mode 1 Displacement, Edge 149
Figure 6.4: ATM-Wing Response Below Flutter Speed, Mode 1 Phase-Plane Trajectory, Edge 149
Figure 6.5: ATM-Wing Response Below Flutter Speed, Mode 2 Displacement, Edge 150
Figure 6.6: ATM-Wing Response Below Flutter Speed, Mode 2 Phase-Plane Trajectory, Edge 150
Figure 6.7: ATM-Wing Response Below Flutter Speed, cZ, Edge.....151
Figure 6.8: ATM-Wing Pre-Flutter Response Near Flutter Speed, Mode 1 Displacement, Edge 153
Figure 6.9: ATM-Wing Pre-Flutter Response Near Flutter Speed, Mode 1 Phase-Plane Trajectory, Edge 153
Figure 6.10: ATM-Wing Pre-Flutter Response Near Flutter Speed, Mode 2 Displacement, Edge 154
Figure 6.11: ATM-Wing Pre-Flutter Response Near Flutter Speed, Mode 2 Phase-Plane Trajectory, Edge 154
Figure 6.12: ATM-Wing Pre-Flutter Response Near Flutter Speed, Mode 3 Displacement, Edge 155

Figure 6.13: ATM-Wing Pre-Flutter Response Near Flutter Speed, Mode 4 Displacement, Edge 155
Figure 6.14: ATM-Wing Pre-Flutter Response Near Flutter Speed, cZ, Edge 156
Figure 6.15: ATM-Wing Post-Flutter Response Near Flutter Speed, Mode 1 Displacement, Edge 158
Figure 6.16: ATM-Wing Post-Flutter Response Near Flutter Speed, Mode 1 Phase-Plane Trajectory, Edge 158
Figure 6.17: ATM-Wing Post-Flutter Response Near Flutter Speed, Mode 2 Displacement, Edge 159
Figure 6.18: ATM-Wing Post-Flutter Response Near Flutter Speed, Mode 2 Phase-Plane Trajectory, Edge 159
Figure 6.19: ATM-Wing Post-Flutter Response Near Flutter Speed, Mode 3 Displacement, Edge 160
Figure 6.20: ATM-Wing Post-Flutter Response Near Flutter Speed, Mode 4 Displacement, Edge 160
Figure 6.21: ATM-Wing Post-Flutter Response Near Flutter Speed, cZ, Edge 161
Figure 6.22: ATM-Wing Estimated Modal Parameters, Edge 163
Figure 6.23: ATM-Wing Response Below Flutter Speed, Mode 1 Displacement, MATLAB (nonlinear) 165
Figure 6.24: ATM-Wing Response Below Flutter Speed, Mode 1 Phase-Plane Trajectory, MATLAB (nonlinear) 165
Figure 6.25: ATM-Wing Response Below Flutter Speed, Mode 2 Displacement, MATLAB (nonlinear) 166
Figure 6.26: ATM-Wing Response Below Flutter Speed, Mode 2 Phase-Plane Trajectory, MATLAB (nonlinear) 166
Figure 6.27: ATM-Wing Response Below Flutter Speed, cZ, MATLAB (nonlinear) 167
Figure 6.28: ATM-Wing Pre-Flutter Response Near Flutter Speed, Mode 1 Displacement, MATLAB (nonlinear) 168
Figure 6.29: ATM-Wing Pre-Flutter Response Near Flutter Speed, Mode 1 Phase-Plane Trajectory, MATLAB (nonlinear) 169
Figure 6.30: ATM-Wing Pre-Flutter Response Near Flutter Speed, Mode 2 Displacement, MATLAB (nonlinear) 169
Figure 6.31: ATM-Wing Pre-Flutter Response Near Flutter Speed, Mode 2 Phase-Plane Trajectory, MATLAB (nonlinear) 170

Figure 6.32: ATM-Wing Pre-Flutter Response Near Flutter Speed, Mode 3 Displacement, MATLAB (nonlinear) 170
Figure 6.33: ATM-Wing Pre-Flutter Response Near Flutter Speed, Mode 3 Displacement, Transition, MATLAB (nonlinear) 171
Figure 6.34: ATM-Wing Pre-Flutter Response Near Flutter Speed, Mode 4 Displacement, MATLAB (nonlinear) 171
Figure 6.35: ATM-Wing Pre-Flutter Response Near Flutter Speed, Mode 4 Displacement, Transition, MATLAB (nonlinear) 172
Figure 6.36: ATM-Wing Pre-Flutter Response Near Flutter Speed, cZ, MATLAB (nonlinear) 172
Figure 6.37: ATM-Wing Post-Flutter Response Near Flutter Speed, Mode 1 Displacement, MATLAB (nonlinear) 174
Figure 6.38: ATM-Wing Post-Flutter Response Near Flutter Speed, Mode 1 Phase-Plane Trajectory, MATLAB (nonlinear) 175
Figure 6.39: ATM-Wing Post-Flutter Response Near Flutter Speed, Mode 2 Displacement, MATLAB (nonlinear) 175
Figure 6.40: ATM-Wing Post-Flutter Response Near Flutter Speed, Mode 2 Phase-Plane Trajectory, MATLAB (nonlinear) 176
Figure 6.41: ATM-Wing Post-Flutter Response Near Flutter Speed, Mode 3 Displacement, MATLAB (nonlinear) 176
Figure 6.42: ATM-Wing Post-Flutter Response Near Flutter Speed, Mode 4 Displacement, MATLAB (nonlinear) 177
Figure 6.43: ATM-Wing Post-Flutter Response Near Flutter Speed, cZ, MATLAB 177
Figure 6.44: ATM-Wing Estimated Modal Parameters, MATLAB (nonlinear) 179
Figure 6.45: ATM-Wing Response Below Flutter Speed, Mode 2 Displacement, MATLAB (linear) 181
Figure 6.46: ATM-Wing Pre-Flutter Response Near Flutter Speed, Mode 2 Displacement, MATLAB (linear) 182
Figure 6.47: ATM-Wing Post-Flutter Response Near Flutter Speed, Mode 2 Displacement, MATLAB (linear) 183
Figure 6.48: ATM-Wing Response Below Flutter Speed, Mode 3 Displacement, MATLAB (linear) 183
Figure 6.49: ATM-Wing System Root Locus Plot, MATLAB (linear) 184

Figure 6.50: ATM-Wing Modal Parameter Variation with Dynamic Pressure, MATLAB (linear) 186
Figure 6.51: ATM-Wing Modal Parameter Variation with Dynamic Pressure Near Flutter, MATLAB (linear) 187
Figure 6.52: ATM-Wing Zimmerman-Weissenberger Flutter Margin Variation with Dynamic Pressure, MATLAB (linear) 188
Figure 6.53: ATM-Wing Envelope Function Shape Parameter Variation with Dynamic Pressure, MATLAB (nonlinear) 189
Figure 6.54: Comparison of Modal Frequencies Modelled for the ATM-Wing by Edge, MATLAB (nonlinear), and MATLAB (linear) 190
Figure 6.55: Flutter Envelope of the ATM-Wing at $\boldsymbol{M = 2.51}$*, MATLAB (linear)* 193
Figure 6.56: Theoretical Calculations of Morgan et al for Model 3451 of the Tuovali-McCarty Flutter Tests [50] 197
Figure 6.57: Theoretical Calculations of Xianxin for Model 5151 of the Tuovali-McCarty Flutter Tests [60] 198
Figure 6.58: Theoretical Calculations of Xianxin for Model 4301 of the Tuovali-McCarty Flutter Tests [60] 199
Figure 6.59: Theoretical Calculations of Xianxin for Model 3451 of the Tuovali-McCarty Flutter Tests [60] 199
Figure 6.60: Theoretical Calculations of Xianxin for Model 1601 of the Tuovali-McCarty Flutter Tests [60] 200
Figure 6.61: Tuovali-McCarty Model 5151A, Comparison of Flutter Predictions 204
Figure 6.62: Tuovali-McCarty Model 5151C, Comparison of Flutter Predictions 204
Figure 6.63: Tuovali-McCarty Model 5151, Flutter Dynamic Pressure Variation with Mach Number 205
Figure 6.64: Tuovali-McCarty Model 5151, Flutter Altitude-Stiffness Parameter Variation with Mach Number 205
Figure 6.65: Tuovali-McCarty Model 5151, Variation of Computational-Experimental Flutter Frequency Ratio with Mach Number 206
Figure 6.66: Tuovali-McCarty Model 4301, Flutter Dynamic Pressure Variation with Mach Number 208
Figure 6.67: Tuovali-McCarty Model 4301, Flutter Altitude-Stiffness Parameter Variation with Mach Number 208

Figure 6.68: Tuovali-McCarty Model 4301, Variation of Computational-Experimental Flutter Frequency Ratio with Mach Number.....209
Figure 6.69: Tuovali-McCarty Model 3451, Flutter Dynamic Pressure Variation with Mach Number.....210
Figure 6.70: Tuovali-McCarty Model 3451, Flutter Altitude-Stiffness Parameter Variation with Mach Number.....211
Figure 6.71: Tuovali-McCarty Model 3451, Variation of Computational-Experimental Flutter Frequency Ratio with Mach Number.....211
Figure 6.72: Tuovali-McCarty Model 1601, Flutter Dynamic Pressure Variation with Mach Number.....213
Figure 6.73: Tuovali-McCarty Model 1601, Flutter Altitude-Stiffness Parameter Variation with Mach Number.....213
Figure 6.74: Tuovali-McCarty Model 1601, Variation of Computational-Experimental Flutter Frequency Ratio with Mach Number.....214
Figure 6.75: Planform of the Unswept Tapered Fins.....216
Figure 6.76: Profile of the Unswept Tapered Fins.....216
Figure 6.77: Variation of the Flutter Dynamic Pressure Envelope with Fin Taper Ratio....218
Figure 6.78: Variation of the Flutter Frequency Envelope with Fin Taper Ratio 219
Figure A.1: Typical Planform of the Tuovali and McCarty Models.....231
Figure A.2: Typical Profile of the Tuovali and McCarty Models.....231
Figure B.1: Coordinate Transformation in the Finite Element Method.....240
Figure B.2: Discontinuity in Strain at Nodes 246
Figure D.1: Normal Force Coefficient vs Angle-of-Attack, Undeformed ATM-Wing, Mach 1.4 259
Figure D.2: Axial Force Coefficient vs Angle-of-Attack, Undeformed ATM-Wing, Mach 1.4 260
Figure D.3: Pitching Moment Coefficient (LE root) vs Angle-of-Attack, Undeformed ATM-Wing, Mach 1.4.....260
Figure D.4: Comparison of Normal Force Coefficients, Undeformed A TM-Wing, Mach 1.4 261
Figure D.5: Comparison of Pitching Moment Coefficients, Undeformed ATM-Wing, Mach 1.4.....261
Figure D.6: Normal Force Coefficient vs Angle-of-Attack, Undeformed ATM-Wing, Mach 1.8 262

Figure D.7: Axial Force Coefficient vs Angle-of-Attack, Undeformed ATM-Wing, Mach 1.8 262
Figure D.8: Pitching Moment Coefficient (LE root) vs Angle-of-Attack, Undeformed ATM-Wing, Mach 1.8 263
Figure D.9: Comparison of Normal Force Coefficients, Undeformed A TM-Wing, Mach 1.8 263
Figure D.10: Comparison of Pitching Moment Coefficients, Undeformed ATM-Wing, Mach 1.8.....264
Figure D.11: Normal Force Coefficient vs Angle-of-Attack, Undeformed ATM-Wing, Mach 5 264
Figure D.12: Axial Force Coefficient vs Angle-of-Attack, Undeformed ATM-Wing, Mach 5 265
Figure D.13: Pitching Moment Coefficient (LE root) vs Angle-of-Attack, Undeformed ATM-Wing, Mach 5 265
Figure D.14: Comparison of Normal Force Coefficients, Undeformed A TM-Wing, Mach 5 266
Figure D.15: Comparison of Pitching Moment Coefficients, Undeformed ATM-Wing, Mach 5 266
Figure E.1: ATM-Wing Deformed Mesh, Mode 1, Wing Tip.....267
Figure E.2: ATM-Wing Deformed Mesh, Mode 2, Wing Tip.....268
Figure E.3: ATM-Wing Deformed Mesh, Mode 3, Wing Tip.....268
Figure E.4: ATM-Wing Deformed Mesh, Mode 4, Wing Tip.....269

List of Tables

Table 2.1: Algorithm Selection Through Choice of Parameters in the Newmark-β Scheme [46] 32
Table 3.1: Comparison of Piston Theories and Associated Coefficients [12] 51
Table 3.2: Comparison of Busemann and Donov Expansions [12] 51
Table 3.3: Definition of Terms in Generalized Piston Theory 64
Table 3.4: Multiplication of Symmetric and Anti-Symmetric Terms 68
Table 3.5: First-Order Downwash Terms and Differences 71
Table 3.6: Second-Order Downwash Terms and Differences 71
Table 3.7: Third-Order Downwash Terms and Differences 71
Table 5.1: Material Properties of the FEM Model of the ATM-Wing 101
Table 5.2: Comparison of Natural Frequencies for the TM-Wing 102
Table 5.3: Computed Natural Frequencies for the TM Wing 107
Table 5.4: Mesh 1 Statistics 109
Table 5.5: Mesh 2 Statistics 112
Table 5.6: Modal Displacements used for Mesh Deformation Calculations in Edge 120
Table 5.7: Flow Conditions for the ATM-Wing, $\boldsymbol{M = 2.51}$, $\boldsymbol{\alpha = 0.5°}$ 124
Table 5.8: Steady Results for the Undeformed ATM-Wing, $\boldsymbol{M = 2.51}$, $\boldsymbol{\alpha = 0.5°}$, $\boldsymbol{q = 108\ kPa}$ 125
Table 5.9: Steady Results for the Elastic ATM-Wing, $\boldsymbol{M = 2.51, \alpha = 0.5°, q = 108\ kPa}$ 131
Table 5.10: Accuracy of MATLAB Computation for the ATM-Wing, Mode 1 Prescribed Step 138
Table 5.11: Accuracy of MATLAB Computation for the ATM-Wing, Mode 2 Prescribed Step 139
Table 5.12: Accuracy of MATLAB Computation for the ATM-Wing, Mode 3 Prescribed Step 140
Table 5.13: Accuracy of MATLAB Computation for the ATM-Wing, Mode 4 Prescribed Step 141

Table 5.14: Modal Aerodynamic Stiffness Matrix of the ATM-Wing,$\boldsymbol{M = 2.51, \alpha = 0.5°, q = 108\ kPa}$ 142
Table 5.15: Estimated Aeroelastic Modal Frequencies of the ATM-Wing, $\boldsymbol{M = 2.51, \alpha = 0.5°, q = 108\ kPa}$ 143
Table 6.1: Natural Frequencies of the Torii and Matsuzaki Wing [54] 144
Table 6.2: Geometry of the Torii and Matsuzaki Wing [54] 145
Table 6.3: Comparison of the Flutter Points Predicted by Simulation 191
Table 6.4: Comparison of Typical Computation Times for the ATM-Wing 192
Table 6.5: Summary of Planform Geometry of the Tuovali and McCarty Test Models [53] 195
Table 6.6: Wind-Tunnel Condition and Flutter Parameters - Model 5151 [53] 196
Table 6.7: Wind-Tunnel Condition and Flutter Parameters - Model 4301 [53] 196
Table 6.8: Wind-Tunnel Condition and Flutter Parameters - Model 3451 [53] 196
Table 6.9: Wind-Tunnel Condition and Flutter Parameters - Model 1601 [53] 196
Table 6.10: Comparison of Flutter Results from ASTROS* with Experimental Data - Model 5151, Test A [52] 201
Table 6.11: Comparison of Flutter Results from ASTROS* with Experimental Data - Model 5151, Test C [52] 201
Table 6.12: Geometry and Material Constants for the Parametric Study 217
Table A.1: Dimensions of the Tuovali and McCarty Models 230
Table B.1: Acceptable QUAD4 Element Distortions 237
Table F.1: Prescribed Motion Results for Mode 1, Step Size $\mathbf{1\ x\ 10-5}$ 270
Table F.2: Prescribed Motion Results for Mode 1, Step Size $\mathbf{1\ x\ 10-6}$ 270
Table F.3: Prescribed Motion Results for Mode 2, Step Size $\mathbf{1\ x\ 10-5}$ 271
Table F.4: Prescribed Motion Results for Mode 2, Step Size $\mathbf{1\ x\ 10-6}$ 271
Table F.5: Prescribed Motion Results for Mode 3, Step Size $\mathbf{1\ x\ 10-5}$ 272
Table F.6: Prescribed Motion Results for Mode 3, Step Size $\mathbf{1\ x\ 10-6}$ 272
Table F.7: Prescribed Motion Results for Mode 4, Step Size $\mathbf{1\ x\ 10-5}$ 273
Table F.8: Prescribed Motion Results for Mode 4, Step Size $\mathbf{1\ x\ 10-6}$ 273

List of Symbols and Abbreviations

Matrices and Vectors

$\{\vec{a}\}$	full-order acceleration vector
$\boldsymbol{C}$	full-order damping matrix
$\boldsymbol{C_{mod}}$	modal-order damping matrix
$\{\vec{d}\}$	full-order displacement vector
$\vec{F}$	loading vector
$\boldsymbol{H}$	defined by equation (4.53)
$\boldsymbol{I}$	identity matrix
$\boldsymbol{K}$	full-order stiffness matrix
$\boldsymbol{K_{mod}}$	modal-order stiffness matrix
$\boldsymbol{M}$	full-order mass matrix
$\boldsymbol{M_{mod}}$	modal-order mass matrix
$\vec{Q}$	generalized aerodynamic force vector
$\{\vec{u}\}$	general displacement vector
$\{\dot{\vec{u}}\}$	general velocity vector
$\{\ddot{\vec{u}}\}$	general acceleration vector
$\{\vec{\tilde{u}}_{t+\Delta t}\}$	predicted general displacement vector at time $t + \Delta t$, predicted from time t
$\{\dot{\vec{\tilde{u}}}_{t+\Delta t}\}$	predicted general velocity vector at time $t + \Delta t$, predicted from time t
$\{\vec{v}\}$	full-order velocity vector
$\boldsymbol{X}$	modal matrix
$\{\vec{x}\}$	modal displacement vector
$\{\dot{\vec{x}}\}$	modal velocity vector
$\{\ddot{\vec{x}}\}$	modal acceleration vector

Symbols

A_i	coefficients of the system characteristic equation
AR	aspect ratio
a	speed of sound
b	semi-span

C_A	axial force coefficient
C_D	drag coefficient
C_L	lift coefficient
$C_{M_{LE}}$	pitching moment coefficient (taken about the leading-edge root)
C_N	normal force coefficient
C_P	pressure coefficient
C_{P_L}	pressure coefficient on the lower surface
C_{P_U}	pressure coefficient on the upper surface
c	chord length
$\bar{c}$	mean aerodynamic chord
c_1, c_2, c_3	piston theory coefficients, defined in equation (3.29) and Table 3.1
E	binomial expansion for unsteady pressure, as defined in equations (3.2) and (3.6)
e_t	white-noise signal in ARMA modelling
$env(t)$	envelope function
F	force
FM	flutter margin
f	frequency (Hz)
$fn(\ \ )$	function of
K	hypersonic equivalence parameter, $K = M\tau$, unless otherwise defined
k	reduced frequency, defined by equation (2.18)
M	Mach number
m	Prandtl-Glauert factor, $m = \sqrt{M^2 - 1}$
P	pressure
q	dynamic pressure
S	shape function
S_{ref}	reference area
s	complex number, $s = \sigma + i\omega$
T	period
T	temperature
t	time
Δt	time step
U	velocity in the x-direction
V	velocity magnitude
w	downwash velocity
w_0	contribution to downwash from steady terms
w_1	contribution to downwash from unsteady terms

w_c	contribution to downwash from the camberline
w_t	contribution to downwash from the thickness distribution
w_α	contribution to downwash from inclination of the chordline to the flow
X	x-direction, defined by the root chordline, positive in the aft direction
$y(t)$	time-response signal at time t
y_t	discrete time-response signal at time t
z	vertical displacement of the piston in piston theory;
α	angle of attack
α_1, α_2, ...	Auto-Regressive coefficients in ARMA modelling
β	oblique shock angle
β	displacement-expression parameter in the Newmark-β method
γ	adiabatic expansion coefficient, $\gamma = 1.4$
γ	velocity-expression parameter in the Newmark-β method
δ	flow turning-angle
ε	error (convergence criteria)
ζ	damping ratio
θ	surface inclination relative to reference (specified by subscript)
Λ	sweep angle (°)
λ	planform taper ratio
λ	eigenvalue, $\lambda = -\zeta\omega_n \pm i\omega_d$
ν	Prandtl-Meyer function, defined in equation (2.6)
ρ	air density
τ	flow thickness-ratio, as defined by $\tau = \tan\delta$
ϕ	potential function
ω	angular frequency (rad/s)
ω_d	damped angular frequency (rad/s)
ω_n	natural angular frequency (rad/s)

Subscripts

∞	free-stream
$0.25c$	quarter-chord position
ae	aeroelastic
$aero$	aerodynamic
cyl	cylinder conditions in piston theory
F	flutter
L	lower surface

LE	leading-edge
max	maximum
min	minimum
PT	from piston theory
ref	reference
SE	from shock-expansion theory
seg	segment
$slip$	slip-plane
ss	at local mean steady-state
str	structural
t	at time t
TE	trailing-edge
U	upper surface
x, y, z	in the x-, y-, or z-direction

Superscripts

(i)	iteration i
$\dot{(\ )}$	$\frac{\partial}{\partial t}$
$\ddot{(\ )}$	$\frac{\partial^2}{\partial t^2}$

Abbreviations / Acronyms

ATM	approximated Torii-Matsuzaki
CFD	computational fluid dynamics
DOF	degree of freedom
FEM	finite element method
GAF	generalized aerodynamic force
LPT	local piston theory
PT	piston theory
SBT	slender body theory
SE	shock-expansion
SE/LPT	local piston theory with steady pressures from shock-expansion theory
SHABP	Supersonic/Hypersonic Arbitrary Body Program
TM	Torii-Matsuzaki

1 INTRODUCTION

1.1 Introduction

A multidisciplinary approach is essential in missile design to ensure that all the required missile performance specifications are achieved. Various discipline often place conflicting requirements on design parameters: for example, minimization of aerodynamic drag may require the thickness of a missile fin to be decreased; however, this reduces the structural stiffness and strength in bending of the missile fin. The interaction between several disciplines is typical of aerospace structures, as is evident from the research [1] conducted on aeroelasticity (interaction of aerodynamics and structure), aero-thermo-elasticity (interaction of aerodynamics, thermal effects, and structure), aero-servo-elasticity (interaction of aerodynamics, control, and structure), and aero-thermo-servo-elasticity (interaction of aerodynamics, thermal effects, control, and structure). These interactions are shown in Figure 1.1.

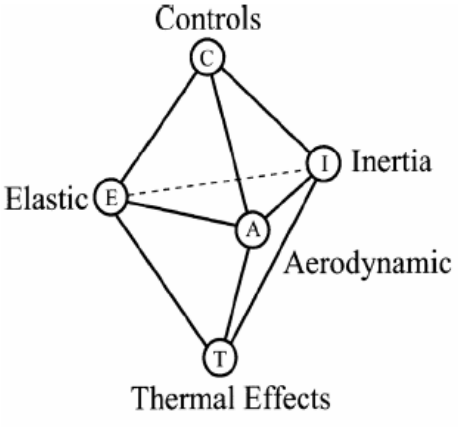


Figure 1.1: Multidisciplinary Interaction in Aerospace Design **[1]**

Consideration of the aeroelastic response of the missile under loading is typically performed in the detailed development phase of the design cycle, as aeroelastic analysis is generally time-consuming and requires modelling of the missile aerodynamics and structural dynamics. If it is found that the design exhibits aeroelastic instabilities or undesirable structural response at this stage, the "fixes" required will add weight to the structure, impacting the predicted performance of the missile.

Preliminary analysis of aeroelastic effects early in the design cycle would broaden the scope of evaluation of design concepts. The more holistic analysis would better filter feasible concepts, thus reducing the risk and cost of corrective modifications later in the design cycle.

Aeroelastic effects on missile fins may have a further impact on other disciplines. Not only must the structural integrity be assessed, but the effectiveness of the missile control must be considered. Controller and actuator design must account for the reduced effectiveness of control input. Furthermore, the shift in centre of pressure due to aeroelastic effects changes the hinge moment required for trim -- this may vary dynamically for a flexible fin undergoing vibration, which poses a control, or aero-servo-elastic, problem.

The prediction of aeroelastic effects, particularly of flutter, is also important from the point of view of operational safety during the development and testing of missiles. Once the design has progressed sufficiently far, wind-tunnel tests of a model of the missile will typically be conducted. When a geometrically-scaled model is tested, the aerodynamic effects and the structural effects scale differently due to the differences in physics for the structure and for aerodynamics. Thus, it may occur that it is unsafe to test a geometrically-scaled model of a full-scale missile, even if the full-scale model was designed with aeroelastic effects accounted for. The loss of wind-tunnel models to unanticipated aeroelastic effects has occurred even with models that were designed to investigate aeroelasticity, as in the case of the loss of Flexible Semi-span Model of NASA's High Speed Civil Transport project to "hard" flutter [2]. The prediction of the aeroelastic behaviour of a model before it is constructed is therefore important not only out of consideration of cost, but also important for safe testing.

1.2 Review of Software for Approximate Aeroelastic Analysis

Several commercial software packages are available which allow the aeroelasticity of various geometries to be modelled. Such software varies in the fidelity of the analysis performed. Generally, the lower-order modelling consists of the coupling of a structural finite element code with unsteady aerodynamic panel methods; however, the number of codes implementing supersonic panel methods is limited. High fidelity analysis may be conducted through the coupled solution of the structural and aerodynamic physics with a coupling of structural finite elements and computational fluid dynamics. Lower-order modelling is implemented earlier in the design phase to obtain approximate solutions at relatively low computational cost. These approximate solutions allow for design refinement, and serve as a filter and guide for higher fidelity analysis later in the design cycle.

In general, the variety of software packages for lower-order modelling that is commercially available allow the user to analyse the aeroelastic response of a general body with lifting surfaces and stores. A variety of aerodynamic methods are used, as well as a variety of methods for the prediction of the flutter speed. Whilst the literature and software available for subsonic aerodynamic panelling and aeroelastic analysis is relatively broad, there are few software packages that allow for approximate aeroelastic analysis. The two main codes for low-order supersonic and hypersonic aeroelastic modelling are the MSC NASTRAN Aeroelasticity module [3] and the ZAERO [4] range of codes.

1.2.1 MSC NASTRAN

MSC NASTRAN incorporates approximate aerodynamic modelling alongside advanced analysis of structural dynamics. For flutter analysis, the aerodynamic modelling includes the double-lattice method and strip theory for subsonic flow, and the Mach box method, piston theory, and ZONA51 for supersonic flow [3]. The flutter calculation may be made using three classical flutter calculation methods, including the k method, and efficient k method, and the p-k method [3].

1.2.2 ZONA7

Zona Technology Inc. offers a wide range of software for high-fidelity aeroelastic analysis [4]. The software ranges from aeroelastic panel methods to a fully coupled nonlinear aeroelastic unsteady Euler solver. ZONA7 is the unsteady supersonic aerodynamics module of the ZAERO software suite, with the capability to analyse unsteady supersonic/hypersonic (ZONA7U) aerodynamics for wing-body/aircraft configurations with external stores/nacelles [5]. It is a high-order panelling method which is linked in the ZAERO formulation to a flutter solver, allowing for flutter solution using the k- / p-k / g-methods [5].

ZONA51U is related to ZONA7U, being an older version of the software, and is implemented in the aeroelastic module of MSC NASTRAN.

1.2.3 NeoCASS

NeoCASS is an aero-structural design tool originally developed at the Dipartimento di Ingegneria Aerospaziale of Politecnico di Milano, which has been embedded in the open source MDD environment CEASIOM [6]. NeoCASS is written as a suite of MATLAB, and combines semi-empirical and analytical methods for weight estimation and sizing of transport aircraft (although the suite may be applied to other configurations). The suite includes a structural FEM solver, panel-method aerodynamics for subsonic flows (vortex-lattice and doublet-lattice methods), and a flutter solver. The results of structural modal analysis in NeoCASS may be exported for high-fidelity aeroelastic analysis in the Edge CFD solver. As of the date of publication, NeoCASS does not include aerodynamic methodology for supersonic flows.

1.2.4 NEAR Software

Nielsen Engineering and Research Inc. (NEAR) have developed a number of codes for the aerodynamic analysis of missiles, with output to FEM solvers such as NASTRAN [7]. The codes vary in complexity from engineering-level prediction codes for missile aerodynamics to reduced-order modelling codes. The MISDL code provides detailed loading on the various components of the missile, including the load distribution over the fin; the effects of body and fin vortices as well as damping due to rotational rates is included. NEAR has also developed

a nonlinear Volterra kernel identification system [7] for the prediction of unsteady aerodynamics. The Volterra kernel represents a modelling of nonlinear systems with memory effects through the use of multi-dimensional convolutions [8]. Whilst the NEAR software provides the aerodynamic loading on the structure, no structural or aeroelastic analysis is performed within the software.

1.3 Objectives of the Dissertation

Whilst the study of aeroelasticity in supersonic flows is by no means a new topic, the literature available on the approximate aeroelastic modelling of cantilevered plates in supersonic flow is relatively sparse compared to the literature on the modelling of 2-dimensional airfoils with rigid cross-section.

Recent literature [1; 9; 10; 11; 12] has shown a renewal in the application of piston theory for the approximate modelling of unsteady aerodynamic pressures, and further developments in its application have been made. Among these developments is the extension to local piston theory and the use thereof to provide the unsteady aerodynamics about a high-fidelity, dynamically linearized steady-state solution [11]. This application of local piston theory has been shown [11] to model the unsteady aerodynamics with good accuracy, leading to vastly reduced computation time for aeroelastic studies. The literature on the application of local piston theory with approximate aerodynamic methods for the steady-state aerodynamics is very limited.

Flight vehicles that operate at high speeds and altitudes are susceptible to potentially catastrophic aeroelastic phenomena, such as "hard" flutter [2]. The design of these vehicles requires aeroelastic analysis to be applied during the design cycle; in practice, it is often applied relatively lately in the design. The implementation of approximate aeroelastic analysis would make it computationally feasible to include the consideration of aeroelastic effects earlier in the design cycle. This carries the potential to save costs associated with more lengthy design cycle, and may identify potentially hazardous test conditions for wind-tunnel or flight testing.

In light of the above considerations, objectives of this dissertation are to:

1. Add to the literature on the modelling of aeroelasticity in cantilevered plates in supersonic flows,
2. Develop a tool suitable for preliminary parametric studies of the effect of fin geometry on flutter boundaries,
3. Compare the performance of flutter prediction methods applied to an analytical system with no signal noise, and to hence determine the metric most suitable for implementation in an approximate aeroelastic analysis method,
4. Investigate the ability of approximate aeroelastic modelling to model dangerous aeroelastic phenomena such as "hard" flutter.

1.4 Outline of the Dissertation

The dissertation is divided into seven chapters, the content and purpose of which is as follows.

Chapter 1 introduces the topic of aeroelastic prediction software for supersonic flows, and the importance of aeroelastic analysis in both the design of new products and their testing. A short review of commercial software packages for low-order aeroelastic analysis in made, and the objectives of the dissertation are introduced.

Chapter 2 provides a literature review on the various facets of aeroelastic modelling. The topics of the review include: approximate methods of modelling steady and unsteady supersonic aerodynamics; the coupling of structural dynamics and aerodynamics; dynamic and spatial linearity and nonlinearity; the characterization of aeroelastic response below flutter speed; literature on experimental investigation of supersonic flutter of cantilevered plates; and flutter prediction methods.

Chapter 3 gives an exposition on piston theory and the differences between classical and local piston theory. The differences introduced in the physics modelled by higher order piston theories are investigated.

Chapter 4 consists of an overview of the methodology used in the structural, aerodynamic, and aeroelastic modelling of a cantilevered plate in supersonic flow, as implemented in the development of an aeroelastic prediction tool for missile fins.

Chapter 5 is on the validation of the developed aeroelastic prediction method through comparison with aeroelastic modelling through computational fluid/structural dynamics. The chapter covers the validation of the structural solver against MSC NASTRAN, and the validation of the aerodynamic solver against 3D Euler computations in the CFD solver Edge. The aerodynamic validation includes the validation of the steady aerodynamics of a rigid, undeformed cantilevered plate, the validation of the transient deformation to steady-state of an elastic cantilevered plate, and the validation of the aerodynamic response to prescribed step motions of the plate.

Chapter 6 shows the application of the developed aeroelastic prediction method in the aeroelastic analysis and flutter prediction for various fin geometries. Comparison to experimental results in literature, where available, is made.

Chapter 7 summarizes the work accomplished in the dissertation and provides recommendations for future work.

2 REVIEW OF APPROXIMATE METHODS OF MODELLING OF AEROELASTICITY IN SUPERSONIC FLOWS

2.1 Approximate Modelling of Supersonic Aerodynamics

2.1.1 Shock-Expansion Theory

Shock-expansion theory assumes local Prandtl-Meyer expansion or compression along the surface of an airfoil behind a shock; the properties immediately behind the shock are calculated using oblique shock theory, or using the Taylor-Maccoll cone results for bodies of revolution [13]. The reflection of expansion wave characteristics off of streamlines and the bow shock is neglected, and it is assumed that the nose is sharp, the leading-edge shock is attached, and flow is locally supersonic everywhere. Shock-expansion theory may be modified for application to 3D flows [14]; here, however, only the application to 2D flows is given.

The equations for the gas properties behind an oblique shock are given [15] below, with reference to Figure 2.1 for the nomenclature:

$$\tan\delta = \frac{2\cot\beta\,(M_1^2\sin^2\beta - 1)}{M_1^2(\gamma + \cos 2\beta) + 2} \qquad (2.1)$$

$$\frac{P_2}{P_1} = 1 + \frac{2\gamma}{\gamma + 1}(M_1^2\sin^2\beta - 1) \qquad (2.2)$$

$$\frac{\rho_2}{\rho_1} = \frac{(\gamma+1)M_1^2 \sin^2\beta}{(\gamma-1)M_1^2 \sin^2\beta + 2} \quad (2.3)$$

$$\frac{T_2}{T_1} = \frac{P_2\rho_1}{P_1\rho_2} \quad (2.4)$$

$$M_2 \sin(\beta-\delta) = \left[\frac{\left(\frac{2}{\gamma-1}\right) + M_1^2 \sin^2\beta}{\left(\frac{2\gamma}{\gamma-1}\right) M_1^2 \sin^2\beta - 1}\right]^{\frac{1}{2}} \quad (2.5)$$

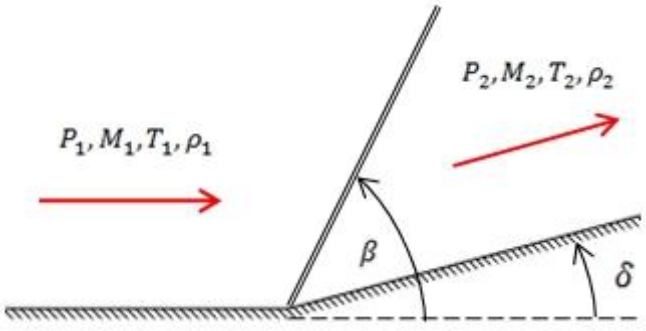


Figure 2.1: Definition of Nomenclature for Oblique Shock Calculations

The equations for the gas properties behind a Prandtl-Meyer expansion fan may be calculated from the Prandtl-Meyer function and from the equations for isentropic flow [15], listed below together with Figure 2.2:

$$\nu = \sqrt{\frac{\gamma+1}{\gamma-1}}\left[\tan^{-1}\left(\sqrt{\frac{\gamma-1}{\gamma+1}(M^2-1)}\right)\right] - \tan^{-1}\left(\sqrt{M^2-1}\right) \quad (2.6)$$

$$\nu_1 = \nu_2 - \delta \quad (2.7)$$

$$\frac{P_2}{P_1} = \left[\frac{1+\left(\frac{\gamma-1}{2}\right)M_1^2}{1+\left(\frac{\gamma-1}{2}\right)M_2^2}\right]^{\frac{\gamma}{\gamma-1}} \quad (2.8)$$

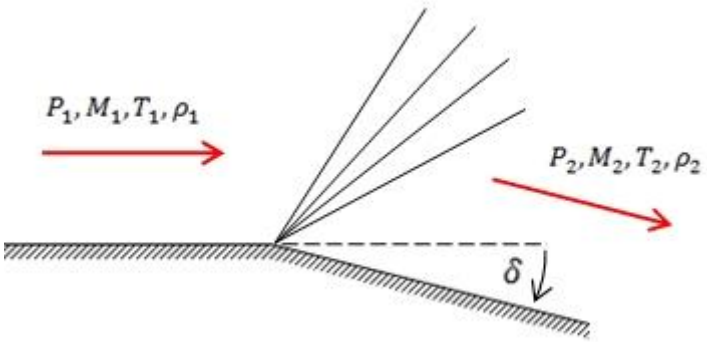


Figure 2.2: Definition of Nomenclature for Prandtl-Meyer Expansion Calculations

Hayes and Probstein [16] reviewed the investigation of the assumption of the absorption of the expansion wave by the bow shock, and reviewed the application and extension of shock-expansion theory by various authors, including extension to axisymmetric bodies at angle of attack. Among the review is the work of Eggers [17], Savin [18], Syverston [17; 19] and Dennis [19]. Shock-expansion theory has been shown to give consistently good results for values of the hypersonic similarity parameter $M_\infty \delta > 1$. Generally, the method gives accurate results for bodies which do not have high curvature at the nose; Hayes and Probstein [16] review the correction that may be applied to surface pressures on the afterbody to account for the reflection of expansion waves from the bock shock.

In the Mark IV version of SHABP [14], shock-expansion theory may be used to find the pressure on body surfaces as well as to compute the shock shape and flowfield.

Shock-expansion theory may be applied over successive chordwise segments for 2D flow; in doing so, the solution marches downstream and the influence of upstream perturbations is accounted for. However, shock-expansion theory assumes steady flow, and the flow history of dynamic perturbations is not washed downstream.

The extension to quasi-steady shock-expansion theory is made in accounting for the downwash contribution in the flow turning-angle δ due to motion at the leading and trailing-edges [10]. For example, for the lower surface of at the leading-edge with wedge angle θ, the flow turning-angle, as shown in Figure 2.3 is given by:

$$\delta = \theta + \alpha' \qquad (2.9)$$

where α' is the quasi-steady angle of attack given by $\alpha' = \alpha + \frac{dz}{dt}$,

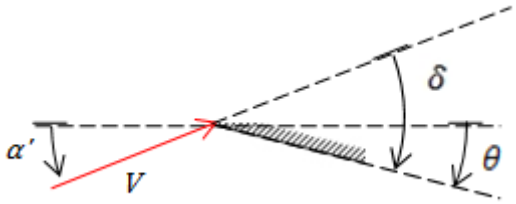


Figure 2.3: Flow Turning-Angle in Quasi-Steady Shock-Expansion Theory

2.1.2 Slender Body Theory

Slender body theory (SBT) has been extended by various authors and its treatment has been widely published. A simple treatment of slender body theory based on linearized supersonic small-disturbance theory, with extension to Munk's airship theory [20] based on the assumption of incompressible cross flow, is given by Gülçat [21]. This places a limit on the range of angles-of-attack for which SBT is valid at supersonic Mach numbers. The treatment provides an expression for the normal-force distribution on the slender body in terms of an axial variation in body cross-section and camber. The equation for unsteady flow is given [21] as:

$$\frac{dL}{dx} = -\rho U_\infty \frac{dS}{dx}\left(\frac{\partial z_a}{\partial t} + U_\infty \frac{\partial z_a}{\partial x}\right) - \rho S\left(\frac{\partial^2 z_a}{\partial t^2} + 2U_\infty \frac{\partial^2 z_a}{\partial x \partial t} + U_\infty^2 \frac{\partial^2 z_a}{\partial x^2}\right) \qquad (2.10)$$

Where $\frac{dL}{dx}$ is the distribution of normal force and z_a denotes the position of the axis of the body (or camberline, for an airfoil with symmetrical thickness). Note that $\left(\frac{\partial z_a}{\partial t} + U_\infty \frac{\partial z_a}{\partial x}\right)$ is equivalent to the upwash of the camberline of the body as it passes through a stationary reference plane (see Section 3.3).

Ashley and Landhal [22] considered SBT without linearizing the potential equation and applying only the small-disturbance approximation. Analytical expressions obtained for the perturbation velocity potential are given in terms of the rate of change of cross-sectional area, from which the surface pressure coefficient may be found. The treatment assumed a smooth variation in cross-section, and was evaluated at low supersonic Mach numbers ($M \approx 1.1$).

Van Dyke [23] treated the extension of SBT to the second-order to extend the range of validity in the parameter $m\delta$ (where $m = \sqrt{M^2 - 1}$), and provided an equation for the pressure coefficient on the surface of a cone from second-order SBT as a function of the cone

semi-vertex angle. Excellent agreement to exact results was obtained for very small cone angles ($\delta = 5°$) for Mach numbers in the range $1 < M_\infty < 5$ as shown in Figure 2.4, whilst poorer agreement was obtained for moderately small cone angles ($\delta = 15°$) at Mach numbers higher than 2, as seen in Figure 2.5. Van Dyke noted that the slender body assumption implied that not only was the thickness small, but that the unified supersonic-hypersonic similarity parameter $m\delta$ was also small. Van Dyke also discussed restrictions on body shape, noting that second-order SBT required a body with sharp ends, with small curvature and a continuous, slow change in curvature.

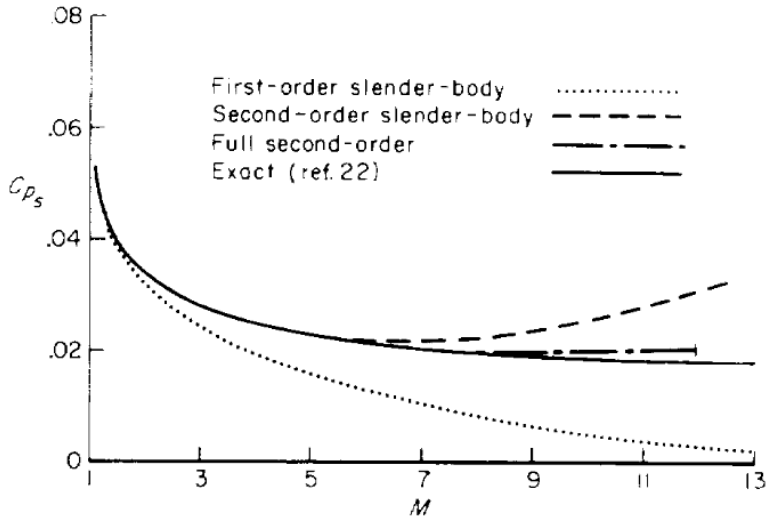


Figure 2.4: Second-Order Slender Body Theory for a Cone with Semi-Vertex Angle 5° **[23]**

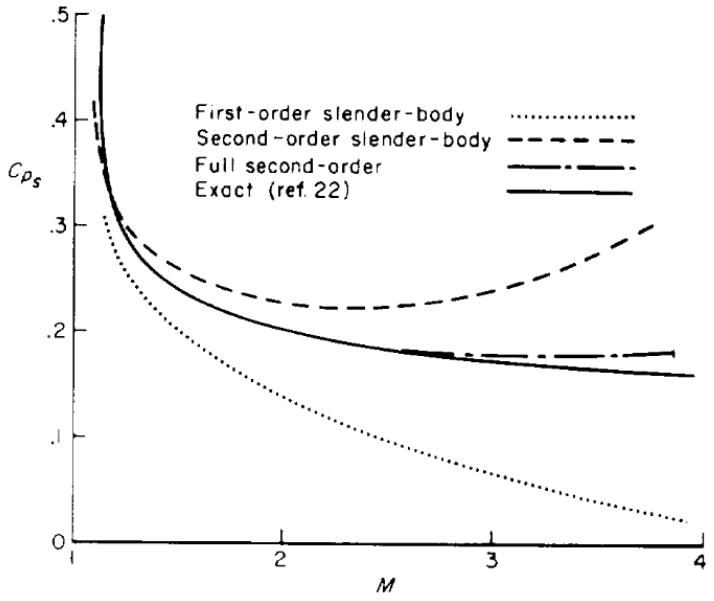


Figure 2.5: Second-Order Slender Body Theory for a Cone with Semi-Vertex Angle 15° **[23]**

Pivko [24] investigated the effect of non-linear velocity perturbation terms on the pressure coefficient predicted by SBT, and also provided a brief review of the development of SBT. Pivko stated that neglecting non-linear terms in the pressure-velocity relation may result in errors in the predicted loading distribution of the order of 100%.

2.1.3 Semi-Empirical Methods

Semi-empirical methods use a combination of empirical data for a variety of body geometries, and of simple analytical expressions (in which empirical approximations are used), to predict the aerodynamic characteristics of a body. Examples of semi-empirical codes for the prediction of supersonic aerodynamics include SHABP [14], the NSWC AeroPrediction codes [25], Missile DATCOM [26]. Typically, the overall aerodynamic coefficients and derivatives are given, with no detailed loading (pressure distribution) given. The load prediction is for rigid geometry; damping derivatives are generally predicted for specified rates of rotation.

2.1.4 Van Dyke's Unified Supersonic/Hypersonic Potential Theory

Hypersonic small-disturbance theory was extended to the supersonic range by Van Dyke [27] through the replacement of the hypersonic similarity parameter $M_\infty \delta$ by the unified supersonic-hypersonic similarity parameter $\left(\sqrt{M^2-1}\right)\delta$. For small deflections with $\delta < 15°$ for wedge flow and $\delta < 10°$ for cones, results from the extension closely correlated [27] to results obtained with the small-disturbance approximation not made, as shown in Figure 2.6. Van Dyke also compared the results of the unified small-disturbance theory with other analytical methods, including Newtonian flows and first-order shock expansion theory. The unified small-disturbance theory was found to give very good results even at small numbers of the unified similarity parameter $(m\delta < 0.5)$ (where $m = \sqrt{M^2-1}$) for small deflection angles. Van Dyke extended existing solutions, as detailed by Hayes and Probstein [16], for the pressure coefficient on the surface of wedges and cones in compression through the use of the unified similarity parameter. The equation for wedges is a function of only the deflection and the unified similarity parameter.

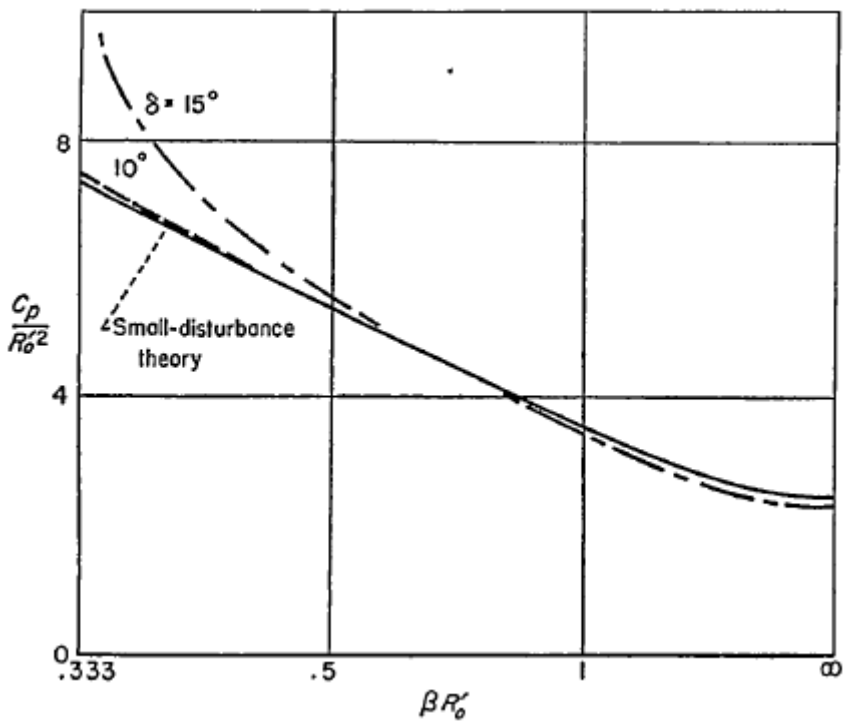


Figure 2.6: Surface Pressure on Wedges from Van Dyke's Unified Supersonic-Hypersonic Small-Disturbance Theory **[27]**

SHABP(PD) [14] includes the wedge equation derived by Van Dyke for wedges in compression, given below:

$$C_P = \delta^2 \left[\frac{\gamma+1}{2} + \sqrt{\left(\frac{\gamma+1}{2}\right)^2 + \frac{4}{(m\delta)^2}} \right] \qquad (2.11)$$

as well as a similar equation for expansion flow with no leading-edge shock:

$$C_P = \delta^2 \frac{2}{\gamma(\beta\delta)^2} \left[\left(1 + \frac{\gamma-1}{2} m\delta\right)^{\frac{2\gamma}{\gamma-1}} - 1 \right] \qquad (2.12)$$

where in both equations, $m = \sqrt{M^2 - 1}$ and δ is the turning angle of the flow.

Hayes and Probstein [16] investigated the extension of application of small-disturbance theory to a variety of bodies, and discussed the extension to large incidences and the correlation to other similarity parameters.

2.1.5 Piston Theory

Piston theory is a method of modelling unsteady aerodynamics in which the local pressure on a surface is approximated by the pressure on an equivalent piston in a 1D cylinder. Several developments and extensions to the method have been made, and will be briefly noted here. The equation for the pressure coefficient at a point (see Chapter 3 for a more general formulation and detailed development) is given by Liu et al [12] as:

$$C_P = \frac{2}{M_\infty^2}\left[c_1\left(\frac{w}{a_\infty}\right) + c_2\left(\frac{w}{a_\infty}\right)^2 + c_3\left(\frac{w}{a_\infty}\right)^3\right] \qquad (2.13)$$

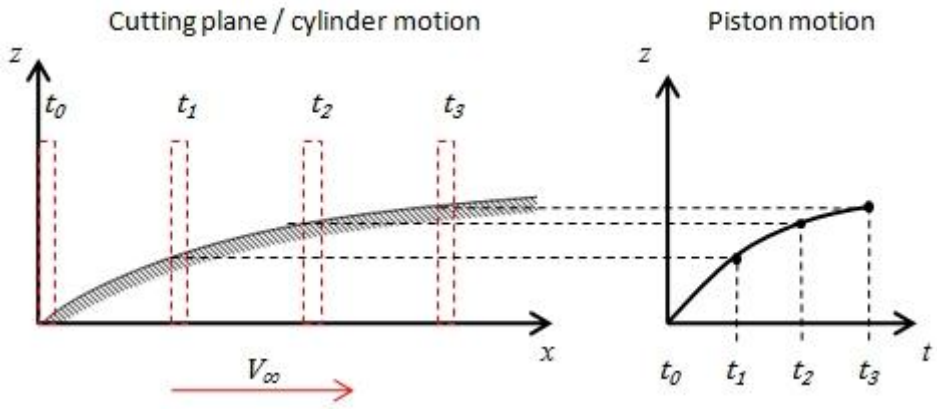


Figure 2.7: The Concept of the Piston in Piston Theory

Gülçat [21] stated that linearized (first-order) piston theory is valid only for values of the hypersonic similarity parameter $0 < M_\infty \tau < 0.15$, where τ is the thickness ratio of the lifting surface (see Figure 2.8), and provided that the body remains at small angles of attack during the motion.

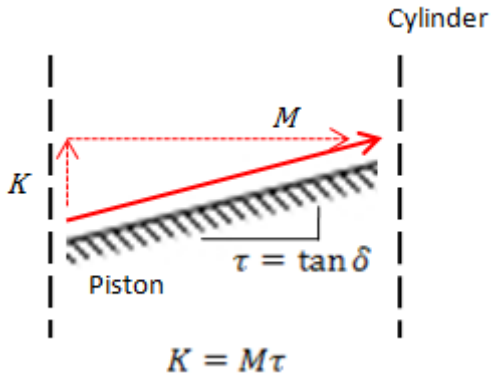


Figure 2.8: Relationship Between Hypersonic Similarity Parameter $\boldsymbol{K = M\tau}$ and Downwash Mach Number

Ashley and Zartarian [28] expanded on the work of Lighthill and Hayes and reviewed related work by other authors at the time, with consideration of a broad range of aeroelastic problems. From the review of literature collected, the limitation on validity of linearized piston theory was made to flows where $M \gg 1$, $kM^2 \gg 1$ or $k^2M^2 \gg 1$, where k is the reduced frequency of oscillation ($k = \omega c/2U_\infty$).

Liu et al. [12] reviewed later developments related to piston theory and investigated the range of validity of piston theory in its various formulations. Particular attention was given to third-order formulations to include nonlinear thickness and angle of attack effects [12] (see Section 3.4 and Section 3.6), with the results of Busemann and Donov cited. It was noted that differences in the third-order terms between piston-theory formulations arose from the theoretical basis for the series-expansion [12] (see also Section 3.4).

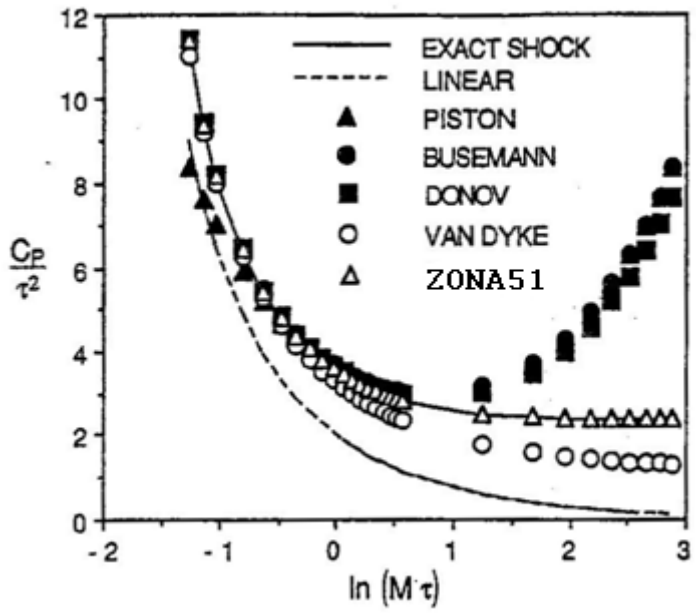


Figure 2.9: Pressure Coefficient on a 15° Wedge from Various Piston Theories **[12]**

Liu et al. deduced that piston theory has a limited range of validity for a wedge of semi-angle 10° of $2.1 < M < 6.0$. From these considerations, Liu et al. [12] developed an extension to a "unified lifting surface method" applicable from low supersonic speeds to hypersonic speeds. The method is essentially a combination of third-order piston theory with a supersonic lifting surface theory. The method was developed into the ZONA51U code. Good agreement of results to more exact analyses and experimental data (where available) was obtained (as shown in Figure 2.9), with good results obtained for stiffness and damping moments, stability

derivatives, and flutter boundaries. Pending further validation, a limitation to wings with sharp leading-edges of thickness $\tau = \tan 15°$ for supersonic Mach numbers up to 10 was estimated [12].

Zhang et al. [11] integrated the use of a local piston theory with a steady mean flow solution by an Euler method. The mean flow was solved by the Euler method to account for 3D effects and upstream influence, and the unsteady component was treated locally by application of piston theory to surface deviations. It was found that the combined analysis gave very accurate results [10; 11; 29] (compared to full unsteady Euler computation) even for airfoils with round leading-edges (such as the NACA 0012), and for reduced frequencies as high as $k = 0.1$, as seen in Figure 2.10. Flutter analysis using local piston theory also produced results in good agreement with full Euler solutions, as shown in Figure 2.11. The method is an extension of piston-theory to CFD, with vastly increased computational efficiency over a full unsteady solution as only a single steady-state solution is required for the method.

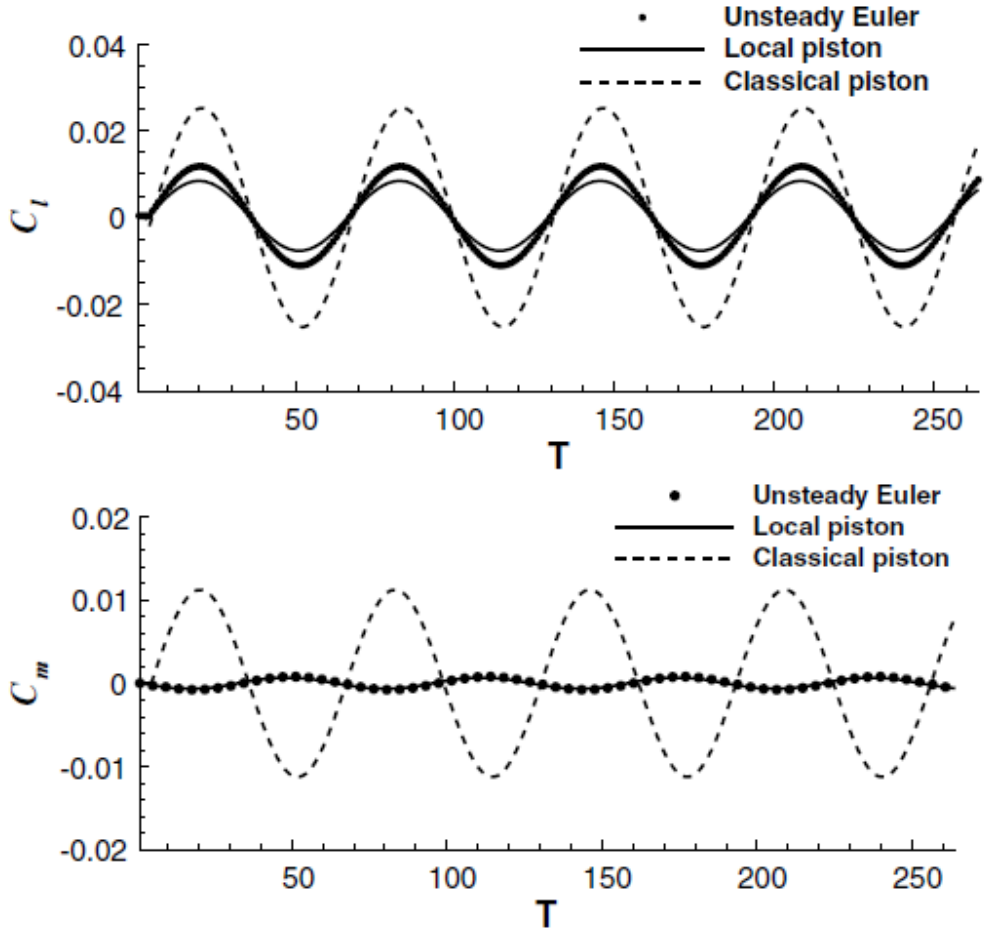


Figure 2.10: Time History of Aerodynamic Loading on a NACA 0012 Airfoil from Local Piston Theory **[11]**

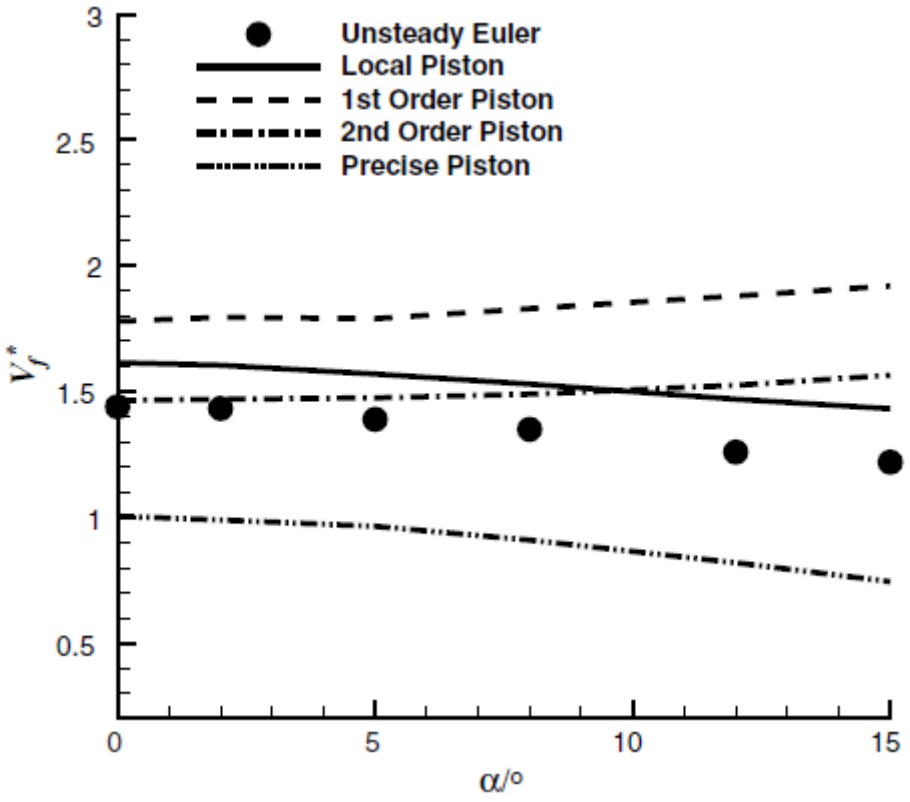


Figure 2.11: Flutter Speed vs α for a NACA 64A010 Airfoil from Local Piston Theory **[11]**

McNamara et al. [10] reviewed the current state of approximate modelling of unsteady aerodynamics for the computation of hypersonic aeroelasticity. First-order, third-order, and local piston theory were investigated relative to other approximate methods (including unsteady shock-expansion, Van Dyke's second-order theory, and unsteady Newtonian impact), relative to methods employing Euler solutions (piston-theory corrected steady-state solutions), and relative to full unsteady Navier-Stokes solutions. Results were compared for a 3.36% thick double-wedge airfoil for Mach numbers $M_\infty > 5$. Results from second-order and third-order piston theory for the flutter boundary prediction were in excellent agreement with the Navier-Stokes results for values of the hypersonic similarity parameter $0.25 < M\tau < 1$. It was found that first-order local piston theory gave excellent correlation, and it was deduced that aeroelastic stability is strongly influenced by thickness effects, the influence of which on the generalized aerodynamic forces may be modelled using steady-state flow analysis [10].

The reader is referred to Chapter 3 for a more detailed discussion on piston theory.

2.1.6 Mach Box Method

The Mach Box method is a numerical solution to determine the unsteady perturbation potential for the linearized supersonic potential flow equations for unsteady 3-dimensional flows [30]:

$$\nabla^2\phi - \frac{1}{a_\infty^2}\left[\frac{\partial^2\phi}{\partial t^2} + 2U_\infty\frac{\partial^2\phi}{\partial x\partial t} + U_\infty^2\frac{\partial^2\phi}{\partial x^2}\right] = 0 \qquad (2.14)$$

or, rearranged with alternative notation for the differentiation with respect to variables:

$$(1-M^2)\phi_{xx} + \phi_{yy} + \phi_{zz} = \frac{1}{a_\infty^2}\phi_{tt} + \frac{2M}{a_\infty}\phi_{xt} \qquad (2.15)$$

The potential function is assumed to vary sinusoidally.

$$\phi = \bar{\phi}(x,y,z)e^{i\omega t} \qquad (2.16)$$

The resulting equation for the potential function at a point in the flowfield is an integral of the downwash over the surface of the flowfield bounded by upstream-facing Mach cone at the point, and the portion of the upstream flowfield which is influenced by the wing. The equation for the amplitude of the harmonically oscillating potential function at a point $(x^*, y^*, 0)$ is given [30] by:

$$\bar{\phi}(x^*,y^*,0) = \frac{-b}{2\pi}\int_0^{x^*}\int_{y^*-\left(\frac{2c}{b}\right)\frac{(x^*-\xi^*)}{m}}^{y^*+\left(\frac{2c}{b}\right)\frac{(x^*-\xi^*)}{m}} \bar{w}(\xi^*,\eta^*)e^{-i\bar{\omega}(x^*-\xi^*)}\frac{\cos\left(\frac{\bar{\omega}r^*}{M}\right)}{r^*}d\xi^*d\eta^* \qquad (2.17)$$

where $\bar{\omega} = \frac{2kM^2}{M^2-1}$, $\quad k = \frac{\omega c}{2U_\infty}$, $\quad x^*, \xi^* = \left(\frac{x}{c}, \frac{\xi}{c}\right)$, $\quad y^*, \eta^* = \left(\frac{2y}{b}, \frac{2\eta}{b}\right)$, $\quad m = \sqrt{M^2-1}$,

and $r^* = \sqrt{(x^*-\xi^*)^2 - m^2\left(\frac{b}{2c}\right)^2(y^*-\eta^*)^2}$

Here, b and c represent the *full* wing span and chord, respectively, and ξ and η represent the integration variables along the x and y directions. The variable $\bar{w}$ represents the downwash.

In the Mach Box method, the wing and the relevant portions of the influenced flowfield are discretized using rectangular panels. An example of the discretization for a rectangular wing at $M = 1.2$ is given by [31] in Figure 2.12. The integral equation (2.17) is approximated by differences, and the downwash is assumed to be constant over a panel. The equation is then

evaluated at each panel to obtain a matrix of aerodynamic influence coefficients. The application of boundary conditions on the surface of the wing as well as in the flowfield allows for the potential function and the downwash to be solved; this in turn allows for the oscillating pressures on the wing to be calculated. The Mach Box method thus accounts for the 3-dimensional upstream influence of the wing and the influenced flowfield.

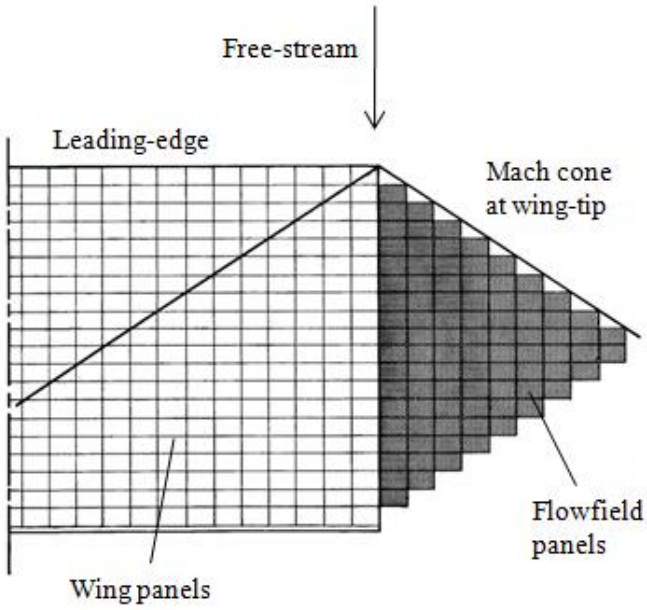


Figure 2.12: Example of Mach Box Spatial Discretization **[31]**

The equations from which the unsteady aerodynamic pressures are derived assume simple harmonic oscillation of the potential function (and implicitly, of the surface of the wing). The mathematical basis of the equations allows the unsteady pressure to be expressed as a function of the frequency of the oscillations, ω. This is of great practical importance in aeroelastic analysis, as it allows for the solution of the flutter determinant in terms of the frequency, and allows the flutter frequency to be found by methods such as the V-g, p-k, and g methods, in which the flutter determinant is formulated in terms of the frequency of oscillation.

Several improvements to the Mach Box method have been made [32; 33], and other supersonic lifting surface formulations and panel methods [12; 34] have been implemented.

2.1.7 Quasi-Steady Approximation to Unsteady Aerodynamics

The degree of the unsteadiness of the flow may be estimated [28] from the reduced frequency of motion, which is given by:

$$k = \frac{\omega c}{2U_\infty} \qquad (2.18)$$

Scanlan [35] notes the difference between the Strouhal number, which is associated with a frequency of the fluid, and reduced frequency, which is associated with a structural frequency of motion. The reduced frequency gives an approximate ratio between the rate of unsteady motion and the rate at which it is washed downstream. Ashley [36] states that for sufficiently small (0.01 -- 0.02) reduced frequencies, the instantaneous aerodynamic loading may be approximated by steady flow at an equivalent quasi-steady angle of attack, and the flow history may be ignored. This allows the use of simpler methods for steady aerodynamics in modelling unsteady motion, provided that the reduced frequency is low.

In quasi-steady modelling, the flow history is not accounted for, and there is thus no lag between structural motion and aerodynamic loading, as would be introduced by accounting for flow history.

2.2 Coupling of Aerodynamics and Structural Dynamics

The essence of aeroelasticity is the interaction of fluid and structure; in modelling aeroelasticity, both the aerodynamics and the structural dynamics must be modelled. Various approaches to the modelling exist which reflect various degrees of complexity in the formulation of the aeroelastic problem.

McNamara and Friedmann [9] classify the methods of fluid-structure coupling as monolithic or partitioned. In monolithic solvers, the equations of both the fluid and the structure are combined into a consistent set of equations which are marched forward in time simultaneously; it should be noted that it is implied that the physics of both the structure and the fluid are solved using the same spatial discretization (mesh) and time-step.

In partitioned solvers, the fluid and the structure are modelled using separate solvers [9], each modelling the physics of the fluid and the structure in isolation, respectively. Different spatial

discretizations and time-steps are employed, each most suited to the physics. McNamara and Friedmann identify that the issues of interpolation of results between the fluid and structural grids, and of time advancement in both solvers, have been solved through various schemes. The issue of grid-interpolation has been broadly studied, including the interpolation onto a common manifold for reduced-order models [37] and studies in coupling the fluid and structure using meshless methods [38].

As the aerodynamic loading is dependent on the structural response (and vice versa), the advancement of the solution in one of the solvers requires an assumption of the response or loading at the next time-step in the other solver. This results in a lag [9] of response and loading, and physically equates to a dynamic imbalance between the aerodynamic and structural forces. This may be overcome (the imbalance may be eliminated) through sub-iterations between the structural and fluid solvers within each time step. The sub-iterations are said to occur in "pseudo-time" [1], whilst the coupled solution marches forward in "physical" time with a global time-step. When sub-iterations are used to achieve dynamic equilibrium between the fluid and structure, it is said that the solvers are strongly coupled [9]; the solvers are loosely coupled when no sub-iterations are performed to achieve dynamic equilibrium.

2.3 Time Variance in Dynamic Systems

In the analysis of dynamic systems, the time-variance of the system affects the methods which can be used to predict the response of the system in time. Consider the response a of an underdamped single degree of freedom mass-spring-damper system with a linear damper and linear spring under harmonic base excitation, shown in Figure 2.13 (example from Rao [39]):

$$m\ddot{x} + c\dot{x} + kx = c\dot{y} + ky \tag{2.19}$$

$$y = A_0 \sin \omega t \tag{2.20}$$

From Rao [39], the solution may be expressed as the sum of a transient component and a steady component, in the following general form:

$$x(t) = x_t(t) + x_s(t) \tag{2.21}$$

in which:

$$x_t(t) = A_1 e^{-\zeta \omega_n t} \cos(\omega_d t - \phi_0) \quad (2.22)$$

$$x_s(t) = A_2 \cos(\omega t - \phi_1) + A_3 \sin(\omega t - \phi_1) \quad (2.23)$$

where all the coefficients in to preceding equations are constant with time.

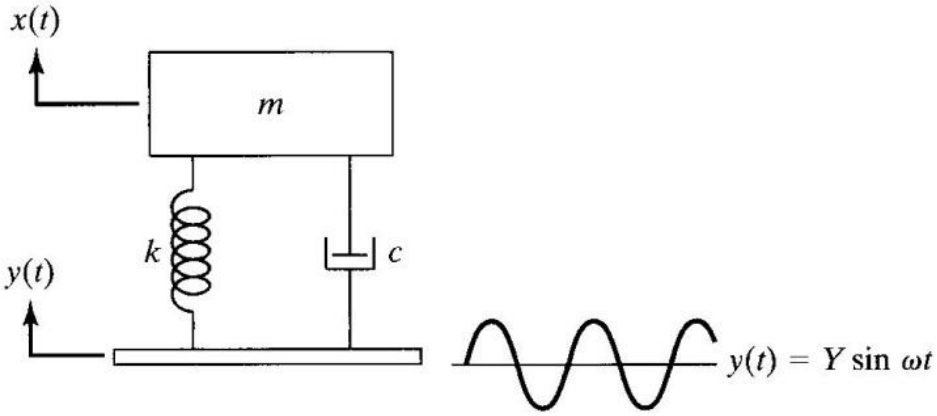


Figure 2.13: Example of a Simple Second-Order System[39]

It may clearly be seen that the displacements vary nonlinearly (sinusoidally) with time. However, when considering the displacements as sinusoidal vibrations, it may be seen that there exists a component for which the nature of the vibration varies with time (transient, $x_t(t)$), and there exists a component for which the nature of the vibration is time-invariant (steady, $x_s(t)$). In particular, the amplitude of the transient component decays with time, whilst the amplitude of the steady component is constant in time. It is worth mentioning that the frequency of each component is constant with time. The response of the example system is shown in Figure 2.14, the total response may clearly be seen as the superposition of the transient and steady responses.

This example highlights the essence of steady and unsteady response. A steady response is one in which the parameters which are used to describe the response are constant with time (in this example, the amplitude and frequency of the sinusoid). An unsteady response is one in which the describing parameters are time-variant (in this example, the amplitude of the sinusoid varied with time, although the frequency of the sinusoid remained constant).

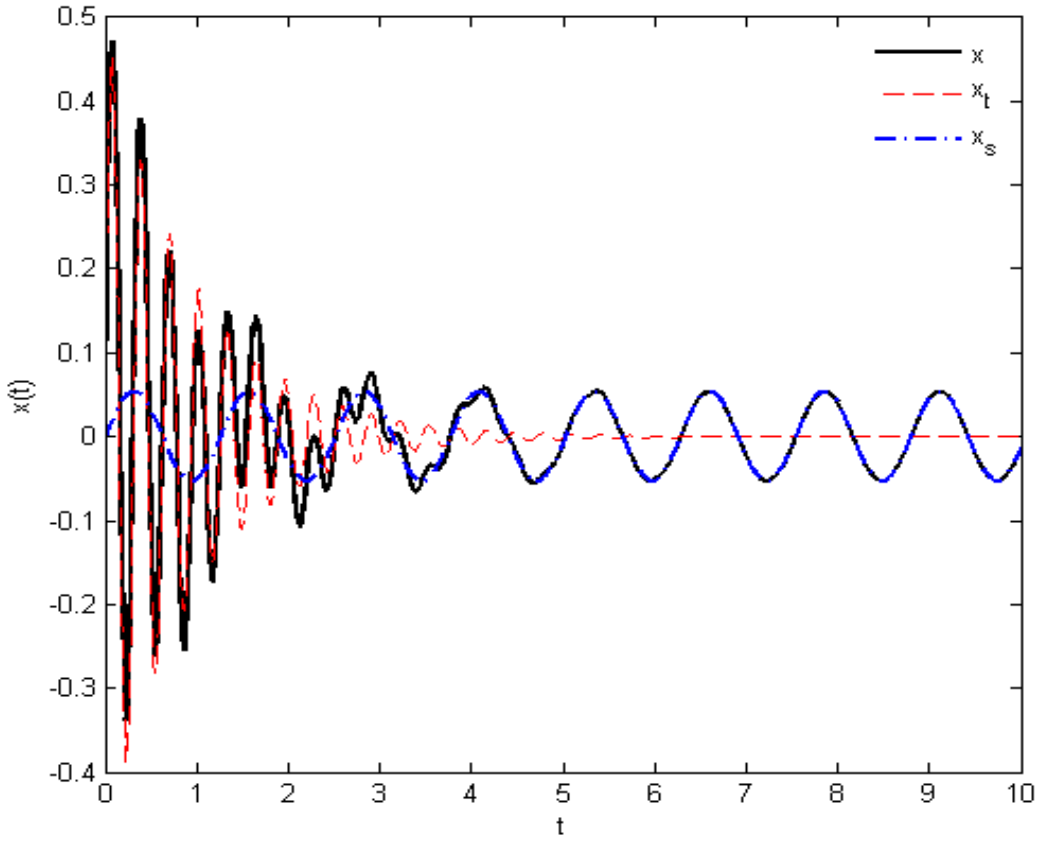


Figure 2.14: Example of Transient and Steady Responses **[39]**

Consider another example, in which the frequency of a sinusoidal response is linearly time variant. The sinusoid is described by:

$$y(t) = \sin(\omega t) \qquad (2.24)$$

in which:

$$\omega(t) = 1 + \frac{t}{10\pi} \qquad (2.25)$$

Although the amplitude remains constant with time, the vibration is clearly unsteady due to the time-variance in the frequency of the vibration. The response is depicted in Figure 2.15.

If the change in the describing parameter of a response is small over the time period under consideration, the response may be considered to be quasi-steady for that time period. Effectively, the time-variant describing parameter (e.g., frequency) is evaluated at an instant in time, and for the purpose of dynamic analysis is assumed to remain time-invariant at that value over the time period of the analysis.

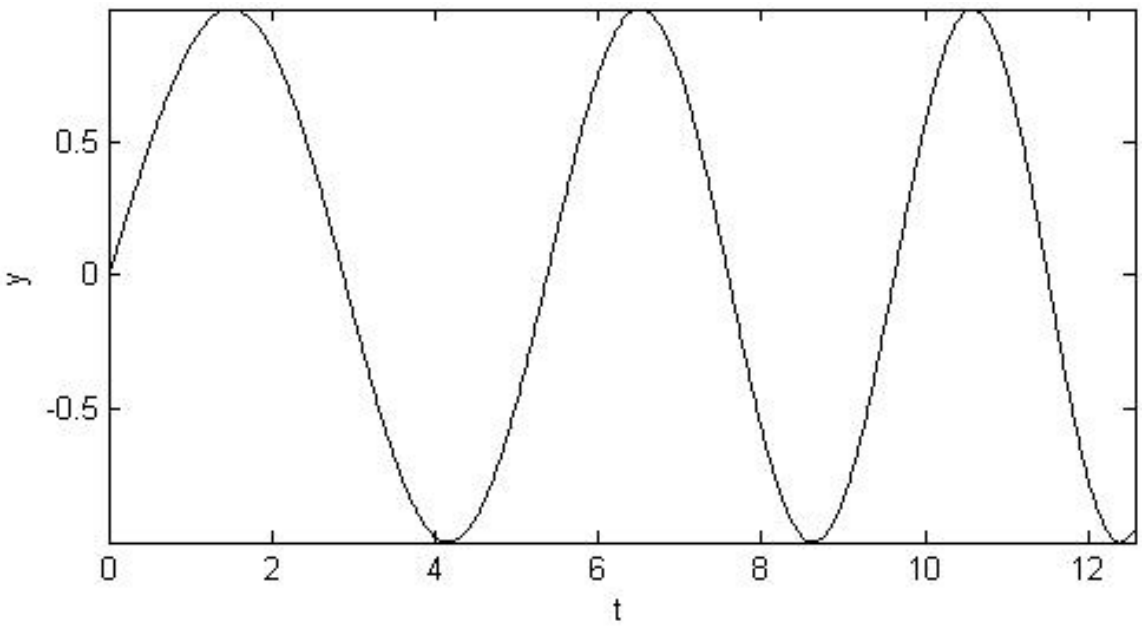


Figure 2.15: Example of a Sinusoid with Variable Frequency

An unsteady response may be analysed by successive quasi-steady approximations, with the describing parameters of the response being updated at each (or at selected) time interval(s) to provide a more accurate representation of the unsteady response. A comparison of the results of single quasi-steady approximation and successive quasi-steady approximations is given in Figure 2.16 for the example sinusoid previously considered.

In this example, for a single quasi-steady approximation (left-hand side plots), the frequency of the sinusoid is evaluated at the start of the time-window $t = 0$, $\omega(0) = 1\ \mathrm{rad/s}$, and is assumed to remain at that value for the duration of the analysis, $0 \leq t \leq 2\pi$ s. The actual wave-form is given by the solid line, whilst the quasi-steady approximation to the wave-form is shown as a dashed line. At each time step, the displacement y at the next time step is predicted from the first evaluation of the sinusoid, $y = \sin(\omega_{|t=0} t)$.

For successive quasi-steady approximations, the frequency of the sinusoid is re-evaluated at each time-step, and a new approximation (shown as the dashed line) to the true wave-form (shown as the solid line) is made. At each time step, the displacement y at the next time step is predicted from the current evaluation of the sinusoid, $y = \sin(\omega_{|t=t} t)$. It may be seen from Figure 2.16 that successive quasi-steady approximations yield better approximations to the unsteady process (sinusoid) than a single quasi-steady approximation.

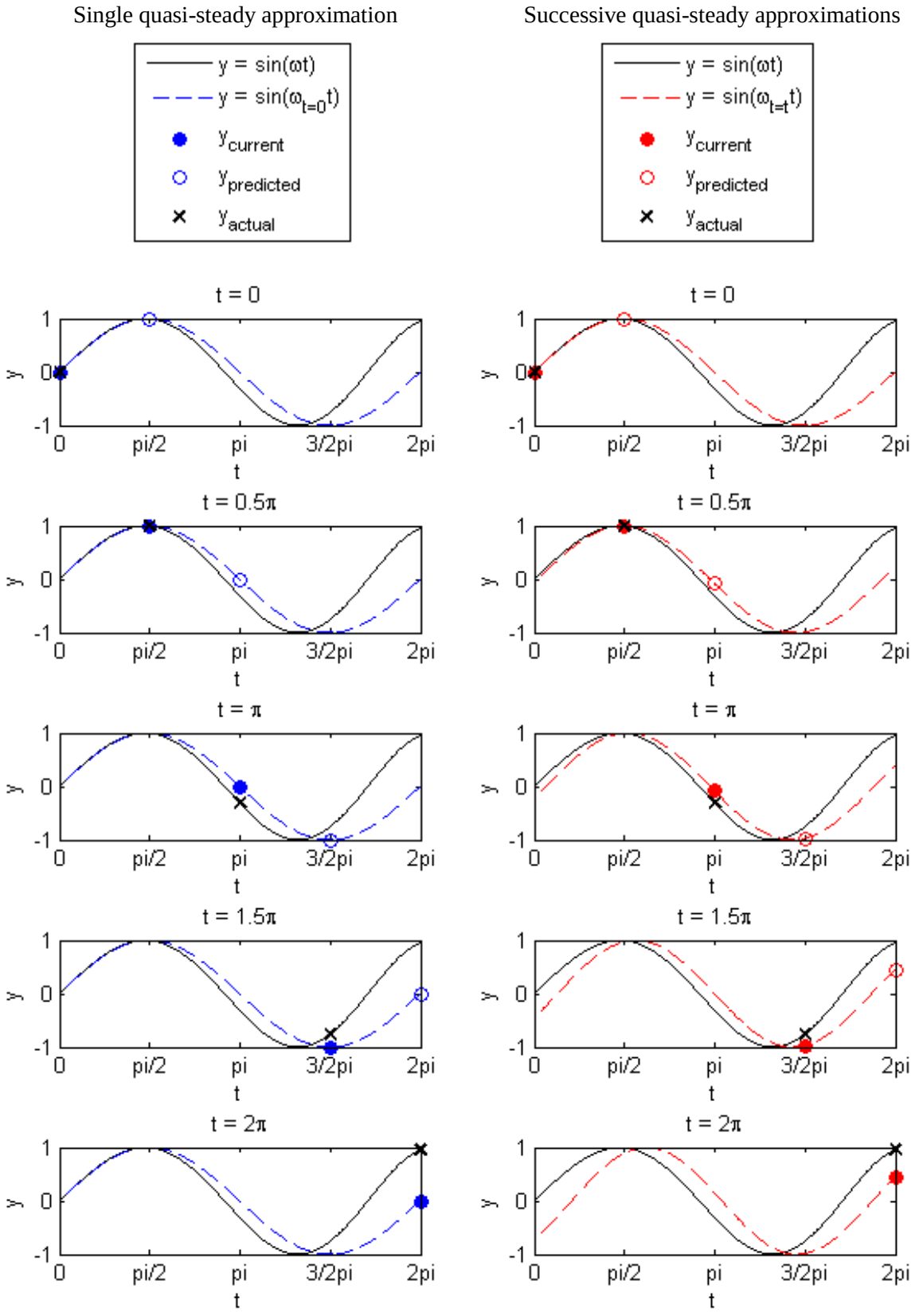


Figure 2.16: Comparison of Quasi-Steady Approximations to Unsteady Phenomena

It may be seen from the example and Figure 2.17 that the quasi-steady approximation can yield accurate results if applied over a sufficiently small time period (in which the change in the frequency is small). However, the error between the actual response and the approximated response grows with time, even when successive quasi-steady approximations are made. The size of the interval over which the successive quasi-steady approximations are made also has an influence on the accuracy of the representation.

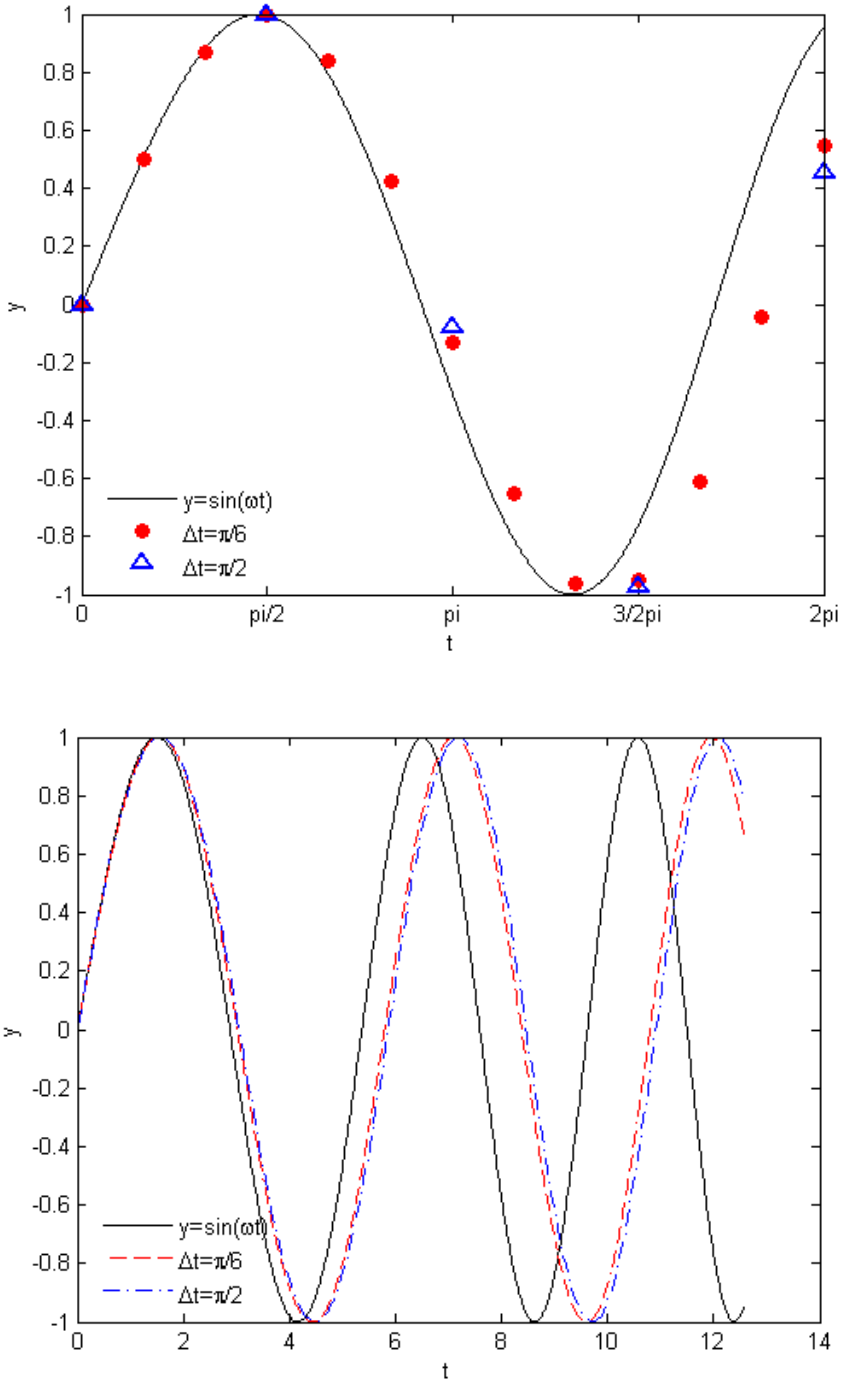


Figure 2.17: Comparison of the Effect of Time-Step in Quasi-Steady Approximations

2.4 Linearity and Nonlinearity

In a spatially linear system, forces may be described as varying directly in only $\vec{d}$, $\vec{v}$ and $\vec{a}$, without cross-coupling or higher order terms appearing. The forces may therefore be described in terms of the associated stiffness-, damping-, and mass-coefficient matrices. This is an important characteristic of linear or linearized systems. Another important characteristic of linear systems is that the principle of superposition may be used [39]. Thus, modal analysis may be used to solve the aeroelastic eigenproblem. Furthermore, the system response may generally be described with sufficient accuracy through considering the contributions of only the first few modes of the system, as the contribution from higher modes is generally negligible in comparison [40] -- this allows a potentially significant reduction in the order of the system.

Non-linearity in a system may introduce coupling between terms. In considering the downwash contributions in piston theory (see Section 3.3), for example, it is seen that nonlinear downwash terms (w^2) introduce coupling between the thickness-dependent terms (w_0) and the motion-dependent terms (w_1).

First-order downwash (linear): $$w = w_0 + w_1 \quad (2.26)$$

Second-order downwash (nonlinear): $$w^2 = w_0^2 + w_1^2 + 2w_0 w_1 \quad (2.27)$$

The solution approach to a nonlinear system depends on whether the system is nonlinear in the unknown parameter being solver for. If the system is linear in the unknown parameter, the solution is straightforward. For a system that is nonlinear in the parameter being solved for, the solution will generally be arrived at iteratively.

Nonlinearity may also be introduced into a linear system if the parameters of the system are time dependent, as may be illustrated through the following example. Consider a spring in which the stiffness is dependent on the deflection of the spring, depicted in Figure 2.18. The equilibrium of the system is given by:

$$F_{spring} = F_{applied} \quad (2.28)$$

where

$$F_{spring} = k_{spring}\, x \quad (2.29)$$

and

$$k_{spring} = k_0 + k_1 x \quad (2.30)$$

and hence

$$k_1 x^2 + k_0 x = F_{applied} \quad (2.31)$$

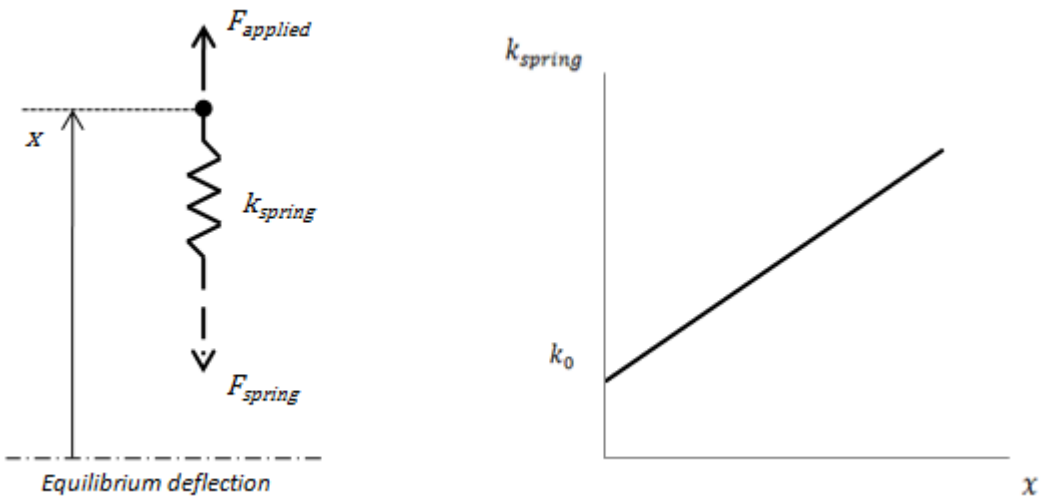


Figure 2.18: Example of a Nonlinear Spring

This is an example of a spatially nonlinear system. In this particular case, the system is nonlinear in the displacement x. The nonlinearity arises from the fact that the stiffness coefficient k_{spring} is not constant in x -- it itself is a function of x. The example above is a static system. Consider an extension of the problem to a dynamic system through introducing a mass, and consider the free response of the system:

$$m\ddot{x} + k_{spring}\, x = 0 \quad (2.32)$$

where

$$k_{spring} = k_0 + k_1 x \quad (2.33)$$

and

$$x = x(t) \quad (2.34)$$

$$\ddot{x} = \ddot{x}(t) \quad (2.35)$$

Whilst the above representation of the system is correct, it is not immediately obvious that the system is nonlinear in x (since the stiffness coefficient k_{spring} is a function of x). If the equation is expanded, the spatial nonlinearity is more obvious:

$$m\ddot{x} + k_0 x + k_1 x^2 = 0 \qquad (2.36)$$

In this formulation, it can be clearly seen that the system is a nonlinear differential equation with time-invariant coefficients m, k_0, and k_1.

Consider the same problem in the original formulation, from equation (2.36):

$$m\ddot{x} + k_{spring}\, x = 0$$

In this formulation, it may be seen that since x is time-variant (dynamic problem), the stiffness coefficient k_{spring} (which is a function of x) is time-variant by association. The system can thus be equivalently considered to be a linear differential equation with the time-variant coefficients (although m is time-invariant, k_{spring} is time-variant).

Parameters may also be linear (or constant) or nonlinear in time. In the simplest case, consider the motion of a single degree of freedom:

$$\ddot{x} = a_3 t + a_2 \qquad (2.37)$$

$$\dot{x} = a_3 t^2 + a_2 t + a_1 \qquad (2.38)$$

$$x = a_3 t^3 + a_2 t^2 + a_1 t + a_0 \qquad (2.39)$$

in which a_0, a_1, a_2 and a_3 represent arbitrary constants.

If the degree of freedom undergoes acceleration (whether linear or constant), the velocity will vary in one higher order of time (quadratic or linear), and the displacement will vary nonlinearly in time (cubic or quadratic). In considering the time-variation of a system, the concepts of a steady (or quasi-steady) and an unsteady system are used.

2.4.1 Nonlinear effects

A body undergoing large motions will be subject to nonlinear effects arising from structural nonlinearity and from nonlinear aerodynamics [41]. The system characteristic effectively becomes time-variant, and the structural response of the body is non-trivial. The response of

nonlinear systems may be very sensitive to initial conditions, such as initial velocity of the body [41]. A system exhibiting bounded response to a set of initial conditions may become unbounded for a small change in the initial conditions. A structure which is aeroelastically stable close to the critical flutter speed (decaying response) may become unstable if it is subjected to a sufficiently large perturbation.

Limit-cycle oscillations (LCO) are an example of the effect of nonlinearity in aeroelastic systems. The unstable growth of oscillations post-flutter is attenuated, and a large-amplitude steady oscillation occurs; LCO may also occur when large oscillations dampen to smaller LCO. Limit-cycle oscillations may be obtained for dynamically-linearized aerodynamics coupled with a nonlinear structure [42], such as plates undergoing large deformations [41]. However, LCO due to fluid nonlinearities is not modelled when the fluid modelling is time-linearized [42].

For further information on LCO and nonlinear effects in aeroelasticity, the reader is referred to Thomas et al [43] and Dotson et al [44].

2.5 Time Integration

The Newmark-β time-integration scheme is broadly used for transient analysis of dynamic systems, and offers flexibility in implementation. Appropriate selection of the β and γ parameters allow for the use of various explicit or implicit schemes; numerical damping may also be introduced directly into the scheme through the parameter γ. An outline of the Newmark-β method follows. Consider a system which is subjected to dynamic loading:

$$M\ddot{u} + C\dot{u} + Ku = F(t) \tag{2.40}$$

Fully knowing the initial conditions of the system at a time t, the velocity and displacement of the system at the next time-step may be expressed as follows [40]:

$$\dot{u}_{t+\Delta t} = \dot{u}_t + \Delta t[(1-\gamma)\ddot{u}_t + \gamma\ddot{u}_{t+\Delta t}] \tag{2.41}$$

$$u_{t+\Delta t} = u_t + \Delta t\dot{u}_t + \frac{(\Delta t)^2}{2}[(1-2\beta)\ddot{u}_t + 2\beta\ddot{u}_{t+\Delta t}] \tag{2.42}$$

It may be shown [45] that the equations are in essence derived from a constant acceleration over the time-step; however, different parameters are used in deriving the expressions for

velocity (factor of γ) and displacement (factor of 2β). It may be seen that in the above equations, $\dot{u}_{t+\Delta t} \neq \frac{d}{dt}(u_{t+\Delta t})$ unless $\gamma = 2\beta$.

The appropriate selection of the parameters γ and β allows the Newmark-β method to be rendered equivalent to a number of other time-marching schemes. The parameters also influence the accuracy and numerical stability of the procedure. In particular, values of $\gamma \neq \frac{1}{2}$ introduce numerical damping into the solution [40]. Katona et al [40] also provide an equation to estimate the error in the frequency for a particular set of time step Δt and β:

$$\frac{\bar{T}}{T} = \frac{2\pi\left(\frac{\Delta t}{T}\right)}{\sin^{-1}\left(\sqrt{1-\frac{b^2}{4}}\right)} \qquad (2.43)$$

where

$$b = \frac{2-(1-2\beta)\left(2\pi\frac{\Delta t}{T}\right)^2}{1+\beta\left(2\pi\frac{\Delta t}{T}\right)^2} \qquad (2.44)$$

where $\frac{\bar{T}}{T}$ represents the ratio of the approximate (achieved by the numerical solution) period to the actual period. The trends generated by the equation diverge from the curves provided by Katona et al [40] around $\frac{\Delta t}{T} > 0.2$, but agree for lower values. Farhat [46] provides estimates for error in periodicity and classifications of algorithms for particular pairs of γ and β in Table 2.1.

Table 2.1: Algorithm Selection Through Choice of Parameters in the Newmark-β Scheme [46]

Algorithm	γ	β	Stability limit $\frac{\Delta t}{T}$	Periodicity error $\frac{\Delta T}{T}$
Central difference	$\frac{1}{2}$	0	0.318	$-\frac{\pi^2}{6}\left(\frac{\Delta t}{T}\right)^2$
Linear acceleration	$\frac{1}{2}$	$\frac{1}{6}$	0.551	$\frac{\pi^2}{6}\left(\frac{\Delta t}{T}\right)^2$
Average constant acceleration	$\frac{1}{2}$	$\frac{1}{4}$	∞	$\frac{\pi^2}{3}\left(\frac{\Delta t}{T}\right)^2$

Katona et al [40] provide the following equation for the maximum time step allowable for numerical stability in the solution:

$$\frac{\Delta t}{T_{min}} \leq \frac{1}{2\pi}\sqrt{\frac{4}{1-4\beta}} \qquad (2.45)$$

where T_{min} is the shortest period of vibration of the system.

Katona el at [40] suggest that provided the time step is chosen such that the highest frequency mode is numerically stable for the given algorithm, the accuracy-requirement on the time-step of $\frac{\Delta t}{T_{min}} < 0.1$ may be relaxed. The reasoning behind this is that in general the higher modes will have very low modal participation factors (modal displacements) compared to the lower modes. This means, even though the higher modes are integrated with significant error, their contribution to the overall response is negligible in comparison to the large participation factors of the dominant lower modes; the integration of the lower modes being more accurate due to their longer periods [40].

2.6 Characterization of Dynamic Aeroelastic Response

The dynamics of linear time-invariant (LTI) second-order systems may be defined by the damped modal frequencies and modal damping ratios. For second-order LTI systems, these parameters are well defined, and are given by the eigenvalues of the system equations of motion.

If, however, the system is second-order linear time-variant, the damping and stiffness matrices are changing with time. The eigenvalues of the system are therefore also time-variant, and so the frequencies and damping ratios become time-variant. The time-variation of instantaneous frequencies and damping ratios may be insightful to the stability of the system, but a graphical representation of the response may provide a clearer representation of the physical response. In such cases, the time-history of the modal response may provide a better representation of the physical response; the stability of the response may be well represented by the phase-plane trajectory of the modal response.

The response of a nonlinear system may best be represented by the time-history of the modal response (as shown in Figure 2.19), or by the phase-plane trajectory of modal responses [44] (as shown in Figure 2.20). An example of the response of a nonlinear system is shown in Figure 2.19 for the Goland wing undergoing limit-cycle oscillations. It may be seen from the response that the concepts of instantaneous damping ratios and frequencies are insufficient to describe the system response.

It has also been shown [47] that identification of a nonlinear aeroelastic system with a NARMAX model allows the nonlinear response to be accurately reproduced.

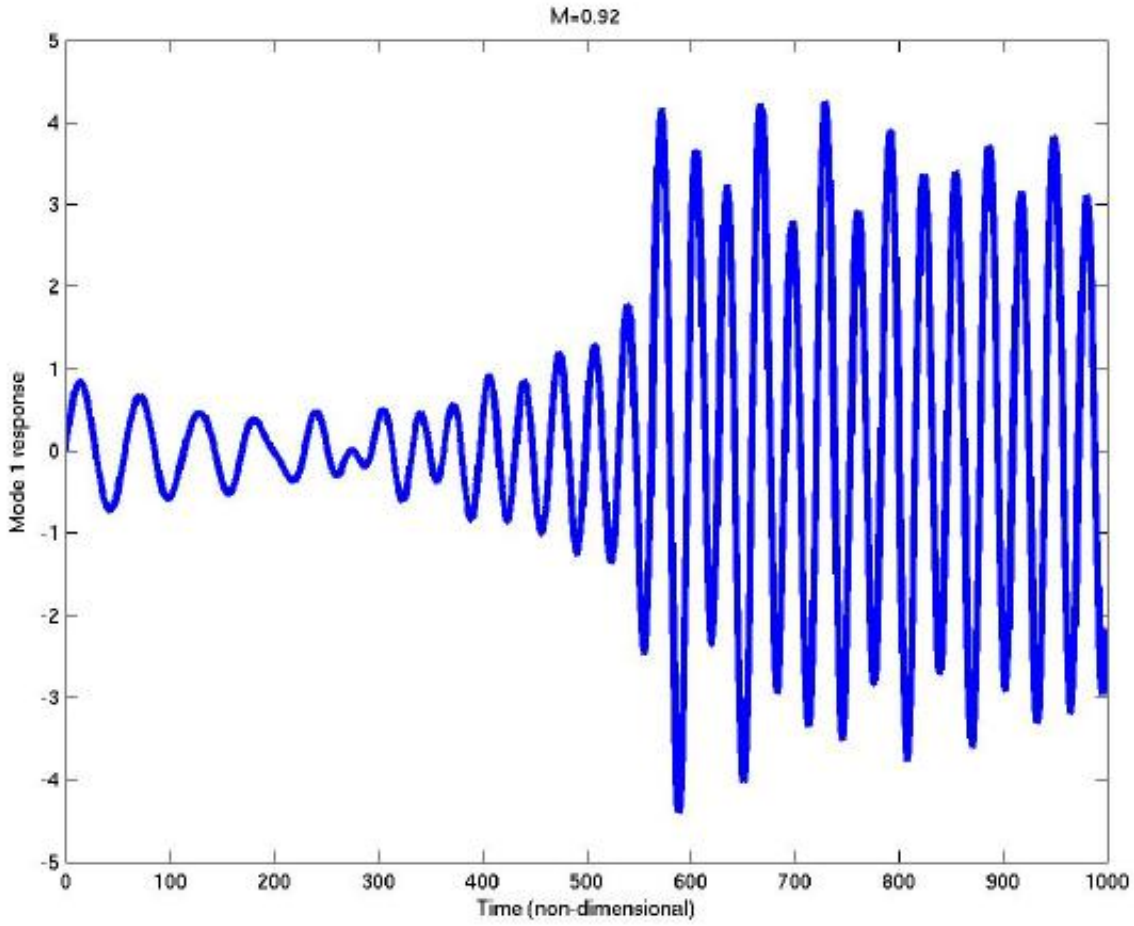


Figure 2.19: Limit-Cycle Oscillations of the Goland Wing **[48]**

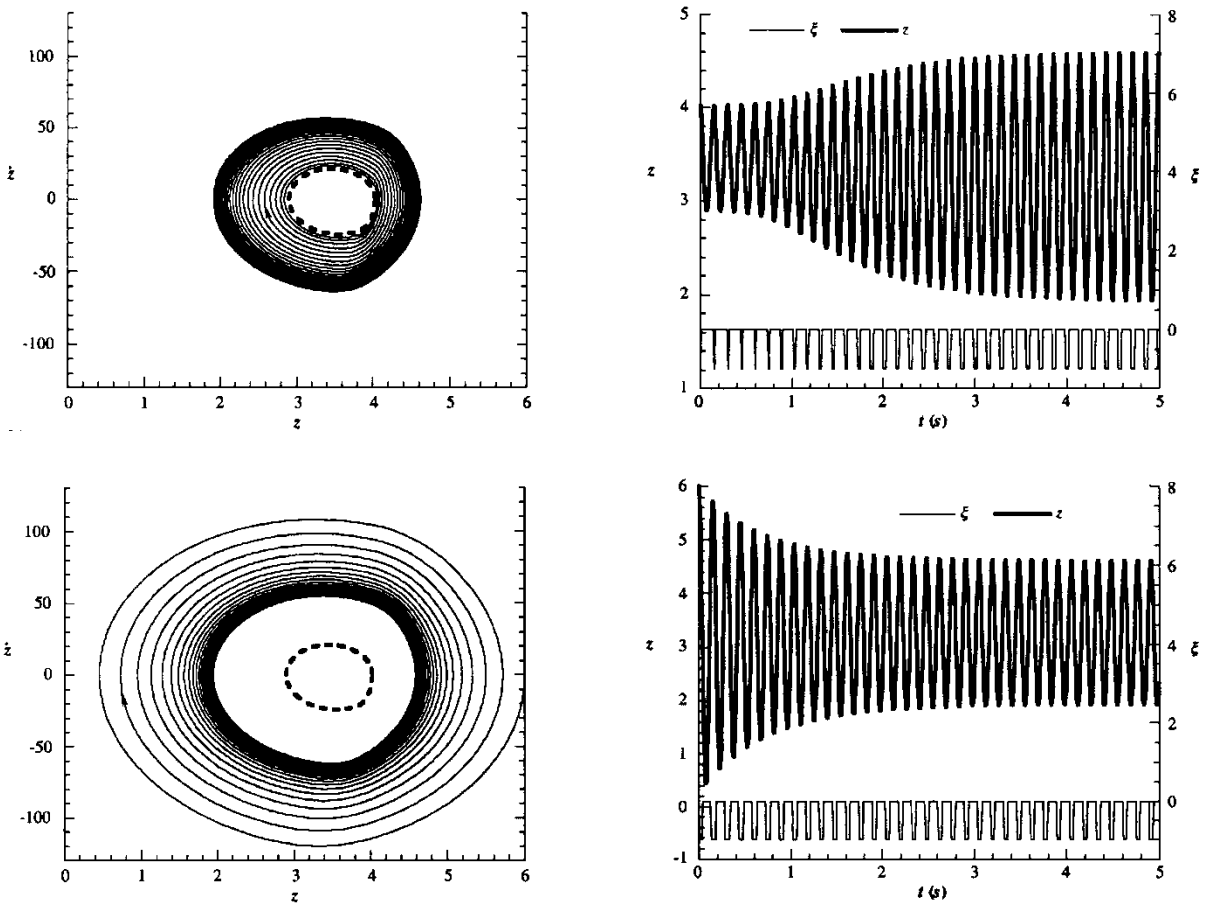


Figure 2.20: Examples of the Phase-Plane Representation of Limit-Cycle Oscillations **[44]**

2.7 Aeroelastic Response at Airspeeds Below Flutter Speed

Multi-mode aeroelastic flutter occurs when two aeroelastic modes excite one another; this is occurs as the frequencies of the two modes shift towards a coalesced frequency [49]. The damping of one of the coalescing modes will decrease and become negative, whilst the damping of the other mode increases. The frequency coalescence and damping separation of the two modes is a general trend for two-mode flutter, regardless of the flow regime (subsonic/supersonic) and sharpness of onset of flutter. These trends are shown in Figure 2.21 and Figure 2.22.

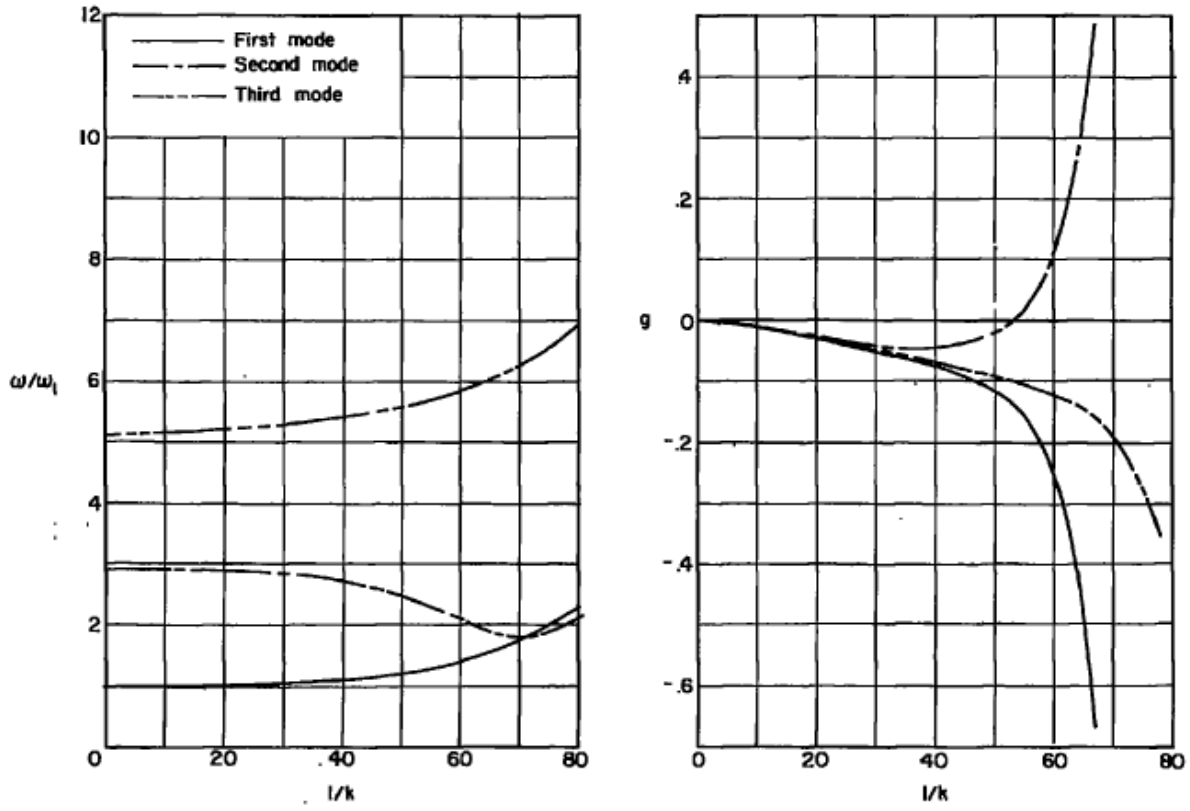


Figure 2.21: Typical Trends in the Variation of Aeroelastic System Parameters with Airspeed **[50]**

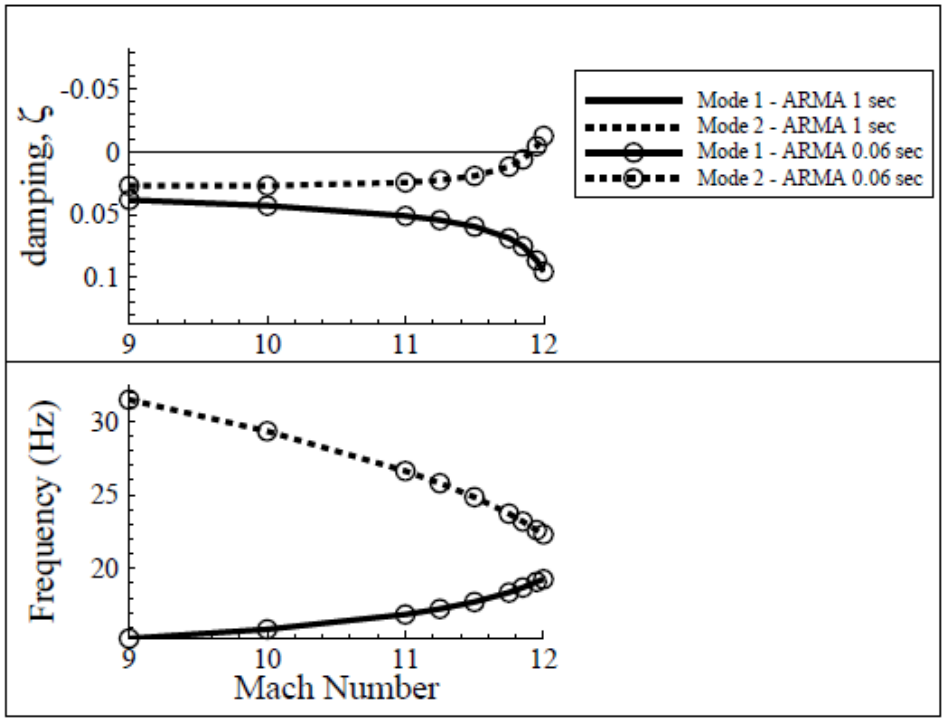


Figure 2.22: Variation of Aeroelastic System Parameters in Hypersonic Flow **[1]**

It may be seen that whilst the general trend of frequency coalescence is observed, the rate of coalescence varies. Together with this, the rate of separation of damping ratios also varies; it is proportional to the difference between the frequencies. The behaviour of the frequency and damping trends at conditions below the flutter speed are of great importance in the ability to predict flutter in flutter flight tests. "Hard" or "explosive" flutter is characterized by a very sharp decrease in the damping ratio of the flutter mode immediately prior to flutter, with no gradual decrease in damping ratio prior to the sharp drop [51]. The plot in the bottom-left of Figure 2.23 is an example of hard flutter. Flutter prediction methods that rely on damping-ratio trends (such as the damping extrapolation method [51]) tend to give highly un-conservative estimates of the flutter speed for systems which experience "hard flutter", as the sharp drop in damping cannot be predicted by these methods [51].

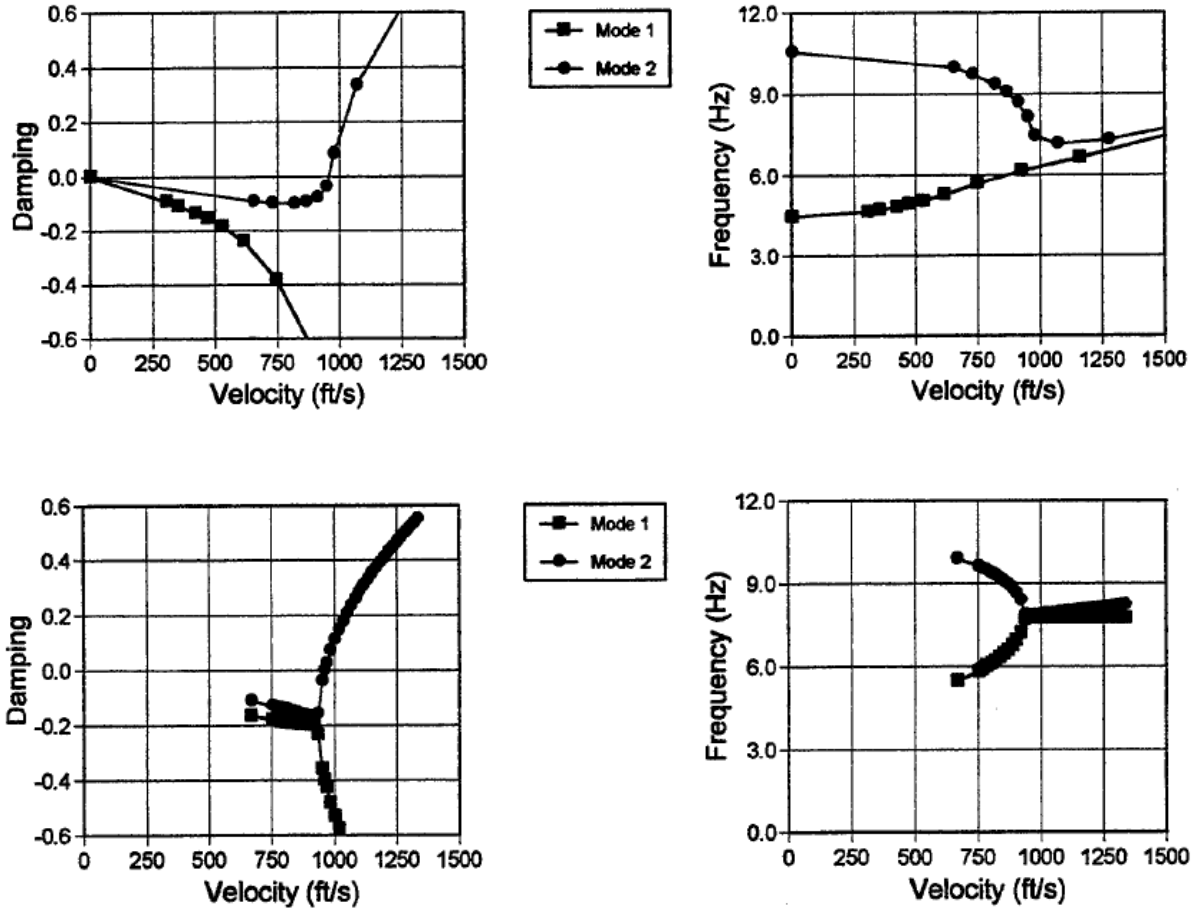


Figure 2.23: Example of the Variation in Aeroelastic System Parameters Produced by ZAERO **[52]**

2.8 Experimental Data for Supersonic Flutter of Cantilevered Plates

The literature on experimental tests on flutter for cantilevered plates is relatively limited. More literature is available for test specimens which are free to rotate (with a spring providing the restoring moment) at the root; the literature in this regard is relatively broad in comparison to that for cantilevered wing models. The literature that is available for cantilevered wings with sharp leading-edges in supersonic flow may be roughly categorized by the geometry considered, and is represented by the following three groups:

- low aspect-ratio ($AR < 0.5$), highly swept ($\Lambda_{LE} > 45°$), highly tapered (or delta) planforms [12; 53], including the HSCT model [2], as depicted in Figure 2.24,

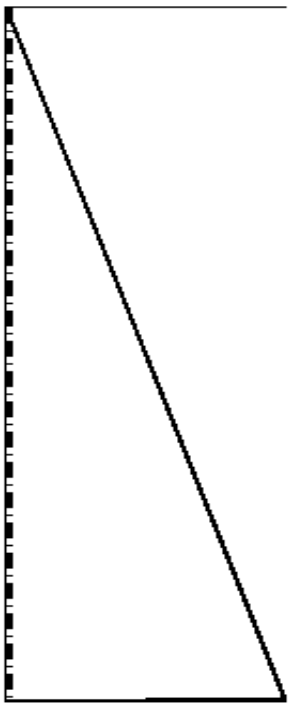


Figure 2.24: A Typical Delta-Planform Cantilevered Plate in Literature

- moderately low aspect-ratio ($0.5 < AR < 3$), swept ($0° \leq \Lambda_{LE} \leq 60°$), untapered ($\lambda = 1$) planforms [12; 53; 54; 55], as shown in Figure 2.25,

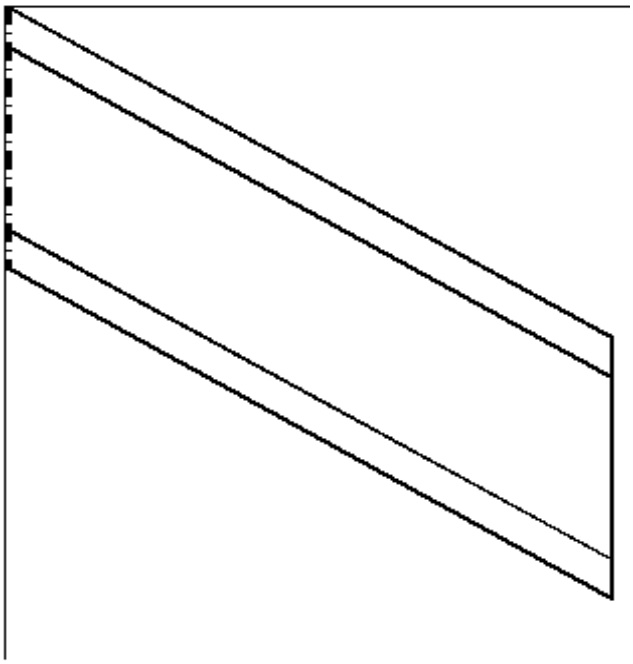


Figure 2.25: A Typical Untapered Cantilevered Plate in Literature

- moderately low aspect-ratio ($1 < AR < 2$), swept ($0 < \Lambda_{0.25c} < 60°$), tapered ($0.2 < \lambda < 0.7$) planforms [11; 53], as represented by Figure 2.26.

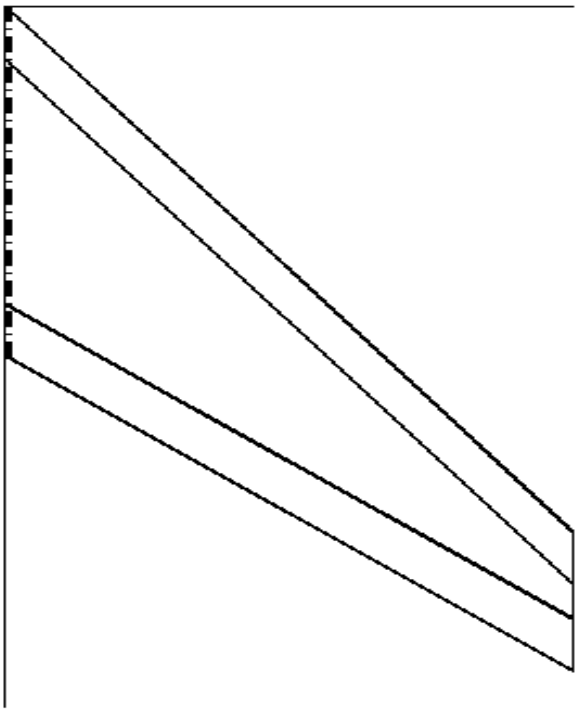


Figure 2.26: A Typical Tapered Cantilevered Plate in Literature

Other literature (here, literature with purely computational modelling is included) is available for low-supersonic and transonic flow, largely focusing on wing profiles such as the NACA 64A004 [55], NACA 65A004 [56; 57], and NACA 64A010 [58]. These airfoils cannot be analysed using shock-expansion theory, as they have rounded leading-edges.

Amongst the literature for swept, untapered planforms, the publications on two series of tests are of particular interest:

Torii [54] and Matsuzaki [55] performed a wind-tunnel flutter test on a single geometry and provided estimates of the variation of modal parameters and flutter prediction metrics with dynamic pressure. The wing was found to undergo hard flutter. The results of Torii and Matsuzaki were used in the present work for the validation of computational aeroelastic analysis and flutter prediction in Chapter 5 and Chapter 6.

Tuovali and McCarty [53] performed a battery of wind-tunnel flutter tests for various geometries at a set of Mach numbers, with experimental determination of the structural modal parameters by Hanson and Tuovila [59]. This provides an experimental reference case for validation of parametric studies (of geometry variation) in computational aeroelasticity. The test results serve as a validation of computational flutter prediction methods by Morgan et al [50], Chen et al [52], and Xianxin [60]. The results of the aforementioned authors were used in the present work for the validation of computational flutter prediction in Chapter 6.

2.9 Flutter Prediction Methods

The prediction of the flutter speed from measurements of structural response at subcritical speeds is a critical part of flutter flight testing. In performing flutter calculations for analytical systems (computational problems), several methods are available for calculating the flutter point; however, many of the classical methods rely on the aerodynamic loading being expressed in terms of the reduced frequency of motion, k.

Where this is not possible, the aerodynamic transfer function $H(i\omega)$ (in which ω represents angular frequency) may be deduced from the aerodynamic response to impulse inputs [42]. This allows for further calculations to be performed in the frequency domain.

Methods for flutter identification in the time domain are available [29], and do not require the aerodynamic response to a sweep of frequencies to be known. This is particularly useful in cases where the aerodynamic loading is calculated from CFD, where the computational cost of generating the aerodynamic transfer function may be prohibitively high. These time-domain methods generally require some estimate of the damping ratio and frequency to be made, involving system identification.

A number of linear flutter prediction methods were considered, and are briefly reviewed here.

2.9.1 Zimmerman-Weissenburger Flutter Margin

The Zimmerman-Weissenburger flutter margin was developed to predict two-mode flutter for a continuous-time system. The application of the method requires the eigenvalues of the aeroelastic system to be known; that is, the modal frequencies and damping ratios must be known. It is assumed that the response of the unforced aeroelastic system may be described as a damped sinusoidal oscillation[61]:

$$\boldsymbol{M}\ddot{x} + \boldsymbol{C}\dot{x} + \boldsymbol{K}x = 0 \tag{2.46}$$

$$x = x_0 e^{\lambda t} \tag{2.47}$$

Let the eigenvalues be described by:

$$\lambda_{1,2} = \sigma_1 \pm i\omega_1 \tag{2.48}$$

$$\lambda_{3,4} = \sigma_2 \pm i\omega_2 \tag{2.49}$$

Recall [39] that for a mode with damping ratio ζ, natural frequency ω_n, and damped frequency ω_d:

$$\lambda = -\zeta\omega_n \pm i\omega_d \tag{2.50}$$

This leads to a quartic characteristic equation [61], given here with coefficients normalized such that λ^4 has a coefficient of 1:

$$\lambda^4 + A_3\lambda^3 + A_2\lambda^2 + A_1\lambda + A_0 = 0 \tag{2.51}$$

The Routh-Hurwitz stability criterion may be applied, giving the limit for a stable system as [61]:

$$FM = \left[A_2\left(\frac{A_1}{A_3}\right) - \left(\frac{A_1}{A_3}\right)^2 + A_0\right] > 0 \qquad (2.52)$$

This may be recast in terms of the real and imaginary parts of the eigenvalues as [62]:

$$FM = \left[\frac{(\omega_2^2 - \omega_1^2)}{2} + \frac{(\sigma_2^2 - \sigma_1^2)}{2}\right]^2 + 4\sigma_1\sigma_2\left[\frac{(\omega_2^2 + \omega_1^2)}{2} + 2\left(\frac{\sigma_2 + \sigma_1}{2}\right)^2\right] - \left[\left(\frac{\sigma_2 - \sigma_1}{\sigma_2 + \sigma_1}\right)\frac{(\omega_2^2 - \omega_1^2)}{2} + 2\left(\frac{\sigma_2 + \sigma_1}{2}\right)^2\right]^2 \qquad (2.53)$$

The flutter margin FM is seen to reach a value of 0 when the real part of either mode (and thus, the damping of the mode) becomes zero.

It is noted [54; 61; 62] that the flutter margin varies quadratically with dynamic pressure q. Yildiz [62] also remarks that the flutter margin is relatively insensitive to uncertainty in modal damping, whilst being sensitive to the modal frequencies (which may generally be obtained with much greater accuracy). Due to the monotonic behaviour of the flutter margin with dynamic pressure, it may be used for the prediction of flutter even when the system exhibits hard flutter [62].

2.9.2 Flutter Margin for Discrete Systems

The flutter margin for discrete systems (FMDS) developed by Matsuzaki and Torii [54] is mathematically equivalent to the Zimmerman-Weissenburger flutter margin for two-mode flutter, as has been noted by several authors. The coefficients of the system characteristic are estimated from the coefficients of the auto-regressive moving average (ARMA) model used to describe the time-domain response of a body. The time-domain data is preprocessed through a bandpass filter to include only the frequencies of coupled modes [54], and is described at the time t by y_t. The system is assumed to contain white noise, represented by e_t. The ARMA model describing the system is then given [29; 54] by:

$$y_t + \sum_{i=1}^{n} \alpha_i y_{t-i} = e_t + \sum_{i=1}^{m} \beta_i e_{t-i} \qquad (2.54)$$

where n is the order of the auto-regressive (AR) component, and m is the order of the moving average (MA) component.

McNamara and Friedmann [29] suggest an alternative formulation, stating that one MA coefficient is sufficient to describe the aeroelastic static offset:

$$y_t + \sum_{i=1}^{n} \alpha_i y_{t-i} = \beta_1 e_{t-1} \qquad (2.55)$$

Recommendations on the selection of the orders n and m varies between authors depending on the application of the modelling. Torii [54] and Yildiz [62] recommend that for two-mode flutter, the order of the AR component should be $n = 4$. Both these authors recommend that the MA component m be determined by minimization of the Akaike Information Criteria, which is a measure of the goodness of fit of a statistical model [62]. Dimitriadis [61] recommends that in the absence of noise, the order of the AR component should be selected to be equal to twice the number of the modes $n = 4$; however, with experimental noise, Dimitriadis recommends a selection of $n > 4$. In both cases, Dimitriadis uses $m = n - 1$.

Torii shows that the system characteristic $G(s)$ is then given[54] by:

$$G(s) = s^4 + \alpha_1 s^3 + \alpha_2 s^2 + \alpha_3 s + \alpha_4 \qquad (2.56)$$

The Jury stability criterion is then applied, and the flutter margin for the 2-mode system is given [54] by:

$$FM_s = \frac{\det(X_3 - Y_3)}{(1 - \alpha_4)^2} \qquad (2.57)$$

where $X_3 = \begin{bmatrix} 1 & \alpha_1 & \alpha_2 \\ 0 & 1 & \alpha_1 \\ 0 & 0 & 1 \end{bmatrix}$ and $Y_3 = \begin{bmatrix} \alpha_2 & \alpha_3 & \alpha_4 \\ \alpha_3 & \alpha_4 & 0 \\ \alpha_4 & 0 & 0 \end{bmatrix}$

The flutter point is reached when FM_s reaches a value of 0.

2.9.3 Damping Extrapolation

Flutter is observed when the modal damping of one of the aeroelastic modes becomes zero. As the flight speed is increased towards flutter, the damping trends usually indicate a separation in the damping trends of the coalescing modes; that is, a decrease in the damping ratio of the flutter mode is generally observed close to flutter. The method of damping extrapolation considers the set of damping ratio data at a number of sub-critical speeds, and

through curve-fitting the data [61], extrapolates the trend to higher speeds. From this, the flutter speed is estimated as the point at which the extrapolated curve shows zero damping.

The damping extrapolation method is one of the earliest methods used for flutter prediction [51]. However, the method may represent some difficulty in implementing due to the difficulty in extracting the modal damping [62] (due to low signal-to-noise ratios, or due to the inaccuracies in extracting modal data from measurements at individual points on the structure), or due to hard flutter [51; 62].

2.9.4 Envelope Function

The envelope function is a simple method to estimate the closeness of the system to flutter through consideration of only the time-history of response to an impulse. The method offers no estimate of damping or frequency, but looks at the tendency of the response to decay. The envelope of oscillation will be larger as the damping in the system decreases, and the stability of the system is estimated by the bias of the data (the position of its centroid) towards the start or end of the time window; flutter is reached when the envelope is rectangular, and the centroid is approximately at the middle of the time window [61].

The envelope may be calculated [62] from the Hilbert transform, $y_H(t)$, of the signal ($y(t)$) as:

$$env(t) = \sqrt{\left(y(t)\right)^2 + \left(y_H(t)\right)^2} \qquad (2.58)$$

The centroid of the envelope over the time window defined by $0 \leq t \leq t_{max}$ is given[62] by:

$$\bar{t} = \frac{\int_0^{t_{max}} env(t)tdt}{\int_0^{t_{max}} env(t)dt} \qquad (2.59)$$

The shape factor of the envelope is defined by [61; 62]:

$$S = \frac{1}{\bar{t}} \qquad (2.60)$$

For which the onset of flutter is indicated by the condition [61; 62]:

$$S_F \approx \frac{2}{t_{max}} \quad (2.61)$$

The prediction of the onset of flutter is then achieved through curve-fitting the shape parameter at a number of sub-critical velocities and extrapolating. It must be noted that extrapolation of the shape parameter, due to it being an indirect damping estimate, is unable to predict the onset of hard flutter. The shape parameter may be redefined in order to be equal to indicate flutter by a value of zero as:

$$S_F^* = \frac{t_{max}}{\bar{t}} - 2 \quad (2.62)$$

2.9.5 Analytical Methods

A number of classical methods for calculating the flutter point are available, and are often implemented in software for aeroelastic analysis using panel method aerodynamics. A key aspect of these methods is that the motion of assumed to be described by either a damped or undamped sinusoid of a specified frequency, and the aerodynamic loading is calculated in terms of that frequency. Two of the classical flutter calculation methods that are outlined are the V-g method (also known as the American k method [3]) and the p-k method (also known as the British flutter method [3]).

2.9.5.1 V-g Method

In the V-g method, motion is assumed to be purely sinusoidal:

$$x(t) = x_0 e^{i\omega} \quad (2.63)$$

The aerodynamic matrices are evaluated in terms of an assumed flutter frequency ω; only artificial structural damping proportional to the stiffness matrix is assumed; the equations of motion become [63]:

$$-\omega^2 \boldsymbol{M_{str}}\{x\} + (1 + ig)\boldsymbol{K_{str}}\{x\} - \frac{\rho V^2}{2}\boldsymbol{Q}(ik)\{x\} = 0 \quad (2.64)$$

where g represents the artificial damping required to make the system oscillate harmonically -- this is negative for stable systems [64]; and $\boldsymbol{Q}(ik)$ represents the GAFs evaluated for the specified ρ, and k.

The problem is rearranged to give the following eigenvalue problem [63]:

$$\Omega\{x\} = \left[\boldsymbol{K_{str}^{-1}}\left[\boldsymbol{M_{str}} - \frac{\rho c^2}{8k^2}\boldsymbol{Q}(ik)\right]\right]\{x\} \qquad (2.65)$$

where $\Omega = \left(\frac{1+ig}{\omega^2}\right)$

The solution procedure is as follows [63]:

1. Specify the altitude (through ρ),
2. For a sweep of k, calculate the GAFs and solve the eigenvalue problem

   For each eigenvalue $z_i = r_i + is_i$, the following are obtained [63]:

   $\omega_i = \sqrt{\frac{1}{s_i}}$, $\quad U_{\infty_i} = \frac{\omega_i c}{2k}$, and $\quad g_i = \frac{s_i}{r_i}$
3. Find the flutter speed as the speed at which g becomes positive.
4. Find the divergence speed as both g and ω approach 0 for $k \to 0$.

An advantage offered by the V-g method is that the divergence speed is found as a by-product of the flutter calculation.

2.9.5.2 p-k Method

The p-k method assumes damped sinusoidal motion [65], in the form:

$$x(t) = x_0 e^{pt} \qquad (2.66)$$

where $p = \sigma + i\omega$

This allows the free response of the system to be written as:

$$p^2\boldsymbol{M_{str}}\{x\} + p[\boldsymbol{C_{str}} - \boldsymbol{C_{aero}}]\{x\} + [\boldsymbol{K_{str}} - \boldsymbol{K_{aero}}]\{x\} = 0 \qquad (2.67)$$

This is seen to be an eigenvalue problem. The aerodynamic matrices have terms dependent on the Mach number, altitude, and reduced frequency of vibration, k. The solution procedure followed in the p-k method is outlined [65] below:

1. Specify altitude (through ρ) and Mach number (through U_∞),
2. Assume a value of k (through $\omega_{assumed}$), where $k = \frac{\omega c}{2U_\infty}$,
3. Compute the aerodynamic matrices $\boldsymbol{K_{aero}}$ and $\boldsymbol{C_{aero}}$ for the assumed values,
4. Solve the eigenvalue problem for p, where $p = \zeta\omega_{solved} + i\omega_{solved}$ for small values of damping,
5. Check that the frequencies are matched: $\omega_{solved} \approx \omega_{assumed}$?
6. Iterate steps 2 through 5 as necessary to obtain a matched-point solution at the specified flight conditions,
7. Sweep the altitude or Mach number (repeat steps 1 through 6 for different values in step 1) to obtain the variation in system parameters with altitude/Mach number and to obtain the flutter point.

The p-k method provides matched-point solutions, and is useful in providing the variation of system parameters not only at the flutter point.

3 DEVELOPMENT OF PISTON THEORY

3.1 Fundamental formulation

The early development of piston theory is generally accredited to Lightill [66] around 1953, and was reviewed by Ashley and Zartarian [28] in 1956. Further developments and higher order theories were developed since; Liu [12] et al in 1997 reviewed the higher order expansions developed by several authors. The various higher order expressions differ to certain extents, due to differences in the fundamental formulation which the series-expansion is based upon, which will expanded upon below. McNamara et al [10] consider the similarities between Van Dyke's second-order theory and Lightill's piston theory, and consider some differences in the formulation of "classical" and "local" piston theory.

The surface pressure on a body is calculated assuming that the downwash resulting from motion of the body and from the body shape can be modelled as a piston moving in a 1D cylinder. This is an application of the equivalence between steady flow in two dimensions around a surface and unsteady flow in one dimension in hypersonic/supersonic flows [13], as is shown in Figure 3.1.

The various formulations of piston theory differ in the theoretical basis used to describe the instantaneous pressure on the surface of the piston; thereafter, the expression for the surface pressure is expanded in a binomial series to the order required. The equation for the surface pressure in Lighthill's piston theory is from the equations of 1D compressible flow for a piston generating isentropic simple waves [28]. The equation for pressure on a slightly curved wall in potential flow from Van Dyke's second-order theory [67] may also be expanded in a binomial series, yielding a similar expression to Lighthill's piston theory; for this reason, Van

Dyke's second-order theory is often referred to as second-order piston theory [10] (although the coefficients differ to those given by Lighthill). Donov [68] derives an expression up to the fourth-order for the pressure on the surface a gently curved wall from consideration of the Prandtl-Meyer function for flow expansion; the equation is for irrotational, isentropic flows resulting from small disturbances [68]. Donov suggests [68] that for small disturbances, the pressure on the surface due to flow compression (shock waves) may be approximated using the expression obtained from Prandtl-Meyer function.

Lighthill's piston theory, based on the equations of 1D compressible isentropic flow, gives [28] the instantaneous pressure on the face of a as:

$$\frac{P}{P_{cyl}} = \left\{1 + \frac{\gamma - 1}{2}\left(\frac{w}{a_{cyl}}\right)\right\}^{\frac{2\gamma}{(\gamma-1)}} \quad (3.1)$$

where w is the downwash on the piston face, a_{cyl} is the speed of sound at the reference point in the cylinder, and P_{cyl} is the corresponding reference pressure.

The pressure coefficient is by definition referenced to free-stream quantities. If the reference pressure in the cylinder, P_{cyl}, is different to that of the free-stream pressure P_∞, an offset term is obtained for the pressure coefficient. The cylinder reference conditions depend on the reference frame in which piston theory is applied -- this is one of the differences between classical piston theory and local piston theory, which is discussed in Section 3.2.1 and Section 3.2.2.

Consider that the binomial expansion for the surface pressure is given by:

$$\frac{P}{P_{cyl}} = 1 + \gamma E \quad (3.2)$$

where E denotes the series in the terms $\left(\frac{w}{a_{cyl}}\right)$, for generality.

Referencing the surface pressure, P, to the free-stream conditions, one obtains:

$$C_P = C_{P\,cyl} + \left(\frac{P_{cyl}}{P_\infty}\right)\frac{2}{M_\infty^2}E \quad (3.3)$$

where

$$C_P = \frac{P - P_\infty}{\frac{1}{2}\gamma P_\infty M_\infty^2} \quad (3.4)$$

$$C_{P\,cyl} = \frac{P_{cyl} - P_\infty}{\frac{1}{2}\gamma P_\infty M_\infty^2} \quad (3.5)$$

$$E = \left[c_1 \left(\frac{w}{a_{cyl}} \right) + c_2 \left(\frac{w}{a_{cyl}} \right)^2 + c_3 \left(\frac{w}{a_{cyl}} \right)^3 \right] \quad (3.6)$$

in which c_1, c_2 and c_3 represent the coefficients associated with the binomial expansion of whichever pressure relation the piston theory is based upon.

Equations (3.2), (3.3) and (3.6) in may be considered the generalized expressions for the pressure on the piston surface for any piston theory. No assumptions have been made regarding the cylinder reference conditions, and no assumptions (other than that the pressure series may be expressed in the form of equation (3.2)) have been made regarding the pressure relation upon which the piston theory is based.

It may be seen that if the cylinder reference conditions are chosen to be equal to the free-stream conditions (classical piston theory), then:

$$P_{cyl} = P_\infty \quad (3.7)$$

$$a_{cyl} = a_\infty \quad (3.8)$$

leading to the expression for the pressure coefficient at the piston surface from equations (3.2) and (3.6):

$$C_P = \frac{2}{M_\infty^2} \left[c_1 \left(\frac{w}{a_\infty} \right) + c_2 \left(\frac{w}{a_\infty} \right)^2 + c_3 \left(\frac{w}{a_\infty} \right)^3 \right] \quad (3.9)$$

This expression is equivalent to the equation given by Liu et al [12], with the coefficients obtained from various theoretical formulations provided [12] in Table 3.1 and Table 3.2.

Table 3.1: Comparison of Piston Theories and Associated Coefficients [12]

$C_P = \frac{2}{M_\infty^2}\left[c_1\left(\frac{w}{a_\infty}\right) + c_2\left(\frac{w}{a_\infty}\right)^2 + c_3\left(\frac{w}{a_\infty}\right)^3\right], \qquad m = \sqrt{M^2-1}$				
	Lighthill's piston theory	**Van Dyke's second-order theory**	**Busemann**	**Donov**
c_1	1	$\frac{M}{m}$	$\frac{M}{m}$	$\frac{M}{m}$
c_2	$\frac{\gamma+1}{4}$	$\frac{M^4(\gamma+1)-4m^2}{4m^4}$	$\frac{M^4(\gamma+1)-4m^2}{4m^4}$	$\frac{M^4(\gamma+1)-4m^2}{4m^4}$
c_3	$\frac{\gamma+1}{12}$	—	$c_{3(B)}$	$c_{3(D)}$

Table 3.2: Comparison of Busemann and Donov Expansions [12]

	Busemann	**Donov**
Equation	$c_{3(B)} = \left(\frac{1}{6m^7}\right)(aM^8 + bM^6 + cM^4 + dM^2 + e)$	$c_{3(D)} = \left(\frac{1}{6Mm^7}\right)(aM^8 + bM^6 + cM^4 + dM^2 + e)$
a	$3\left(\frac{\gamma+1}{4}\right)^2$	$\gamma+1$
b	$\frac{3\gamma^2-12\gamma-7}{4}$	$2\gamma^2-7\gamma-5$
c	$\frac{9(\gamma+1)}{2}$	$10(\gamma+1)$
d	-6	-12
e	4	8

3.2 Cylinder conditions

The formulation presented thus far has remained general in terms of the specification of the cylinder reference conditions. These conditions are defined through the choice of the reference frame in which the cylinder is placed. The difference between classical piston theory and local piston theory arises primarily from the difference in reference frames applied.

Consider a sectioning-plane, or "cutting plane" fixed in space. Also consider a body undergoing general motion (translation and rotation), passing through (normal to) the cutting plane at constant speed. For a 2D body or airfoil, the cutting plane is effectively a line in the plane of the airfoil -- it is a "cylinder" of infinitesimal width. The cylinder over time would show the movement of the loci of the upper and lower surfaces of the airfoil as it passes through the cutting plane, as shown in Figure 3.1. The loci of the surfaces are considered infinitesimally narrow "piston" surfaces moving down the length of a cylinder (the cutting plane) perpendicular to the freestream velocity vector, V_∞.

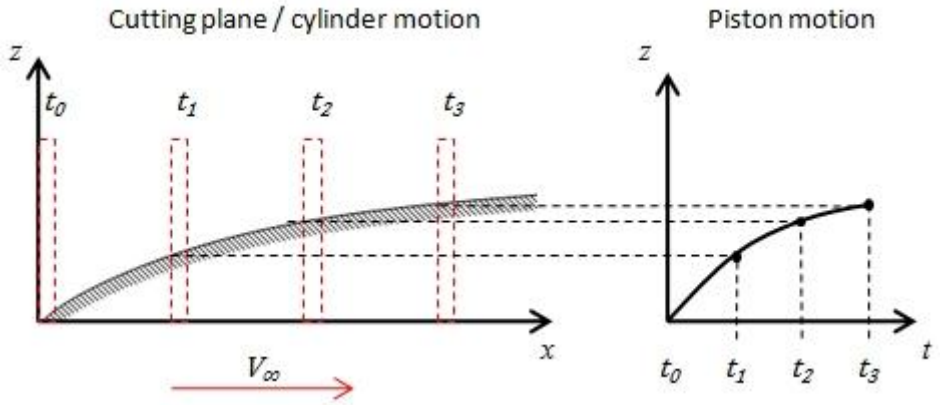


Figure 3.1: Definition of the Cylinder in Piston Theory

3.2.1 Classical piston theory

In Lighthill's formulation of classical piston theory, one may consider the cylinder to be fixed in space (earth-fixed reference system), with the atmosphere at rest. Under these conditions, the cylinder conditions are given by the free-stream conditions; that is:

$$P_{cyl} = P_{\infty} \quad (3.10)$$

$$a_{cyl} = a_{\infty} \quad (3.11)$$

The reference conditions in classical piston theory are modelled as remaining unchanged as the body passes through the cylinder. The use of the free-stream conditions as cylinder reference conditions in equations (3.3) and (3.6) leads to the pressure on the surface of the piston given by Lighthill's classical piston theory [12]:

$$C_P = \frac{2}{M_{\infty}^2}\left[\left(\frac{w}{a_{\infty}}\right) + \left(\frac{\gamma+1}{4}\right)\left(\frac{w}{a_{\infty}}\right)^2 + \left(\frac{\gamma+1}{12}\right)\left(\frac{w}{a_{\infty}}\right)^3\right] \quad (3.12)$$

The cylinder-piston relationship in classical piston theory is shown in Figure 3.2 on page 55.

3.2.2 Local piston theory

In local piston theory, the cylinder is fixed to an axial location on the body, at a fixed height in space; movement of the body results in motion of the piston surfaces down the length of the cylinder, and there is no motion through the cylinder (through the cutting plane). This reference frame is analogous to the laboratory reference frame for a body mounted in a wind-tunnel, with pitch and plunge motion permitted, but translation down the length of the test section restricted. The relationship between the cylinder and piston motion is shown in Figure 3.3 on page 56.

The choice of this reference frame renders the cylinder to be local (axially) to the body. For no motion of the body, the cylinder conditions are seen to be determined by the steady flowfield around the stationary body. In applying local piston theory, McNamara et al [10] use the local steady flow conditions as cylinder reference conditions. This may be motivated as follows.

> In each of the theoretical formulations from which the pressure equation has been derived for supersonic free-stream flow (that is: from Van Dyke's second-order theory [67], from isentropic Prandtl-Meyer expansion [12; 68], and from the oblique shock equations [12; 68]), the pressure equation derived gives the ratio of the surface pressure to the pressure in the undisturbed flow. The equations have the form:

$$\frac{P}{P_\infty} = 1 + \gamma \left[c_1 \left(\frac{w}{a_\infty} \right) + c_2 \left(\frac{w}{a_\infty} \right)^2 + c_3 \left(\frac{w}{a_\infty} \right)^3 \right] \quad (3.13)$$

In which the P_∞ and a_∞ are the undisturbed flow conditions.

The equations for the piston pressure are derived for the steady flow around a stationary geometry from an undisturbed state. The same equations may be used to describe the unsteady pressure due to airfoil motion at a point in time. In an extension of the reasoning of equivalence in hypersonic/supersonic flow between unsteady flow in one dimension and steady flow in two dimensions, the unsteady flow at a point is modelled as being equivalent to the steady flow over the two-dimensional surface traced by the point through time. This is shown in Figure 3.4 on page 57. The undisturbed flow conditions for the surface in time correspond to the steady flow conditions for the stationary two-dimensional geometry.

Thus, in local piston theory, the "undisturbed" (reference) conditions for the cylinder are taken to be the steady flow conditions at the piston surface for no motion of the airfoil.

$$P_{cyl} = P_{ss} \quad (3.14)$$

$$a_{cyl} = a_{ss} \quad (3.15)$$

where the subscript "ss" denotes the local flow conditions at the mean steady state.

This allows the same formulations of piston theory to be used through substitution of the local flow properties for cylinder conditions:

$$\frac{P}{P_{ss}} = 1 + \gamma \left[c_1 \left(\frac{w}{a_{ss}} \right) + c_2 \left(\frac{w}{a_{ss}} \right)^2 + c_3 \left(\frac{w}{a_{ss}} \right)^3 \right] \quad (3.16)$$

where P represents the total pressure at the surface of the piston, including the unsteady pressure due to motion.

However, care should be taken to note that the pressure coefficient is still referenced to free-stream conditions in local piston theory, i.e.:

$$C_P = \frac{P_{ss} - P_\infty}{\frac{1}{2}\gamma P_\infty M_\infty^2} + \left(\frac{P_{ss}}{P_\infty} \right) \frac{2}{M_\infty^2} \left[c_1 \left(\frac{w}{a_{ss}} \right) + c_2 \left(\frac{w}{a_{ss}} \right)^2 + c_3 \left(\frac{w}{a_{ss}} \right)^3 \right] \quad (3.17)$$

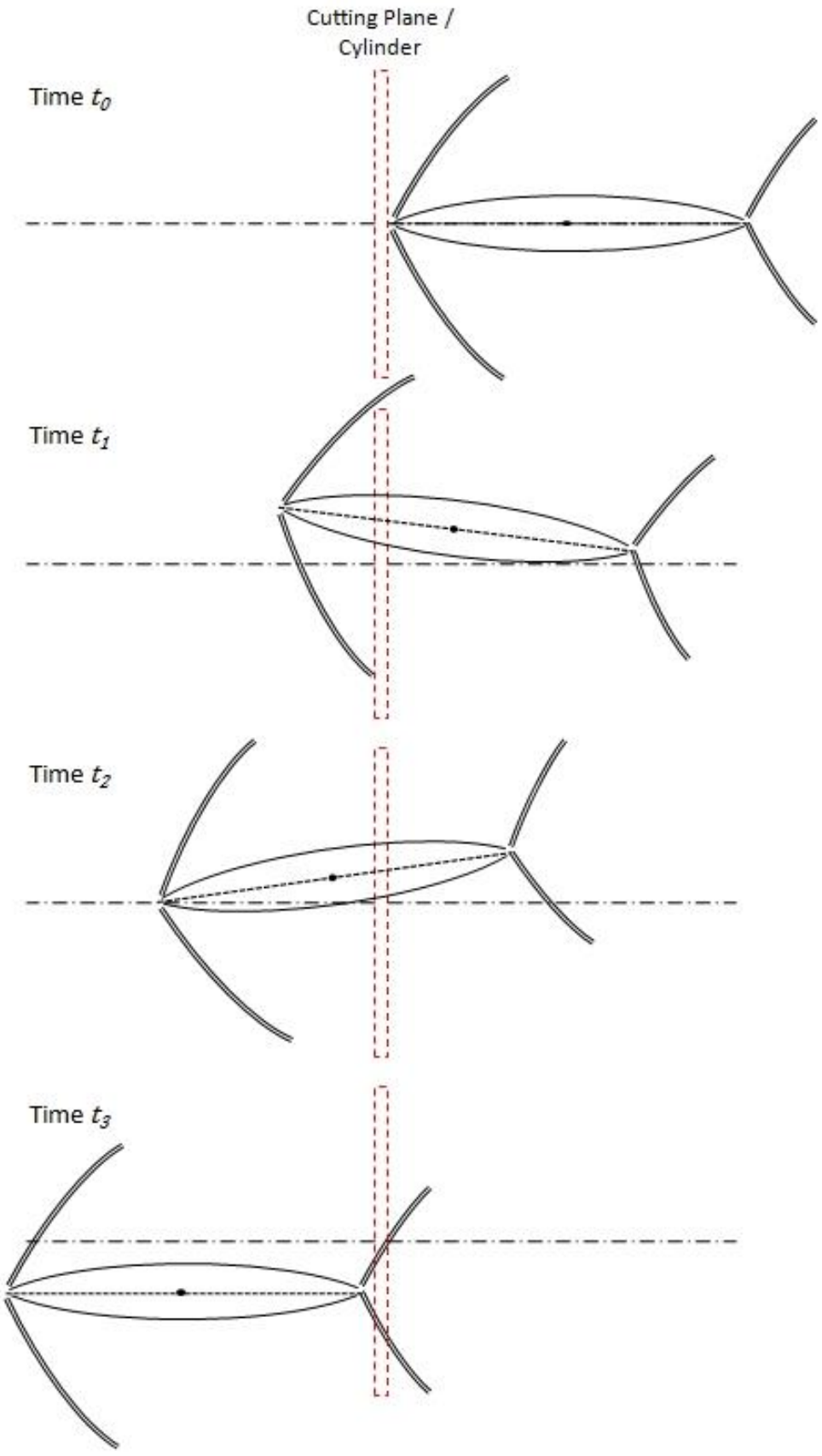


Figure 3.2:The Piston-Cylinder Relationship in Classical Piston Theory

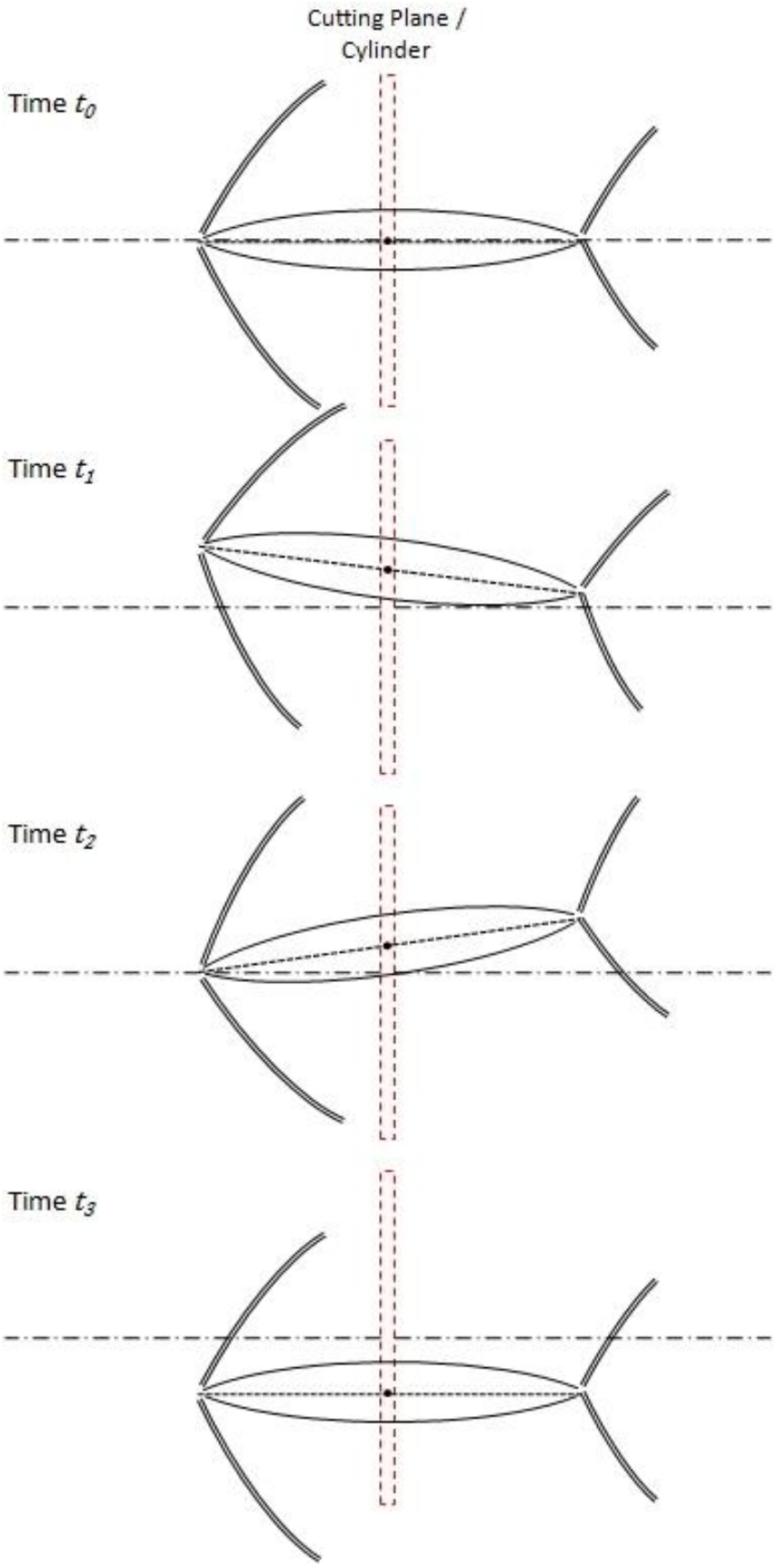


Figure 3.3: The Piston-Cylinder Relationship in Local Piston Theory

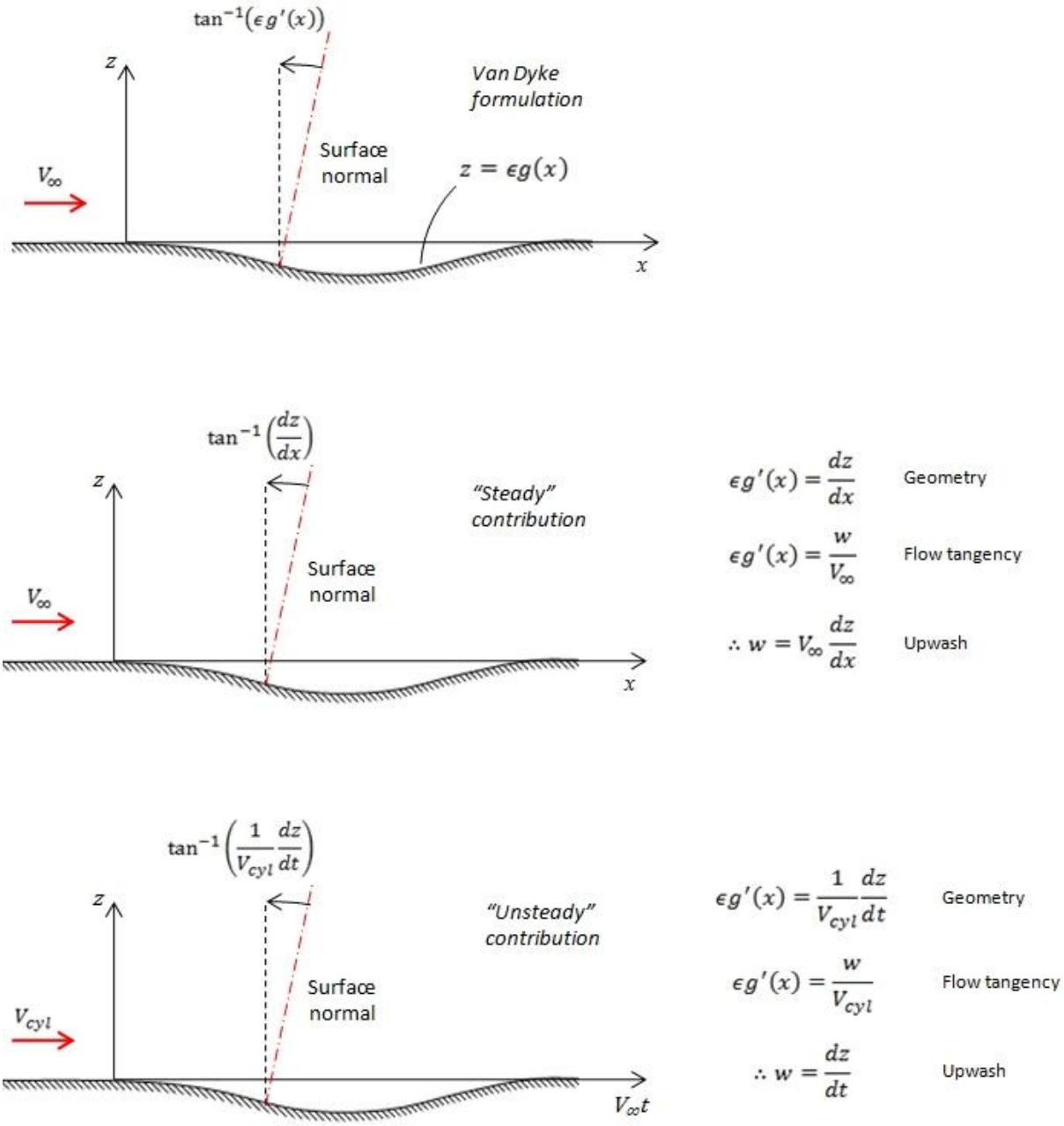


Figure 3.4: Equivalence Between Piston Theory and Van Dyke's Second Order Theory

The essence of local piston theory, as noted by Zhang [11], is the dynamic-linearization of the flow; small perturbations about a mean steady flow are considered. It is assumed that the oscillation (or unsteady deviation from its mean location) of the airfoil surface is assumed to be small enough in amplitude that the local flowfield does not deviate significantly from its mean steady state. The mean steady flow solution is then obtained through another aerodynamic method (in the case of Zhang [11] et al, by a full Euler method), which may be accurately describe complex effects arising from airfoil geometry or flow conditions.

3.3 Downwash terms

The downwash terms in piston theory, $\frac{w}{a_{cyl}}$, arise due to "steady" and "unsteady" contributions; the "steady" contributions include effects due to the body shape, whilst the "unsteady" contributions arise from motion of the airfoil down the length of the cylinder. The general motion of a body, as shown in Figure 3.5, may be separated into what will be termed "steady" motion and "unsteady" motion without a loss in generality, as per Figure 3.6.

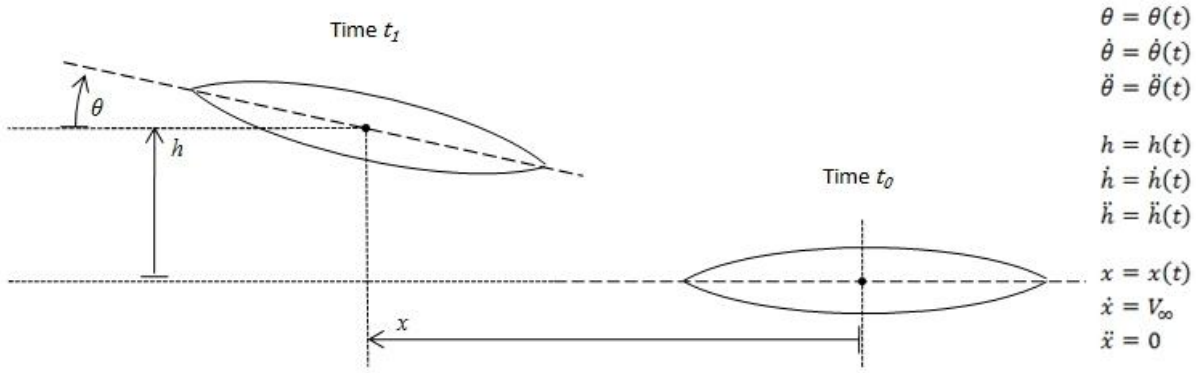


Figure 3.5: General Motion for a 2-Dimensional Body

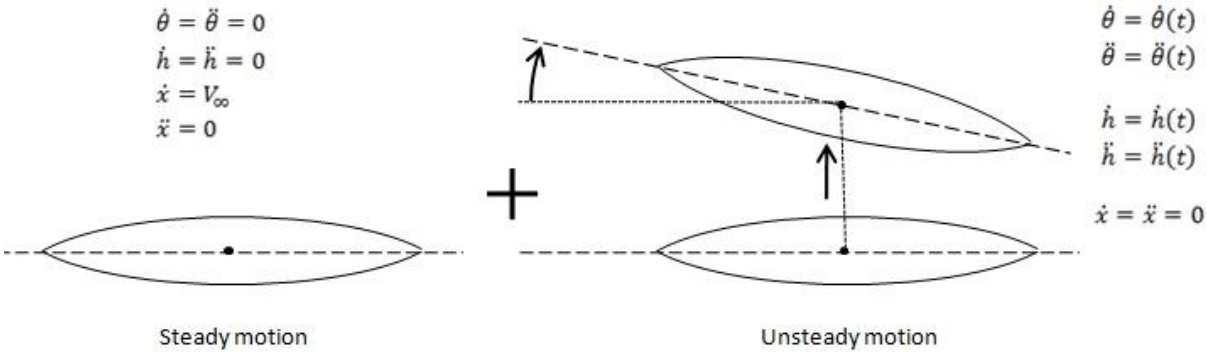


Figure 3.6: "Steady" and "Unsteady" Motion of a Body in Piston Theory

It may be seen that for steady motion, all time-derivatives of the motion are zero; in contrast, for unsteady motion, all time-derivatives of the motion (except in the direction of the steady motion) are non-zero. The steady motion may be aerodynamically modelled as steady flow over a stationary body; this will be done in considering the upwash contribution due to steady motion. Unsteady motion corresponds to pitch and plunge, as well as dynamic deformations of the camberline.

The downwash, w, on the piston face is given [28] by:

$$w = \left[\left(\frac{\partial}{\partial t}\right) + V_{cyl}\left(\frac{\partial}{\partial X}\right)\right] z \qquad (3.18)$$

in which V_{cyl} is the velocity in the cylinder parallel to the free-stream, X is the coordinate parallel to the free-stream (the cylinder is perpendicular to X), and z represents the position of the piston in the cylinder.

Here, the two sources of downwash are evident, and are shown in Figure 3.7 for classical piston theory in which the cylinder conditions are given by the free-stream. The first term in the equation, $\frac{\partial z}{\partial t}$, consists of the unsteady contribution arising from motion of the piston down the cylinder, in particular from:

- rigid body pitching of the airfoil,
- rigid body plunging of the airfoil,
- local dynamic deformations (vibration) of the airfoil surface.

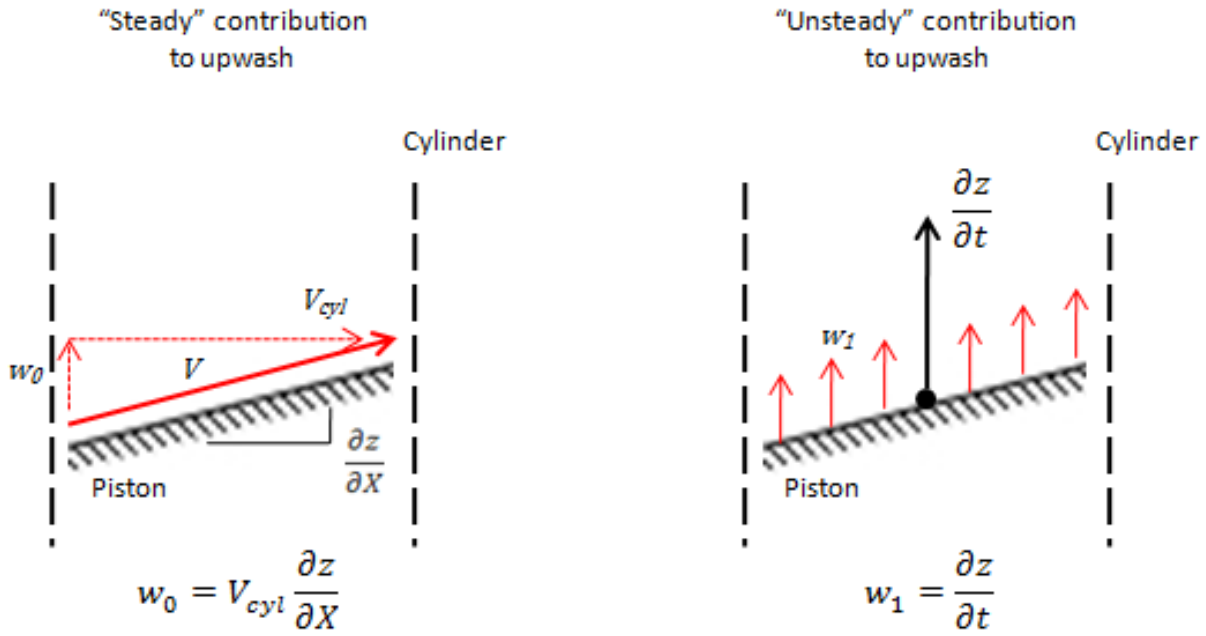


Figure 3.7: Contributions to Downwash in Piston Theory

The second term in the equation, $V_{cyl}\left(\frac{\partial z}{\partial X}\right)$, consists of "convection" terms, or a steady contribution from the body shape and angle of attack (as would arise from steady motion (see Figure 3.6) of the airfoil through the "cutting plane" (cylinder)); contributions to this term are from:

- the local inclination of the chordline to the free-stream (angle of attack),
- the local inclination of the camberline to the free-stream (including static deformations of the camberline),
- the local rate of change of thickness down the chordline.

These contributions to the downwash may also be deduced from a consideration of the disturbances produced, and considering the formulation of Van Dyke's second-order theory [67], adapted for comparison in Figure 3.4.

Whilst the contribution of the body shape, flow incidence, and unsteady motion to downwash in piston theory are immediately obvious, the contribution to the flow physics requires a more thorough consideration of the piston theory modelling. To this end, the downwash equation is recast, following the notation of Liu et al [12], as:

$$w = w_0 + w_1 \qquad (3.19)$$

where

$w_0 = V_{cyl}\frac{\partial z}{\partial X}$ represents the contribution from body shape and angle of attack

$w_1 = \frac{\partial z}{\partial t}$ represents the contribution from body motion

The expressions for the surface pressure in piston theory are dependent on the series expansion in terms of the downwash. In order to maintain generality of description between the various formulations, let the downwash terms be considered in isolation; considering up to third-order terms:

$$w = \underbrace{w_0 + w_1}_{\text{uncoupled contributions}} \qquad (3.20)$$

$$w^2 = \underbrace{w_0^2 + w_1^2}_{\text{uncoupled contributions}} + \underbrace{2w_0w_1}_{\text{coupled contributions}} \qquad (3.21)$$

$$w^3 = \underbrace{w_0^3 + w_1^3}_{\text{uncoupled contributions}} + \underbrace{3w_0^2w_1 + 3w_0w_1^2}_{\text{coupled contributions}} \qquad (3.22)$$

From the consideration of the downwash terms, it may be seen that from second-order terms and higher, coupling terms between the steady and the unsteady contributions arise.

The w_0, w_0^2 and w_0^3 terms represent the contribution to downwash arising purely from the steady motion of the airfoil. These terms effectively give the steady flow around the stationary airfoil. In a wind-tunnel analogy, these terms are for "wind on" and "motion off".

The w_1, w_1^2 and w_1^3 terms are associated with the unsteady motion of the airfoil. These terms account only for the motion of the airfoil surface down the length of the cylinder. In a wind-tunnel analogy, these terms are the downwash due to "wind off" with "motion on".

The terms involving products of w_0 and w_1 (i.e., $2w_0w_1$, $3w_0^2w_1$, and $3w_0w_1^2$) are coupled; these terms represent the nonlinear effects associated with a "wind on" and "motion on" state.

Recall that the w_0 terms are associated with the body shape and steady flow, whilst w_1 terms are associated with body motion. When these terms are substituted into the expression for pressure, these terms will represent (to an extent) the aerodynamic stiffness and aerodynamic damping, respectively.

Hence it may be seen that the second-order downwash term introduces thickness and angle of attack effects into the aerodynamic damping (through $2w_0w_1$).

The third-order introduces nonlinear damping with linear thickness dependency (through $3w_0w_1^2$), as well as extending the linear damping to include nonlinear thickness and angle of attack effects (through $3w_0^2w_1$).

3.3.1 Downwash terms in local piston theory

In applying local piston theory, the reference conditions in the cylinder are set to the quasi-steady flow conditions at the point in time under consideration. When the solution to the mean steady flow is obtained from other aerodynamic methods, the terms in the pressure

equation from local piston theory associated with the steady flow (w_0, w_0^2 and w_0^3) are replaced by the steady pressure calculated using the other methods. That is:

$$\frac{P}{P_{ss}} = 1 + \gamma \left[c_1 \left(\frac{w_1}{a_{ss}} \right) + c_2 \left(\frac{2w_0 w_1 + w_1^2}{a_{ss}^2} \right) + c_3 \left(\frac{3w_0^2 w_1 + 3w_0 w_1^2 + \ w_1^3}{a_{ss}^3} \right) \right] \qquad (3.23)$$

or, rearranging:

$$\frac{P}{P_{ss}} = 1 + \gamma \left[\left(\frac{c_1}{a_{ss}} + \frac{2w_0 c_2}{a_{ss}^2} + \frac{3w_0^2 c_3}{a_{ss}^3} \right) w_1 + \left(\frac{c_2}{a_{ss}^2} + \frac{3w_0 c_3}{a_{ss}^3} \right) w_1^2 + \left(\frac{c_3}{a_{ss}^3} \right) w_1^3 \right] \qquad (3.24)$$

in which P_{ss} is the steady pressure calculated for the mean steady flow, and P is the total pressure on the piston face.

3.4 Third-order terms

It has been shown [10; 12] that the third-order downwash terms in piston theory introduce nonlinear thickness and angle of attack effects on the aerodynamic damping, as well as increasing the order of the damping to two.

Furthermore, the third-order terms in piston theory represent an important extension in the flow physics that is modelled relative to second-order piston theory. The coefficients of the third-order terms begin to differ between various piston theories due to the difference in the flow physics: a difference is shown [12; 68] to exist between the pressure due to isentropic expansion of the flow, and due to small compressions resulting in oblique shocks.

Donov shows that effects from the leading-edge shock on an airfoil only enter into his expression for the pressure on the surface from third-order terms and higher; these effects include the vorticity caused by the shock [68]. Liu et al [12] similarly show that the pressure on the piston surface differs for shocks and expansions only from the third-order term onwards in piston theory; the approach adopted by Liu et al to show this is significantly shorter and simpler than the rigorous treatment of Donov [68], and is based on consideration of the expressions for the surface pressure in the hypersonic limit on a wedge in compression and expansion [12]. This is outlined as follows.

Consider the equations for C_P as based on irrotational, isentropic expansions, and from oblique shocks:

From the equation for the pressure due isentropic expansion in the hypersonic limit [12]:

$$C_P = \frac{2}{\gamma M^2}\left[\left(1 + \frac{\gamma - 1}{2}K\right)^{\frac{2\gamma}{\gamma-1}} - 1\right] \quad (3.25)$$

This may be expanded to the third-order term to yield:

$$C_P = \frac{2}{M^2}\left[K + \left(\frac{\gamma + 1}{4}\right)K^2 + \left(\frac{\gamma + 1}{12}\right)K^3\right] \quad (3.26)$$

It may be seen that the same coefficients are obtained as in Lighthill's piston theory [28], because the pressure equation which is subsequently expanded is the same [12].

From the equation for the pressure behind an oblique shock on a wedge in the hypersonic limit [12]:

$$C_P = \frac{2K^2}{M^2}\left[\frac{\gamma + 1}{4} + \sqrt{\left(\frac{\gamma + 1}{4}\right)^2 + \frac{1}{K^2}}\right] \quad (3.27)$$

This may be expanded to the third-order term to yield:

$$C_P = \frac{2}{M^2}\left[K + \left(\frac{\gamma + 1}{4}\right)K^2 + \frac{(\gamma + 1)^2}{32}K^3\right] \quad (3.28)$$

Here, the third-order term differs from that given by the pressure coefficient due to isentropic expansion. Liu et al [12] note that the difference in the coefficient, $\Delta c_3 = (3\gamma^2 - 2\gamma - 5)/96 < 0$, represents the rotationality in the flow due to the shock wave.

In summary, the third-order terms in piston theory allow nonlinear thickness and angle of attack effects on aerodynamic damping to be modelled, and model the difference in flow physics for small disturbances between expansion and compression of the flow.

3.5 Generalized Formulation

A generalized formulation of piston theory is put forward, which encompasses both classical piston theory and local piston theory through description of the pressure equation in terms of cylinder reference conditions. The specification of these reference conditions allows the general formulation to reduce to classical or local piston theory. The formulation is put forward as:

$$\frac{P_{piston}}{P_{cyl}} = 1 + \gamma \left[c_1 \left(\frac{w_{cyl}}{a_{cyl}} \right) + c_2 \left(\frac{w_{cyl}}{a_{cyl}} \right)^2 + c_3 \left(\frac{w_{cyl}}{a_{cyl}} \right)^3 \right] \qquad (3.29)$$

in which the coefficients c_1, c_2, and c_3 are given as in Table 3.1 and Table 3.2. The reference pressure and speed of sound in the cylinder, P_{cyl} and a_{cyl}, respectively, are determined by the application of classical or local piston theory. The downwash to be used in the pressure equation, w_{cyl}, similarly depends on the reference system used in the piston theory. The differences are summarized in Table 3.3.

Table 3.3: Definition of Terms in Generalized Piston Theory

Variable	Classical Piston Theory	Local Piston Theory
P_{cyl}	P_∞	P_{ss}
a_{cyl}	a_∞	a_{ss}
w_0	$V_\infty \frac{\partial z}{\partial X}$	$V_{ss} \frac{\partial z}{\partial X}$
w_1	$\frac{\partial z}{\partial t}$	$\frac{\partial z}{\partial t}$
w_{cyl}	$w_0 + w_1$	w_1
w_{cyl}^2	$w_0^2 + 2w_0 w_1 + w_1^2$	$2w_0 w_1 + w_1^2$
w_{cyl}^3	$w_0^3 + 3w_0^2 w_1 + 3w_0 w_1^2 + w_1^3$	$3w_0^2 w_1 + 3w_0 w_1^2 + w_1^3$

The equation for the pressure coefficient is similarly given by:

$$C_P = C_{P_{cyl}} + \left(\frac{P_{cyl}}{P_\infty}\right)\frac{2}{M_\infty^2}\left[c_1\left(\frac{w_{cyl}}{a_{cyl}}\right) + c_2\left(\frac{w_{cyl}}{a_{cyl}}\right)^2 + c_3\left(\frac{w_{cyl}}{a_{cyl}}\right)^3\right] \quad (3.30)$$

where

$$C_{P_{cyl}} = \frac{P_{cyl} - P_\infty}{\frac{1}{2}\gamma P_\infty M_\infty^2} \quad (3.31)$$

It may be shown that the generalized formulation reduces to that given by Liu et al [12] when cylinder conditions are chosen corresponding to classical piston theory. Similarly, if the cylinder conditions are assumed to be equal to the steady flow conditions at the surface of the body, the equation reduces to that used by Zhang et al [11] in using first-order local piston theory.

From consideration of the similarity in the theoretical basis of the formulation of piston theory to that of Van Dyke's second order theory, and the similarity by extension to the work by Donov [68], it is recommended that the coefficients provided for Donov's third-order formulation by Liu et al [12] be evaluated with due consideration of the cylinder conditions.

3.6 Physical Effects Modelled by Classical Piston Theory

Having established the "steady" and "unsteady" contributions to the downwash terms, further insight may be obtained into the modelling achieved by piston theory through consideration of the contributions to the "steady" term of thickness, camber, and angle-of-attack effects. In considering the physical effects modelled, the analysis will be limited to classical piston theory. The physical interpretation may be extended to local piston theory as well.

Consider that the steady downwash w_0 consists of downwash from the thickness distribution (w_t), downwash from the camber distribution (w_c), and downwash from the angle-of-attack (w_α), as shown in Figure 3.8.

$$w_0 = w_t + w_c + w_\alpha \quad (3.32)$$

It may be seen from the Figure 3.8 that for the camber and angle-of-attack contributions, the flow turning angle at a point differs for the upper and lower surfaces; though the magnitude of the angle is the same, the flow is alternately turned into or away from itself, resulting in compression or expansion, respectively.

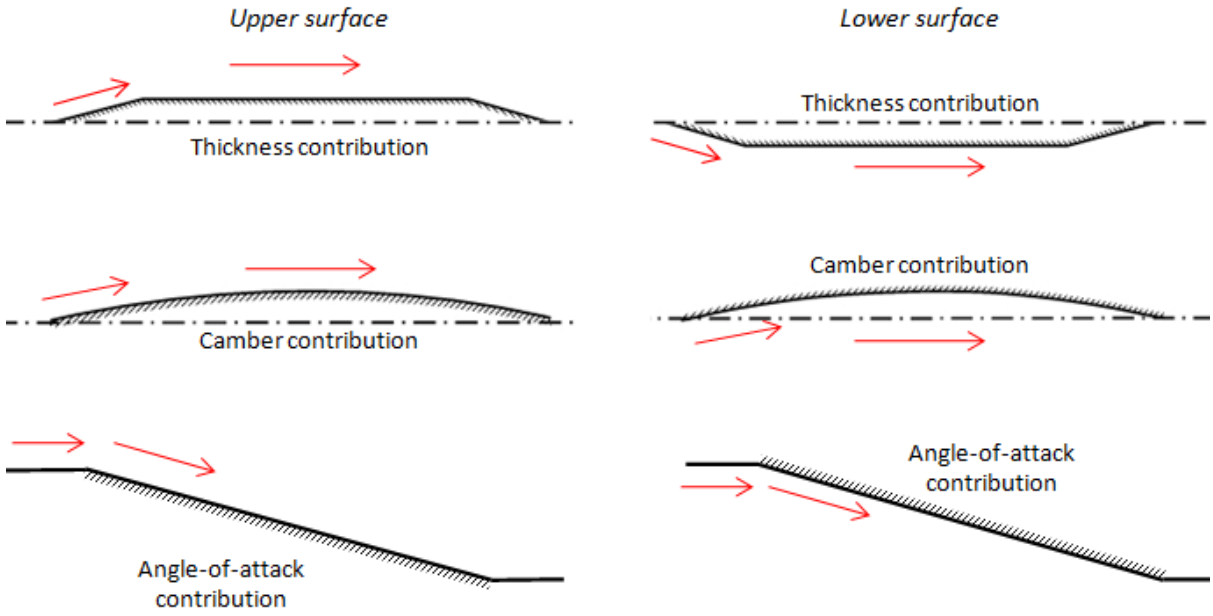


Figure 3.8: Contributions to the Steady Downwash Terms

In the following development, the camber and angle-of-attack contributions will be referred to as "anti-symmetric" between the upper and lower surfaces; the thickness contribution to the downwash may be seen to be "symmetric" between the surfaces. It is seen that:

$$w_{t_U} = w_{t_L} \quad (3.33)$$

$$w_{c_U} = -w_{c_L} \quad (3.34)$$

$$w_{\alpha_U} = -w_{\alpha_L} \quad (3.35)$$

where the subscripts "U" and "L" denote the upper and lower surfaces, respectively.

Extending this classification to the unsteady contribution to downwash, w_1, it may be seen that it is anti-symmetric.

$$w_{1_U} = -w_{1_L} \quad (3.36)$$

The classification of the downwash contributions is summarized on page 71. The symmetry or anti-symmetry of the downwash terms becomes important when computing the lift and

moment about the airfoil, as this involves the difference between the pressures on the upper and lower surfaces.

For classical piston theory, the pressure coefficient on the surface of the airfoil is given by

$$C_P = \frac{2}{M_\infty^2}\left[c_1\left(\frac{w}{a_\infty}\right) + c_2\left(\frac{w}{a_\infty}\right)^2 + c_3\left(\frac{w}{a_\infty}\right)^3\right] \quad (3.37)$$

in which the coefficients c_1, c_2, and c_3 are determined by the piston theory selected, as detailed in Table 3.1 and Table 3.2.

The normal-force coefficient for a 2D airfoil is given by

$$C_N = \frac{1}{c}\int \left(C_{P_L} - C_{P_U}\right) dX \quad (3.38)$$

in which c is the airfoil chord, and X is the chordwise coordinate.

Thus, it is seen that the lift is proportional to the difference in pressure between the upper and lower surfaces. For classical piston theory, in which the coefficients c_1, c_2, and c_3 are computed for the same conditions (M_∞ and a_∞) for the upper and lower surfaces, the difference in pressure will then be directly proportional to the difference in downwash. That is,

$$C_{P_L} - C_{P_U} = \frac{2c_1}{a_\infty M_\infty^2}(w_L - w_U) + \frac{2c_2}{a_\infty^2 M_\infty^2}(w_L^2 - w_U^2) + \frac{2c_3}{a_\infty^3 M_\infty^2}(w_L^3 - w_U^3) \quad (3.39)$$

The influence of the symmetry or anti-symmetry in downwash terms between the upper and lower surface may thus be seen to directly influence their contribution to the lift modelled by piston theory. The contributions of the terms in various orders of piston theory will now be investigated.

Introduce the notation Δ to represent the difference between the lower and upper surfaces of some quantity, as below:

$$\Delta w \equiv w_L - w_U \quad (3.40)$$

where for higher-order terms, for example:

$$\Delta w^2 \equiv w_L^2 - w_U^2 \quad (3.41)$$

and where for mixed terms, for example:

$$\Delta(w_0 w_1) = w_{0_L} w_{1_L} - w_{0_U} w_{1_U} \quad (3.42)$$

Equation (3.39) may then be re-written as:

$$C_{P_L} - C_{P_U} = \frac{2c_1}{a_\infty M_\infty^2}(\Delta w) + \frac{2c_2}{a_\infty^2 M_\infty^2}(\Delta w^2) + \frac{2c_3}{a_\infty^3 M_\infty^2}(\Delta w^3) \quad (3.43)$$

It may be shown that the difference Δ for terms which are symmetric between the upper and lower surfaces will be zero; the difference Δ will be non-zero for anti-symmetric terms. Consider for example, the thickness contribution and the camber contribution:

symmetric: $\Delta w_t = w_{t_L} - w_{t_U} = w_{t_L} - \left(w_{t_L}\right) = 0$

anti-symmetric: $\Delta w_c = w_{c_L} - w_{c_U} = w_{c_L} - \left(-w_{c_L}\right) = 2w_{c_L}$

Similarly, it may be shown that the multiplication of symmetric and anti-symmetric terms follows the guidelines outlined in the 2x2 matrix of Table 3.4.

Table 3.4: Multiplication of Symmetric and Anti-Symmetric Terms

Terms multiplied:	**Symmetric**	**Anti-symmetric**
Symmetric	Symmetric	Anti-symmetric
Anti-symmetric	Anti-symmetric	Symmetric

For example, consider the following symmetric/anti-symmetric multiplication:

$$\Delta(w_t w_c) = w_{t_L} w_{c_L} - w_{t_U} w_{c_U} \quad (3.44)$$

$$\therefore \Delta(w_t w_c) = w_{t_L} w_{c_L} - \left[\left(w_{t_L}\right)\left(-w_{c_L}\right)\right] \quad (3.45)$$

$$\therefore \Delta(w_t w_c) = 2w_{t_L} w_{c_L} \neq 0 \quad (3.46)$$

Furthermore, for an anti-symmetric/anti-symmetric multiplication:

$$\Delta(w_c^2) = w_{c_L}^2 - w_{c_U}^2 \quad (3.47)$$

$$\therefore \Delta(w_c^2) = w_{c_L}^2 - \left(-w_{c_L}\right)\left(-w_{c_L}\right) \quad (3.48)$$

$$\therefore \Delta(w_c^2) = w_{c_L}^2 - w_{c_L}^2 = 0 \quad (3.49)$$

To gain insight into the contributions of the downwash terms to lift, as in equation (3.43), the difference in the downwash terms must be considered. The downwash terms may be expanded as follows.

First-order downwash terms:

$$w = w_0 + w_1 \tag{3.50}$$

with

$$w_0 = w_t + w_c + w_\alpha \tag{3.51}$$

Second-order downwash terms:

$$w^2 = (w_0^2 + w_1^2) + 2w_0 w_1 \tag{3.52}$$

in which

$$w_0^2 = w_t^2 + w_c^2 + w_\alpha^2 + 2w_t w_c + 2w_t w_\alpha + 2w_\alpha w_c \tag{3.53}$$

Third-order downwash terms:

$$w^3 = (w_0^3 + w_1^3) + (3w_0^2 w_1 + 3w_0 w_1^2) \tag{3.54}$$

where

$$w_0^3 = (w_t^3 + w_c^3 + w_\alpha^3) + [3(w_\alpha + w_c)w_t^2 + 3(w_\alpha + w_t)w_c^2 + 3(w_t + w_c)w_\alpha^2] + 6w_t w_\alpha w_c \tag{3.55}$$

The difference equations may then be expressed as follows.

First-order downwash terms:

$$\Delta w = \Delta w_0 + \Delta w_1 \tag{3.56}$$

with

$$\Delta w_0 = \Delta w_t + \Delta w_c + \Delta w_\alpha \tag{3.57}$$

Second-order downwash terms:

$$\Delta w^2 = (\Delta w_0^2 + \Delta w_1^2) + 2\Delta(w_0 w_1) \quad (3.58)$$

in which

$$\Delta w_0^2 = \Delta w_t^2 + \Delta w_c^2 + \Delta w_\alpha^2 + 2\Delta(w_t w_c) + 2\Delta(w_t w_\alpha) + 2\Delta(w_\alpha w_c) \quad (3.59)$$

and

$$\Delta(w_0 w_1) = \Delta(w_t w_1) + \Delta(w_c w_1) + \Delta(w_\alpha w_1) \quad (3.60)$$

Third-order downwash terms:

$$\Delta w^3 = (\Delta w_0^3 + \Delta w_1^3) + [3\Delta(w_0^2 w_1) + 3\Delta(w_0 w_1^2)] \quad (3.61)$$

where

$$\begin{aligned}\Delta w_0^3 = {} & (\Delta w_t^3 + \Delta w_c^3 + \Delta w_\alpha^3) \\ & + [3\Delta(w_\alpha w_c^2) + 3\Delta(w_t w_c^2) + 3\Delta(w_\alpha w_t^2) + 3\Delta(w_c w_t^2) + 3\Delta(w_t w_\alpha^2) \\ & + 3\Delta(w_c w_\alpha^2)] + 6\Delta(w_t w_\alpha w_c)\end{aligned} \quad (3.62)$$

and

$$\begin{aligned}\Delta(w_0^2 w_1) = {} & \Delta(w_t^2 w_1) + \Delta(w_c^2 w_1) + \Delta(w_\alpha^2 w_1) + 2\Delta(w_\alpha w_c w_1) + 2\Delta(w_t w_c w_1) \\ & + 2\Delta(w_\alpha w_t w_1)\end{aligned} \quad (3.63)$$

finally

$$\Delta(w_0 w_1^2) = \Delta(w_t w_1^2) + \Delta(w_c w_1^2) + \Delta(w_\alpha w_1^2) \quad (3.64)$$

The symmetry and anti-symmetry of the downwash terms determine whether the difference in the terms will be zero or non-zero; the differences of the various terms are given in Table 3.5 through Table 3.7.

Table 3.5: First-Order Downwash Terms and Differences

Term x	Difference Δx
w_t	0
w_c	$\neq 0$
w_α	$\neq 0$
w_1	$\neq 0$

Table 3.6: Second-Order Downwash Terms and Differences

Term x	Difference Δx	Term x	Difference Δx
w_t^2	0	$w_c w_\alpha$	0
w_c^2	0	$w_t w_1$	$\neq 0$
w_α^2	0	$w_c w_1$	0
$w_t w_c$	$\neq 0$	$w_\alpha w_1$	0
$w_t w_\alpha$	$\neq 0$	w_1^2	0

Table 3.7: Third-Order Downwash Terms and Differences

Term x	Difference Δx	Term x	Difference Δx	Term x	Difference Δx
Δw_t^3	0	$3\Delta(w_\alpha^2 w_t)$	0	$6\Delta(w_t w_\alpha w_1)$	0
Δw_c^3	$\neq 0$	$3\Delta(w_\alpha^2 w_c)$	$\neq 0$	$6\Delta(w_c w_\alpha w_1)$	$\neq 0$
Δw_α^3	$\neq 0$	$6\Delta(w_t w_c w_\alpha)$	0	$3\Delta(w_t w_1^2)$	0
$3\Delta(w_t^2 w_c)$	$\neq 0$	$3\Delta(w_t^2 w_1)$	$\neq 0$	$3\Delta(w_c w_1^2)$	$\neq 0$
$3\Delta(w_t^2 w_\alpha)$	$\neq 0$	$3\Delta(w_c^2 w_1)$	$\neq 0$	$3\Delta(w_\alpha w_1^2)$	$\neq 0$
$3\Delta(w_c^2 w_t)$	0	$3\Delta(w_\alpha^2 w_1)$	$\neq 0$	w_1^3	$\neq 0$
$3\Delta(w_c^2 w_\alpha)$	$\neq 0$	$6\Delta(w_t w_c w_1)$	0		

In summary, the contributions to the pressure difference between the upper and lower surfaces on an airfoil for classical piston theory may be given as:

$$\Delta C_P = \Delta C_{P_1} + \Delta C_{P_2} + \Delta C_{P_3} \tag{3.65}$$

where, from considerations of symmetry, the orders of contribution are given by:

First-order pressure difference:

$$\Delta C_{P_1} = \frac{2c_1}{a_\infty M_\infty^2}[\Delta w_c + \Delta w_\alpha] + \frac{2c_1}{a_\infty M_\infty^2}[\Delta w_1] \tag{3.66}$$

Second-order pressure difference:

$$\Delta C_{P_2} = \frac{2c_2}{a_\infty^2 M_\infty^2}[2\Delta(w_t w_c) + 2\Delta(w_t w_\alpha)] + \frac{2c_2}{a_\infty^2 M_\infty^2}[2\Delta(w_t w_1)] \tag{3.67}$$

Third-order pressure difference:

$$\begin{aligned}\Delta C_{P_3} = {} & \frac{2c_3}{a_\infty^3 M_\infty^2}[\Delta w_c^3 + \Delta w_\alpha^3 + 3\Delta(w_\alpha w_t^2) + 3\Delta(w_\alpha w_c^2) + 3\Delta(w_c w_\alpha^2)] \\ & + \frac{2c_3}{a_\infty^3 M_\infty^2}[3\Delta(w_t^2 w_1) + 3\Delta(w_c^2 w_1) + 3\Delta(w_\alpha^2 w_1) + 6\Delta(w_c w_\alpha w_1)] \\ & + \frac{2c_3}{a_\infty^3 M_\infty^2}[3\Delta(w_c w_1^2) + 3\Delta(w_\alpha w_1^2)] \\ & + \frac{2c_3}{a_\infty^3 M_\infty^2}[\Delta w_1^3]\end{aligned} \tag{3.68}$$

The following conclusions may be drawn regarding the physical contributions to lift in classical piston theory:

First-order piston theory models lift as directly proportional to the downwash resulting from the camber of the profile and the angle of attack. No coupling is modelled. Linear damping (proportional to w_1) is modelled.

Second-order piston theory adds thickness effects to the first-order damping term in the pressure difference. In the steady contribution to lift, it is seen that thickness effects on the linear contribution from angle-of-attack and from camber are included. Second-order piston theory thus adds thickness effects to both the steady and unsteady contributions to lift.

Third-order piston theory includes nonlinear thickness, camber, and angle-of-attack effects in the steady contribution to the lift. This marks a jump in the degree of modelling, as second-order theory only adds thickness effects to otherwise linear terms in camber and angle-of-attack. Similarly, nonlinear effects on linear damping are added, and nonlinear damping terms are introduced.

First-order classical piston theory is thus seen to ignore thickness effects in both the steady and unsteady lift. Thickness effects are only introduced from second-order piston theory, with nonlinear thickness effects only being modelled by third-order piston theory. With regards to the steady contribution to lift, first-order classical piston theory may be shown to reduced to supersonic linearized theory [69]. Nonlinearity in the steady and unsteady contributions to lift is only modelled from third-order piston theory; nonlinear thickness, camber, and alpha effects are modelled for the steady contribution.

This is reflected in the comparison made by Zhang et al [11] between the flutter speeds given by various orders of piston theory for a 4% thickness circular arc airfoil, with the effect of Mach number shown in Figure 3.9 (for $\alpha = 5°$) and the effect of angle of attack shown in Figure 3.10 (for $M = 6$); in Figure 3.10 the trends of first-order and second-order classical piston theory are the same, with an offset in flutter velocity index being introduced by thickness effects. The change in trends with angle-of-attack is only noted for piston theory of order greater than 2.

The reader is reminded that in first-order local piston theory, linear damping is modelled, with no coupling between effects on damping. From Figure 3.10 it is seen that the aeroelastic behaviour of the airfoil is accurately modelled with first-order damping (through first-order local piston theory) if the nonlinearities in the steady contribution are accurately described. The more approximate modelling of the steady contribution by classical piston theory is clearly seen to lead to poorer modelling of the aeroelastic behaviour. The importance of the nonlinear effects in the steady contribution is highlighted in Figure 3.10 through the improvement in the modelling of the aeroelastic trends in extension to classical piston theory of order greater than two; this supports McNamara's assertion of the importance of thickness effects in hypersonic flows [1]. It is also seen that the modelling of the coupling between linear terms in the steady contribution that is achieved in second-order classical piston theory reduces the error in modelling at low angles of attack (see Figure 3.10), but does not correct the incorrect modelling of the trend with angle-of-attack.

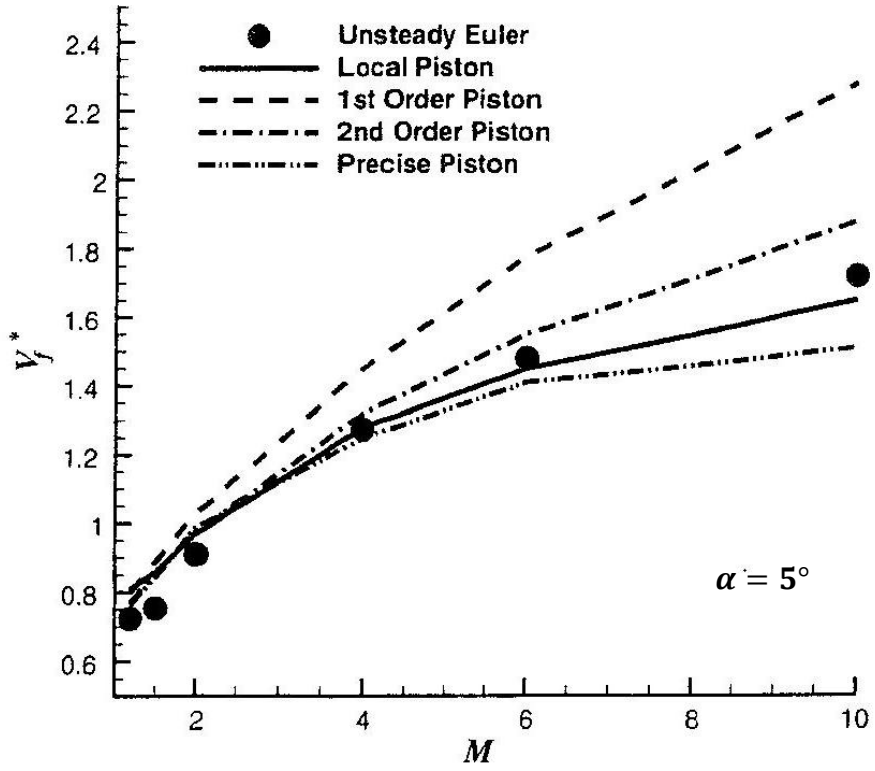


Figure 3.9: Comparison of Mach Number Effects Between Piston Theories for a 4% Circular Arc Airfoil **[11]**

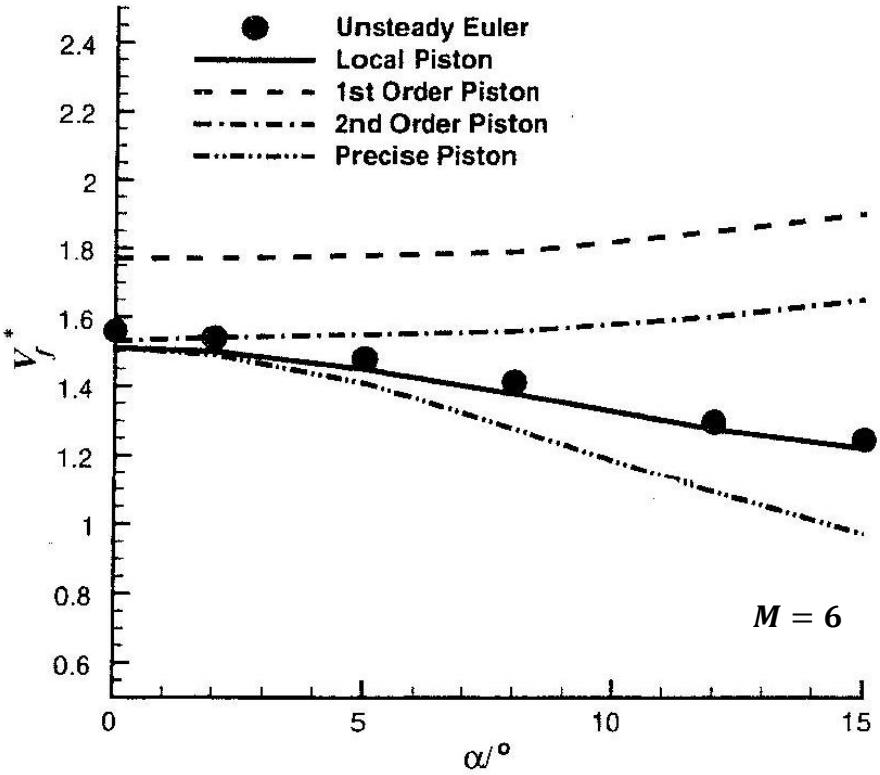


Figure 3.10: Comparison of Angle-of-Attack Effects Between Piston Theories for a 4% Circular Arc Airfoil **[11]**

4 DEVELOPMENT OF A FINITE ELEMENT BASED AEROELASTIC PREDICTION TOOL IN MATLAB FOR CANTILEVERED PLATES IN SUPERSONIC FLOWS

4.1 Geometry and Material Properties of the Analysed Cantilevered Plate

The analysis developed in MATLAB using approximate aerodynamic modelling and finite elements is limited in the geometries it may be applied to. The use of shock-expansion theory limits the plate geometry to a plate with sharpened leading- and trailing-edges; furthermore, the degree of sharpening is determined by the flow conditions -- the shock must remain attached.

The use of the structural mesh for approximate aerodynamic modelling dictates that the wing-tip be parallel to the root. This is so that the loci of trapezoidal element edges form chordwise lines (parallel to the free-stream) along which shock-expansion theory is applied.

The finite element formulation that was implemented places further limitations on the range of geometries. The use of four-noded quadrilateral elements limits the plate planform to being trapezoidal; the trapezoid may be stepped, but the leading- and trailing-edges may not have discontinuities (e.g. dogtooth). The plate mechanics upon which the elements are modelled requires that the thickness distribution about the camberline be symmetrical; furthermore, the thickness-to-chord ratio should be sufficiently small $\frac{t}{c} \leq 0.10$.

The finite element formulation assumed that the material of the plate is isotropic and linear.

For more information on the finite element formulation used, the reader is referred to Appendix B.

4.2 Structural Modelling of the Plate Using Finite Elements

The plate was modelled using 4-noded bilinear quadrilateral bending panel elements, based on Mindlin-Reissner plate mechanics (see Appendix B). The modelling of the cantilevered plate reduced the structural representation of the plate to a 2D plane passing through the camberline of the plate. Elements were modelled with a bilinear thickness distribution over the surface of the element; this allowed the thickness to taper in both the spanwise and chordwise directions. The deformation of points on the physical surface of the plate was obtained through adding the symmetrical thickness distribution to the deformation of the camberline.

The equations used for in the modelling of the plate-mechanics modelled each structural node as having three degrees of freedom (DOF) -- a transverse deflection, and two fibre rotations. (the reader is referred to the Appendix B). The cantilevered boundary-condition of the plate was modelled by restraining all three DOFs of each node in the root of the plate.

The mass-matrix was formulated using lumped masses; the plate was modelled with uniform density, with no additional masses (e.g. mass balances) present.

Stress-smoothing was applied in post-processing to smoothen the stresses across nodes.

The plate was modelled as being subjected to bilinearly distributed transverse loading only (no point loads were included, other than reaction forces at the root). The resultant forces acting on the plate were resolved into components along each of the axes of the coordinate system; however, the contribution of non-transverse forces to the plate loading was not included.

The coordinate system used in the structural modelling is shown in Figure 4.1:

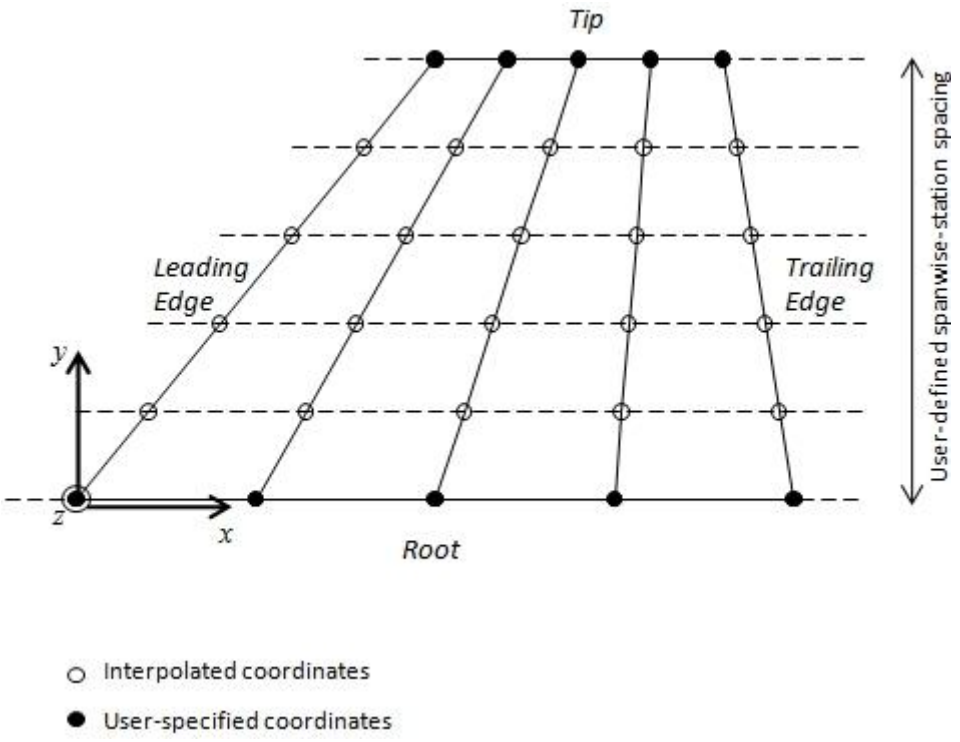


Figure 4.1: Coordinate System Definition for Structural Analysis and Structural Discretization

The range of validity of the linear plate equations is limited to transverse deflections of the order of the plate thickness.

4.3 Aerodynamic Modelling of the Plate Using Shock-Expansion Theory and Piston Theory

The application of local piston theory to model the damping of a body undergoing small oscillations about a mean steady state has been shown [10; 11] to compare very well (see Figure 2.10) to time-accurate Navier-Stokes modelling. This motivated the current attempt to model the aerodynamics of a vibrating plate through the use of local piston theory to calculate the damping terms, and the use of an approximate aerodynamic model (shock-expansion theory) to model the mean steady flow about the plate. The combination of piston theory with approximate steady aerodynamic models has been investigated previously, with the combination of piston theory with conical flow theory being investigated by Xianxin [60].

In the current work, shock-expansion theory has been used to model the contribution to the aerodynamic loading from the plate deformation and shape, whilst local piston theory has

been used to model the damping contribution. The coefficients in local piston theory and the cylinder conditions are calculated from the local steady flow conditions as modelled by shock-expansion theory. The aerodynamic loading is thus given as:

$$F_{aero} = F_{SE} + F_{PT} \quad (4.1)$$

where

$$F_{SE} = fn_{SE}\big(x(t)\big) \quad (4.2)$$

$$F_{PT} = fn_{PT}\big(x(t), \dot{x}(t)\big) \quad (4.3)$$

4.3.1 Shock-Expansion Contribution

The loading from shock-expansion theory, F_{SE}, is calculated from the pressures over the wing given by shock-expansion theory. Strip-theory is applied (and hence, no 3-dimensional influence is modelled) along chordwise sections parallel to the direction of the free-stream (in terms of the coordinate system defined in Figure 4.1, shock-expansion is applied in the x-direction for stations of constant y).

Note that the full oblique-shock and Prandtl-Meyer expansion equations have been used. These have been given by equations (2.1) through (2.8). The turning angle δ is calculated from the difference in the slope of the element edges across nodes; the slope is calculated for the upper surface and lower surface from consideration of the thickness contribution and from the camber contribution, as shown in Figure 4.2.

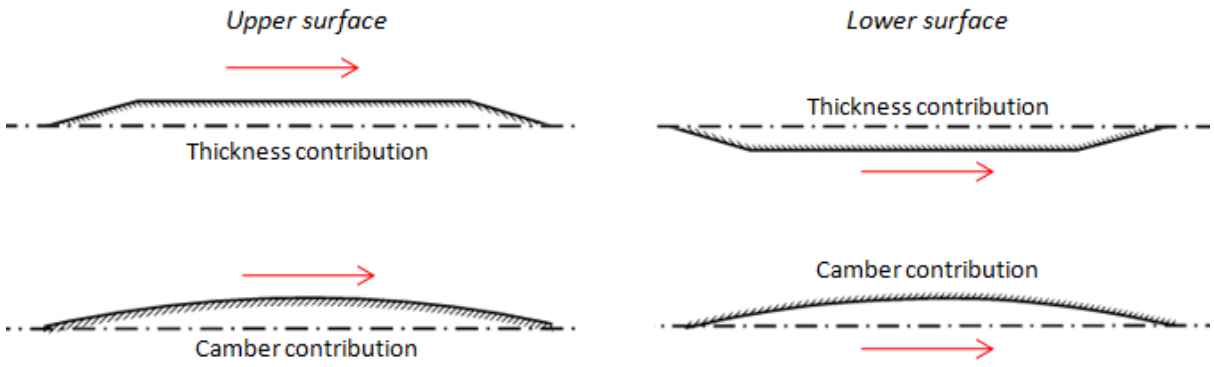


Figure 4.2: Contributions to the Surface Angle to the Flow

At the leading-edge, the turning angle accounts for the slope of the plate surface and for the angle of attack; at the trailing-edge, the turning angle is calculated such that the pressures in the "upper" and "lower" portions of the slip-plane are balanced.

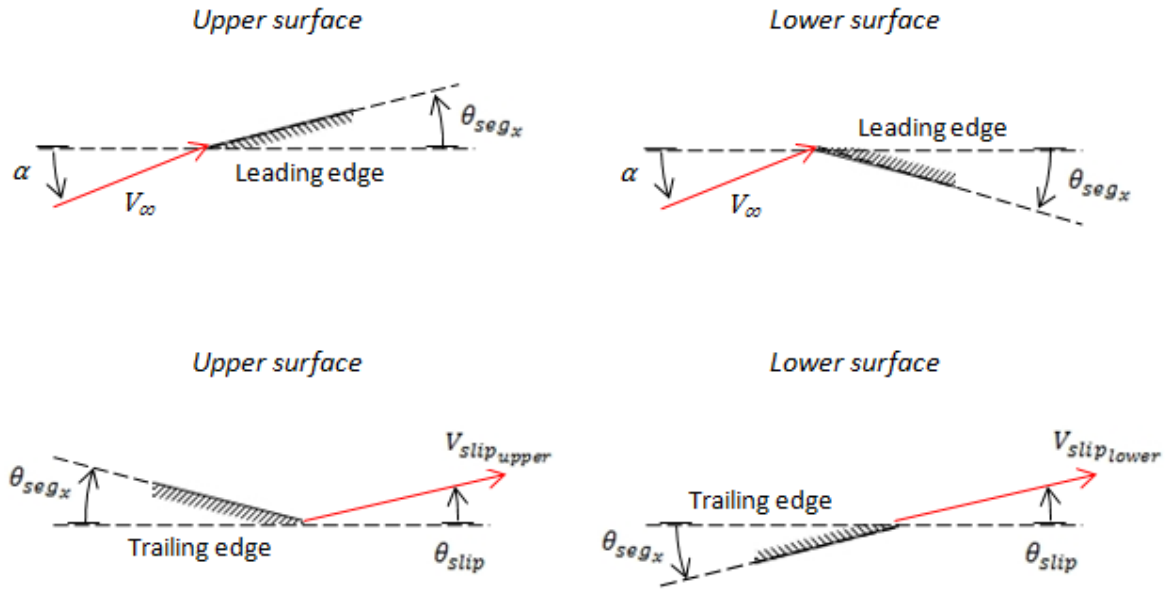


Figure 4.3: Definition of Angles for Flow Turning-Angle Determination at the Leading- and Trailing-Edges

From Figure 4.3, for the leading-edge:

upper surface: $\delta = \theta_{seg_x} - \alpha$ (4.4)

lower surface: $\delta = \theta_{seg_x} + \alpha$ (4.5)

where δ is defined positive for flow turning into itself (compression).

From Figure 4.3, the flow turning angles at the trailing-edge are given by:

upper surface: $\delta = \theta_{seg_x} + \theta_{slip}$ (4.6)

lower surface: $\delta = \theta_{seg_x} - \theta_{slip}$ (4.7)

where δ is again defined positive for flow turning into itself (compression), and θ_{slip} is the angle of the slip-plane relative to the root chordline, as defined in the figure.

The camber deformation of the plate is accounted for in the shock-expansion contribution to the aerodynamic loading. The pressures at the nodes are smoothed over elements in order to model a continuous pressure distribution.

When calculating the shock-expansion contribution, the effect of the motion-induced downwash is not accounted for, i.e. steady shock-expansion theory is used, as opposed to quasi-steady shock-expansion theory (see section 2.1.1). The motion-induced downwash is not accounted for here, as it is modelled in piston theory. With reference to equation (3.19) for the downwash in piston theory, shock-expansion theory is used to modelled the pressures resulting from w_0, where

$$w_0 = V_{cyl}\frac{\partial z}{\partial X} \tag{4.8}$$

4.3.2 Piston Theory Contribution

The loading from piston theory, F_{PT}, is calculated from the unsteady pressures over the wing that arise from motion. The quasi-steady flow conditions at the instant in time in consideration are obtained from the shock-expansion calculation, and the cylinder conditions are calculated using these local conditions. The unsteady pressures at the structural nodes are then calculated using local piston theory:

$$P_{PT} = \gamma P_{SE}\left\{c_1\left(\frac{w_{LPT}}{a_{SE}}\right) + c_2\left(\frac{w_{LPT}}{a_{SE}}\right)^2 + c_3\left(\frac{w_{LPT}}{a_{SE}}\right)^3\right\} \tag{4.9}$$

where a_{SE} is the local speed of sound from shock-expansion theory, and P_{PT} represents the unsteady increment to the steady pressure P_{SE}. Here, w_{LPT} is the downwash as calculated for local piston theory. The coefficients c_1, c_2, and c_3 are the first-, second-, and third-order coefficients, modelled here using Donov's [68] coefficients :

$$c_1 = \frac{M_{SE}}{m_{SE}} \tag{4.10}$$

$$c_2 = \frac{(\gamma+1)M_{SE}^4 - 2m_{SE}^2}{4m_{SE}^4} \tag{4.11}$$

$$c_3 = \frac{1}{12M_{SE}m_{SE}^7}\left[aM_{SE}^8 + bM_{SE}^6 + cM_{SE}^4 + dM_{SE}^2 + e\right] \tag{4.12}$$

where $m_{SE} = \sqrt{M_{SE}^2 - 1}$, and M_{SE} is the local Mach number at the structural node as calculated from shock-expansion theory. The coefficients a, b, c, d, and e in the equation for c_3 are given by Donov [68] as:

$$a = (\gamma + 1) \quad (4.13)$$

$$b = 2\gamma^2 - 7\gamma - 5 \quad (4.14)$$

$$c = 10(\gamma + 1) \quad (4.15)$$

$$d = -12 \quad (4.16)$$

$$e = 8 \quad (4.17)$$

In calculating the unsteady contribution to the total aerodynamic loading from local piston theory, the downwash terms for local piston-theory (as defined in Table 3.3 and discussed in Section 3.3.1) must be used:

$$w_{LPT} = w_1 \quad (4.18)$$

$$w_{LPT}^2 = 2w_0 w_1 + w_1^2 \quad (4.19)$$

$$w_{LPT}^3 = 3w_0^2 w_1 + 3w_0 w_1^2 + w_1^3 \quad (4.20)$$

in which

$$w_1 = \frac{\partial z}{\partial t} \quad (4.21)$$

In the local piston theory contribution to the loading, the downwash calculated for shock-expansion theory, w_0, must be accounted for in second- and third-order local piston theory to model thickness- and angle-of-attack effects on the aerodynamic damping.

4.3.3 Total Aerodynamic Loading

The pressure distributions from the shock-expansion contribution and from the piston theory contribution are added to obtain the total pressure acting on the surface of the plate. This is integrated over the surface, accounting for surface inclination, to give the resultant forces in the x-, y-, and z-directions (corresponding to the axial force, side force, and the normal force, respectively). Moments are computed about the leading-edge of the wing root, $(x, y, z) = (0,0,0)$.

Due to the approximate aerodynamic models chosen, the plate is modelled with no 3-dimensional effects; the portions of the plate that are influenced by the tip shock and the root

shock are modelled as being free of the influence of these shocks. However, the use of the full oblique shock and Prandtl Meyer equations render the aerodynamic loading nonlinear.

The use of steady shock-expansion and of piston theory renders the aerodynamic loading as quasi-steady in flow-history. Although the unsteady pressures from piston theory contain terms with nonlinear terms in time-derivatives ($\dot{x}$), no aerodynamic lag with $\dot{x}$ is modelled.

The resulting aerodynamic loading is summarized as being nonlinear in displacement and velocity, with no 3-dimensional effects; the loading may be modelled as dynamically nonlinear (no assumption of small perturbation about a constant mean flow), with quasi-steady modelling of the flow history.

4.4 Formulation of the Coupled Aeroelastic Equations of Motion

The aerodynamic loading was coupled as the external force to the structural equations of motion. The loading at the structural nodes was calculated using finite element methodology (see Appendix B), with the values of the distributed pressure at the nodes being provided directly from the aerodynamic modelling. In using approximate aerodynamic modelling to calculate the loading at the structural nodes, the inter-grid interpolation between a separate aerodynamic mesh and the structural mesh was avoided.

The system dynamics may be represented in a number of ways, with varying degrees of simplification. The simplifications are made from the point-of-view of shorter computation time, and inevitably lead to some reduction in the accuracy of the. However, the simplifications may also give greater insight into the system dynamics, as in the case of the modal formulation.

The formulation of and solution of the aeroelastic equations of motion was approached from the point of nonlinear aerodynamic loading, and from the point of linearized GAFs. The differences in the formulation and solution of the aeroelastic systems follow.

4.4.1 Full-Order Formulation with Dynamically-Nonlinear Unsteady Aerodynamic Loading

In the full-order formulation, the full order of the FEM model is coupled to the full-order aerodynamic loading vector. The order of the system is very large, and its solution is computationally expensive. The aeroelastic equations of motion are given by:

(full order) $$\boldsymbol{M_{str}}\{\vec{a}\} + \boldsymbol{C_{str}}\{\vec{v}\} + \boldsymbol{K_{str}}\{\vec{d}\} = \{\vec{F}_{aero}\} \quad (4.22)$$

The equation is solved through implicit time-marching using the Newmark-Beta scheme, with sub-iterations to convergence being performed at each time-step. The aerodynamic loading is re-calculated from the structural response at each sub-iteration. No simplifications beyond those implicit in the structural and aerodynamic methods are made, and the full dynamics of the system is retained.

4.4.2 Modal Formulation with Dynamically-Nonlinear Unsteady Aerodynamic Loading

The structural dynamics of the system may be represented through the normal modes of the structure; it has been shown [62] that the system response may be well modelled whilst retaining the contribution from only a small number of the modes. This leads to a significant reduction in the order of the structural equations. A further advantage of the modal formulation is the insight gained into the system response and parameters. The modal formulation, retaining the dynamics of the aerodynamic loading, is given by:

(modal order) $$\boldsymbol{M_{mod_{str}}}\{\ddot{\vec{x}}\} + \boldsymbol{C_{mod_{str}}}\{\dot{\vec{x}}\} + \boldsymbol{K_{mod_{str}}}\{\vec{x}\} = \boldsymbol{X^T}\{\vec{F}_{aero}\} \quad (4.23)$$

The solution approach to the system is unchanged, with the aerodynamic loading being implicit; however, the number of equations being solved is significantly less, which results in faster computation. Nonetheless, the solution of the system is still computationally expensive, as the modal response must be transformed to full-order displacements and velocities, and the full-order aerodynamic loading must be recalculated at each step. The calculation of the aerodynamic loading was identified as the computational bottleneck using the aerodynamic methods described. Good accuracy of modelling of the aerodynamics is achieved for motions and loadings that may be well-described by the normal modes.

4.4.3 Modal Formulation with Linearized Quasi-Steady Aerodynamic Loading

The system formulation may be further simplified to allow for significantly faster computation and for simple direct extraction of system parameters. The dynamically-nonlinear aerodynamic loading may be linearized about a specific system state in order to yield time-invariant matrices for the first-order aerodynamic stiffness and damping in the modal formulation. This results in the system dynamics being simplified to a linear time-invariant (LTI) system, the solution of which is straightforward. The computational requirements for the solution of the system response are reduced by a number of orders of magnitude; however, the simplifications lead to an associated loss in accuracy of the modelling of the actual system dynamics. The reader is referred to Section 4.5.1 for the linearization procedure adopted and for the development of the system equation, which is given below:

(modal order) $$\boldsymbol{M}_{\boldsymbol{mod}_{\boldsymbol{ae}}}\{\ddot{\vec{x}}\} + \boldsymbol{C}_{\boldsymbol{mod}_{\boldsymbol{ae}}}\{\dot{\vec{x}}\} + \boldsymbol{K}_{\boldsymbol{mod}_{\boldsymbol{ae}}}\{\vec{x}\} = \vec{Q}_{offset} \qquad (4.24)$$

where $\vec{Q}_{offset}$ is defined by equation (4.44).

The linearization of the GAFs, which yields the aerodynamic stiffness and damping matrices, provides further insight into the system dynamics. The coupled aeroelastic system characteristic is seen to result from a combination of the structural and aerodynamic systems; from this it is seen why the aeroelastic characteristics and system parameters differ from the purely-structural system. The aerodynamic matrices have non-zero off-diagonal terms, which provide coupling between the structural modes.

4.5 Linearization of the Generalized Aerodynamic Forces

4.5.1 Linearization Procedure

The equations of motion for the coupled aeroelastic system in modal order with dynamically-nonlinear aerodynamic loading was given by equation (4.23) as:

(modal order) $$\boldsymbol{M}_{\boldsymbol{mod}_{\boldsymbol{str}}}\{\ddot{\vec{x}}\} + \boldsymbol{C}_{\boldsymbol{mod}_{\boldsymbol{str}}}\{\dot{\vec{x}}\} + \boldsymbol{K}_{\boldsymbol{mod}_{\boldsymbol{str}}}\{\vec{x}\} = \boldsymbol{X}^{\boldsymbol{T}}\{\vec{F}_{aero}\}$$

Recall that the aerodynamic loading is the sum of the shock-expansion contribution, $\vec{F}_{SE}$, and the piston-theory contribution, $\vec{F}_{PT}$. The notation of $\boldsymbol{X^T}\{\vec{F}_{aero}\}$ for the generalized aerodynamic forces is used to remind the reader that the aerodynamic loading is still calculated from full-order displacements and velocities. Expanding the aerodynamic loading vector:

$$\vec{F}_{aero} = \vec{F}_{SE} + \vec{F}_{PT} \quad (4.25)$$

where

$$\vec{F}_{SE} = fn_{SE}(\vec{d}) \quad (4.26)$$

$$\vec{F}_{PT} = fn_{PT}(\vec{d}, \vec{v}) \quad (4.27)$$

The loading contributions are calculated separately. It is required that the loading contributions be linearized about the steady-state displacements (or any other set of displacements and velocities) and be reduced to modal form as:

$$\boldsymbol{X^T}\{\vec{F}_{SE}\} = \boldsymbol{K_{mod_{aero}}}\{\vec{x}\} \quad (4.28)$$

$$\boldsymbol{X^T}\{\vec{F}_{PT}\} = \boldsymbol{C_{mod_{aero}}}\{\dot{\vec{x}}\} \quad (4.29)$$

In the following procedure outline, the example system will be restricted to considering the first three modes for brevity in the equations. The system may be linearized as follows:

1. Calculate $\vec{F}_{SE}$ and $\vec{F}_{PT}$ for the mean displacements and velocities about which the linearization is performed.

$$\boldsymbol{X^T}\{\vec{F}_{SE}\}_{mean} = fn_{SE}(\vec{d}_{mean}) \quad (4.30)$$

$$\boldsymbol{X^T}\{\vec{F}_{PT}\}_{mean} = fn_{PT}(\vec{d}_{mean}, \vec{v}_{mean}) \quad (4.31)$$

2. Calculate the change in $\vec{F}_{SE}$ associated with an incremental change (for the purposes of illustration, a modal displacement of magnitude b_i is used) in each of the modal displacements.

   For example, for the first mode:

$$\Delta\left(\boldsymbol{X^T}\{\vec{F}_{SE}\}\right) = \boldsymbol{K_{mod_{aero}}}\Delta(\{\vec{x}\}_1) \quad (4.32)$$

where

$$\Delta(\{\vec{x}\}_1) = \{\vec{x}\}_1 - \{\vec{x}\}_{mean} = \begin{Bmatrix} b_1 \\ 0 \\ 0 \end{Bmatrix} \quad (4.33)$$

and

$$\Delta\left(\boldsymbol{X^T}\{\vec{F}_{SE}\}\right) = \boldsymbol{X^T}\{\vec{F}_{SE}\} - \boldsymbol{X^T}\{\vec{F}_{SE}\}_{mean} = \begin{Bmatrix} \Delta Q_{SE1_{mode\ 1}} \\ \Delta Q_{SE2_{mode\ 1}} \\ \Delta Q_{SE3_{mode\ 1}} \end{Bmatrix} \quad (4.34)$$

where the subscript $mean$ represents values at the linearization point, and where $\boldsymbol{X^T}\{\vec{F}_{SE}\}$ is the loading computed for the geometry $\{\vec{x}\}_1$.

3. Compute each column of the aerodynamic stiffness matrix by considering the incremental change in loading with increments in modal displacements.

   For example, for the second mode:

$$\Delta\left(\boldsymbol{X^T}\{\vec{F}_{SE}\}_2\right) = \boldsymbol{K_{mod_{aero}}}\Delta(\{\vec{x}\}_2)$$

$$\therefore \begin{Bmatrix} \Delta F_{SE1_{mode\ 2}} \\ \Delta F_{SE2_{mode\ 2}} \\ \Delta F_{SE3_{mod\ e\ 2}} \end{Bmatrix} = \begin{bmatrix} K_{11} & K_{12} & K_{13} \\ K_{21} & K_{22} & K_{23} \\ K_{31} & K_{32} & K_{33} \end{bmatrix} \begin{Bmatrix} 0 \\ b_2 \\ 0 \end{Bmatrix} \quad (4.35)$$

   whence

$$\begin{Bmatrix} K_{12} \\ K_{22} \\ K_{32} \end{Bmatrix} = \frac{1}{b_2} \begin{Bmatrix} \Delta F_{SE1_{mode\ 2}} \\ \Delta F_{SE2_{mode\ 2}} \\ \Delta F_{SE3_{mode\ 2}} \end{Bmatrix} \quad (4.36)$$

   Note that here K_{ij} refers to the elements of the aerodynamic stiffness matrix, and are not to be confused with the elements of the structural stiffness matrix.

4. Having computed $\boldsymbol{K_{mod_{aero}}}$, assume that the system undergoes small perturbations about the linearization point. Calculate the piston-theory coefficients associated with the mean local flow conditions. Assume these coefficients do not vary with the small displacements.

5. Calculate the change in $\vec{F}_{PT}$ associated with an incremental change (for the purposes of illustration, a modal velocity of magnitude e_i is used) in each of the modal velocities.

   For example, for the first mode:

$$\Delta\left(\boldsymbol{X^T}\{\vec{F}_{PT}\}\right) = \boldsymbol{C_{mod_{aero}}}\Delta\left(\{\vec{x}\}_1\right) \tag{4.37}$$

   where

$$\Delta\left(\{\vec{x}\}_1\right) = \{\vec{x}\}_1 - \{\vec{x}\}_{mean} = \begin{Bmatrix} e_1 \\ 0 \\ 0 \end{Bmatrix} \tag{4.38}$$

   and

$$\Delta\left(\boldsymbol{X^T}\{\vec{F}_{PT}\}\right) = \boldsymbol{X^T}\{\vec{F}_{PT}\} - \boldsymbol{X^T}\{\vec{F}_{PT}\}_{mean} = \begin{Bmatrix} \Delta F_{PT1_{mode\ 1}} \\ \Delta F_{PT2_{mode\ 1}} \\ \Delta F_{PT3_{mode\ 1}} \end{Bmatrix} \tag{4.39}$$

   where $\boldsymbol{X^T}\{\vec{F}_{PT}\}$ is the loading computed for the incremental modal velocity $\{\vec{x}\}_1$.

6. Compute each column of the aerodynamic damping matrix by considering the incremental change in loading with increments in modal velocities.

   For example, for the second mode:

$$\Delta\left(\boldsymbol{X^T}\{\vec{F}_{PT}\}_2\right) = \boldsymbol{C_{mod_{aero}}}\Delta\left(\{\vec{x}\}_2\right)$$

$$\therefore \begin{Bmatrix} \Delta F_{PT1_{mode\ 2}} \\ \Delta F_{PT2_{mode\ 2}} \\ \Delta F_{PT3_{mode\ 2}} \end{Bmatrix} = \begin{bmatrix} C_{11} & C_{12} & C_{13} \\ C_{21} & C_{22} & C_{23} \\ C_{31} & C_{32} & C_{33} \end{bmatrix} \begin{Bmatrix} 0 \\ e_2 \\ 0 \end{Bmatrix} \tag{4.40}$$

   whence

$$\begin{Bmatrix} C_{12} \\ C_{22} \\ C_{32} \end{Bmatrix} = \frac{1}{e_2} \begin{Bmatrix} \Delta F_{PT1_{mode\ 2}} \\ \Delta F_{PT2_{mode\ 2}} \\ \Delta F_{PT3_{mode\ 2}} \end{Bmatrix} \tag{4.41}$$

Note that here C_{ij} refers to the elements of the aerodynamic damping matrix, and are not to be confused with the elements of the structural damping matrix.

The generalized aerodynamic forces are thus linearized about a set of modal displacements and velocities, $\vec{x}_{mean}$ and $\dot{\vec{x}}_{mean}$, with the associated generalized aerodynamic forces $\vec{Q}_{mean}$. As such, the generalized aerodynamic forces for other modal displacements and velocities in the range of the linearization are given by (note that the notation has now shifted to $\vec{Q}$ to remind the reader that the aerodynamic loading is now calculated from the modal linearized aerodynamic matrices):

$$\vec{Q} = \vec{Q}_{mean} + \boldsymbol{K_{mod_{aero}}}\{\vec{x} - \vec{x}_{mean}\} + \boldsymbol{C_{mod_{aero}}}\{\dot{\vec{x}} - \dot{\vec{x}}_{mean}\} \quad (4.42)$$

The aerodynamic loading is then substituted back into the system equation of motion giving:

$$\boldsymbol{M_{mod_{ae}}}\{\ddot{\vec{x}}\} + \boldsymbol{C_{mod_{ae}}}\{\dot{\vec{x}}\} + \boldsymbol{K_{mod_{ae}}}\{\vec{x}\} = \vec{Q}_{offset} \quad (4.43)$$

in which

$$\vec{Q}_{offset} = \vec{Q}_{mean} - \boldsymbol{K_{mod_{aero}}}\{\vec{x}_{mean}\} - \boldsymbol{C_{mod_{aero}}}\{\dot{\vec{x}}_{mean}\} \quad (4.44)$$

$$\boldsymbol{M_{mod_{ae}}} = \boldsymbol{M_{mod_{str}}} \quad (4.45)$$

$$\boldsymbol{C_{mod_{ae}}} = \boldsymbol{C_{mod_{str}}} - \boldsymbol{C_{mod_{aero}}} \quad (4.46)$$

$$\boldsymbol{K_{mod_{ae}}} = \boldsymbol{K_{mod_{str}}} - \boldsymbol{K_{mod_{aero}}} \quad (4.47)$$

In the linearization of the GAFs, it has been assumed that the change in the aerodynamic matrices is small for small perturbations about the linearization point. Under the assumption of constant matrices, the system is effectively assumed to be quasi-steady and is dynamically linearized.

4.5.2 Effect of the Size of the Linearization Increment

The linearization step-size was found to influence the linearization of the GAFs when analysed using SE/LPT in MATLAB. A step-size too small would lead to numerical issues and inflation of error, whilst a step-size too large would not be representative of the motion undergone by the wing for small vibrations.

The linearization step-size used was calculated such that the Δx_2 would result in 2° twist at the wingtip, as the linearization results in MATLAB for the ATM-wing were relatively step-size sensitive for smaller step sizes.

An example of the influence that the linearization step-size has on the terms of the aerodynamic stiffness matrix are shown in Figure 4.4, where the notation follows the equation below (for a modal aerodynamic stiffness matrix limited to four modes):

$$\boldsymbol{K}_{\boldsymbol{mod}_{\boldsymbol{aero}}} = \begin{bmatrix} K_{11} & K_{12} & K_{13} & K_{14} \\ K_{12} & K_{22} & K_{23} & K_{24} \\ K_{31} & K_{32} & K_{33} & K_{34} \\ K_{41} & K_{42} & K_{43} & K_{44} \end{bmatrix} \quad (4.48)$$

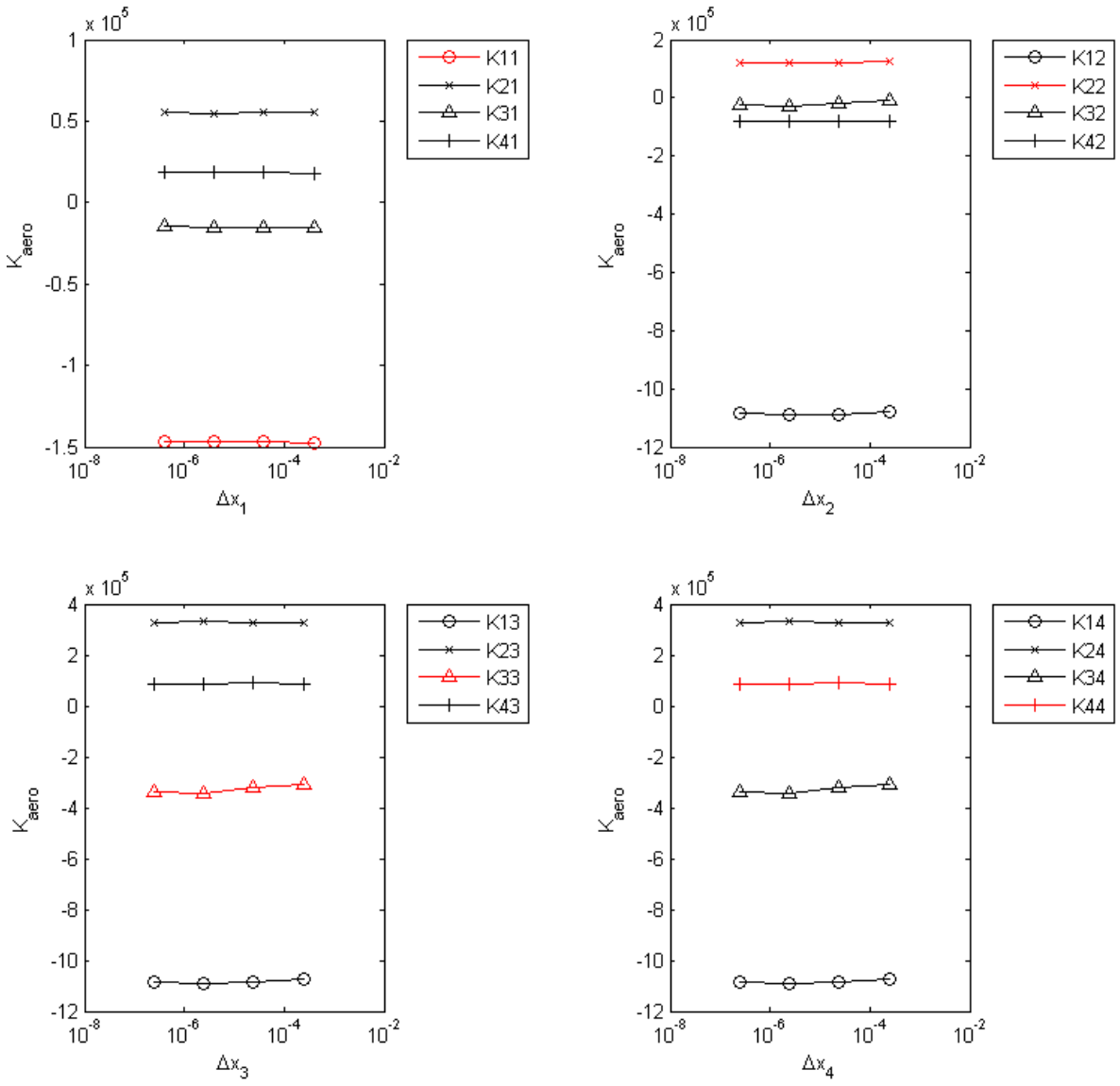


Figure 4.4: Linearization Step-Size Influence on Aerodynamic Stiffness Terms from SE/LPT in MATLAB

4.6 Solution of the Aeroelastic Equations of Motion

Whilst several methods are available for the linear and nonlinear analysis of systems with time-invariant coefficients, the solution of systems with time-variant coefficient matrices is generally less elegant. In such systems, the equations of motion are solved by time-marching, with the coefficient matrices being re-computed at each time-step. This is obviously a relatively more computationally expensive analysis. The time-marching scheme and its implementation influence the numerical stability of the solution, as well as whether the system is modelled as strongly or weakly coupled.

4.6.1 Implicit Time-Marching of Systems with Dynamically-Nonlinear Aerodynamic Loading

The Newmark-β scheme is used to integrate the aeroelastic equation of motion in time. Strong coupling is achieved through iteratively solving the structural and aerodynamic equations to convergence at each "physical" time step. The procedure followed is outlined below.

The values chosen for the Newmark-β scheme were as follows:

$$\gamma = {}^{1}/_{2} \qquad (4.49)$$

$$\beta = {}^{1}/_{4} \qquad (4.50)$$

$$\Delta t = \frac{T_{min}}{\pi^2} \qquad (4.51)$$

where T_{min} was the shortest modal period of the truncated mode set.

The values were chosen such that the time-marching algorithm is unconditionally stable, with good resolution (>30 points per cycle) of the lower modes. The error in periodicity (or equivalently, frequency) estimated from Table 2.1 is approximately 3.4%. The choice of parameters for the Newmark-β scheme results in a single-step implicit time-marching scheme.

Consider the equation of motion at time $t + \Delta t$:

$$\boldsymbol{M}_{t+\Delta t}\{\vec{\ddot{u}}_{t+\Delta t}\} + \boldsymbol{C}_{t+\Delta t}\{\vec{\dot{u}}_{t+\Delta t}\} + \boldsymbol{K}_{t+\Delta t}\{\vec{u}_{t+\Delta t}\} = \vec{F}_{t+\Delta t} \quad (4.52)$$

Here, the notation has been modified to accommodate both the full-order and modal-order formulation. The vector $\vec{u}$ represents a displacement vector (whether modal or full-order), and the matrices $\boldsymbol{M}$, $\boldsymbol{C}$, and $\boldsymbol{K}$ represent the structural mass, damping, and stiffness matrices (whether modal or full-order). The vector $\vec{F}$ represents the aerodynamic loading (whether GAFs or full-order loading).

In modelling the structure as being linear, the structural matrices are rendered time-invariant. It is assumed that the dynamic system response at the previous time step, as well as the associated aerodynamic load, is known. In the following equations, time subscript is dropped from the structural matrices, and the vector notation $\left\{\vec{\ }\right\}$ is dropped.

Define the following quantities, which are based on the known response of the previous time step and the solution parameters, and which are invariant in the iteration to convergence for the time step:

$$\boldsymbol{H} = \boldsymbol{M} + \gamma\Delta t\boldsymbol{C} + \beta\Delta t^2\boldsymbol{K} \quad (4.53)$$

$$\tilde{\dot{u}}_{t+\Delta t} = \dot{u}_t + \Delta t(1-\gamma)\ddot{u}_t \quad (4.54)$$

$$\tilde{u}_{t+\Delta t} = u_t + \Delta t\dot{u}_t + \frac{\Delta t^2}{2}(1-2\beta)\ddot{u}_t \quad (4.55)$$

The Newmark-β expressions for velocity and displacement may then be written as:

$$\dot{u}_{t+\Delta t} = \tilde{\dot{u}}_{t+\Delta t} + (\gamma\Delta t)\ddot{u}_{t+\Delta t} \quad (4.56)$$

$$u_{t+\Delta t} = \tilde{u}_{t+\Delta t} + (\beta\Delta t^2)\ddot{u}_{t+\Delta t} \quad (4.57)$$

Substituting the above expressions (equations (4.53) through (4.57)) into the equation of motion at time $t + \Delta t$ (equation (4.52)) gives:

$$\boldsymbol{M}\ddot{u}_{t+\Delta t} + \boldsymbol{C}\{\tilde{\dot{u}}_{t+\Delta t} + (\gamma\Delta t)\ddot{u}_{t+\Delta t}\} + \boldsymbol{K}\{\tilde{u}_{t+\Delta t} + (\beta\Delta t^2)\ddot{u}_{t+\Delta t}\} = F_{t+\Delta t}$$

$$\therefore [\boldsymbol{M} + \gamma\Delta t\boldsymbol{C} + \beta\Delta t^2\boldsymbol{K}]\ddot{u}_{t+\Delta t} = F_{t+\Delta t} - \boldsymbol{C}\tilde{\dot{u}}_{t+\Delta t} - \boldsymbol{K}\tilde{u}_{t+\Delta t}$$

$$\therefore\ \ddot{u}_{t+\Delta t} = \boldsymbol{H}^{-1}\{F_{t+\Delta t} - \boldsymbol{C}\tilde{\dot{u}}_{t+\Delta t} - \boldsymbol{K}\tilde{u}_{t+\Delta t}\} \quad (4.58)$$

Consider that the aerodynamic force is a function of the shape (u) and rate of deformation ($\dot{u}$) of the body. These are in turn a function of the acceleration ($\ddot{u}$), through equations (4.56) and (4.57). Express this as:

$$F_{t+\Delta t} = fn_A(\ddot{u}_{t+\Delta t}) \quad (4.59)$$

The solution of the equation of motion at time $t + \Delta t$ thus requires the above equations to be implemented, and the equations for force and acceleration to be solved simultaneously. In modelling the aeroelastic system as strongly coupled, $F_{t+\Delta t}$ and $\ddot{u}_{t+\Delta t}$ are solved iteratively until convergence to dynamic equilibrium is obtained. Let the solutions at the i-th sub-iteration (the physical time remains $t + \Delta t$) be represented by the superscript $^{(i)}$. The sub-iteration procedure is then as follows:

1. Start the sub-iteration procedure (for $i = 1$) by assuming:

$$F_{t+\Delta t}^{(1)} = F_t \quad (4.60)$$

2. Calculate the structural response for the assumed loading:

$$\ddot{u}_{t+\Delta t}^{(1)} = \boldsymbol{H}^{-1}\left\{F_{t+\Delta t}^{(1)} - \boldsymbol{C}\tilde{\dot{u}}_{t+\Delta t} - \boldsymbol{K}\tilde{u}_{t+\Delta t}\right\} \quad (4.61)$$

$$\dot{u}_{t+\Delta t}^{(1)} = \tilde{\dot{u}}_{t+\Delta t} + (\gamma\Delta t)\ddot{u}_{t+\Delta t}^{(1)} \quad (4.62)$$

$$u_{t+\Delta t}^{(1)} = \tilde{u}_{t+\Delta t} + (\beta\Delta t^2)\ddot{u}_{t+\Delta t}^{(1)} \quad (4.63)$$

This concludes the starting procedure.

For the following sub-iterations, $i \geq 2$.

3. Calculate the aerodynamic load for the current sub-iteration from the previous response:

$$F_{t+\Delta t}^{(i)} = fn_A\left(\ddot{u}_{t+\Delta t}^{(i-1)}\right) \quad (4.64)$$

4. Calculate the structural response for the current sub-iteration:

$$\ddot{u}_{t+\Delta t}^{(i)} = \boldsymbol{H}^{-1}\left\{F_{t+\Delta t}^{(i)} - \boldsymbol{C}\tilde{\dot{u}}_{t+\Delta t} - \boldsymbol{K}\tilde{u}_{t+\Delta t}\right\} \quad (4.65)$$

$$\dot{u}_{t+\Delta t}^{(i)} = \tilde{\dot{u}}_{t+\Delta t} + (\gamma\Delta t)\ddot{u}_{t+\Delta t}^{(i)} \quad (4.66)$$

$$u_{t+\Delta t}^{(i)} = \tilde{u}_{t+\Delta t} + (\beta \Delta t^2)\ddot{u}_{t+\Delta t}^{(i)} \quad (4.67)$$

5. Check for convergence between the sub-iterations:

$$\frac{F_{t+\Delta t}^{(i)} - F_{t+\Delta t}^{(i-1)}}{F_{t+\Delta t}^{(i-1)}} < \varepsilon_F \, ? \quad (4.68)$$

$$\frac{\ddot{u}_{t+\Delta t}^{(i)} - \ddot{u}_{t+\Delta t}^{(i-1)}}{\ddot{u}_{t+\Delta t}^{(i-1)}} < \varepsilon_{\ddot{u}} \, ? \quad (4.69)$$

$$\frac{\dot{u}_{t+\Delta t}^{(i)} - \dot{u}_{t+\Delta t}^{(i-1)}}{\dot{u}_{t+\Delta t}^{(i-1)}} < \varepsilon_{\dot{u}} \, ? \quad (4.70)$$

$$\frac{u_{t+\Delta t}^{(i)} - u_{t+\Delta t}^{(i-1)}}{u_{t+\Delta t}^{(i-1)}} < \varepsilon_u \, ? \quad (4.71)$$

6. Repeat steps 3 through 5 to convergence.

Once convergence of sub-iterations has been reached, the solution for the aerodynamic loading and the structural response is taken to be the solution to the implicit problem at the physical time $t + \Delta t$. The solution steps forward in physical time to $t + 2\Delta t$, and the sub-iteration procedure is then repeated for the new physical time.

4.6.2 Explicit Time-Marching of Systems with Time-Linearized Aerodynamic Loading and Time-Invariant Matrices

The time-history of response for LTI systems was obtained through explicit time-marching of the state-space formulation of the aeroelastic equations of motion. The state-space representation was constructed as:

$$\begin{Bmatrix} \dot{\vec{x}} \\ \vec{x} \end{Bmatrix} = \begin{bmatrix} -\boldsymbol{M}_{\boldsymbol{mod}_{ae}}^{-1}\boldsymbol{C}_{\boldsymbol{mod}_{ae}} & -\boldsymbol{M}_{\boldsymbol{mod}_{ae}}^{-1}\boldsymbol{K}_{\boldsymbol{mod}_{ae}} \\ \boldsymbol{I} & \boldsymbol{0} \end{bmatrix} \begin{Bmatrix} \dot{\vec{x}} \\ \vec{x} \end{Bmatrix} + \begin{Bmatrix} \vec{Q}_{offset} \\ \vec{0} \end{Bmatrix} \quad (4.72)$$

The set of first-order differential equations was solved in MATLAB using either the `ode23t` or the `ode45` functions. The `ode23t` function is a one-step implementation of the trapezoidal scheme of integration and gives a solution free of numerical damping [70]; the `ode45` function is based on a one-step, explicit Runge-Kutta (4,5) formulation [70]. The `ode23t` function was used for the explicit time-marching as far as possible due to its lack of numerical damping. The `ode45` function was used where the `ode23t` function failed due to

poor numerical conditioning of the Jacobian matrix. It was found that in the general case, the difference in results produced by the two solvers (`ode23t` and `ode45`) was negligible, as shown by the coinciding peaks of the two time-responses in Figure 4.5.

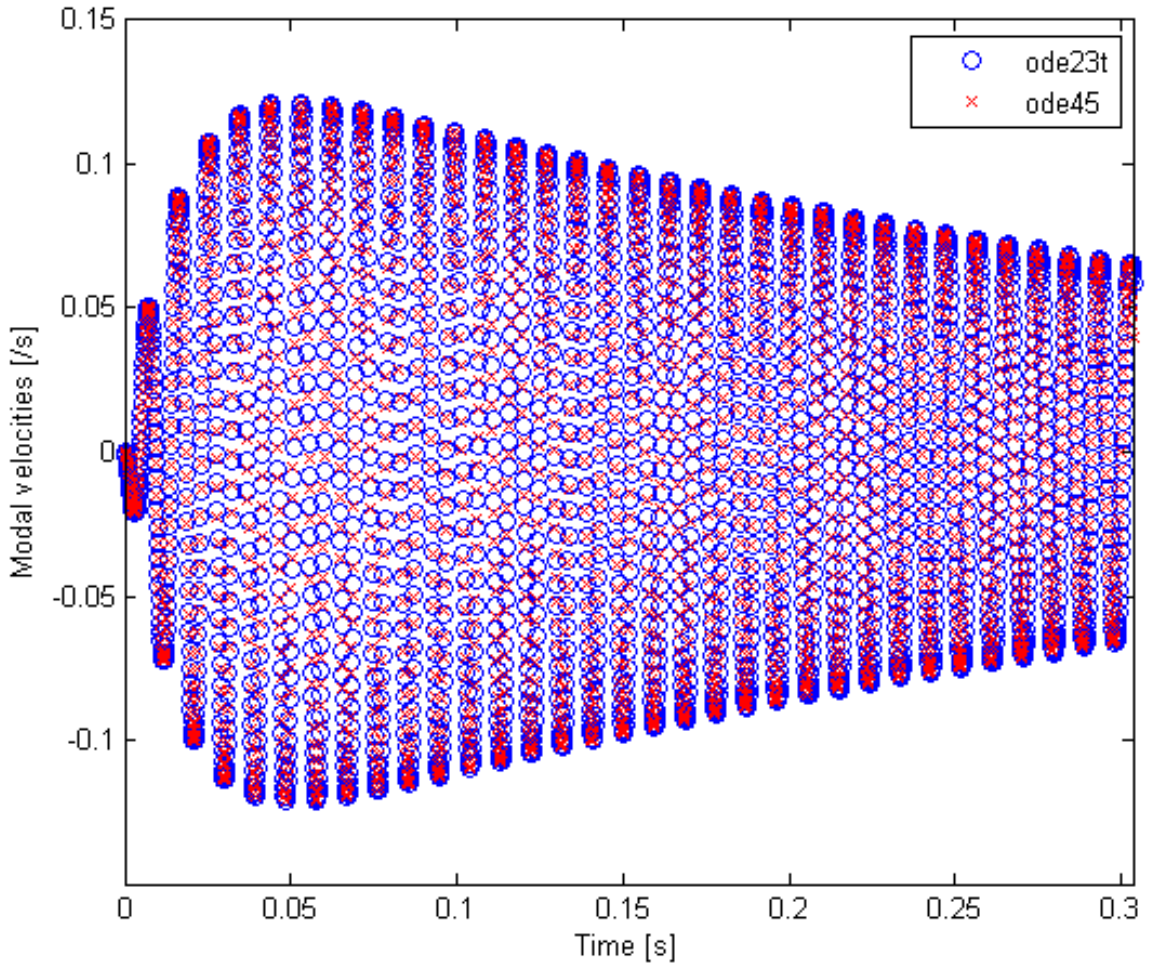


Figure 4.5: Comparison of the ode23t and ode45 Solvers in MATLAB

4.7 Representation of System Response

The system response with time and with flight conditions was represented by consideration of the time-history of various modal responses, including displacements, velocities, and GAFs; similarly, histories of the aerodynamic coefficients C_L, C_D and $C_{M_{LE}}$ were considered.

For linearized systems, the trajectories of the system roots with flight conditions were considered, as were the system parameters.

In characterizing the response of nonlinear systems, the time-histories of both modal and full-order responses were considered, as were the phase-plane trajectories of modal displacements.

4.7.1 Time-History of Modal Response

The holistic time-response of the system may be well-described by the modal displacements and velocities of a small number of dominant modes. Moreover, the history of the generalized modal forces provides insight to the coupling between modes and the external loading. The structural response of any single degree of freedom may be found through superposition of the modal contributions at the point. An example of the time-history of modal response for a nonlinearly damped system is given in Figure 4.6.

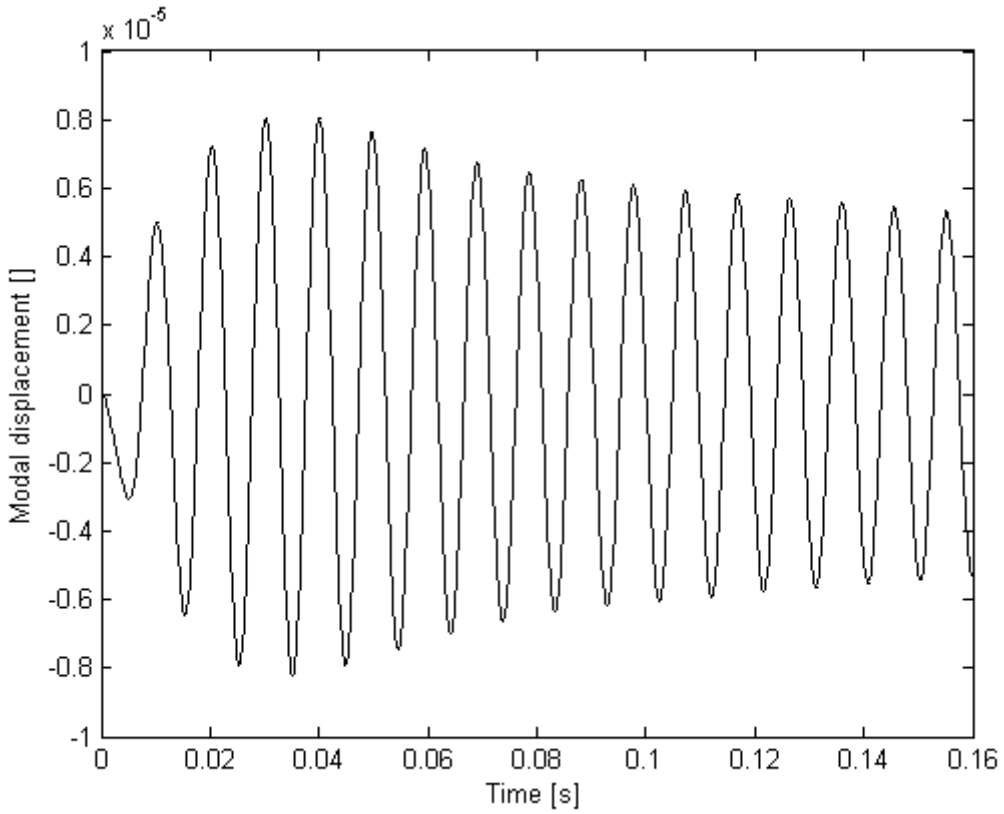


Figure 4.6: Example of Time-History of Modal Response for an Aeroelastic System in MATLAB

4.7.2 Phase-Plane Trajectory of Modal Response

In a similar manner, the phase-plane trajectory of modal displacements and velocities may be used to assess the structural response and stability [44]. The phase-plane trajectory of a nonlinearly damped system is shown in Figure 4.7; the corresponding modal displacement history is given in Figure 4.6.

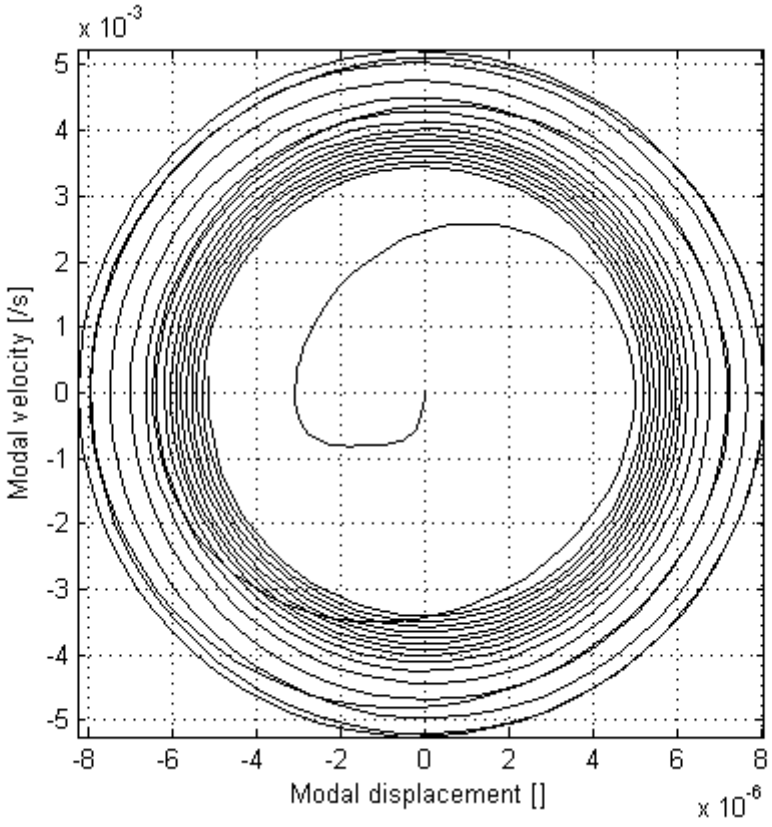


Figure 4.7: Example of Phase-Plane Representation of an Aeroelastic System in MATLAB

4.7.3 System Eigenvalues and Parameters

For linear time-invariant systems, eigenanalysis may be performed on the coupled fluid-structure system; the root loci of the system [11; 41] may be plotted to give a condensed but detailed representation of the system characteristics. In particular, the information is directly relevant to analysing the system stability. An example of an root locus plot for a 6-mode system is given in Figure 4.8. The corresponding variation of the frequencies and damping ratios of the two lowest-frequency roots is shown in Figure 4.9. Note the coalescence of frequencies and separation of damping ratios, which is typical of aeroelastic systems approaching flutter.

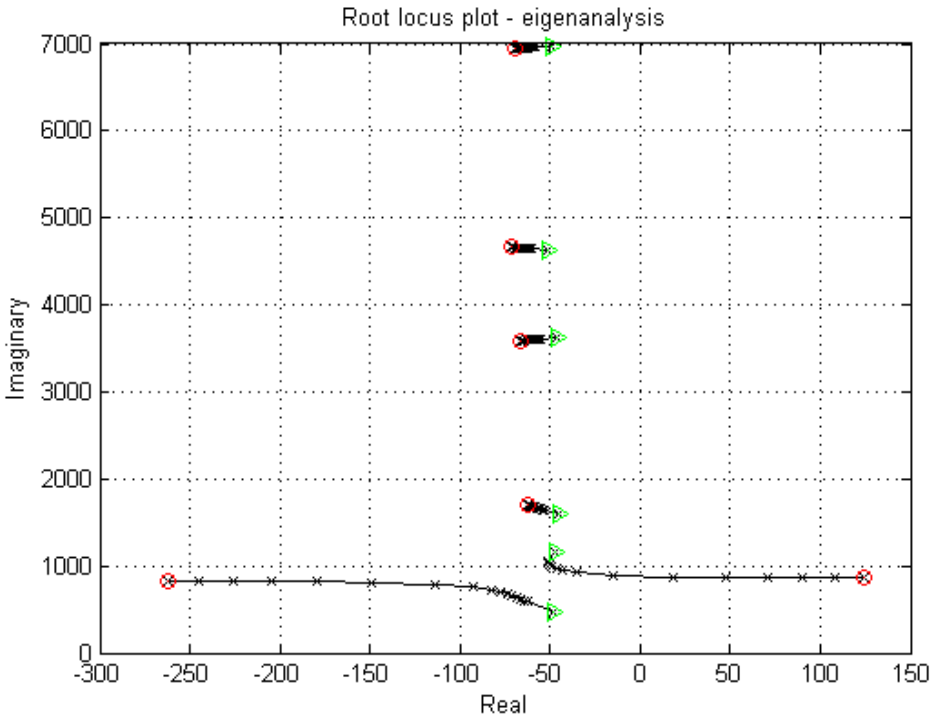


Figure 4.8: Example of a Root Locus Plot for an Aeroelastic System in MATLAB

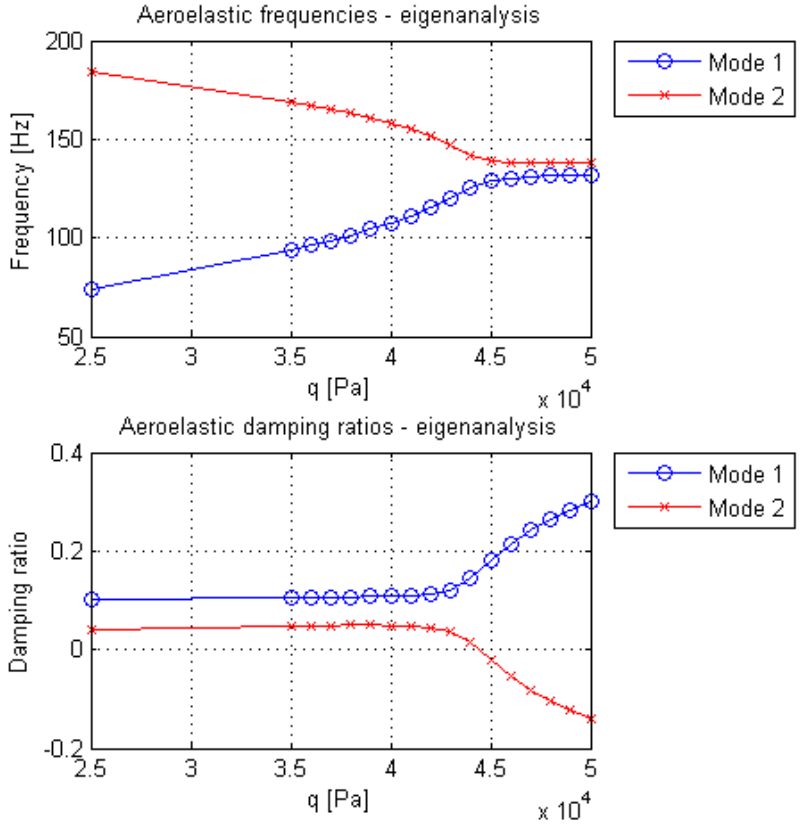


Figure 4.9: Example of Variation in Aeroelastic System Parameters in MATLAB

4.7.4 Response of Individual Points on the Structure

When the mode shapes and modal displacements are not known or are difficult to extract, the response of the structure at a number of points may be considered. Yildiz [62] provides recommendations on the selection of measurement (as well as excitation) points on the structure which provide the best insight into the individual modal contributions. The time-history of response of the individual points may be plotted, but offers little insight to the system stability, or the response of the structure as a whole as shown in Figure 4.10.

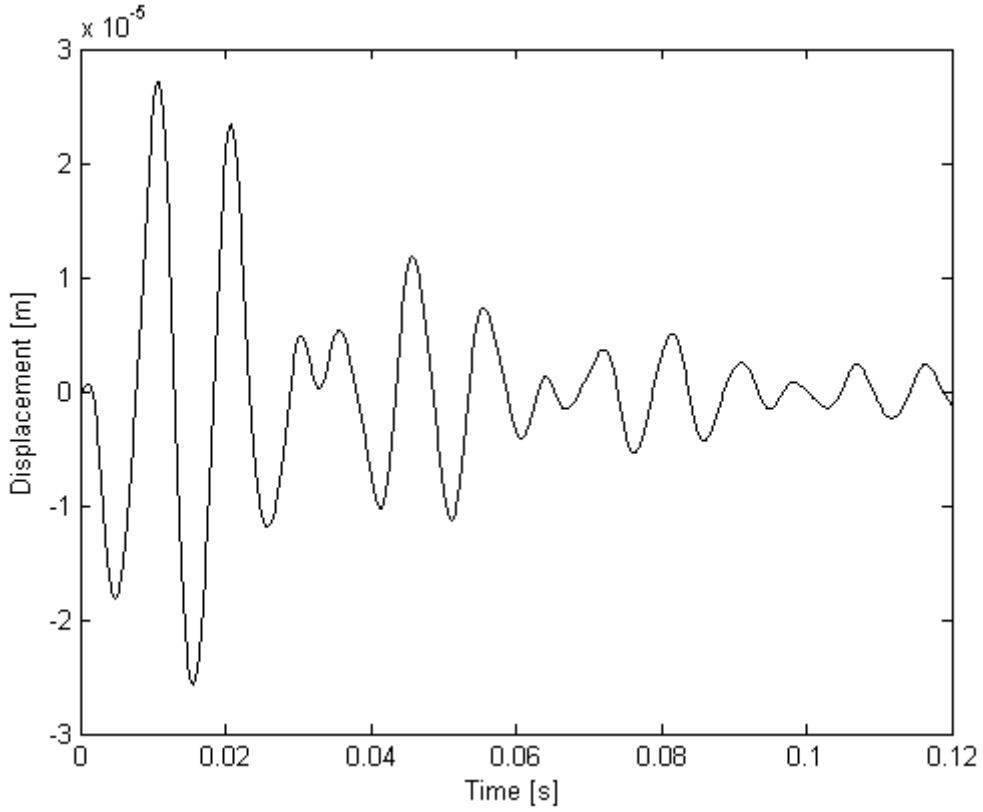


Figure 4.10: Example of the Response Obtained from an Individual Degree of Freedom in MATLAB

5 VALIDATION OF THE AEROELASTIC PREDICTION TOOL AGAINST COMPUTATIONAL FLUID DYNAMICS

5.1 The Edge CFD Solver

Edge is a computational fluid dynamics solver for unstructured grids of arbitrary elements developed by FOI of Sweden [71]. Edge solves the Reynolds-Averaged Navier Stokes compressible equations using a node-centred finite-volume technique, and has several turbulence models available [71]. The formulation is edge-based; control volumes are non-overlapping and are formed from a dual grid obtained from the control surfaces of the element edges, as shown in Figure 5.1. The control volumes for the node-centred computations are given by the dual grid, which is derived from the input (primary) grid.

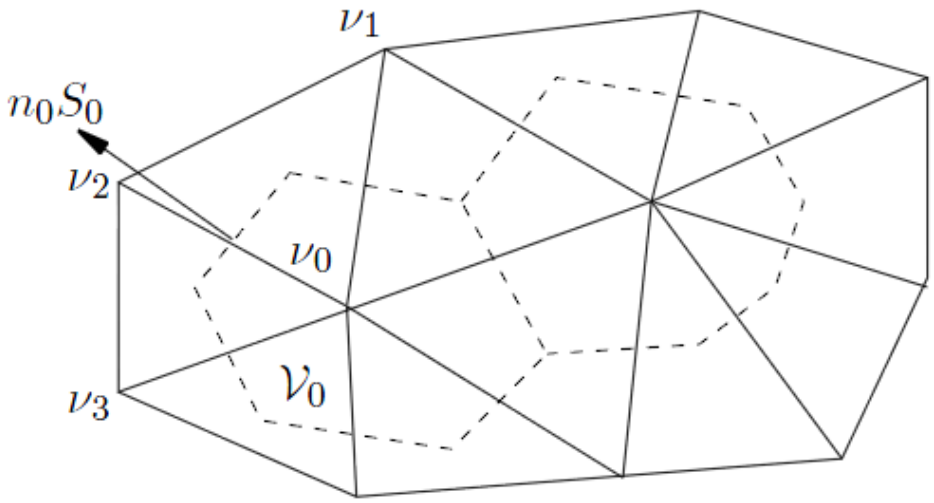


Figure 5.1: The Primary (solid line) and Dual (dashed line) Grids in Edge **[71]**

For steady solutions, convergence may be accelerated through multi-gridding and implicit residual smoothing; however, for explicit time-accurate solutions, these features must be disabled. With implicit time-accurate solutions, multi-gridding and implicit residual smoothing are employed in the sub-iterations (in pseudo-time) at each real (or physical) time step [71].

Edge also allows for a number of options for aeroelastic analysis, including coupling to external structural solvers [71]. For solutions without coupling to external solvers, the structural analysis is performed using a modal description of the structure. The structural modal-mass, modal-damping, and modal-stiffness matrices are modelled to be time-invariant, and so the structural is effectively modelled as being linear.

The deformation of the wetted surface boundary must be computed from specified structural mode-shapes; the boundary displacement is then used in Edge subroutines and helper programs to generate a deformed mesh corresponding to the structural modeshape. Since the displacements of the nodes on the wetted boundary corresponding to the mode-shapes are known, no transformation matrix is needed to interpolate loads between structural and fluid grids to obtain the generalized aerodynamic forces [71]. The mesh deformation is performed "offline" (before the flow computation) for deflections of a specified magnitude for each mode, and the resulting differences in nodal coordinates between the deformed and "base" meshes are used to compute the modal "perturbation field" [71].

The mesh deformation operations are applied to the primary grid nodes, requiring the dual grid and resulting cell volumes and surfaces to be recomputed for each incremental deflection [71]. The mesh deformation must also be limited to magnitudes that do not result in negative cell volumes.

The aeroelastic solver in Edge is a partitioned solver, with the solution of the aerodynamic and structural equations being strongly coupled (sub-iterations in pseudo-time are performed to convergence at each real time step). The aeroelastic equations of motion are solved by implicit time-marching. The modal displacements and forces are evaluated using three-point averaging in time, and time derivatives are modelled using central differences in time [71]. This leads to [71] the following equations of motion,

$$\boldsymbol{M}_{\boldsymbol{mod}_{\boldsymbol{str}}}\{\ddot{x}\} + \boldsymbol{C}_{\boldsymbol{mod}_{\boldsymbol{str}}}\{\dot{x}\} + \boldsymbol{K}_{\boldsymbol{mod}_{\boldsymbol{str}}}\{x\} = Q_{aero} \qquad (5.1)$$

in which

$$x = \frac{1}{4}(x_{t+\Delta t} + 2x_t + x_{t-\Delta t}) \quad (5.2)$$

$$Q = \frac{1}{4}(Q_{t+\Delta t} + 2Q_t + Q_{t-\Delta t}) \quad (5.3)$$

where t is the time at the current real time step.

The time-marching scheme is implicit in $x_{t+\Delta t}$, and is solved to convergence at each real time step, with the dual grid being recomputed at each pseudo-time step as the modal displacement $x_{t+\Delta t}$ changes.

5.2 Geometry and Structural Parameters of the ATM-Wing

The geometry was modelled after the untapered cantilevered plate of Torii [54] and Matsuzaki [55]. The bevel on the leading- and trailing-edges was assumed to be 15mm in length on each edge, and the geometry is hence referred to as the approximated Torii-Matsuzaki wing (ATM-wing). The geometry is given in Figure 5.2 and Figure 5.3 on page 102. This geometry was chosen for the results published by Torii [54] and Matsuzaki [55], which include the flutter velocity and the variation in identified system parameters below flutter speed.

A finite element model of the geometry was analysed in MSC NASTRAN Student Version to obtain the natural modal frequencies of the model. The plate was modelled using 2078 Tet 10 solid elements, with 4412 nodes in the model. The material properties used are given in Table 5.1, with the first three modal frequencies given in Table 5.2. The first three modeshapes are shown in Figure 5.4 through Figure 5.6. Structural damping was not modelled.

Table 5.1: Material Properties of the FEM Model of the ATM-Wing

Material	Aluminium
Young's Modulus, E [GPa]	73.1
Poisson's Ratio, υ	0.33
Density, ρ [kg/m^3]	2780
Mass [kg]	0.104

Table 5.2: Comparison of Natural Frequencies for the TM-Wing

Mode No.	Description	Torii [54] FEM Frequency [Hz]	Torii [54] Experimental Frequency [Hz]	Estimated Model MSC NASTRAN Frequency [Hz]
1	1st Bending	27.9	27.2	26.6
2	1st Twist	145.7	142.0	148.5
3	2nd Bending	207.1	192.3	195.0

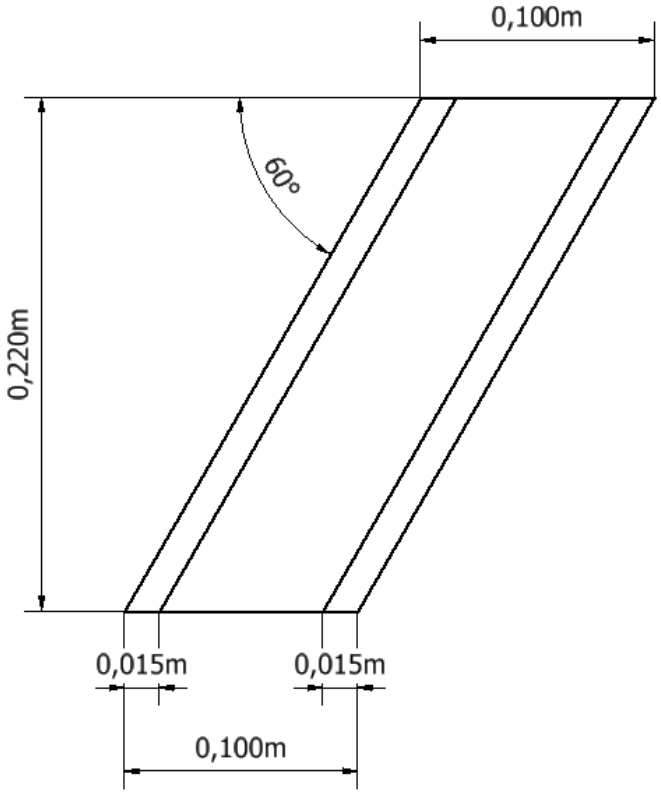


Figure 5.2: ATM-Wing Planform

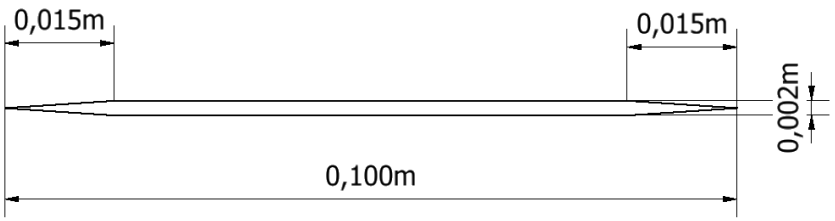


Figure 5.3: ATM-Wing Profile

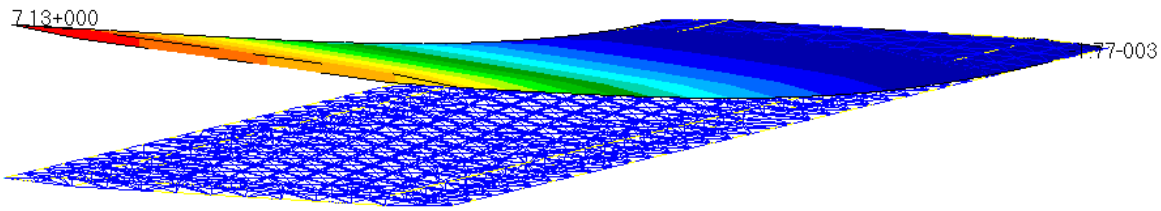


Figure 5.4: ATM-Wing, Mode 1 -- First Bending, 26.6 Hz

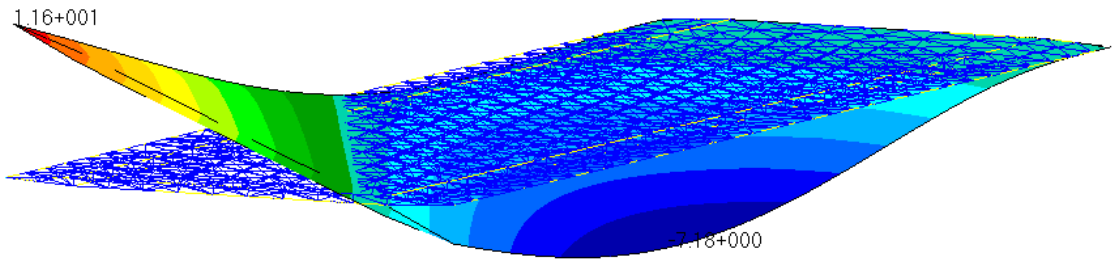


Figure 5.5: ATM-Wing, Mode 2 -- First Twist, 148.5 Hz

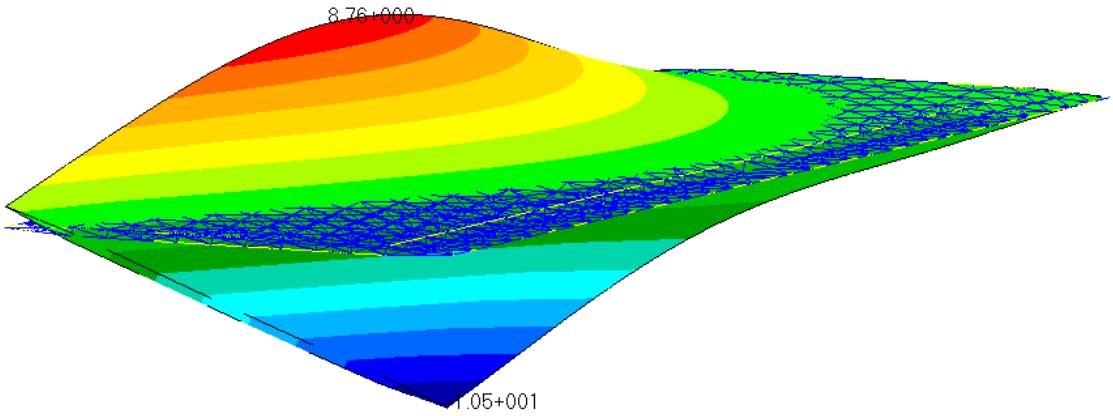


Figure 5.6: ATM-Wing, Mode 3 -- Second Bending, 195.0 Hz

Higher natural frequencies and the associated structural mode-shapes are shown as viewed from the wing-tip, from above, in Figure 5.7 and Figure 5.8.

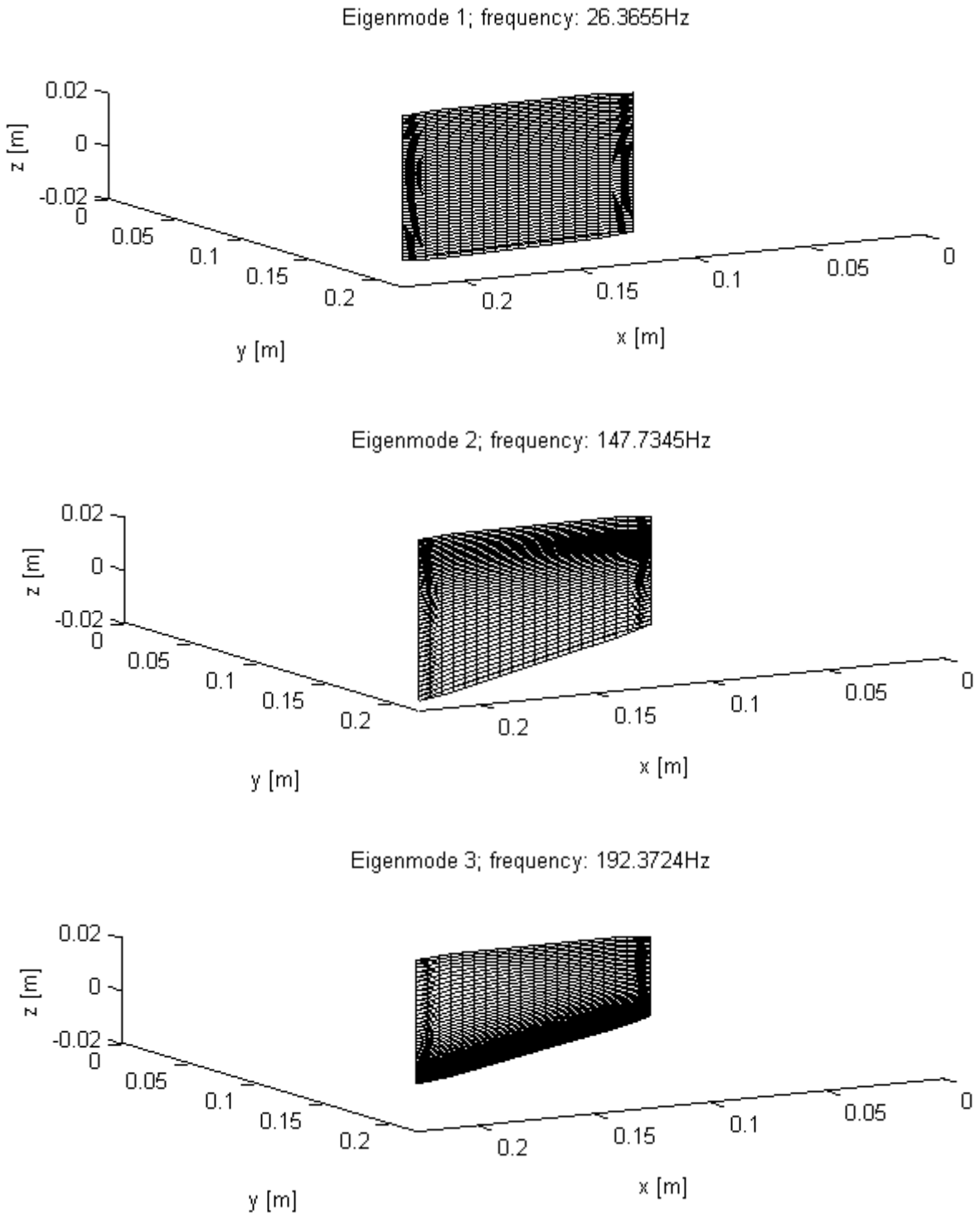


Figure 5.7: ATM-Wing Structural Mode-Shapes 1 - 3, View from Wing-Tip

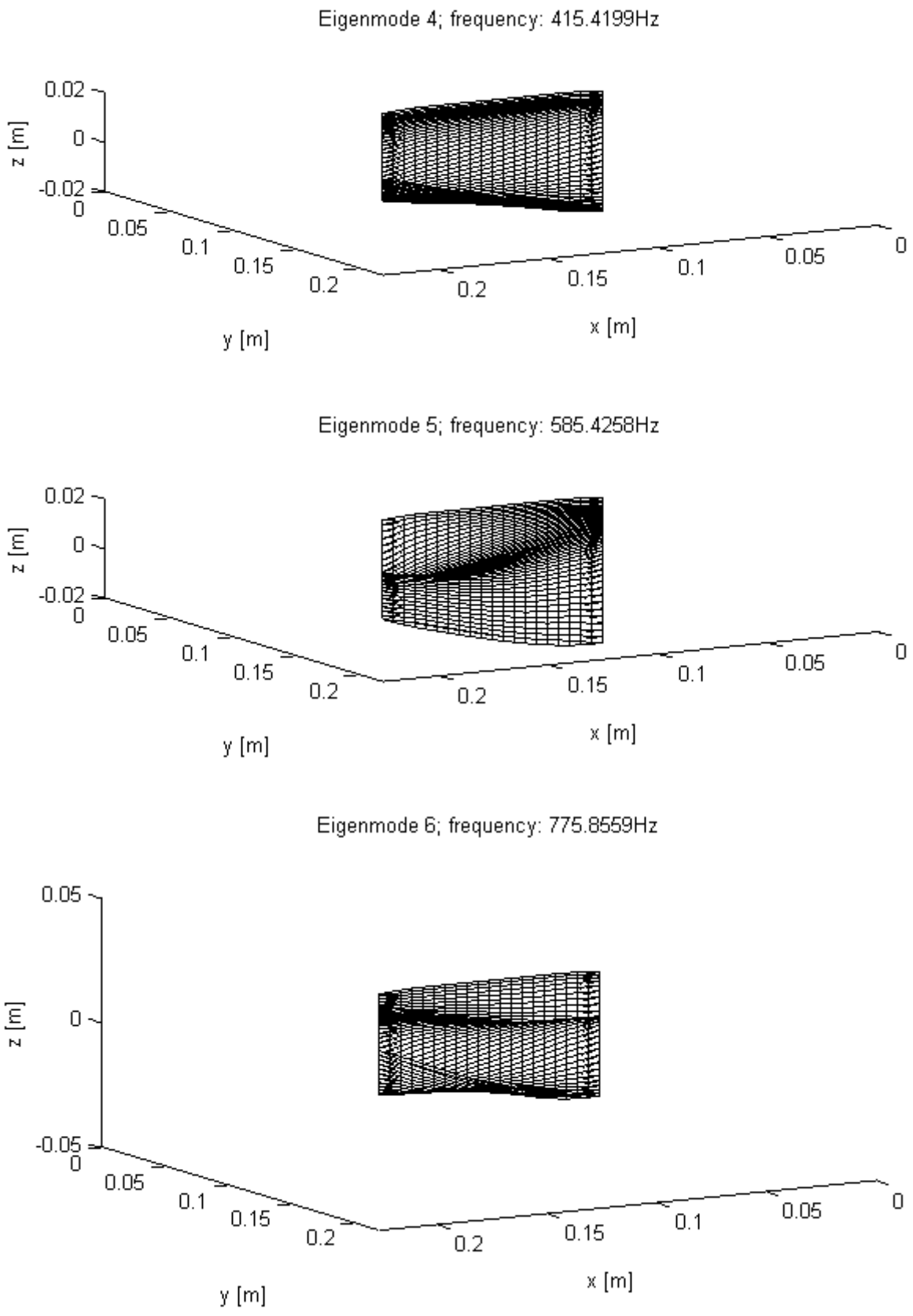


Figure 5.8: ATM-Wing Structural Mode-Shapes 4 - 6, View from Wing-Tip

5.3 Validation of the Finite Element Solver

The Finite Element solver of the aeroelastic prediction tool developed in MATLAB was validated for ATM-wing against modelling in MSC NASTRAN.

In MATLAB, the wing was modelled using trapezoidal bending-plate elements. The mesh consisted of 20 chordwise segments and 44 spanwise segments, to give the elements an aspect ratio of 1. The resulting mesh consisted of 880 elements and 945 nodes, with 2835 degrees of freedom. The mesh is shown in Figure 5.9. All degrees of freedom of the root nodes ($y = 0$) were constrained to model the wing as cantilevered.

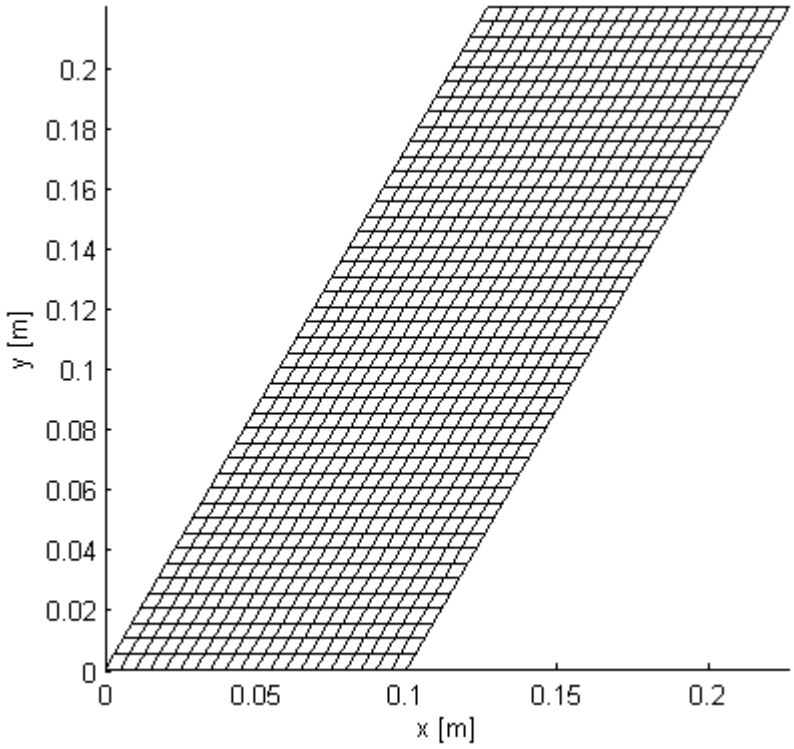


Figure 5.9: Structural Mesh used for the ATM-Wing

The modelling of the wing in MSC NASTRAN was described in Section 5.2, and the same material properties were used for each model, given in Table 5.1. Modal analysis was carried out (SOL103 in MSC NASTRAN), and the mode-shapes and natural frequencies of the ATM-wing were calculated. The first four modal frequencies were calculated to within 1.4% in MATLAB; the comparison of results is given in Table 5.3. The reader is referred to Figure 5.7 and Figure 5.8 for the depiction of the mode-shapes. It was concluded that the Finite Element solver gave sufficiently accurate results.

Table 5.3: Computed Natural Frequencies for the TM Wing

Mode number	Mode description	Frequency [Hz] -- MSC NASTRAN	Frequency [Hz] -- MATLAB	% error
1	1st bending	26.56	26.37	-0.86%
2	1st torsion	148.50	147.73	-0.52%
3	2nd bending	194.97	192.37	-1.33%
4	2nd torsion	417.77	415.42	-0.56%
5	3rd bending	594.91	585.43	-1.59%
6	3rd torsion	781.21	775.86	-0.68%

Further comparison between the results of the MATLAB-based Finite Element solver and MSC NASTRAN were made for a series of cantilevered un-swept trapezoidal plates subjected to uniform transverse pressure. The taper ratio and thickness of the plates were varied for a constant value of root-chord to span of $\frac{c_R}{b} = 1$. The error in maximum displacement calculated was found to decrease with decreasing plate thickness and with increasing taper ratio; the results are shown in Figure 5.10 and Figure 5.11.

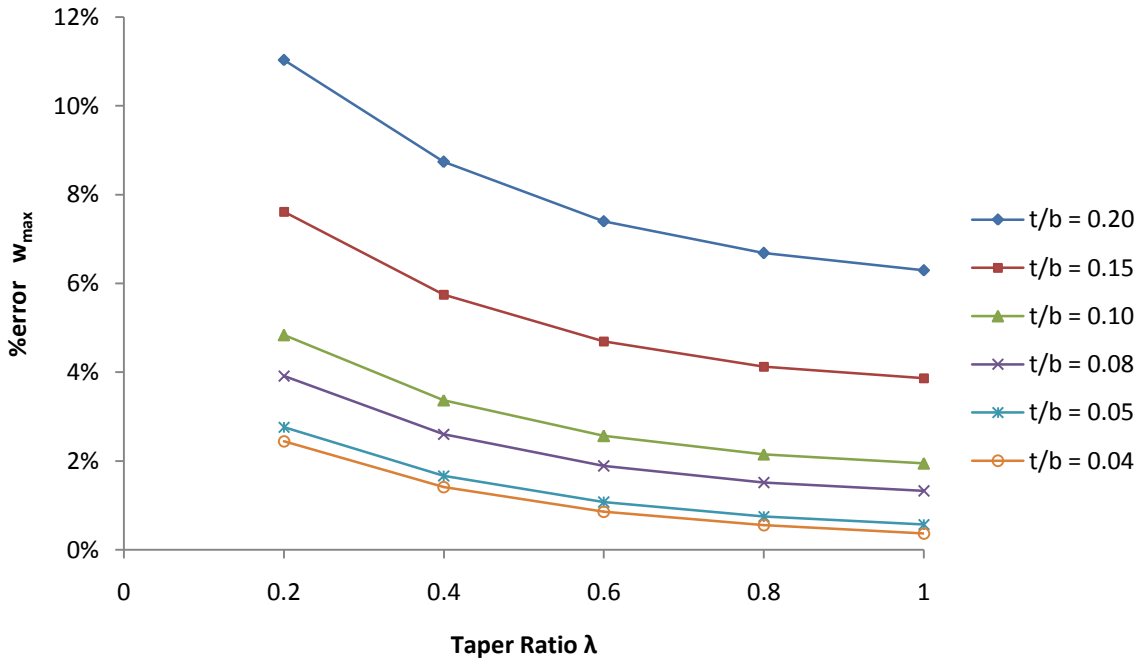


Figure 5.10: Variation in MATLAB-Based Finite Element Solver Accuracy with Taper Ratio

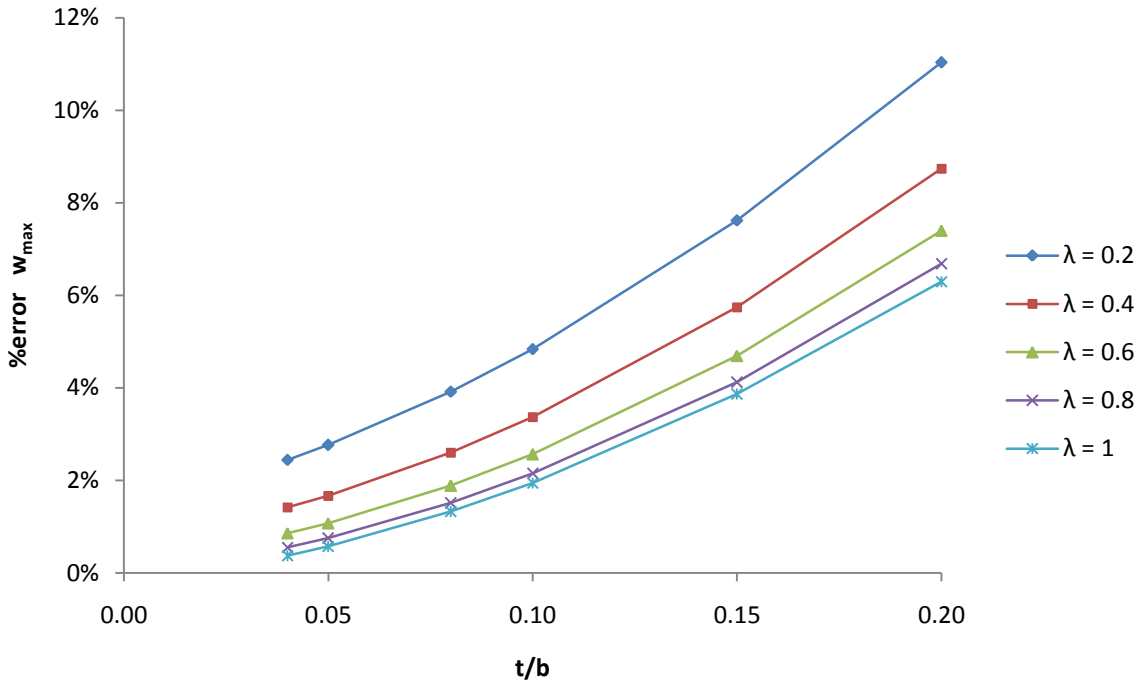


Figure 5.11: Variation in MATLAB-Based Finite Element Solver Accuracy with Plate Thickness

The modal frequencies of the ATM-wing, as calculated in MATLAB, were used in the aeroelastic modelling in Edge. The mode-shapes from MATLAB were interpolated onto the fluid mesh, and the boundary displacement (`.bdis`) files for each mode (needed for mesh deformation) were written in MATLAB for use in Edge.

5.4 Meshing of the Fluid Domain

The fluid domain was discretized using two unstructured meshes; the shape and size of the domains differed, and the difference in results between the meshes were investigated. Both meshes were generated in ICEM.

5.4.1 Mesh 1

In Mesh 1, the fluid domain was modelled as cylindrical, with a hemispherical inlet. The mesh statistics are given in Table 5.4, and details of the mesh are given by Figure 5.12 through Figure 5.16.

Table 5.4: Mesh 1 Statistics

Total number of elements:	1 923 812
Total number of nodes:	331 822
Number of TETRA_4 elements:	1 843 997
Number of TRI_3 elements:	77 840

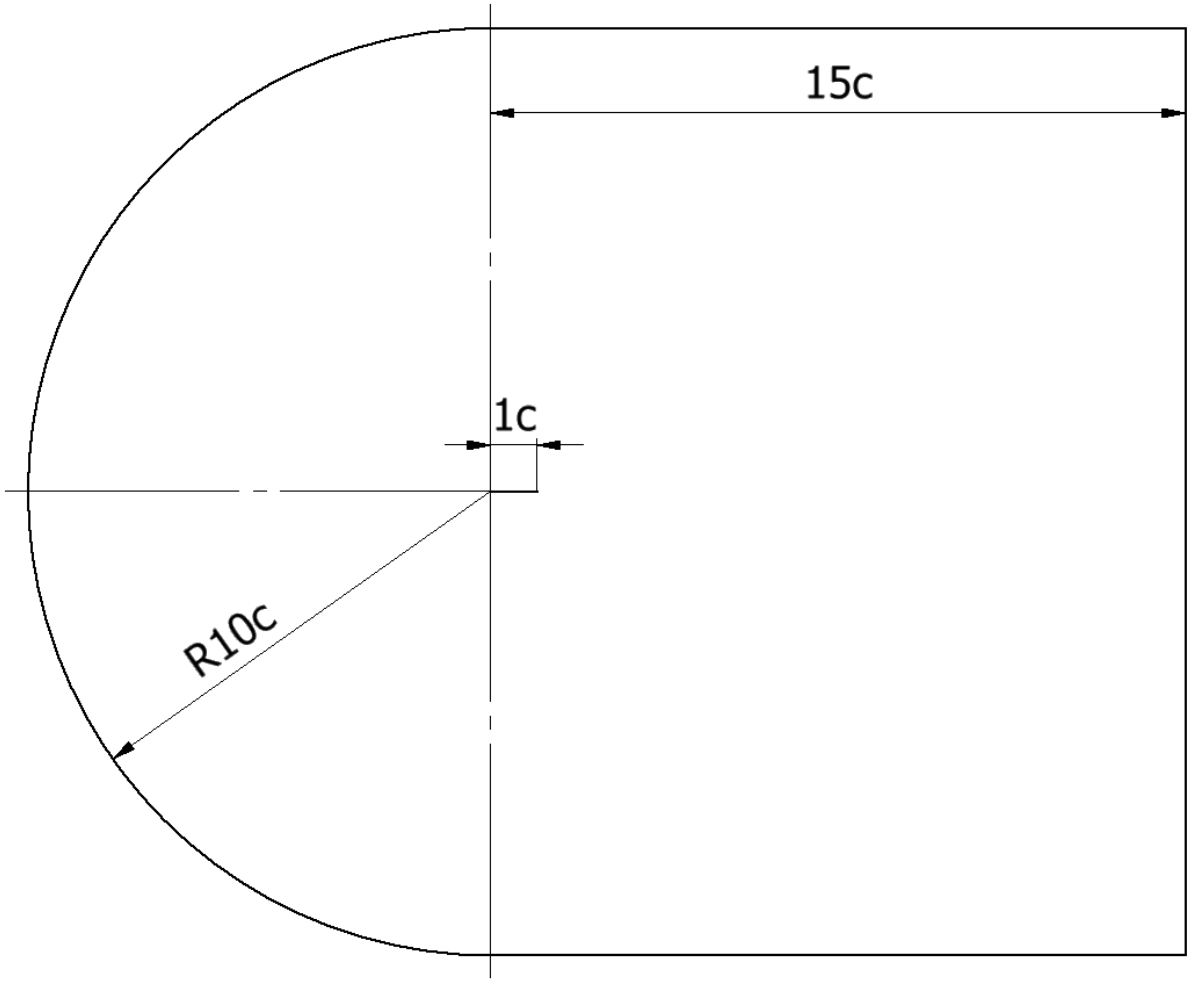


Figure 5.12: Mesh 1, Domain Side View

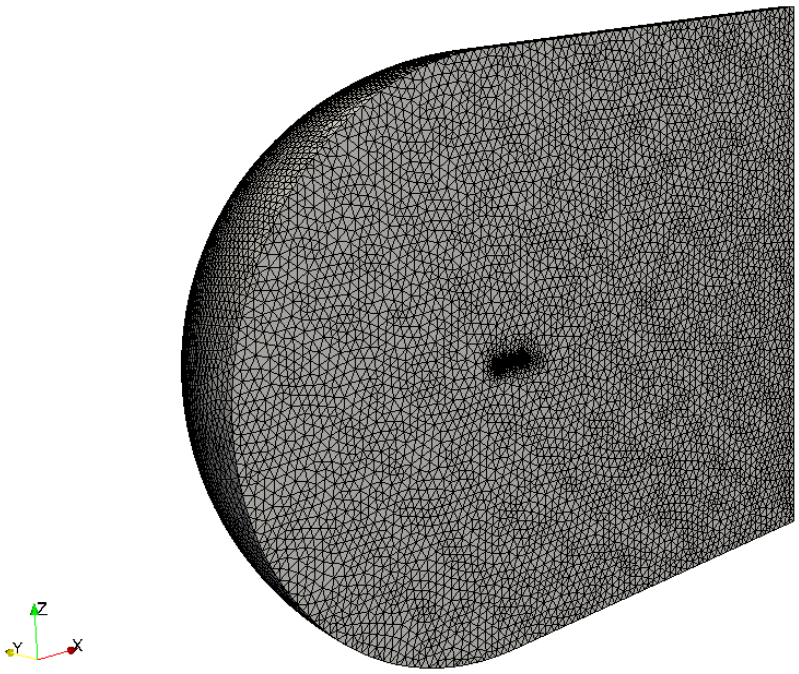


Figure 5.13: Mesh 1, Domain Perspective View

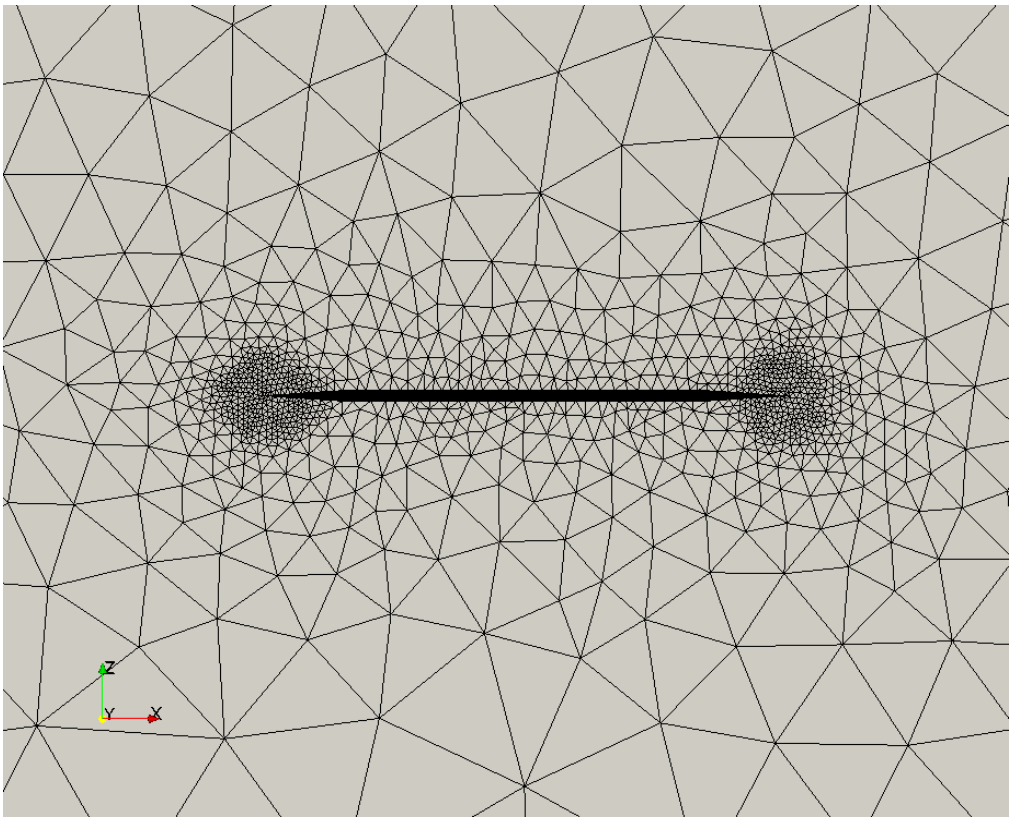


Figure 5.14: Mesh 1, Symmetry Boundary Surface Mesh

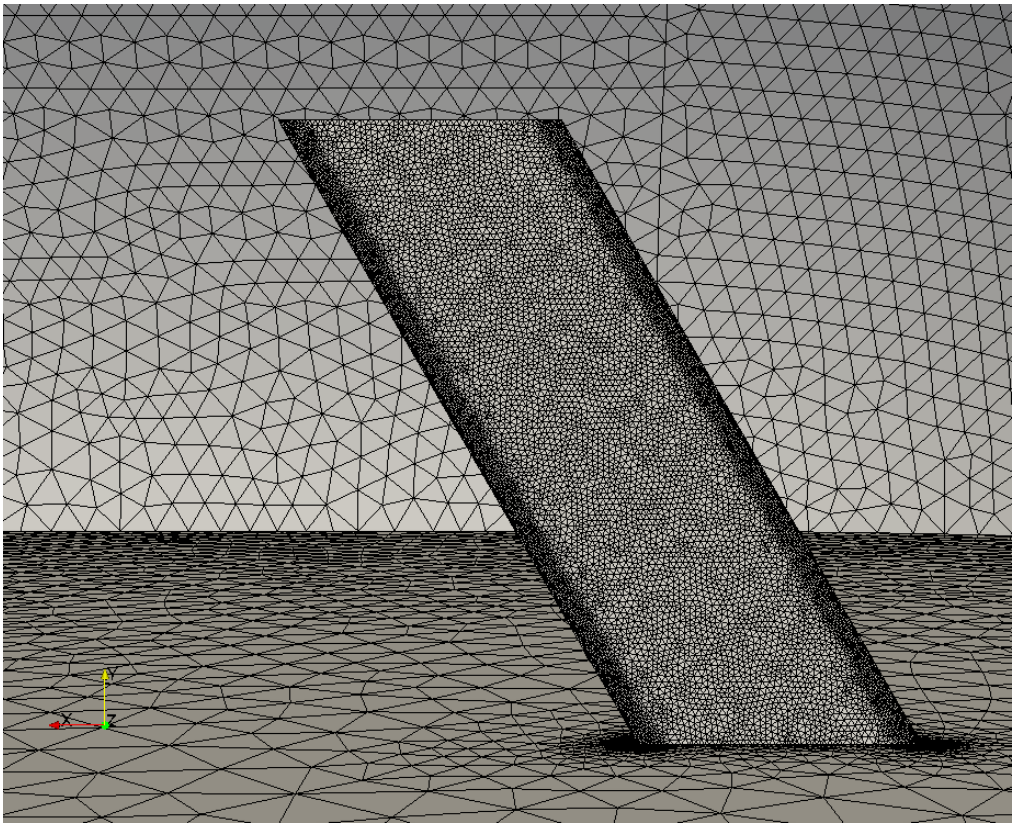


Figure 5.15: Mesh 1, Wing Surface Mesh

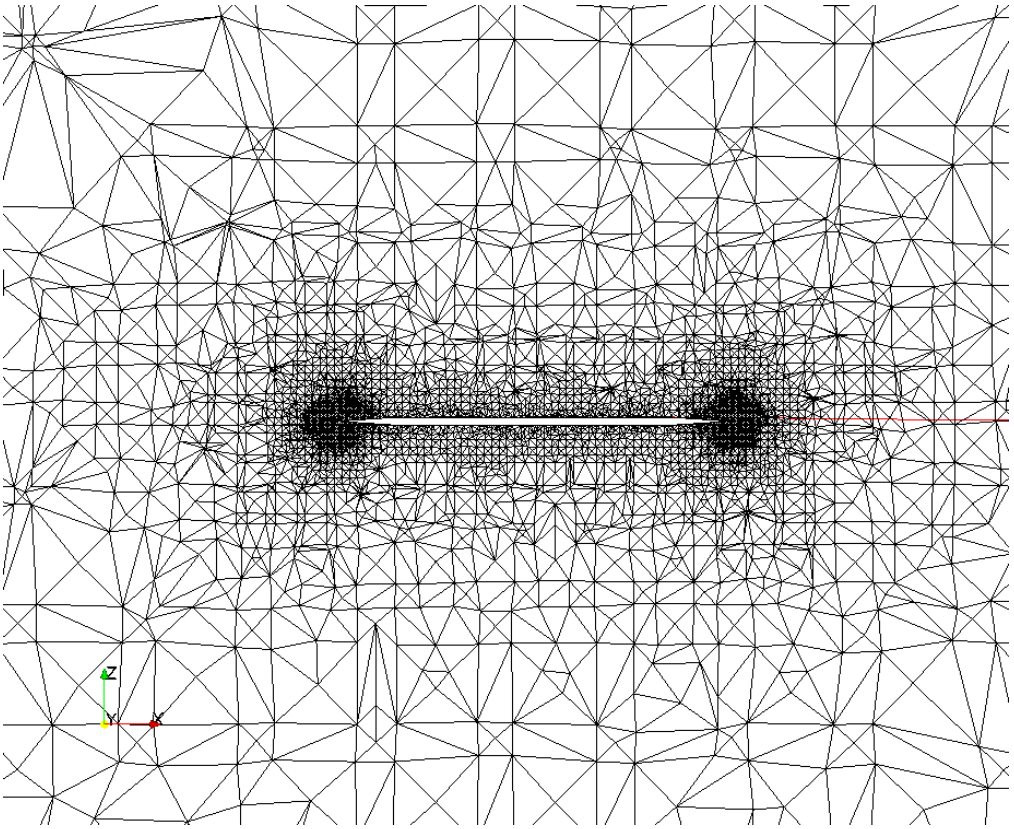


Figure 5.16: Mesh 1, Volume Mesh at the Mid-Span, $\boldsymbol{y = 0.1\mathbf{m}}$

5.4.2 Mesh 2

In Mesh 2, the fluid domain was modelled as a rectangular prism, with a rounded inlet. The mesh statistics are given in Table 5.5, and details of the mesh are given by Figure 5.17 through Figure 5.21.

Table 5.5: Mesh 2 Statistics

Total number of elements:	1 430 723
Total number of nodes:	241 879
Number of TETRA_4 elements:	1 393 356
Number of TRI_3 elements:	35 828

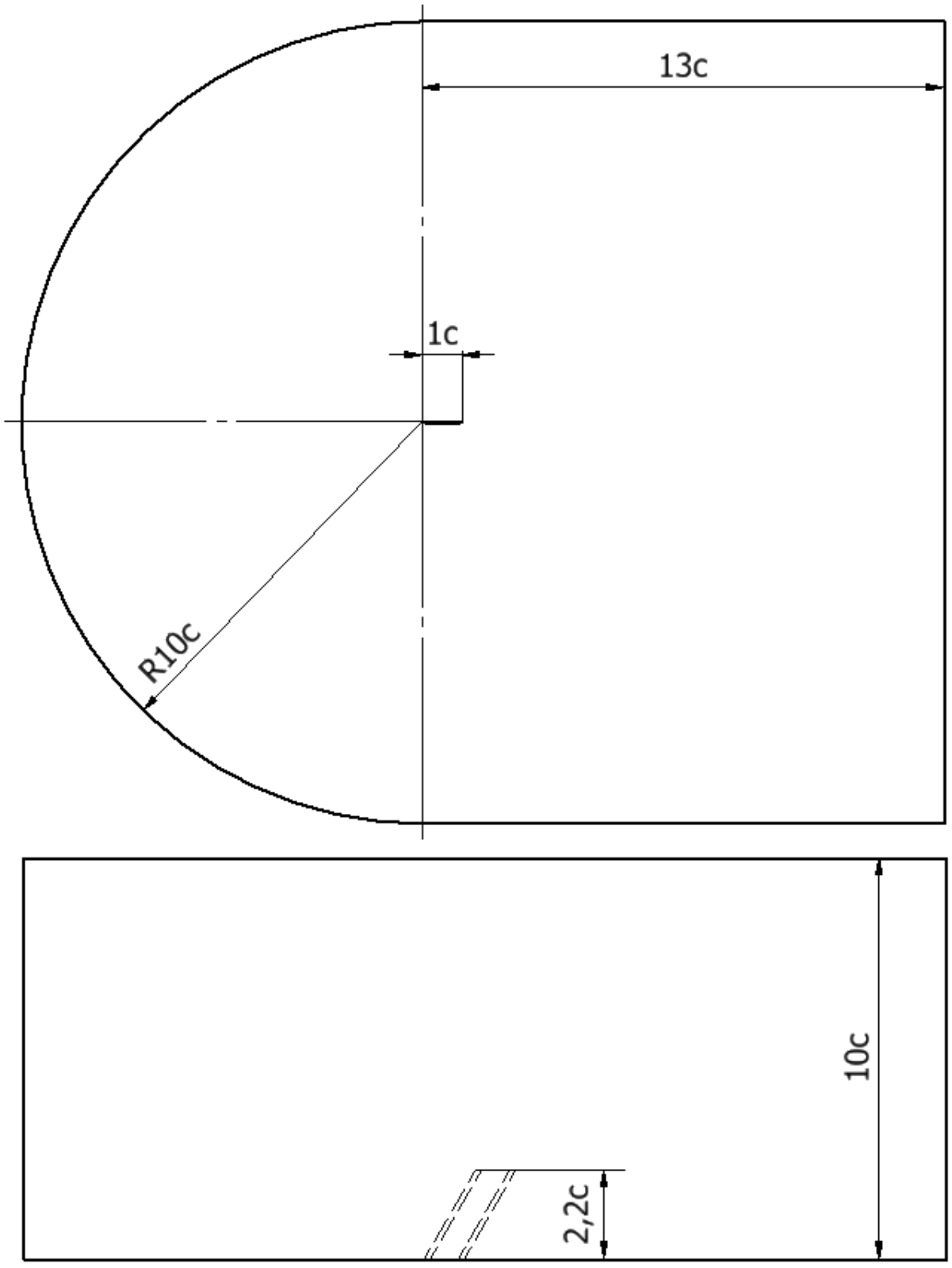


Figure 5.17: Mesh 2, Domain Dimensions

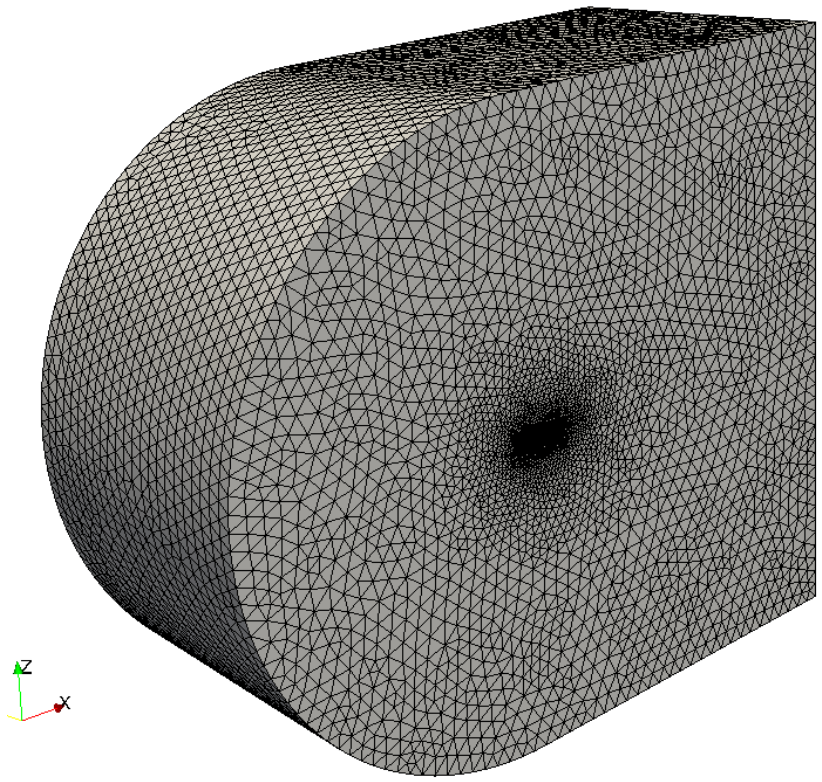


Figure 5.18: Mesh 2, Domain Perspective View

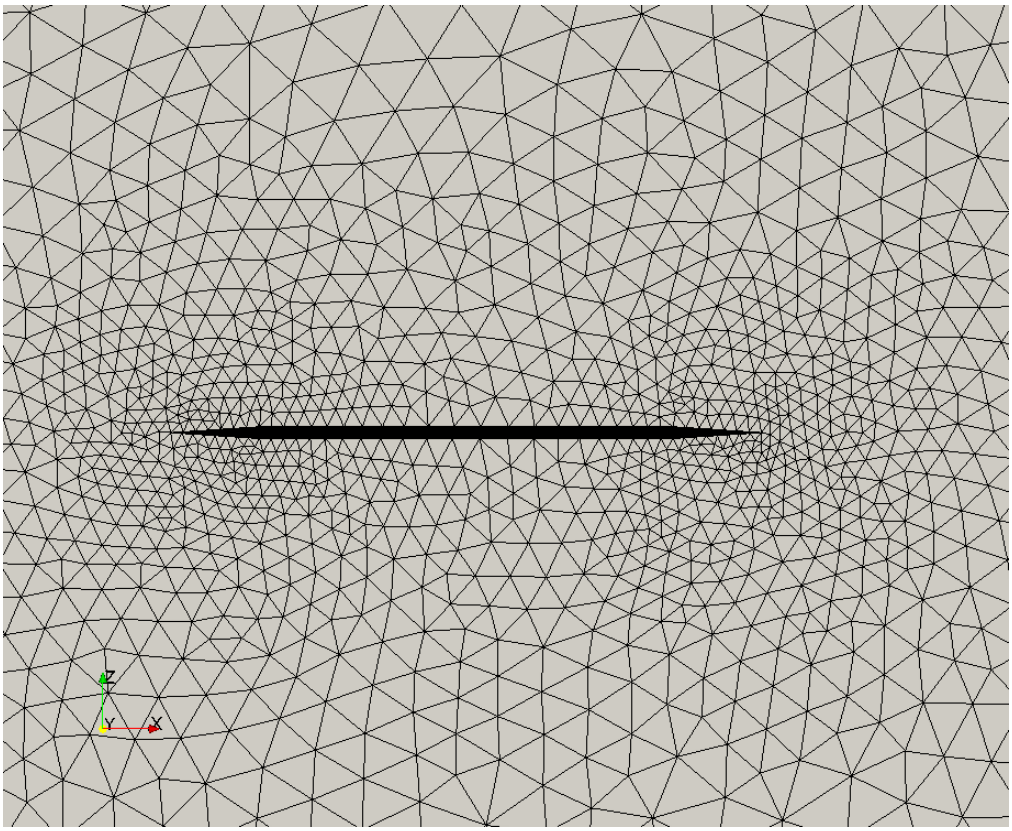


Figure 5.19: Mesh 2, Symmetry Boundary Surface Mesh

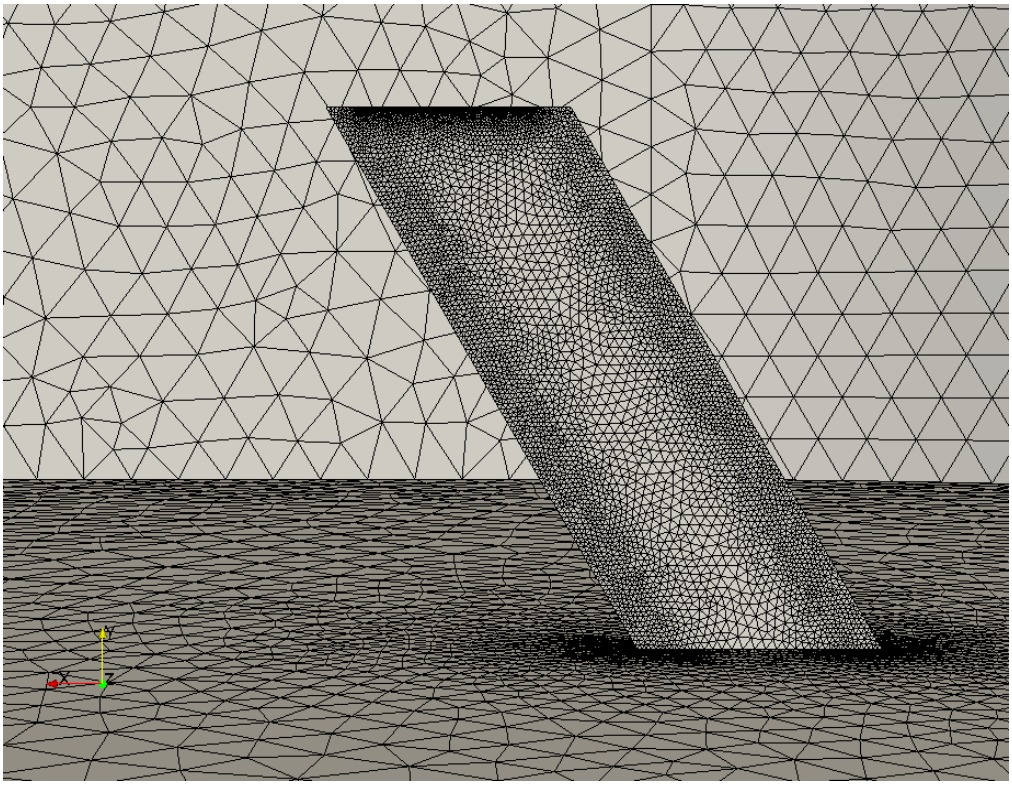


Figure 5.20: Mesh 2, Wing Surface Mesh

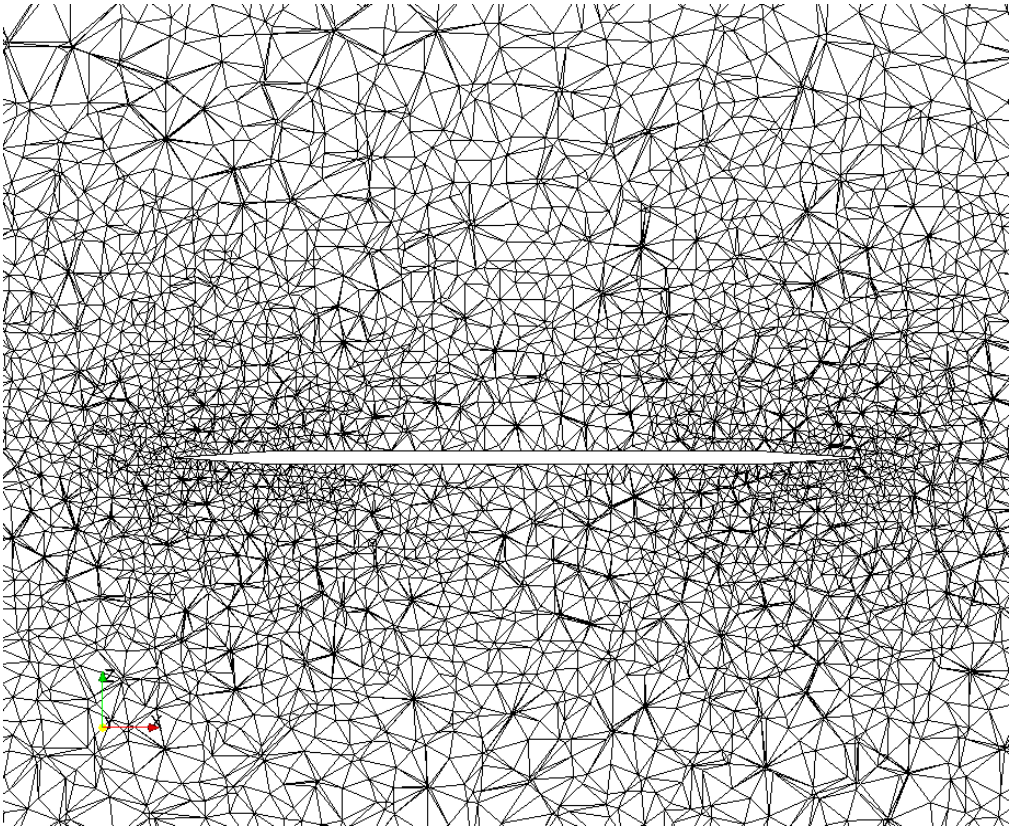


Figure 5.21: Mesh 2, Volume Mesh at Mid-Span, $\boldsymbol{y = 0.1\mathrm{m}}$

5.4.3 Grid Independence

The steady flow around the ATM-wing was computed using the two meshes in Edge and by shock-expansion theory in MATLAB for a sweep of Mach number and of angle-of-attack. The resultant aerodynamic loads were compared, with the results of Mesh 2 used as a baseline.

For all the flight conditions analysed in the parameter sweep, the free-stream pressure and temperature were 101 325 Pa and 288.15K, respectively. An Euler solution was run, with a laminar turbulence model used for the sake of simplicity (the other options available in Edge 5.2.0 being differential turbulence models, DES, and LES models [71]).

The variation of aerodynamic coefficients at Mach 3 with angle-of-attack is shown for the undeformed ATM-wing in Figure 5.22 through Figure 5.24. For this Mach number, it may be seen that good agreement was obtained between 2D shock expansion theory in MATLAB and the Euler computations of Mesh 1 and 2 for $\alpha < 5°$.

In Figure 5.25 and Figure 5.26, the difference in results are compared for Mach 3, with Mesh 2 used as a baseline. The normal force and pitching moment coefficients are calculated to within 5% using shock-expansion theory. The difference in results between Mesh 1 and Mesh 2 were within 1% for all angles-of-attack.

Mesh 2 was used for all subsequent computations as the computation time per iteration was approximately 25% lower than required for Mesh 1.

The reader is referred to Appendix D for further results of the parameter sweep. The difference in results computed by Mesh 1 and Mesh 2 is within 2% for all Mach numbers, within increasingly better agreement as the Mach number is increased.

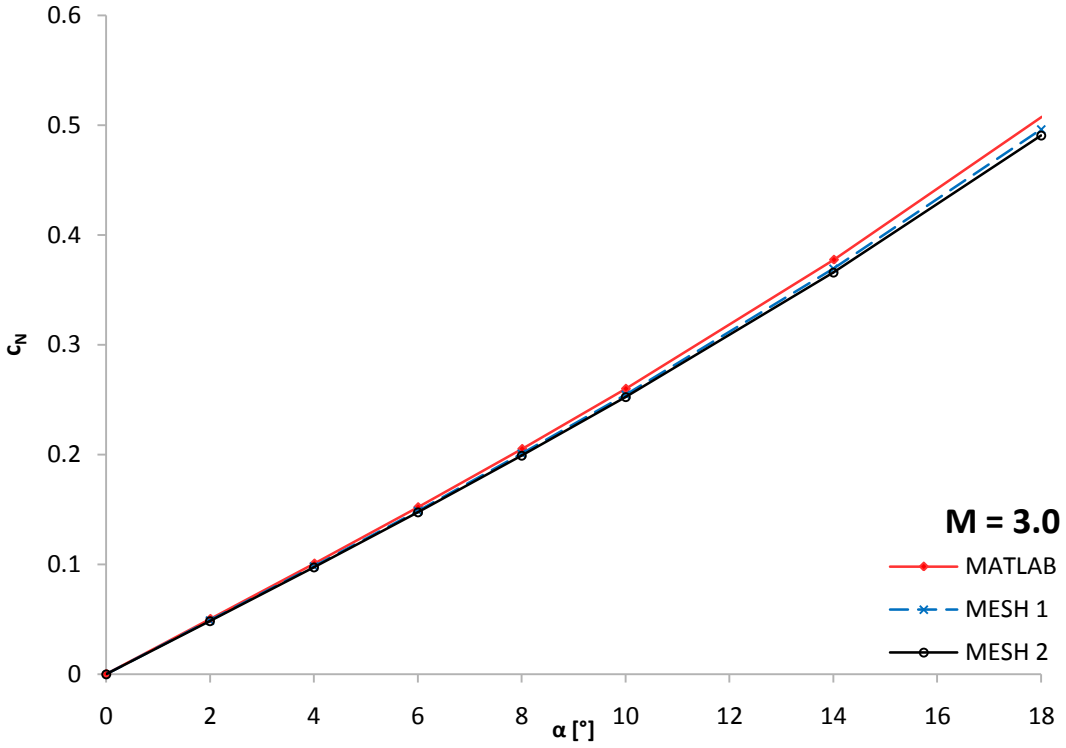


Figure 5.22: Normal Force Coefficient vs Angle-of-Attack, Undeformed ATM-Wing, Mach 3

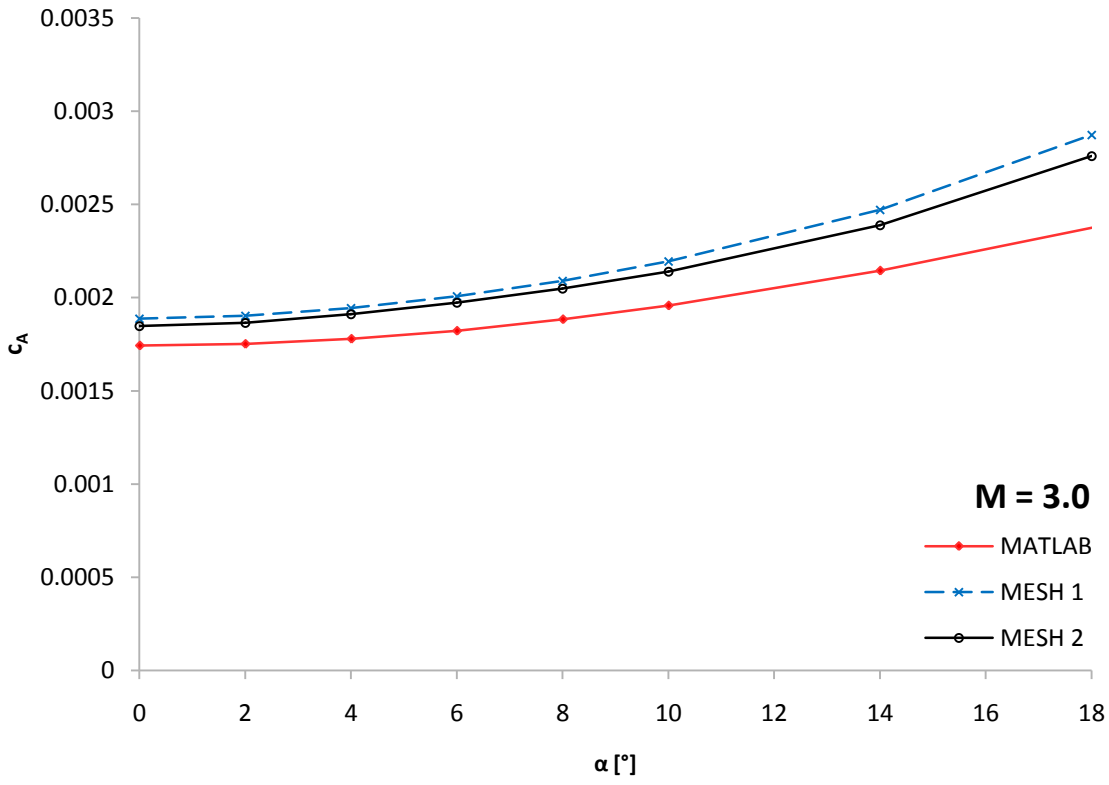


Figure 5.23: Axial Force Coefficient vs Angle-of-Attack, Undeformed ATM-Wing, Mach 3

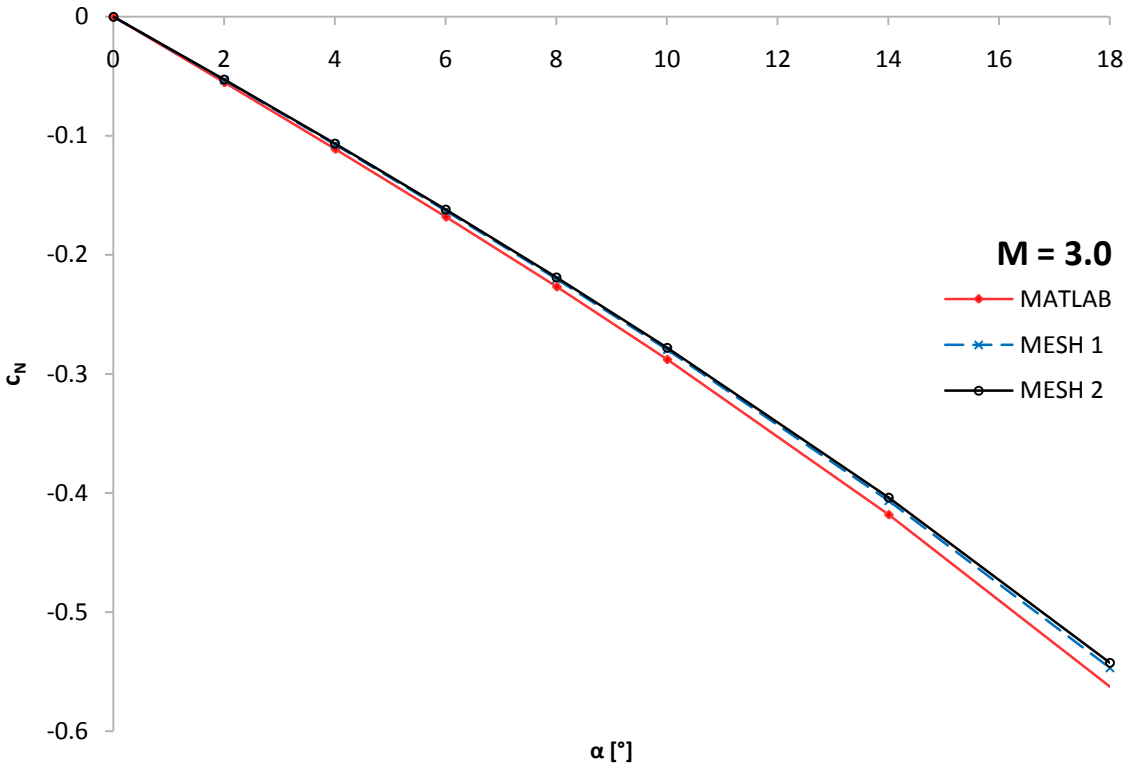


Figure 5.24: Pitching Moment Coefficient (LE root) vs Angle-of-Attack, Undeformed ATM-Wing, Mach 3

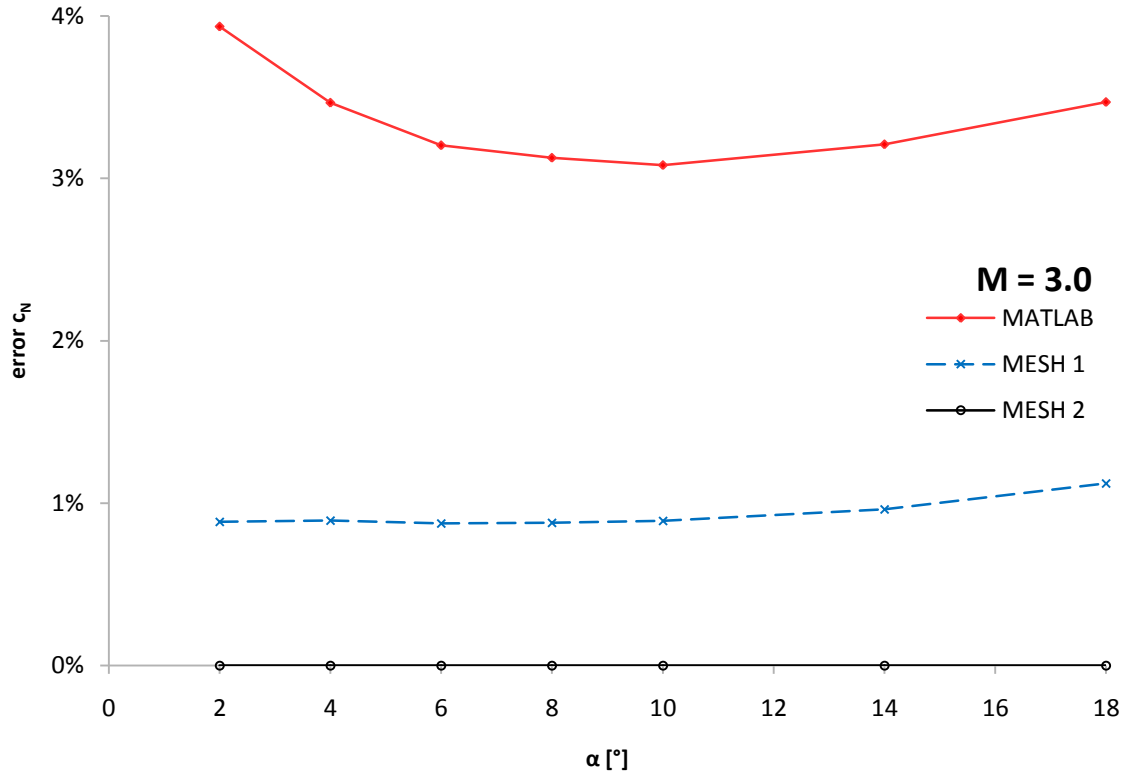


Figure 5.25: Comparison of Normal Force Coefficients, Undeformed A TM-Wing, Mach 3

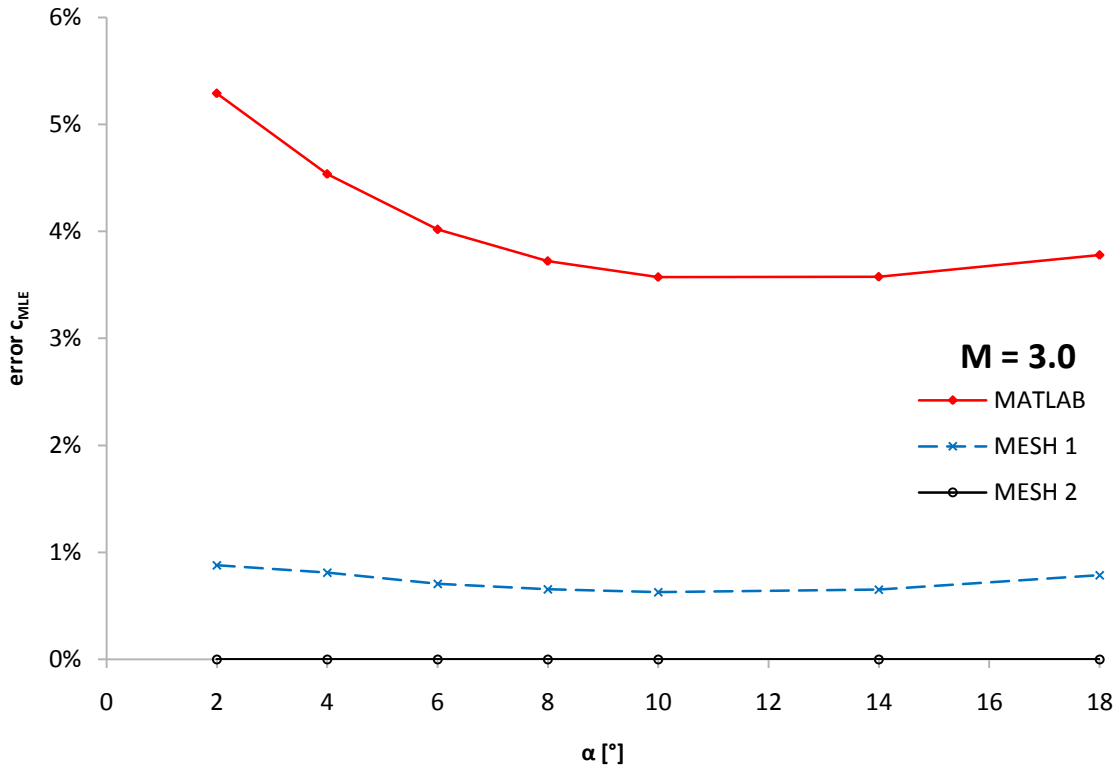


Figure 5.26: Comparison of Pitching Moment Coefficients, Undeformed ATM-Wing, Mach 3

5.4.4 Mesh Deformation

The mesh deformation that was used for the aeroelastic modelling in Edge 5.2.0 utilized a "perturbation field". Producing the perturbation field consisted of the following steps:

1. Specification of moving, sliding and fixed boundaries in the mesh,
2. Interpolation of the structural mode-shapes onto the wetted surface mesh,
3. Writing the boundary displacement (`.bdis`) file associated with each mode-shape, in which the coordinates of the fluid nodes on the wetted surface associated with a specified modal displacement are defined,
4. Meshing of the fluid domain for the deformed geometry of each mode-shape,
5. Calculation of the displacement of each node in the mesh associated with the specified modal displacement.

The perturbation field is defined as follows:

$$\Delta\chi_i = \chi_i - \chi_0 \quad (5.4)$$

in which χ_0 represents the coordinates of the undeformed base mesh, χ_i is the coordinates field of the deformed mesh associated with the specified modal displacement of mode i, and $\Delta\chi_i$ is the perturbation field for mode i.

The use of perturbation field allows the main deformation computation to be performed offline [71], only once for each mode shape. However, the disadvantage is that the deformed mesh, from which the perturbation field is extracted, is computed for an arbitrarily specified modal displacement, rather than for the actual deflection of the moving surface [71]. It is recommended that the modal displacements specified for computation of the mesh deformation be chosen to reflect the order of magnitude of the expected modal responses.

Once the perturbation fields have been computed, the coordinates of each node are computed from calculated modal displacements as [71]:

$$\chi(t) = \chi_0 + \sum_{i=1}^{n_{modes}} x_i(t)\,\Delta\chi_i \quad (5.5)$$

where $\chi(t)$ is the time-variant coordinates field of the mesh, n_{modes} is the number of modes, and $x_i(t)$ is the modal displacement (response) of mode i.

The perturbation field may clearly be seen to be equivalent to the extension of the structural mode-shape into the fluid volume [71].

Whenever the modal displacements change, the new coordinates of the fluid nodes are calculated from Equation (5.5) and the primary grid (mesh) is moved, and the metrics of the dual grid are recomputed [71].

The modal displacements used in the boundary displacement files for the generation of the deformed meshes for the ATM-wing were as given in Table 5.6.

Table 5.6: Modal Displacements used for Mesh Deformation Calculations in Edge

x_1	1 x 10^{-5}
x_2	1 x 10^{-5}
x_3	1 x 10^{-5}
x_4	1 x 10^{-5}

The deformed geometries associated with the given modal displacements are given in Appendix E. The deformed mesh associated with mode 2 (first twisting) is shown along the trailing-edge of the wing in Figure 5.27 and Figure 5.28.

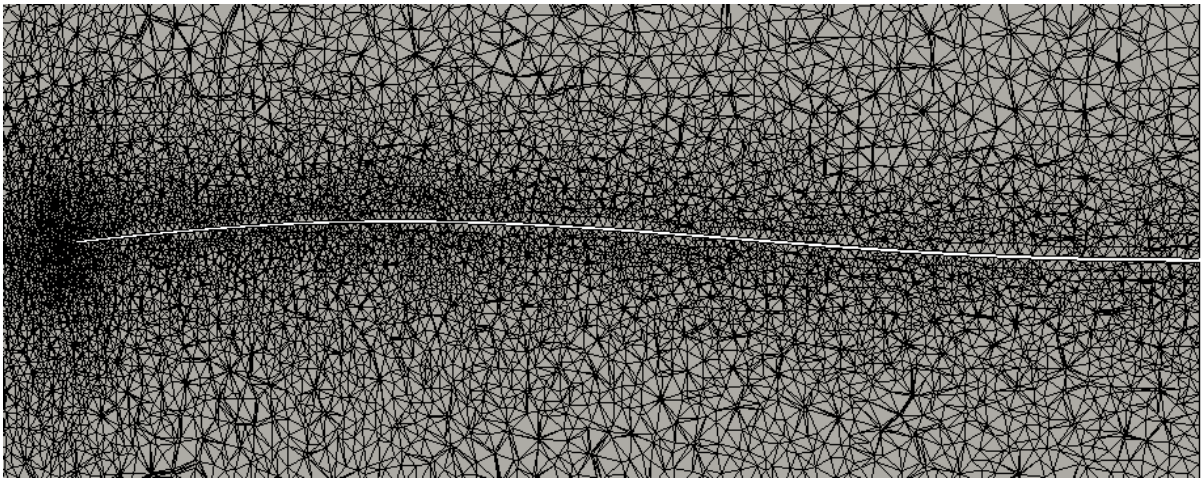


Figure 5.27: Cross-Section of the Deformed Mesh of Mode 2 of the ATM-Wing, Trailing-Edge

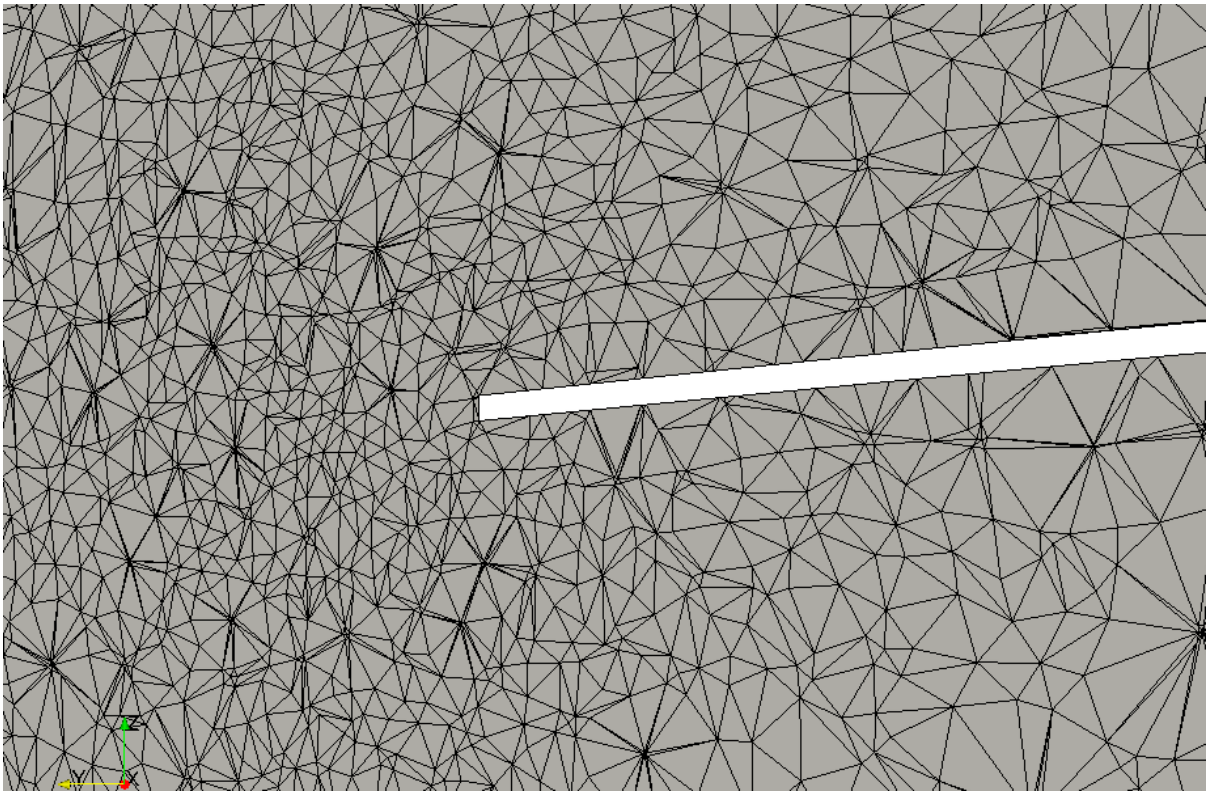


Figure 5.28: Cross-Section of the Deformed Mesh of Mode 2 of the ATM-Wing, Trailing-Edge Tip

5.5 Validation of the Aerodynamic Modelling using Shock-Expansion Theory

The results of shock-expansion theory in MATLAB and of Mesh 2 were seen to give increasingly better agreement as Mach number increases. This is shown in Figure 5.29 and Figure 5.30. Poor agreement is obtained at moderately low Mach numbers ($M = 1.4$), at which the leading-edge shock is close to detachment. At low Mach numbers, the portion of the wing affected by 3D tip effects (including the tip shocks) is larger than at higher Mach numbers -- this reduces the validity of the strip-theory approximation used for the shock-expansion calculations.

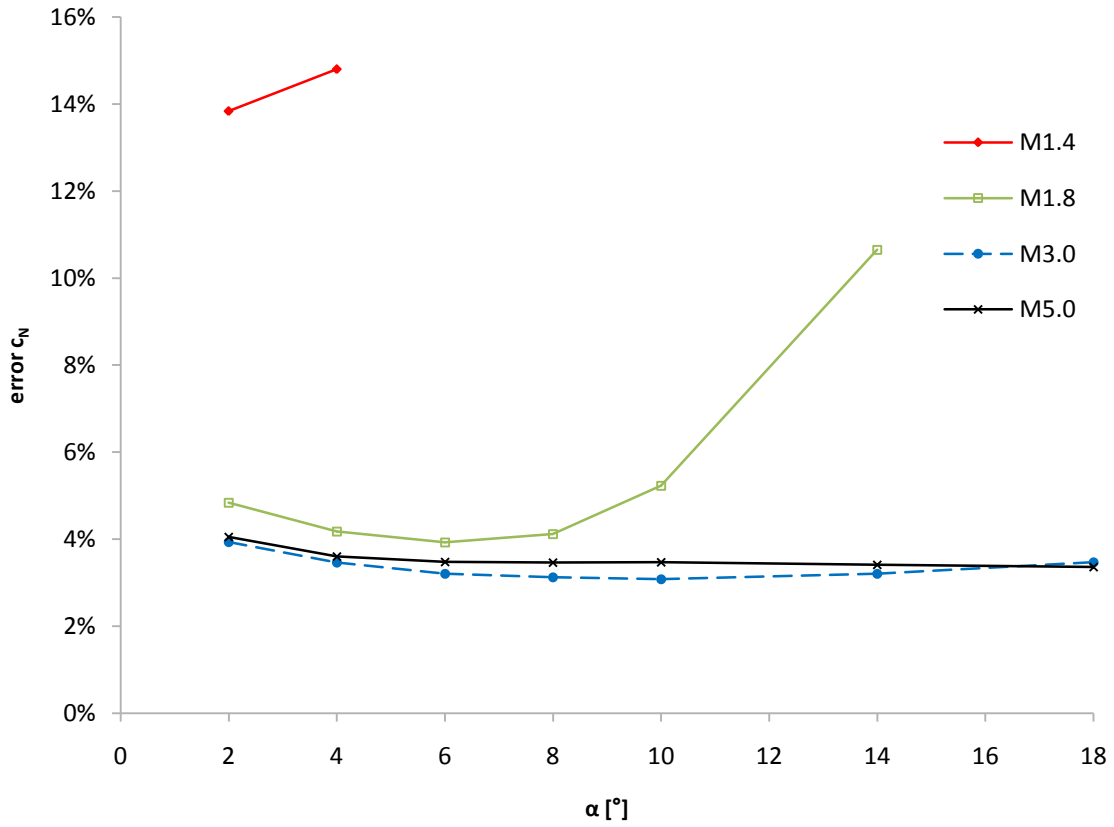


Figure 5.29: Variation in the Accuracy of MATLAB-Based Shock-Expansion Normal Force Coefficient with Angle-of-Attack and Mach Number

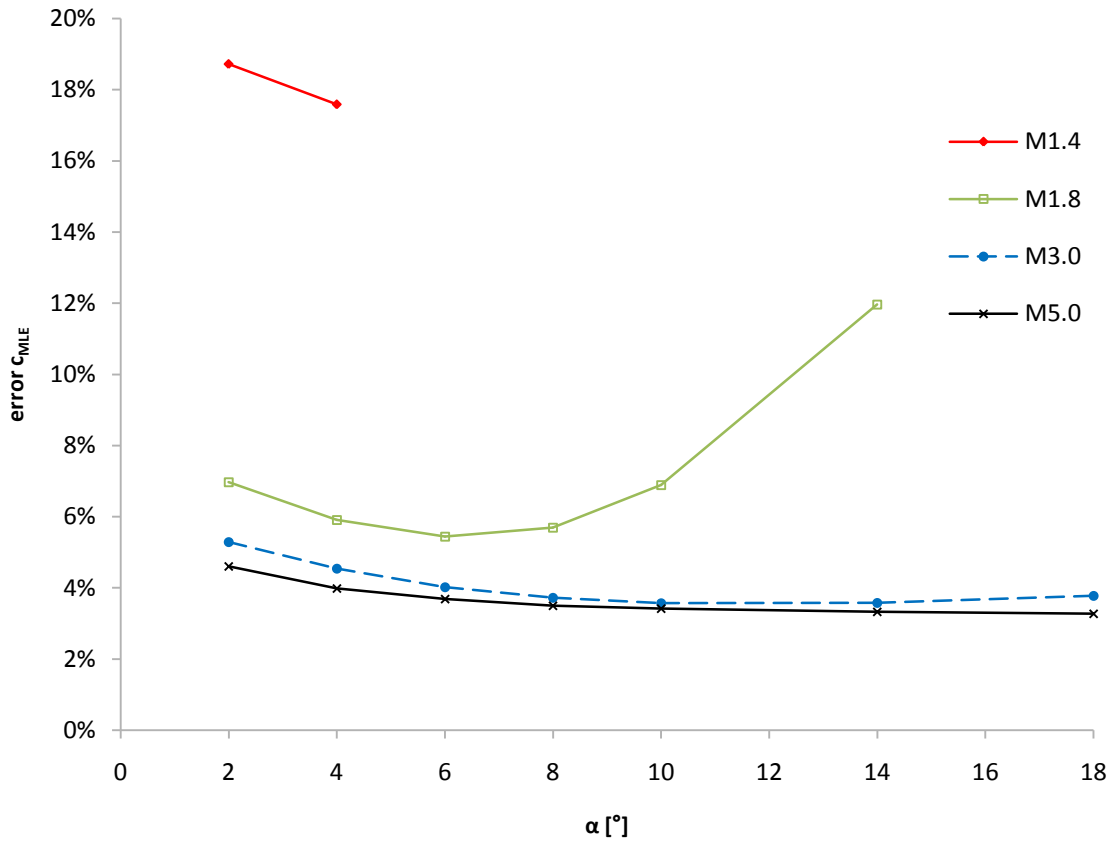


Figure 5.30: Variation in the Accuracy of MATLAB-Based Shock-Expansion Pitching Moment Coefficient with Angle-of-Attack and Mach Number

5.6 Steady Computation of the Undeformed ATM-Wing

The aerodynamic loading on the undeformed ATM-wing was calculated at flight conditions corresponding to the wind-tunnel test conditions of Torii and Matsuzaki's test [55] just before flutter ($M = 2.51,\ q = 108\,\text{kPa}$). The angle-of-attack modelled, $\alpha = 0.5°$, was chosen to avoid numerical issues associated with $\alpha = 0°$ (such as slower convergence of residuals due to small initial residuals). The aerodynamic coefficients as well as the generalized aerodynamic forces were computed in Edge and using the aeroelastic prediction tool developed in MATLAB.

5.6.1 Flow Conditions

The flow conditions were determined for a specified Mach number and dynamic pressure. The free-stream static pressure was determined from:

$$P_\infty = \frac{2q_\infty}{\gamma M_\infty^2} \qquad (5.6)$$

The associated air temperature and density were interpolated from the 1976 US Standard Atmosphere for the determined pressure P_∞. The flow conditions that were used for the computation (q_∞) are compared to the conditions at the experimental flutter point (q_F) are given in Table 5.7.

Table 5.7: Flow Conditions for the ATM-Wing, $M = 2.51$, $\alpha = 0.5°$

	$q_\infty = 108$ kPa	$q_F = 113.5$ kPa
P_∞ [Pa]	24 490	25 740
T_∞ [K]	219.93	222.01
ρ_∞ [kg.m^{-3}]	0.3879	0.4038

5.6.2 Results

The aerodynamic coefficients obtained for the given flow conditions are compared in Table 5.8. The results predicted by shock-expansion theory in MATLAB show a slightly higher aerodynamic stiffness (larger aerodynamic force for the same α).

Also compared in Table 5.8 are the generalized aerodynamic forces (GAFs); it may be seen that a larger difference is shown between the 3D Euler computation of Edge, and the 2D strip-theory shock-expansion computation in MATLAB.

As the GAFs represent the mode-shape weighted integral of lift, and as the deflection of the mode-shapes is generally greatest at the wingtip, it is expected that an important source of the larger error is the tip effects. The effect of the tip shocks is not modelled by 2D the strip-theory application of shock-expansion theory in MATLAB; it is, however, modelled in the 3D Euler computation in Edge. The differences are more heavily weighted when computing the GAFs; the contribution of the tip pressures becomes important due to the weighting provided by the tip displacement of the mode-shape.

Table 5.8: Steady Results for the Undeformed ATM-Wing, $M = 2.51$, $\alpha = 0.5°$, $q = 108$ kPa

Result	Edge	MATLAB	% Error
c_N	1.476 x 10^{-2}	1.529 x 10^{-2}	3.6%
c_A	2.286 x 10^{-3}	2.137 x 10^{-3}	-6.5%
c_M	-1.609 x 10^{-2}	-1.697 x 10^{-2}	5.4%
Q_1 [N.m]	-7.946 x 10^{1}	-8.556 x 10^{1}	7.7%
Q_2 [N.m]	5.349 x 10^{1}	4.612 x 10^{1}	-13.8%
Q_3 [N.m]	-2.259 x 10^{1}	-2.082 x 10^{1}	-7.8%
Q_4 [N.m]	2.486 x 10^{1}	3.078 x 10^{1}	-23.8%

The convergence of the aerodynamic coefficients in the steady computation in Edge is shown in Figure 5.31 through Figure 5.33. The multi-gridding strategy employed in Edge is seen as the four distinct jumps (corresponding to the four grids used) in the coefficients.

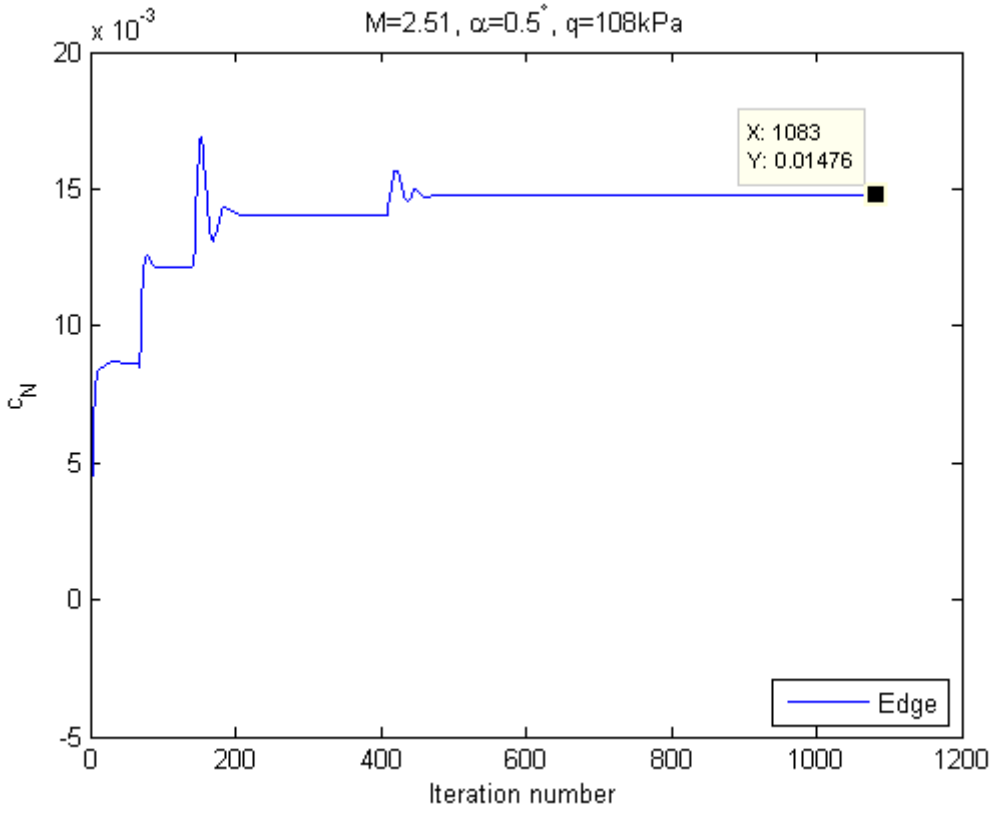


Figure 5.31: Steady Computation for the Undeformed ATM-Wing, Normal Force Coefficient

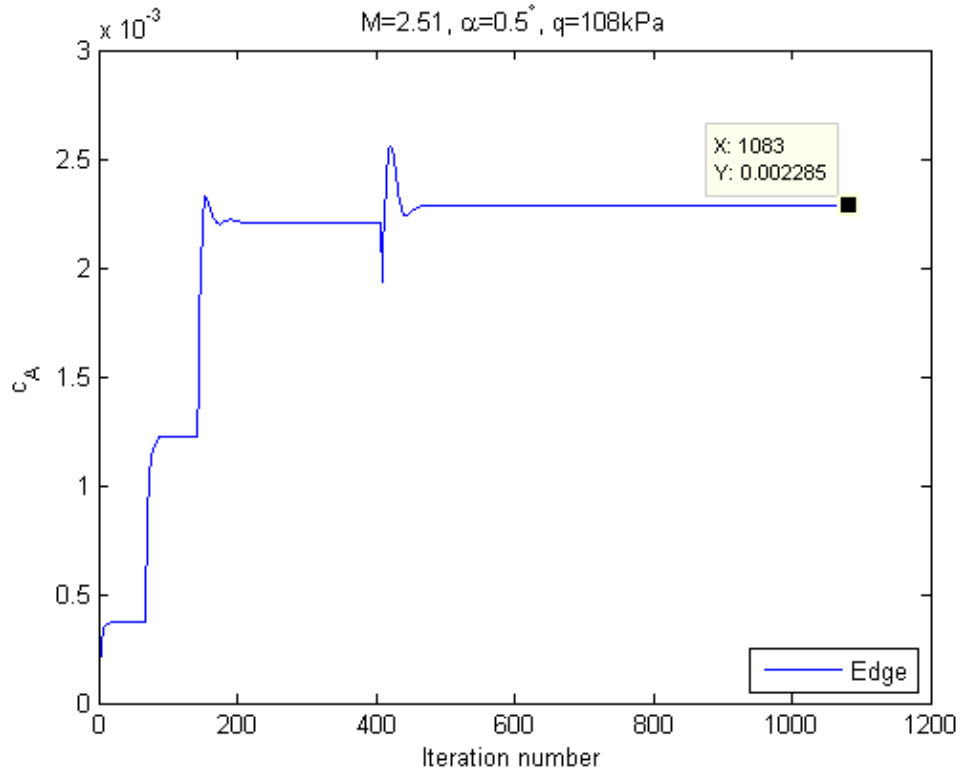


Figure 5.32: Steady Computation for the Undeformed ATM-Wing, Axial Force Coefficient

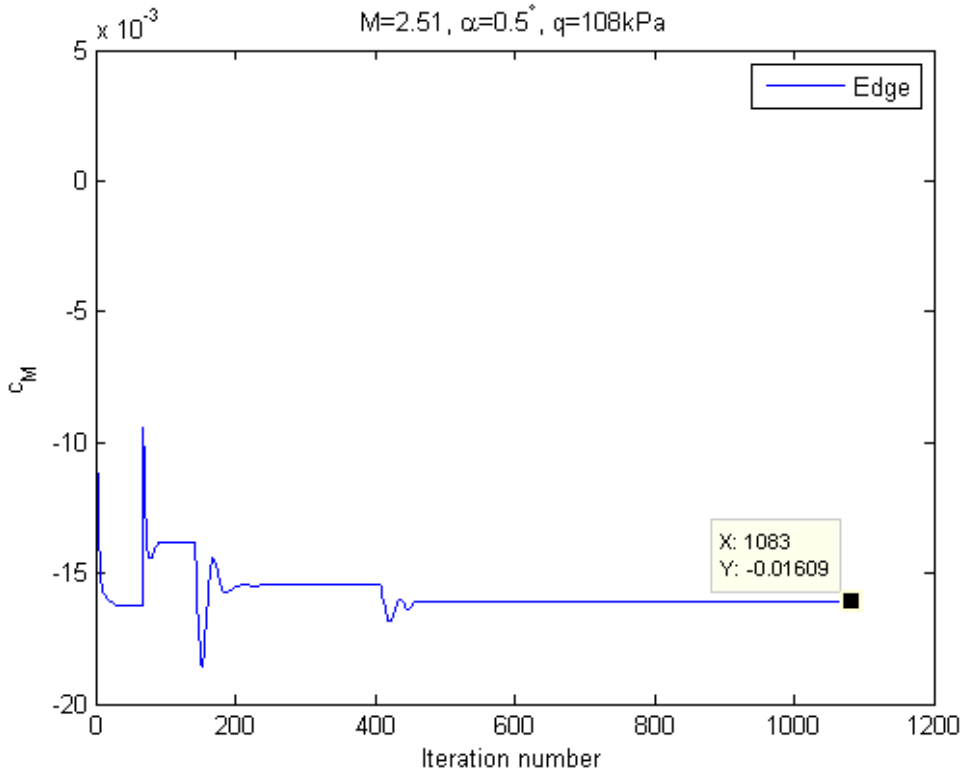


Figure 5.33: Steady Computation for the Undeformed ATM-Wing, Pitching Moment (LE root) Coefficient

In Figure 5.34, the chordwise pressure distribution given by Edge is compared to shock-expansion theory at the spanwise station $y = 0.15\text{m}$; this station corresponds to approximately the 68% span position. Good agreement is obtained, suggesting that the 2D strip-theory approximation is valid at this point. It is expected that better agreement would be obtained with a refined mesh, with the appropriate fineness over the bevel of the leading and trailing edges. The flowfield at this station is shown in Figure 5.35.

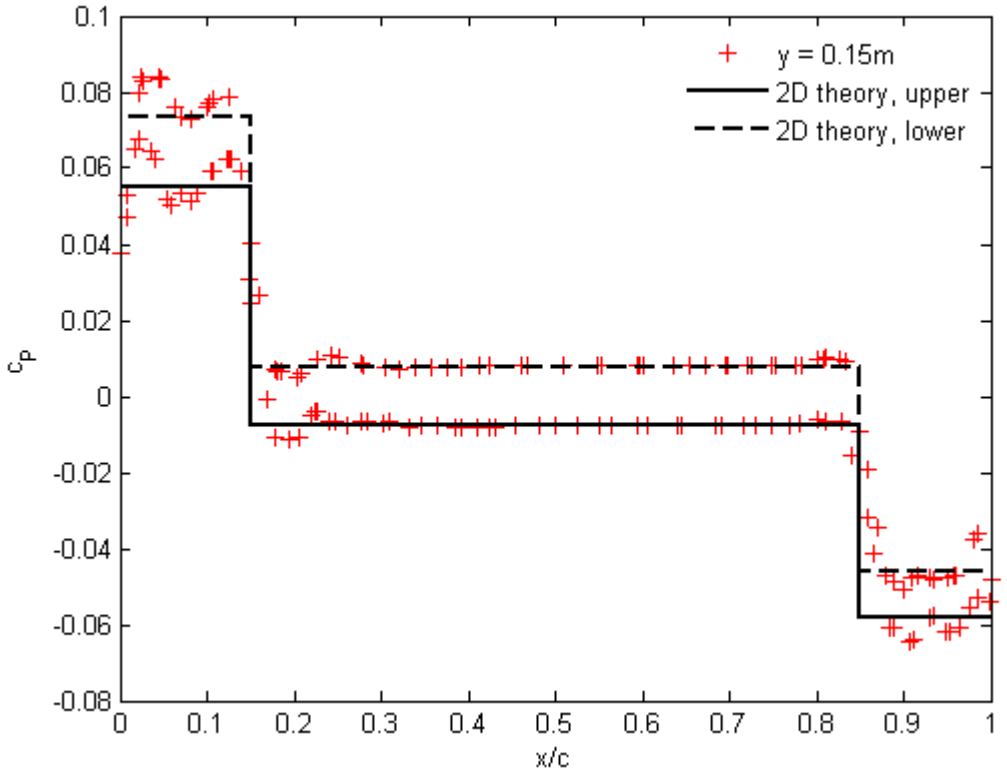


Figure 5.34: Steady Computation for the Undeformed ATM-Wing, Chordwise Pressure Distribution

The spanwise distribution of the normal force coefficient is given in Figure 5.36; again, the 3D Euler computation of Edge is compared to the 2D strip-theory shock-expansion calculation in MATLAB. It may be seen that at the wingtip and at the wing root, the normal force is lower than predicted by 2D strip theory. This suggests that tip effects are important in these regions. This is confirmed by the visualization of the flowfield over the expansion (upper) surface of the wing in Figure 5.37, in which the tip shocks / expansion fans and the leading-edge root expansion fan are shown by the pressure contour lines.

The extent of the leading-edge shock in the fluid domain is shown in Figure 5.38,.

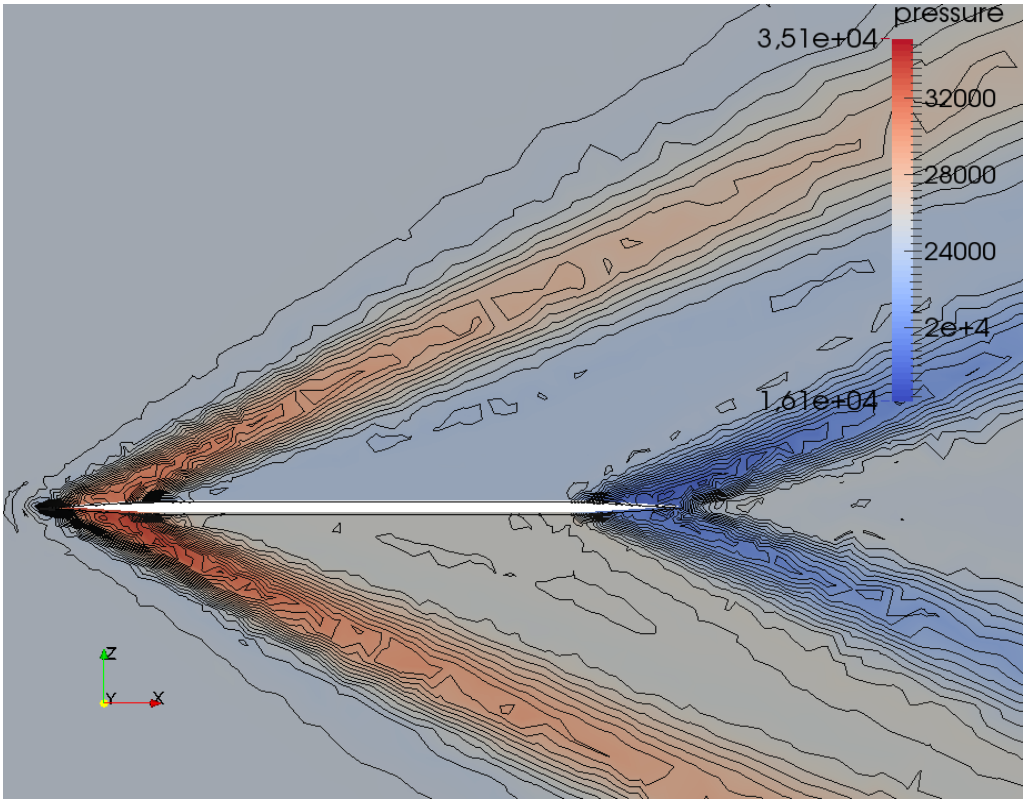


Figure 5.35: Steady Computation, Undeformed ATM-Wing, Shock Front, $\boldsymbol{M = 2.51,\ \alpha = 0.5°,\ q = 108\ \text{kPa},\ y = 0.15\text{m}}$

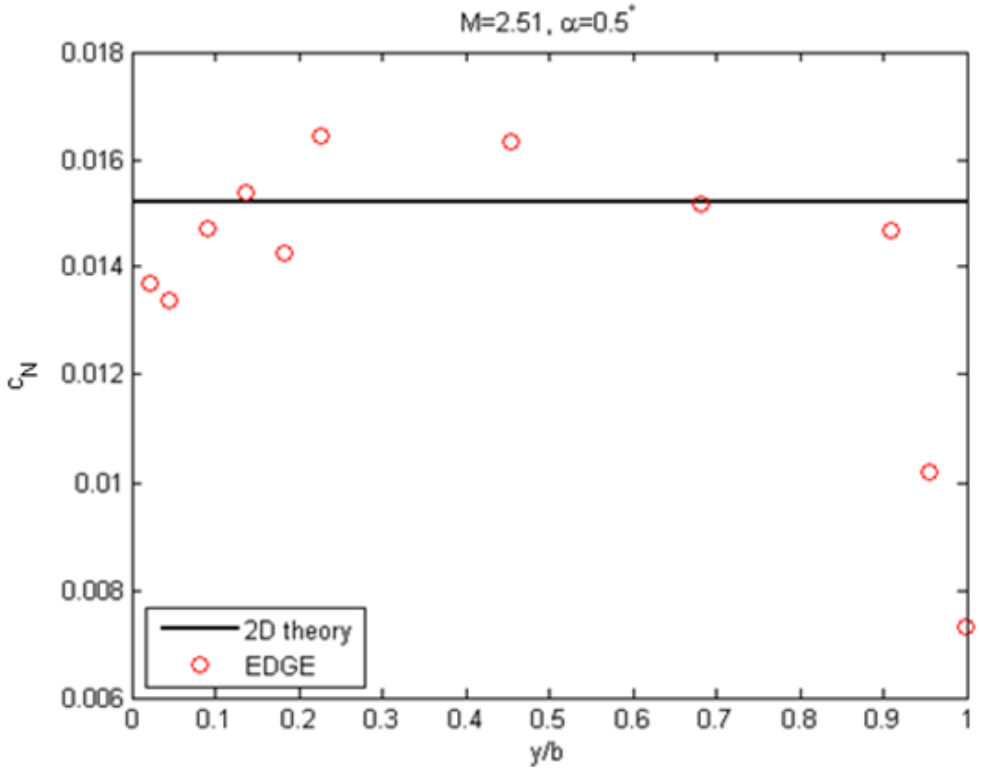


Figure 5.36: Steady Computation for the Undeformed ATM-Wing, Spanwise Normal Force Distribution

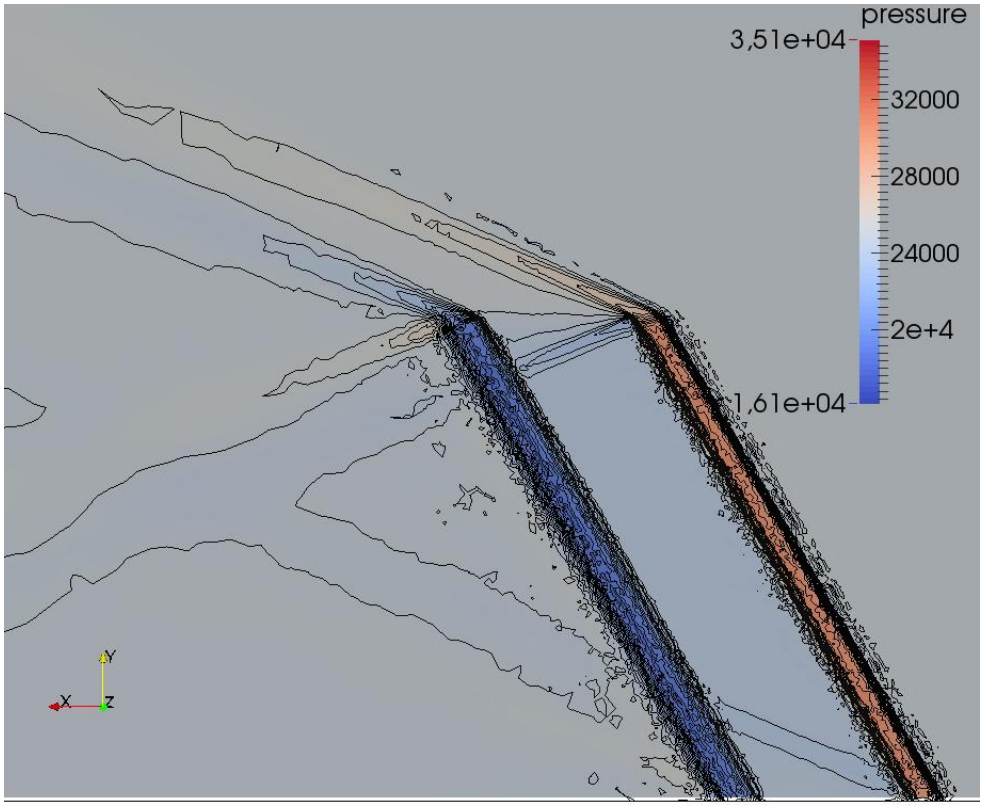


Figure 5.37: Steady Computation, Undeformed ATM-Wing, Planform, $\boldsymbol{M = 2.51,\ \alpha = 0.5°,\ q = 108\ \text{kPa},\ z = 0.002\text{m}}$

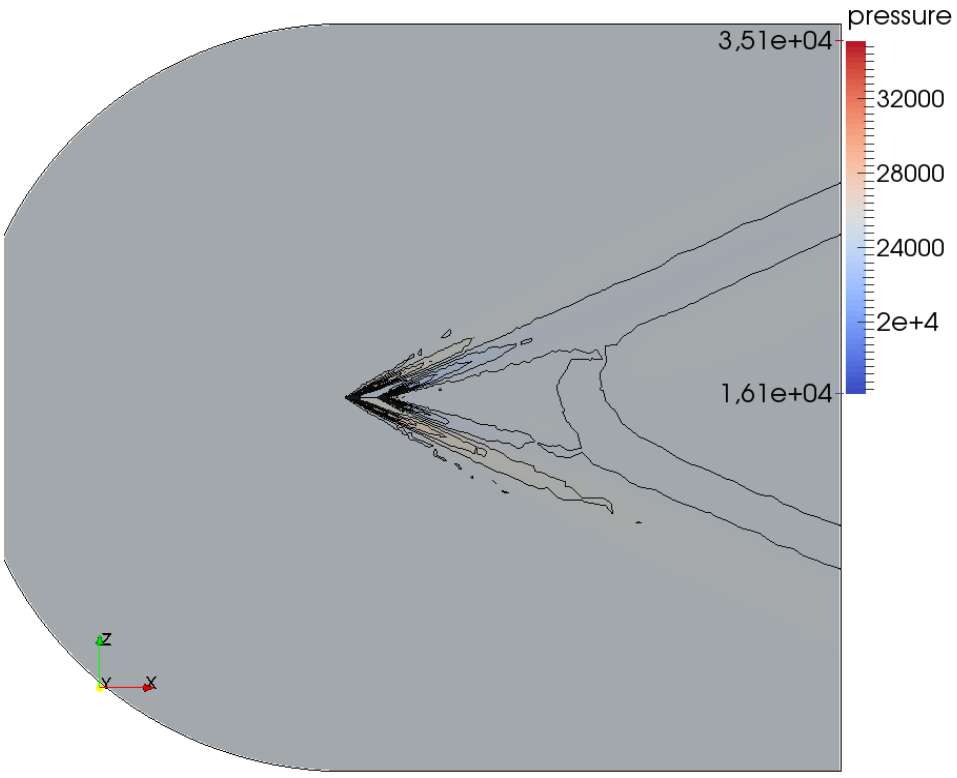


Figure 5.38: Steady Computation, Undeformed ATM-Wing, Shock Front, $\boldsymbol{M = 2.51,\ \alpha = 0.5°,\ q = 108\ \text{kPa},\ y = 0.005\text{m}}$

5.7 Transient Computation of Static Aeroelastic Deflection

The steady aeroelastic deformation of the ATM-wing at $M = 2.51, \alpha = 0.5°, q = 108$ kPa was computed from the initial solution obtained for the undeformed wing (Section 5.6). The solution was obtained through time-marching the coupled aeroelastic equations with heavy artificial damping ($\zeta \approx 0.9 - 1$) until convergence.

The computations of the developed aeroelastic prediction tool in MATLAB were performed using 3rd order local piston theory, with the steady pressures obtained from shock-expansion theory (with a strip-theory approximation).

The time-step was chosen such that $\Delta t = \frac{T_6}{\pi^2} = 1.306 \text{ x } 10^{-4}$ s. to ensure numerical stability of the Newmark-β time-marching scheme for up to the 6th mode. This corresponds to $\frac{\Delta t}{T_4} \approx 0.054$.

5.7.1 Results

The steady-state aerodynamic coefficients obtained for the elastic ATM-wing at the given flow conditions are compared in Table 5.9. The normal force and pitching moment (about the leading-edge root) coefficients for the elastic wing show very good agreement, both within 1% difference.

The GAFs and the modal displacements in Table 5.9 show similar trends, with the displacement of the first mode and its GAF being computed in MATLAB to within 2% of the results given Edge. The error in the displacements and GAFs of the higher modes, however, is significantly larger.

The transient computations of the aerodynamic coefficients for the elastic ATM-wing are shown in Figure 5.39 through Figure 5.41.

The transient computations of the modal displacements for the elastic ATM-wing are shown in Figure 5.42 through Figure 5.45.

The transient computations of the generalized aerodynamic forces for the elastic ATM-wing are shown in Figure 5.46 through Figure 5.49.

Table 5.9: Steady Results for the Elastic ATM-Wing, $M = 2.51, \alpha = 0.5°, q = 108$ kPa

Result	Edge	MATLAB (time-marching)	% Error
c_N	5.719 x 10^{-3}	5.737 x 10^{-3}	0.31%
c_A	2.262 x 10^{-3}	2.147 x 10^{-3}	-5.1%
c_M	-4.095 x 10^{-3}	-4.898 x 10^{-3}	-0.17%
x_1	-5.696 x 10^{-4}	-5.598 x 10^{-4}	-1.7%
x_2	2.196 x 10^{-5}	1.903 x 10^{-5}	-13.4%
x_3	-9.083 x 10^{-6}	-7.282 x 10^{-6}	-19.8%
x_4	2.723 x 10^{-6}	2.394 x 10^{-6}	-12.1%
Q_1 [N.m]	-1.563 x 10^{1}	-1.540 x 10^{1}	-1.5%
Q_2 [N.m]	1.892 x 10^{1}	1.688 x 10^{1}	-10.8%
Q_3 [N.m]	-1.327 x 10^{1}	-1.117 x 10^{1}	-15.8%
Q_4 [N.m]	1.855 x 10^{1}	1.949 x 10^{1}	-5.1%

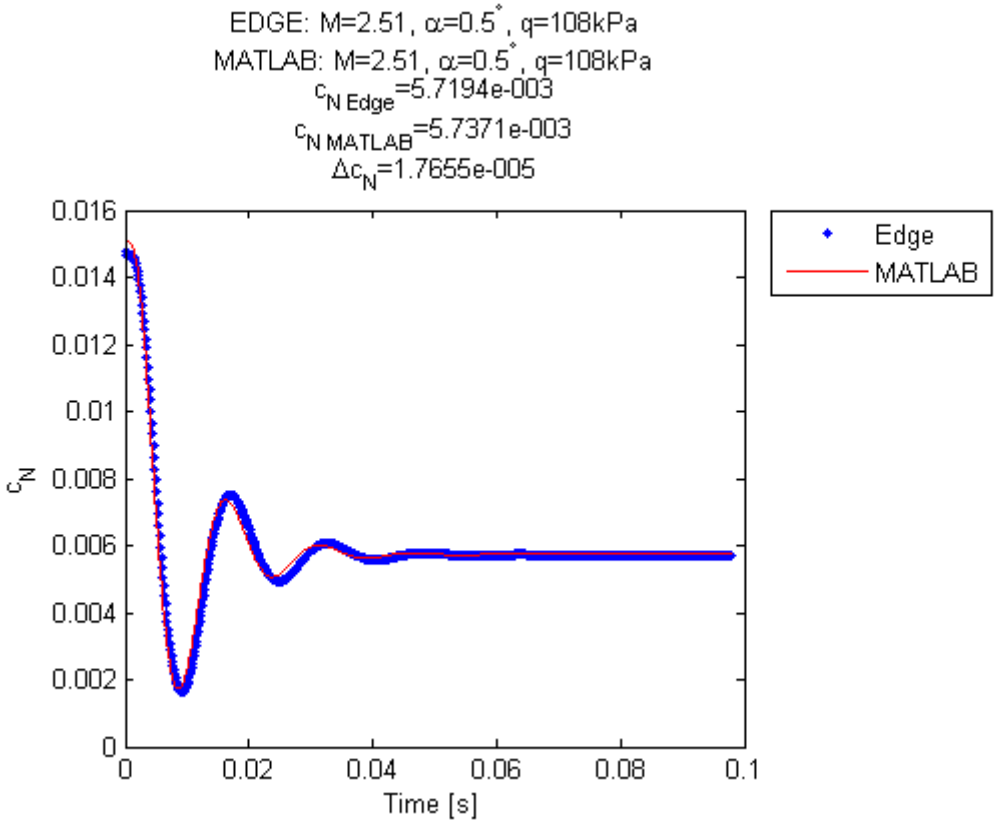


Figure 5.39: Determination of Steady-State Normal Force Coefficient for the Elastic ATM-Wing

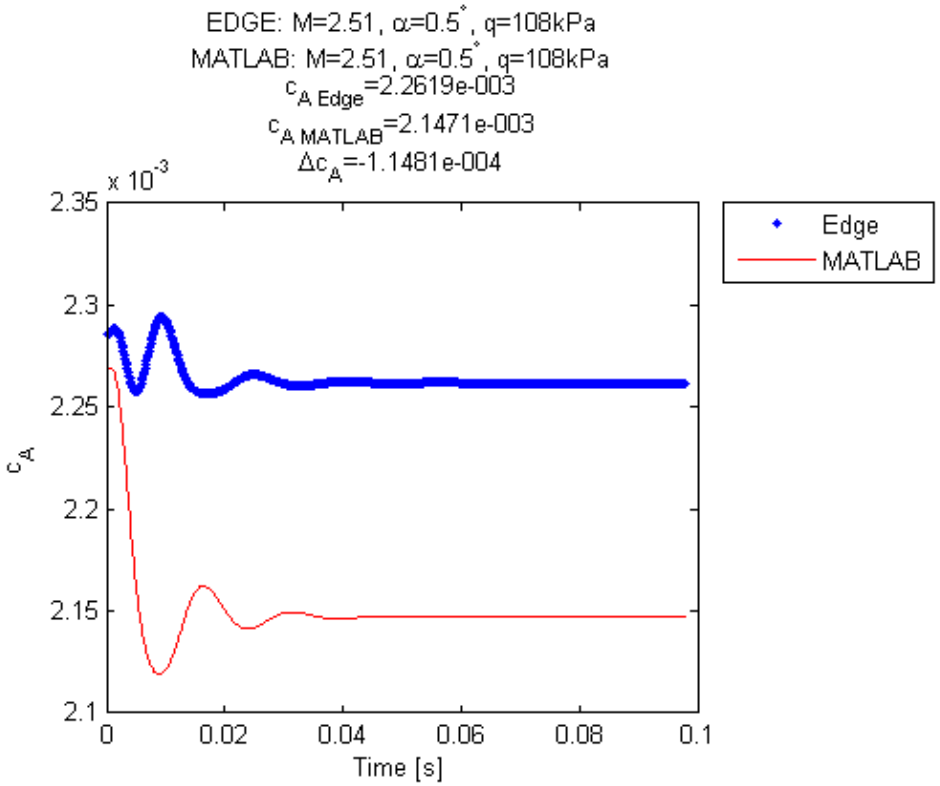


Figure 5.40: Determination of Steady-State Axial Force Coefficient for the Elastic ATM-Wing

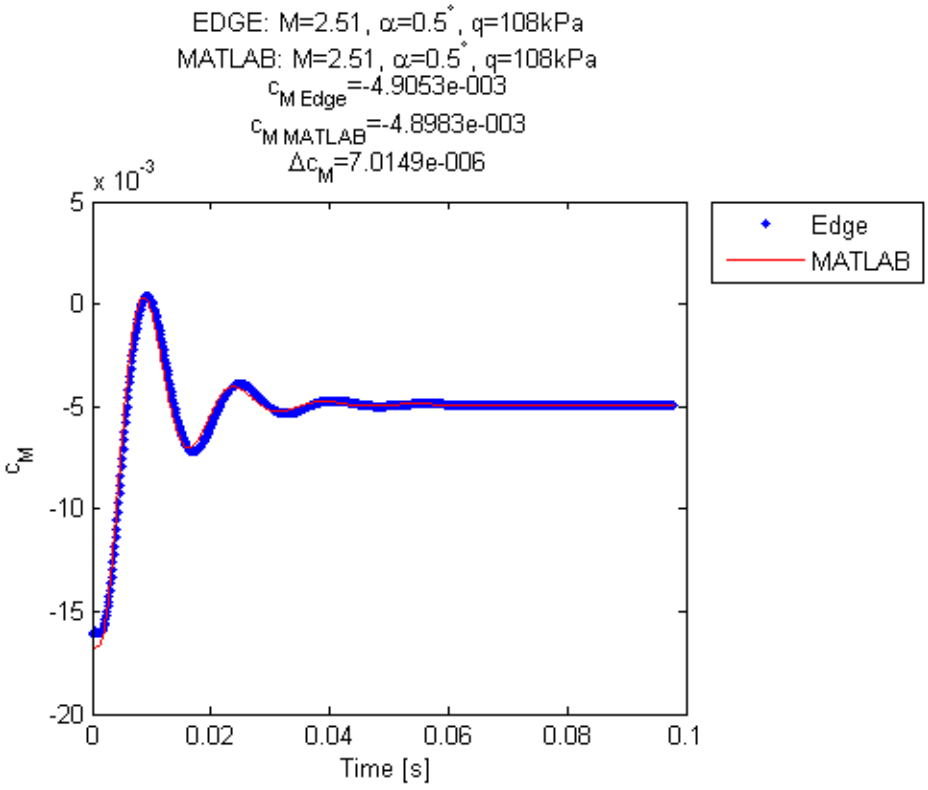


Figure 5.41: Determination of Steady-State Pitching Moment (LE root) Coefficient for the Elastic ATM-Wing

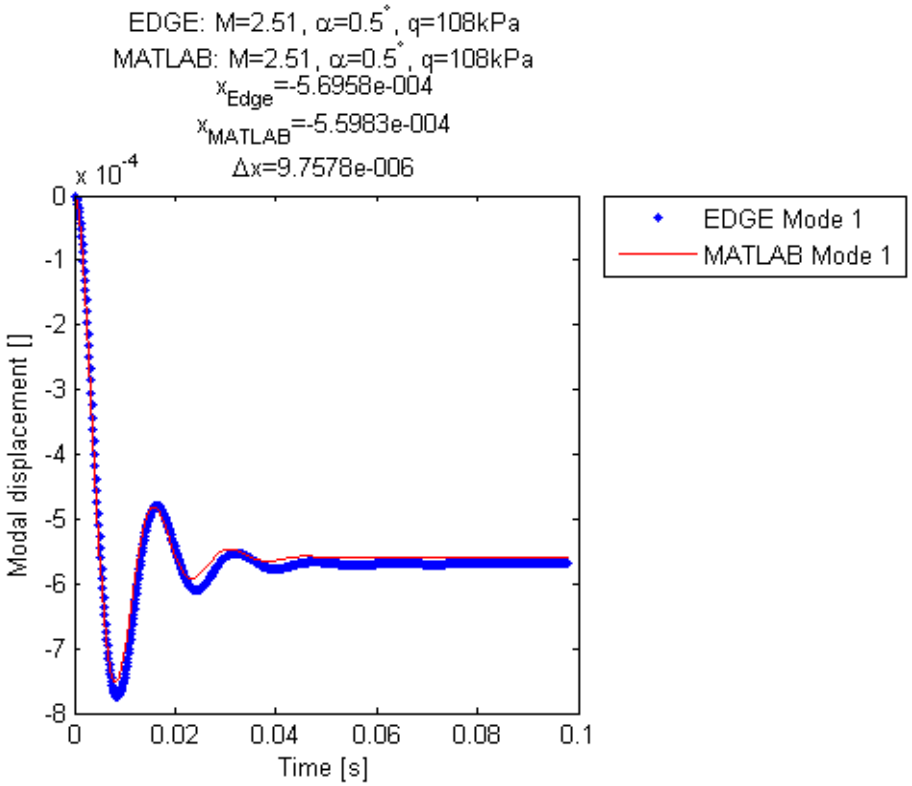


Figure 5.42: Determination of Steady-State Displacement for the Elastic ATM-Wing, Mode 1

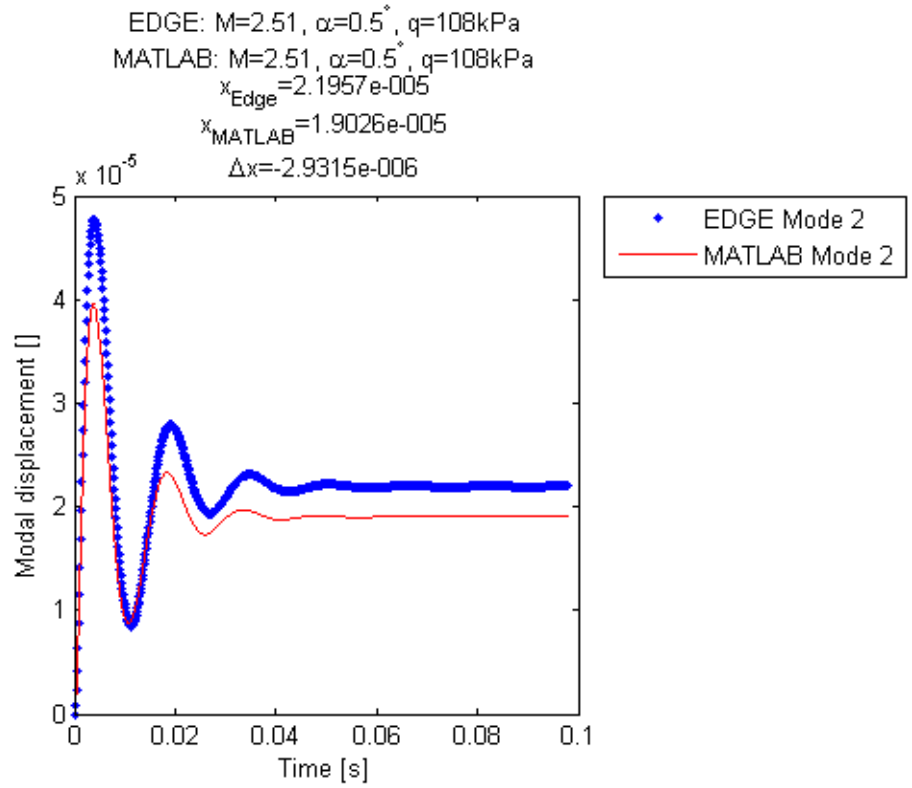


Figure 5.43: Determination of Steady-State Displacement for the Elastic ATM-Wing, Mode 2

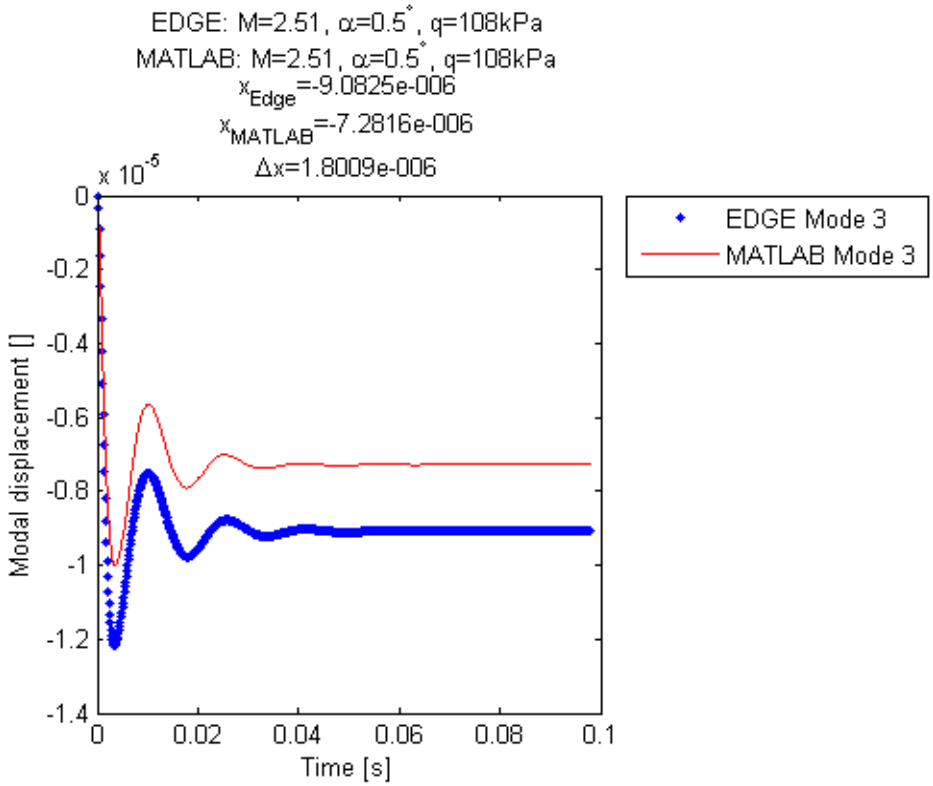


Figure 5.44: Determination of Steady-State Displacement for the Elastic ATM-Wing, Mode 3

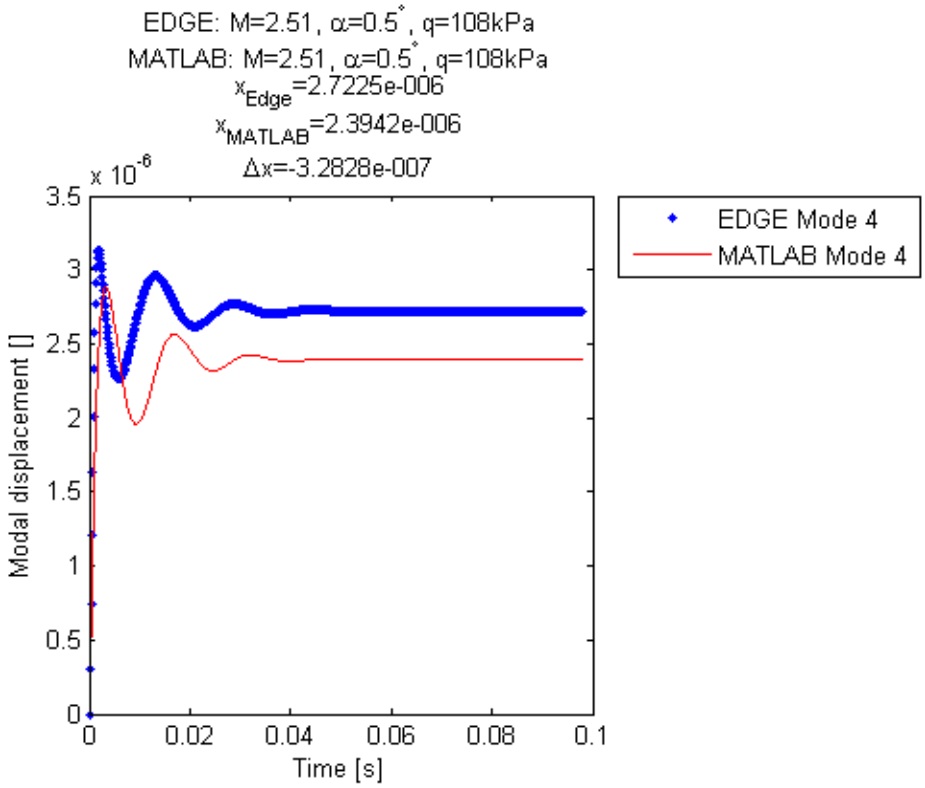


Figure 5.45: Determination of Steady-State Displacement for the Elastic ATM-Wing, Mode 4

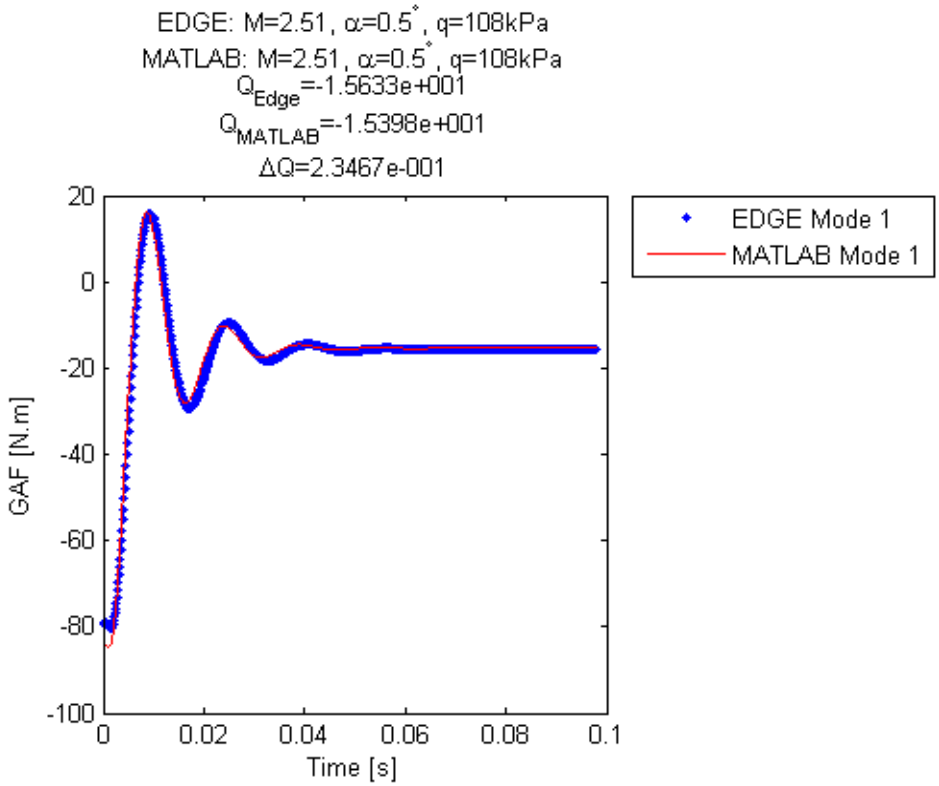


Figure 5.46: Determination of Steady-State GAFs for the Elastic ATM-Wing, Mode 1

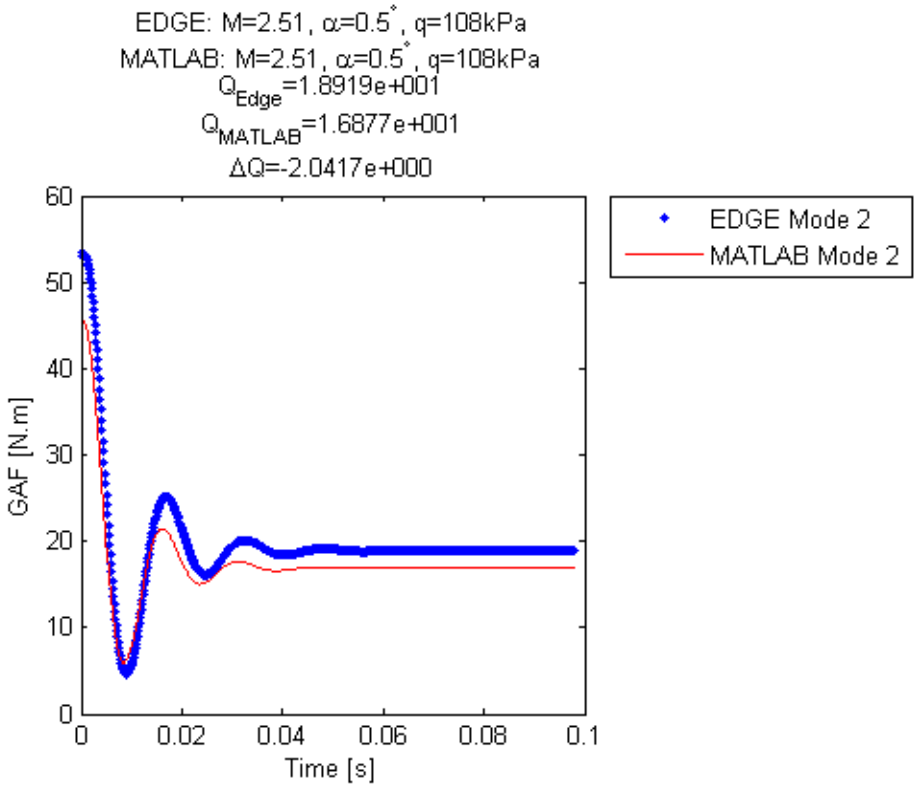


Figure 5.47: Determination of Steady-State GAFs for the Elastic ATM-Wing, Mode 2

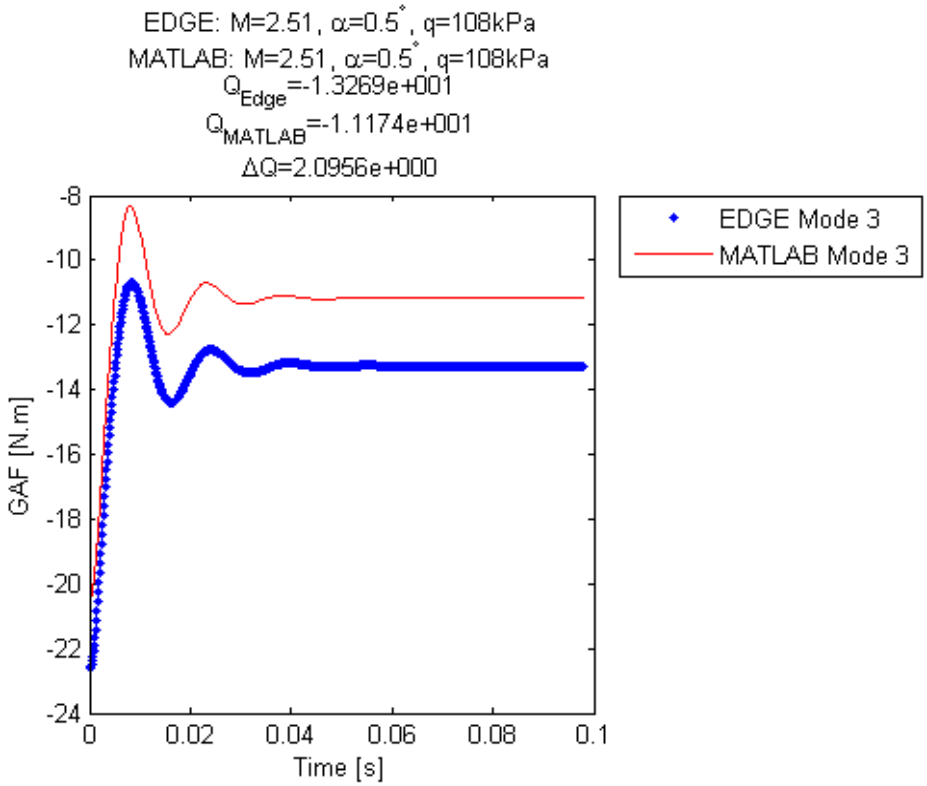


Figure 5.48: Determination of Steady-State GAFs for the Elastic ATM-Wing, Mode 3

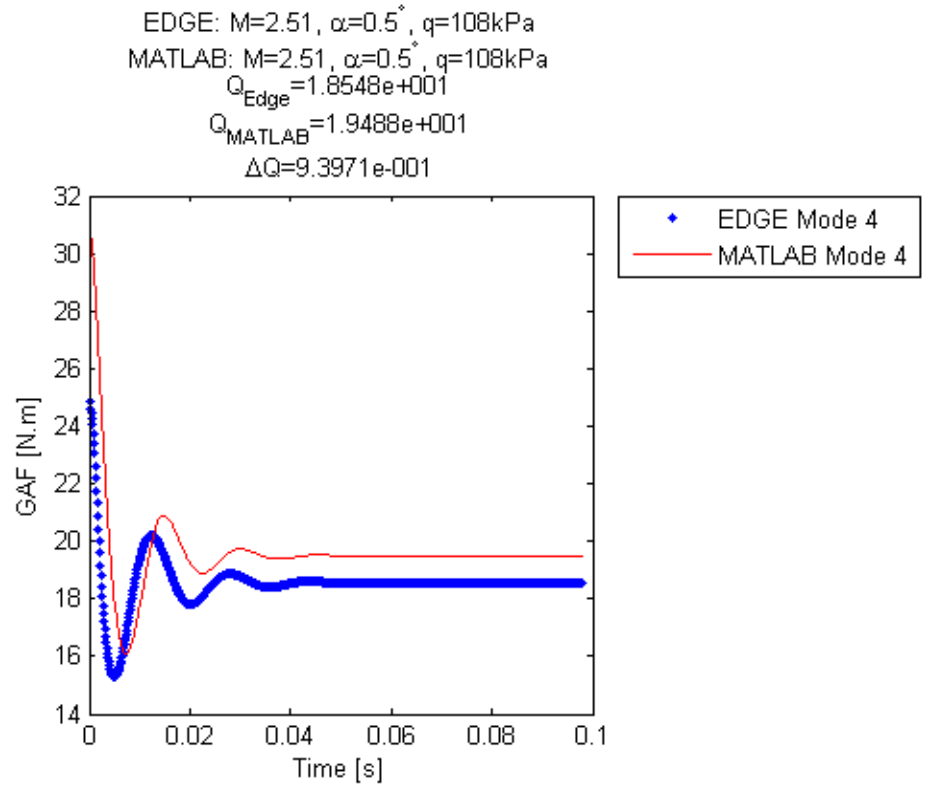


Figure 5.49: Determination of Steady-State GAFs for the Elastic ATM-Wing, Mode 4

5.8 Transient Computations of Prescribed Modal Motion of the Model

Computations were run to determine the aerodynamic response to prescribed step modal displacements. The change in the GAFs in response to modal displacement were used in Section 5.9 to linearize the GAFs and find their derivatives with respect to modal displacement -- effectively allowing the columns of the aerodynamic stiffness matrix to be extracted.

The prescribed modal displacements were about the steady-state deformed geometry of the elastic ATM-wing, for the same flow conditions of $M = 2.51, \alpha = 0.5°, q = 108$ kPa. The displacements of the first mode were scaled by a factor of 5 relative to the higher modes in order to give similar magnitudes of wingtip displacement. The same time-step was used for all the transient computations, with $\Delta t = 1.306 \text{ x } 10^{-4}$ s as in Section 5.7.

The displacements were stepped "up" (positive increment) and "down" (negative increment) to investigate nonlinearity with modal displacement.

The effect of the linearization step size (amplitude of the prescribed step) was investigated by considering the response for displacements differing by an order of magnitude ($\Delta x = 1 \text{ x } 10^{-5}$ vs $\Delta x = 1 \text{ x } 10^{-6}$).

Finally, the response history of the 3D Euler computations in Edge were compared with the 2D strip-theory shock-expansion calculations in MATLAB. In interpreting the results, it is important to recall that the modal displacements (and GAFs) in Edge are time-averaged over three points, as in Equation (5.2); thus, although a step input is prescribed, a pure step is not achieved due to the time-averaging of displacements. The modelling of aerodynamics using SE/LPT in MATLAB does not account for aerodynamic lag effects in the flow resulting from the instantaneous change in geometry.

The results of the computations are summarized on the pages that follow; further results from the computations may be found in Appendix F.

The results in Section 5.8.1 through Section 5.8.4 will show that better agreement of the SE/LPT computations in MATLAB is obtained for the larger prescribed step displacement. Even so, the accuracy of the change in GAFs predicted by SE/LPT is generally very poor for the GAFs of modes other than the excited (prescribed) mode. This leads to large errors in the prediction of the off-diagonal terms in the aerodynamic stiffness matrix (Section 5.9).

5.8.1 Prescribed Motion of Mode 1 Only

The percentage difference between the results obtained by Edge and by MATLAB for the prescribed motion of mode 1 are given in Table 5.10. An example of the response in given in Figure 5.50.

Table 5.10: Accuracy of MATLAB Computation for the ATM-Wing, Mode 1 Prescribed Step

	$\lvert\Delta x_1\rvert = 5 \text{ x } 10^{-5}$		$\lvert\Delta x_1\rvert = 5 \text{ x } 10^{-6}$	
	up	down	up	down
% Error Δc_N	9.4%	7.2%	20.6%	-1.8%
% Error Δc_A	-9.3%	13.8%	-94.6%	76.9%
% Error Δc_M	11.7%	9.3%	18.4%	-5.4%
% Error ΔQ_1	12.1%	10.3%	6.8%	-12.0%
% Error ΔQ_2	-19.0%	-18.6%	-28.2%	-24.5%
% Error ΔQ_3	37.5%	19.8%	198%	19.7%
% Error ΔQ_4	228%	220%	449%	350.1%

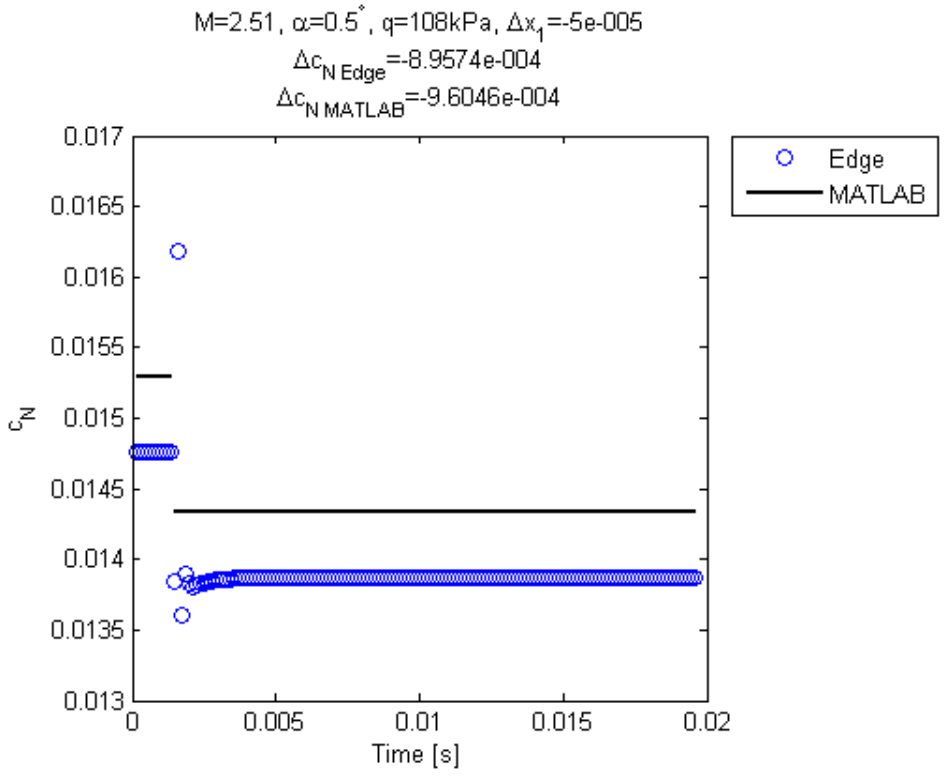


Figure 5.50: Aerodynamic Response of the ATM-Wing to Prescribed Step Modal Displacement, Mode 1

5.8.2 Prescribed Motion of Mode 2 Only

The percentage difference between the results obtained by Edge and by MATLAB for the prescribed motion of mode 2 are given in Table 5.11. An example of the response in given in Figure 5.51.

Table 5.11: Accuracy of MATLAB Computation for the ATM-Wing, Mode 2 Prescribed Step

	$\lvert\Delta x_2\rvert = 5 \text{ x } 10^{-5}$		$\lvert\Delta x_2\rvert = 5 \text{ x } 10^{-6}$	
	up	down	up	down
% Error Δc_N	17.8%	16.0%	72.9%	39.9%
% Error Δc_A	-13.9%	22.8%	-95.0%	48.6%
% Error Δc_M	20.9%	19.3%	73.0%	42.5%
% Error ΔQ_1	21.4%	20.2%	60.3%	40.3%
% Error ΔQ_2	-50.6%	-50.4%	-49.9%	-17.9%
% Error ΔQ_3	510.9%	356.6%	4540%	74.0%
% Error ΔQ_4	-57.0%	-55.5%	-102%	15300%

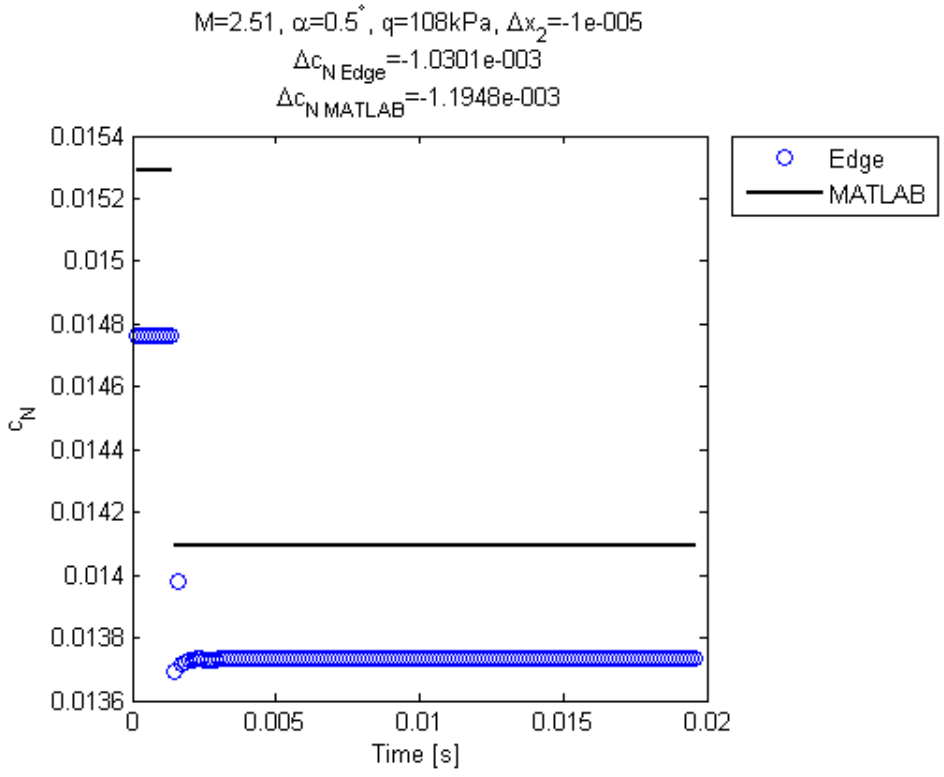


Figure 5.51: Aerodynamic Response of the ATM-Wing to Prescribed Step Modal Displacement, Mode 2

5.8.3 Prescribed Motion of Mode 3 Only

The percentage difference between the results obtained by Edge and by MATLAB for the prescribed motion of mode 1 are given in Table 5.12. An example of the response in given in Figure 5.52.

Table 5.12: Accuracy of MATLAB Computation for the ATM-Wing, Mode 3 Prescribed Step

	$\lvert\Delta x_3\rvert = 5 \text{ x } 10^{-5}$		$\lvert\Delta x_3\rvert = 5 \text{ x } 10^{-6}$	
	up	down	up	down
% Error Δc_N	11.9%	10.5%	54.8%	39.9%
% Error Δc_A	-8.2%	12.6%	-76.2%	48.6%
% Error Δc_M	14.5%	13.1%	58.0%	42.5%
% Error ΔQ_1	15.9%	14.8%	53.2%	40.3%
% Error ΔQ_2	-21.6%	-21.5%	-21.0%	-17.9%
% Error ΔQ_3	15.8%	12.1%	115%	74.0%
% Error ΔQ_4	8910%	11100%	18100%	15300%

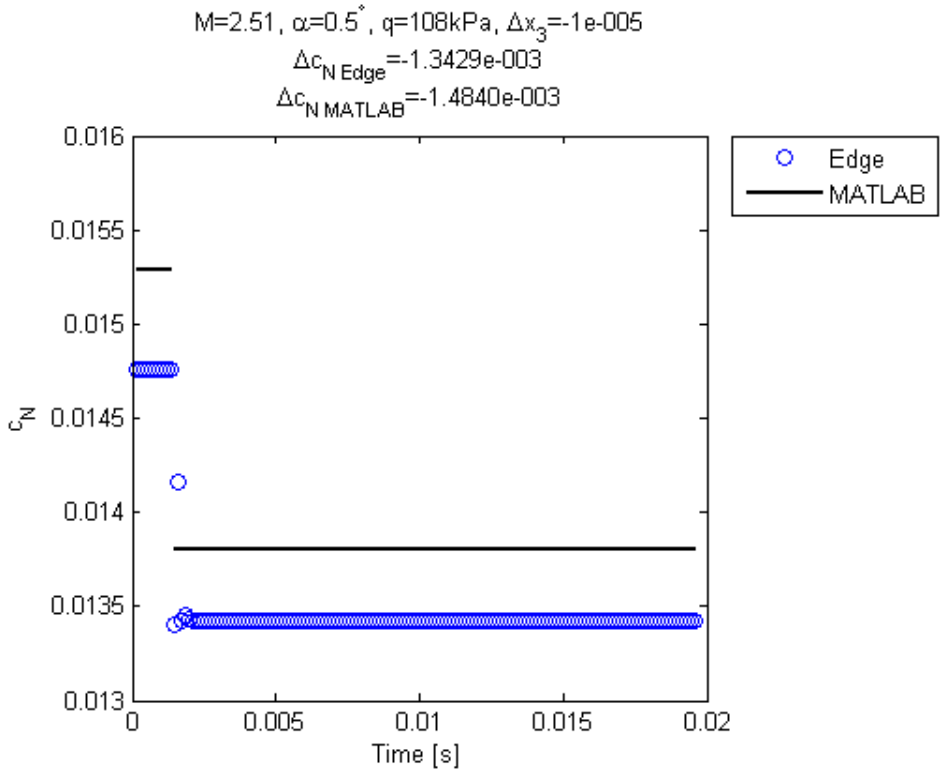


Figure 5.52: Aerodynamic Response of the ATM-Wing to Prescribed Step Modal Displacement, Mode 3

5.8.4 Prescribed Motion of Mode 4 Only

The percentage difference between the results obtained by Edge and by MATLAB for the prescribed motion of mode 1 are given in Table 5.13. An example of the response in given in Figure 5.53.

Table 5.13: Accuracy of MATLAB Computation for the ATM-Wing, Mode 4 Prescribed Step

	$\lvert\Delta x_4\rvert = 5 \text{ x } 10^{-5}$		$\lvert\Delta x_4\rvert = 5 \text{ x } 10^{-6}$	
	up	down	up	down
% Error Δc_N	-23.1%	-27.4%	-26.4%	-74.1%
% Error Δc_A	-40.7%	18.7%	-209%	205%
% Error Δc_M	-79.7%	-88.5%	-134%	-232%
% Error ΔQ_1	491.9%	514.3%	950%	1260%
% Error ΔQ_2	30.8%	31.0%	45.4%	47.2%
% Error ΔQ_3	26.3%	23.5%	28.5%	-4.3%
% Error ΔQ_4	-50.5%	-51.4%	-5.5%	-15.9%

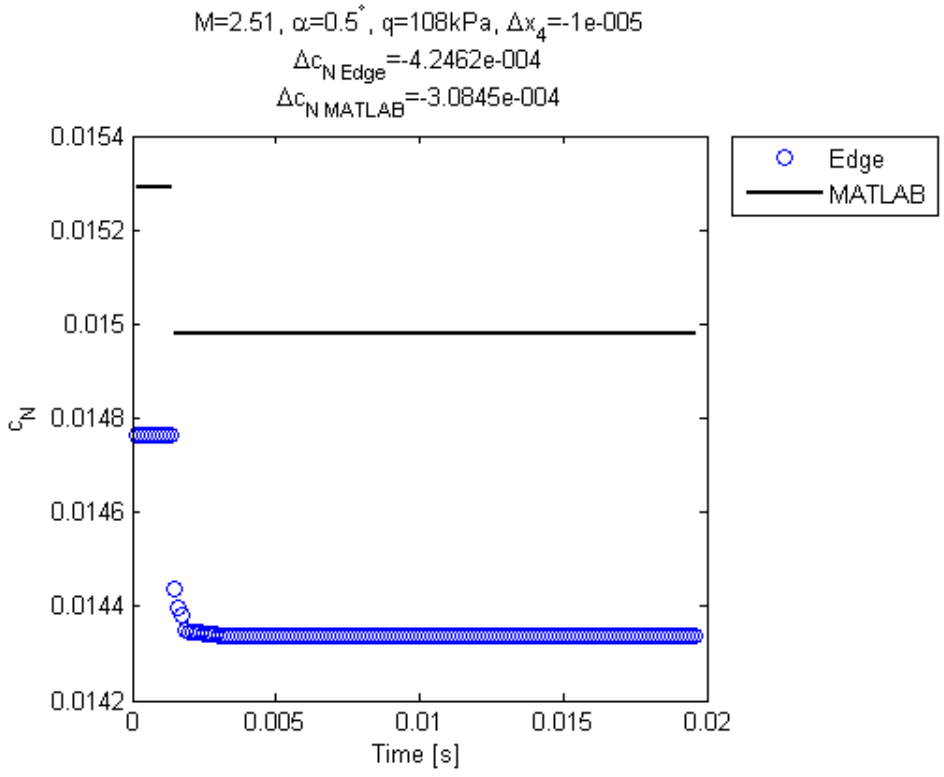


Figure 5.53: Aerodynamic Response of the ATM-Wing to Prescribed Step Modal Displacement, Mode 4

5.9 Linearization of the Generalized Aerodynamic Forces

Using the results of the prescribed motion computations of Section 5.8, the GAF linearization procedure outlines in Section 4.5.1 was followed, and the partial derivatives of the GAFs with respect to modal displacements were obtained. These partial derivatives make up the modal aerodynamic stiffness matrix, $\boldsymbol{K_{mod_{aero}}}$. The terms of the matrix are given in Table 5.14 for the two linearization step-sizes investigated, and are given as estimated from the results of the 3D Euler computation in Edge and from the SE/LPT computation in MATLAB. It is noted that the aerodynamic stiffness matrix derived from Edge results is essentially independent of the linearization step-size for the two considered sizes.

Table 5.14: Modal Aerodynamic Stiffness Matrix of the ATM-Wing, $\boldsymbol{M = 2.51, \alpha = 0.5°, q = 108}$ kPa

	$\Delta x = 1 \times 10^{-5}$	$\Delta x = 1 \times 10^{-6}$
Edge	$1 \times 10^4 \begin{bmatrix} -13.2 & -92.5 & -96.3 & 4.1 \\ 6.7 & 24.4 & 41.3 & 70.4 \\ -1.4 & -0.7 & -30.2 & -38.0 \\ 0.6 & -17.1 & 0.2 & 26.6 \end{bmatrix}$	$1 \times 10^4 \begin{bmatrix} -13.2 & -92.5 & -96.3 & 4.1 \\ 6.7 & 24.4 & 41.3 & 70.4 \\ -1.4 & -0.7 & -30.2 & -38.0 \\ 0.6 & -17.1 & 0.2 & 26.6 \end{bmatrix}$
MATLAB	$1 \times 10^4 \begin{bmatrix} -14.7 & -111.7 & -111.1 & 24.7 \\ 5.4 & 12.1 & 32.4 & 92.2 \\ -1.8 & -3.9 & -34.4 & -47.5 \\ 1.9 & -7.5 & 9.3 & 13.0 \end{bmatrix}$	$1 \times 10^4 \begin{bmatrix} -12.9 & -142.0 & -141.3 & 49.3 \\ 4.9 & 12.8 & 33.3 & 103.0 \\ -2.9 & -28.1 & -58.7 & -42.6 \\ 2.9 & -1.2 & 15.6 & 23.7 \end{bmatrix}$

The aeroelastic modal frequencies of the ATM-wing at $M = 2.51,\ \alpha = 0.5°, q = 108$ kPa were estimated by neglecting the aeroelastic damping matrix and finding the eigenvalues of the undamped aeroelastic system given by:

$$\boldsymbol{M_{mod_{ae}}}\{\ddot{\vec{x}}\} + \boldsymbol{K_{mod_{ae}}}\{\vec{x}\} = 0 \qquad (5.7)$$

The estimated aeroelastic modal frequencies are given in Table 5.15 for the two linearization step-sizes investigated, and are given as estimated from the results of the 3D Euler computation in Edge and from the SE/LPT computation in MATLAB. As a result of the linearization step-size independence of the aerodynamic stiffness matrix derived from Edge results, the estimated aeroelastic modal frequencies from Edge are similarly independent. The frequencies estimated from the MATLAB results give better agreement for the larger linearization step-size. Even so, the MATLAB results for the first two modes show poor agreement with the Edge results -- the separation of the first and second modal frequencies is over-predicted by ≈700%. This will have in turn result in the flutter speed being over-

predicted. From the results, it is evident that accurate prediction of the aerodynamic stiffness will be of great importance for accurate flutter speed prediction.

Table 5.15: Estimated Aeroelastic Modal Frequencies of the ATM-Wing, $M = 2.51, \alpha = 0.5°, q = 108$ kPa

	$\Delta x = 1$ x 10^{-5}			$\Delta x = -1$ x 10^{-6}		
	Edge	MATLAB	% Error	Edge	MATLAB	% Error
ω_1 [Hz]	97.3	84.3	-15.4%	97.3	77.1	-26.2%
ω_2 [Hz]	102.8	128.1	19.8%	102.8	135.5	24.1%
ω_3 [Hz]	211.8	214.2	-3.5%	211.8	224.5	1.2%
ω_4 [Hz]	406.6	410.8	1.0%	406.6	407.7	0.27%

6 AEROELASTIC ANALYSIS AND FLUTTER PREDICTION OF CANTILEVERED PLATES IN SUPERSONIC FLOW

6.1 Free Aeroelastic Response of the ATM-Wing

6.1.1 Literature on the Experimentally Determined Flutter Conditions

Torii [54] and Matsuzaki [55] provide data for flutter tests of a cantilevered plate, with parameter and stability estimation. The plate is made of 2mm thick aluminium alloy (unspecified alloy), with double-wedge leading and trailing-edges. Torii provides the frequencies of the 3 first structural modes, as determined from FEM and from experiment, as give in Table 6.1:

Table 6.1: Natural Frequencies of the Torii and Matsuzaki Wing [54]

	Frequencies (Hz)	
Mode	FEM	Experiment
1	27.9	27.2
2	145.7	142.0
3	207.1	192.3

The planform of the cantilevered plate is given in Figure 6.1; note that the geometry of the sharpening of the leading and trailing-edges was not specified:

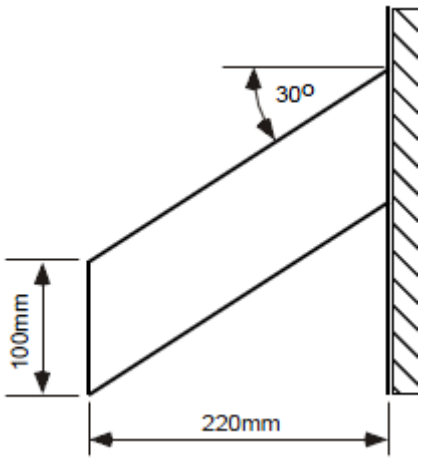


Figure 6.1: Planform of the Torii and Matsuzaki Wing **[54]**

The planform geometry is summarized in Table 6.2:

Table 6.2: Geometry of the Torii and Matsuzaki Wing [54]

S_{ref} [m^2]	AR	$\bar{c}$ [m]	Λ_{LE} [°]	λ	t/c
0.022	2.2	0.100	30	1	0.02

The geometry of the TM-wing was replicated, with the bevel length estimated to be equal to 15mm on each bevel. This approximated geometry is described in Section 5.2, and the subsequent approximate Torii and Matsuzaki wing (ATM-wing) was used in the present work for all computations relating to the Torii [54] and Matsuzaki [55] test.

The cantilevered plate was tested by Torii [54] and Matsuzaki [55] in a supersonic wind-tunnel for a constant Mach number of $M = 2.51$ at a range of dynamic pressures; the dynamic pressure at the experimentally determined flutter point is quoted as $q_F = 113.5$ kPa. No forced excitation was provided to the model; the onset of flutter was caused by the random excitation of turbulence. The modal damping and frequencies were estimated through an ARMA (Auto-Regressive Moving Average) model [54; 55], and the FMDS (flutter margin for discrete systems) was calculated for two-mode flutter [55] and for three-mode flutter [54].

Tests were also conducted [55] in which the dynamic pressure was increased linearly with time until the onset of flutter. The time-history of the strain-gauge response shows a very slight growth in the amplitude of the strain oscillations (suggesting a decrease in damping) at a dynamic pressure of approximately $q = 110$ kPa. The onset of flutter is extremely sharp, as

seen by the sudden growth in oscillations in Figure 6.2, indicating that the plate undergoes hard flutter.

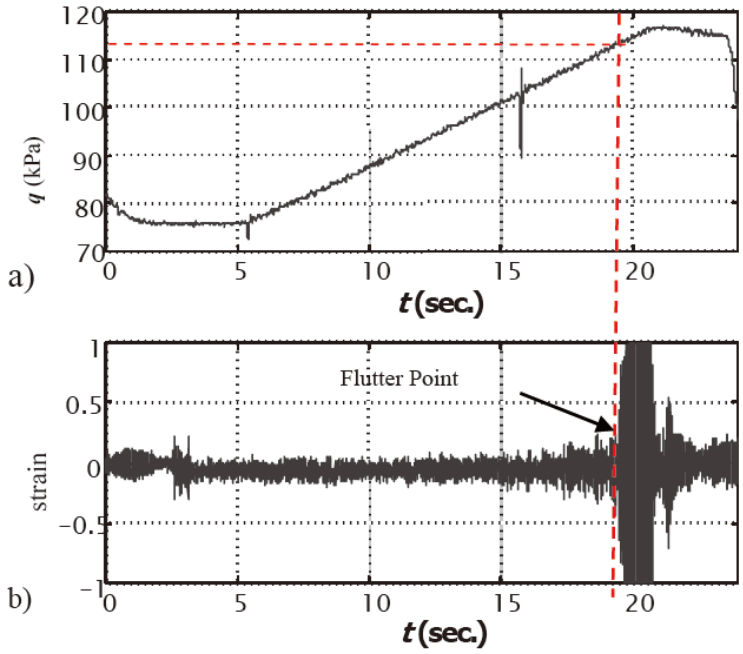


Figure 6.2: Time History of Response of the Torii-Matsuzaki Flutter Test **[55]**

6.1.2 Outline of the Computational Procedure

The aeroelastic response of the ATM-wing to a small initial disturbance was analysed using three different methods: transient 3D Euler computation in Edge (Section 6.1.3); time-marching of the nonlinear coupled aeroelastic equations formulated from SE/LPT in MATLAB (Section 6.1.4); and stability analysis and time-marching of the linearized coupled aeroelastic equations formulated from SE/LPT in MATLAB (Section 6.1.5). These methods will be referred to in shorthand as Edge, MATLAB (nonlinear), and MATLAB (linear), respectively.

With each analysis method, the free aeroelastic response was computed about the static aeroelastic deflection of the ATM-wing at the given flight conditions.

Various methods were used for the estimation of the modal parameters. The linearized model rendered the system of equations a linear time-invariant (LTI) system (see Section 4.4.3), for which eigenanalysis was performed to determine the system roots. For the nonlinear models,

Auto-Regressive Moving-Average (ARMA) (see Section 2.9.2) and Auto-Regressive (AR) models were estimated using the MATLAB system identification toolbox.

The variation in the modal parameters with dynamic pressure at $M = 2.51$ and $\alpha = 0.5°$ was investigated by each of the three analyses to determine the flutter dynamic pressure for the given M–α pair.

The same time-step of $\Delta t = 1.306 \text{ x } 10^{-4}$ s was used for all the transient computations for numerical stability of the implicit time-marching, as detailed in Section 5.7.

For the initial modal excitation, the second mode (first twisting mode) of the ATM-wing was given an initial modal velocity of $\dot{x}_2 = 1 \text{ x } 10^{-2}$ /s. This was implemented as initial conditions for the time-marching in MATLAB for both the nonlinear and linearized SE/LPT models. The given modal excitation was chosen as it was believed that the GAFs would be dominated by α-effects, and excitation of the second mode would result in the largest change in α.

The computation of the free response of the ATM-wing in Edge consisted of the following steps:

1. Steady computation of the flow about the undeformed ATM-wing,
2. Transient computation of the steady-state response of the elastic ATM-wing with artificial structural damping to the initial steady aerodynamic loading,
3. Transient computation of the transient response of the elastic ATM-wing with no structural damping to an initial modal excitation about the aeroelastic equilibrium deflection.

A detailed description of the set-up of the computations in Edge for the analysis of the free response is given in Appendix C.

The computation of the free response of the ATM-wing in MATLAB (nonlinear) followed the same procedure as the computation in Edge.

The computation of the free response of the ATM-wing in MATLAB (linear) consisted of the following steps:

1. Quasi-steady determination of the aeroelastic equilibrium deflection through iterative linearization of the GAFs and calculation of the structural deflection under constant loading,
2. Linearization of the GAFs about the static aeroelastic deflection,
3. Time-marching of the state-space formulation of the linearized aeroelastic equations.

The implementation of the initial modal excitation in Edge was through the prescription of the initial modal velocity in the modal parameters file (`.amop`) for the restart of the unsteady solution in Edge. It was found that due to the time-averaging of modal displacements and GAFs in the Edge solver, as per Equations (5.2) and (5.3), the initial modal velocity was "smoothed out", and was not properly modelled as an initial condition. However, the perturbation was found to be sufficient to disturb the equilibrium of the ATM-wing and induce a transient response.

6.1.3 Analysis in Edge

The aeroelastic free response of the ATM-wing was analysed in Edge at dynamic pressures between 100 kPa and 110 kPa. The flutter dynamic pressure was found to lie between 108 kPa and 108.5 kPa, and was estimated as $q_F \approx 108.3$ kPa.

6.1.3.1 System Response Below Flutter Speed

The system response to the initial modal excitation at $q = 100$ kPa is shown in Figure 6.3 through Figure 6.7.

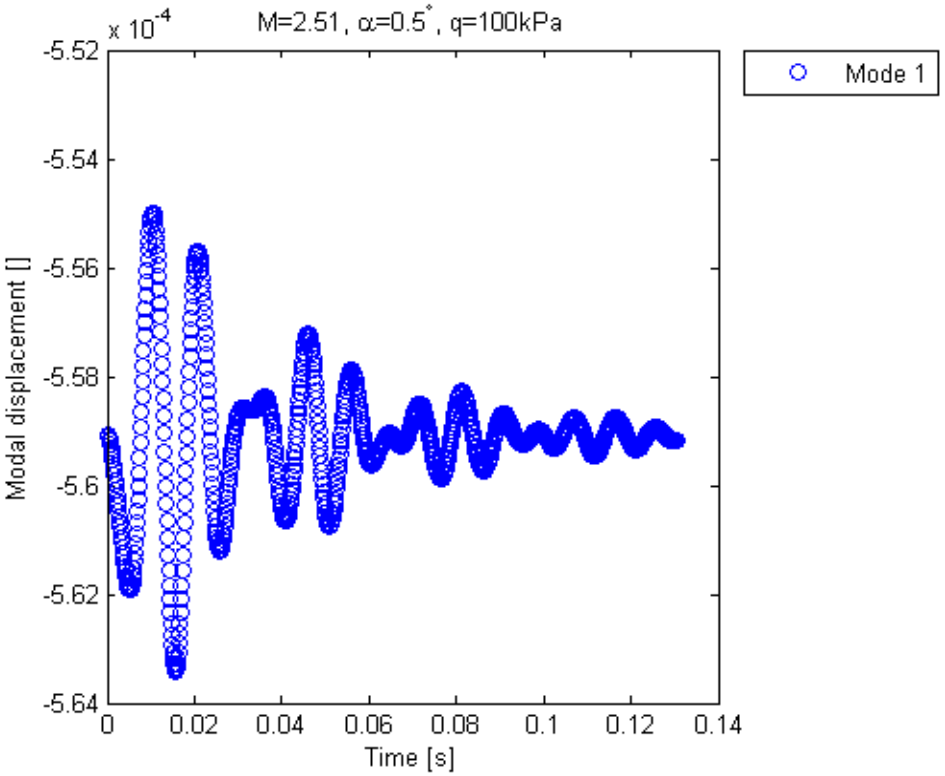


Figure 6.3: ATM-Wing Response Below Flutter Speed, Mode 1 Displacement, Edge

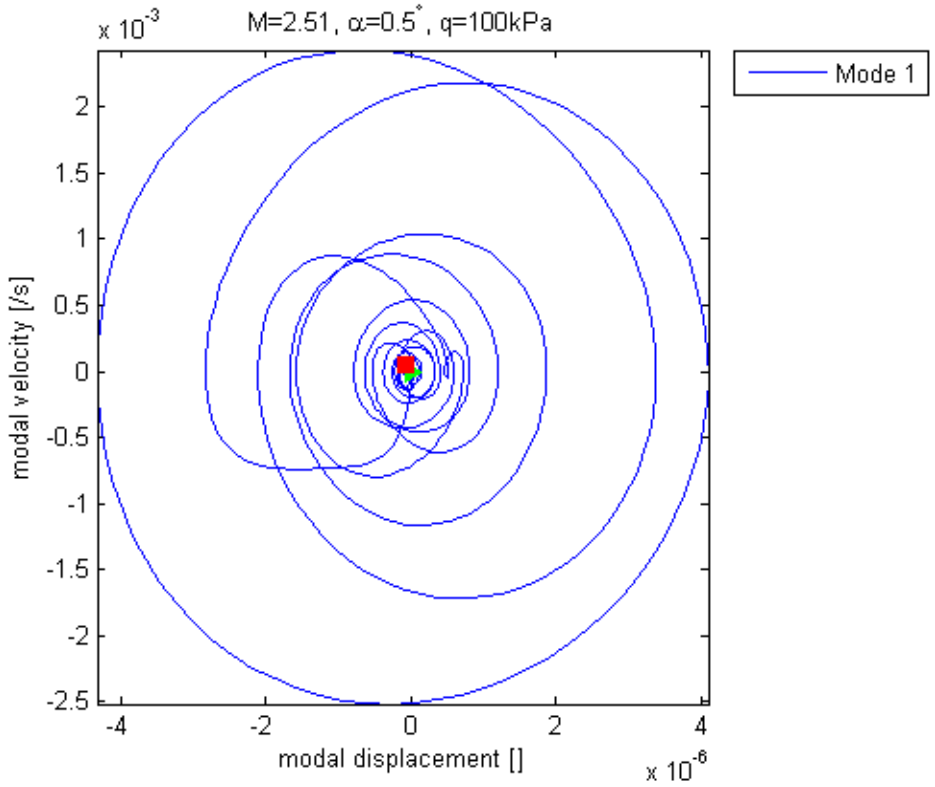


Figure 6.4: ATM-Wing Response Below Flutter Speed, Mode 1 Phase-Plane Trajectory, Edge

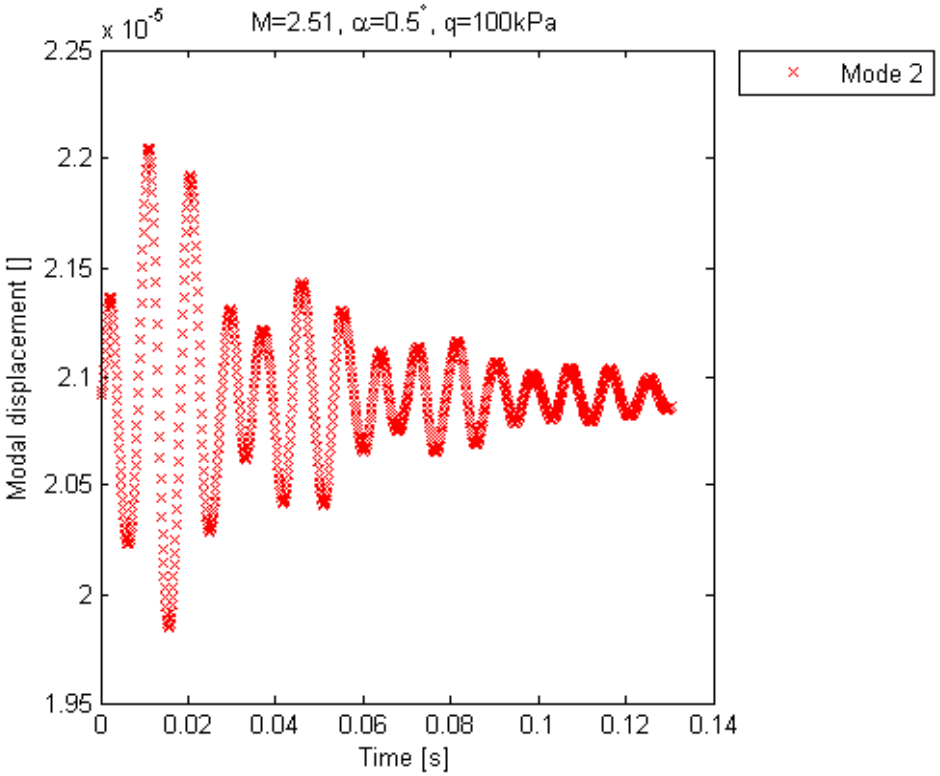


Figure 6.5: ATM-Wing Response Below Flutter Speed, Mode 2 Displacement, Edge

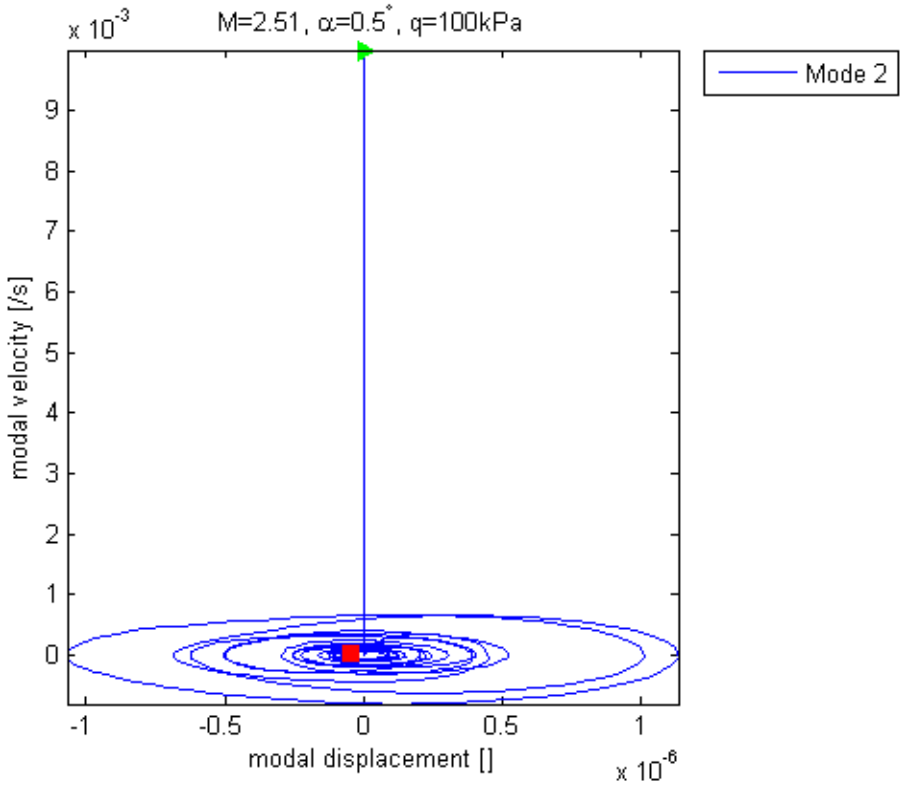


Figure 6.6: ATM-Wing Response Below Flutter Speed, Mode 2 Phase-Plane Trajectory, Edge

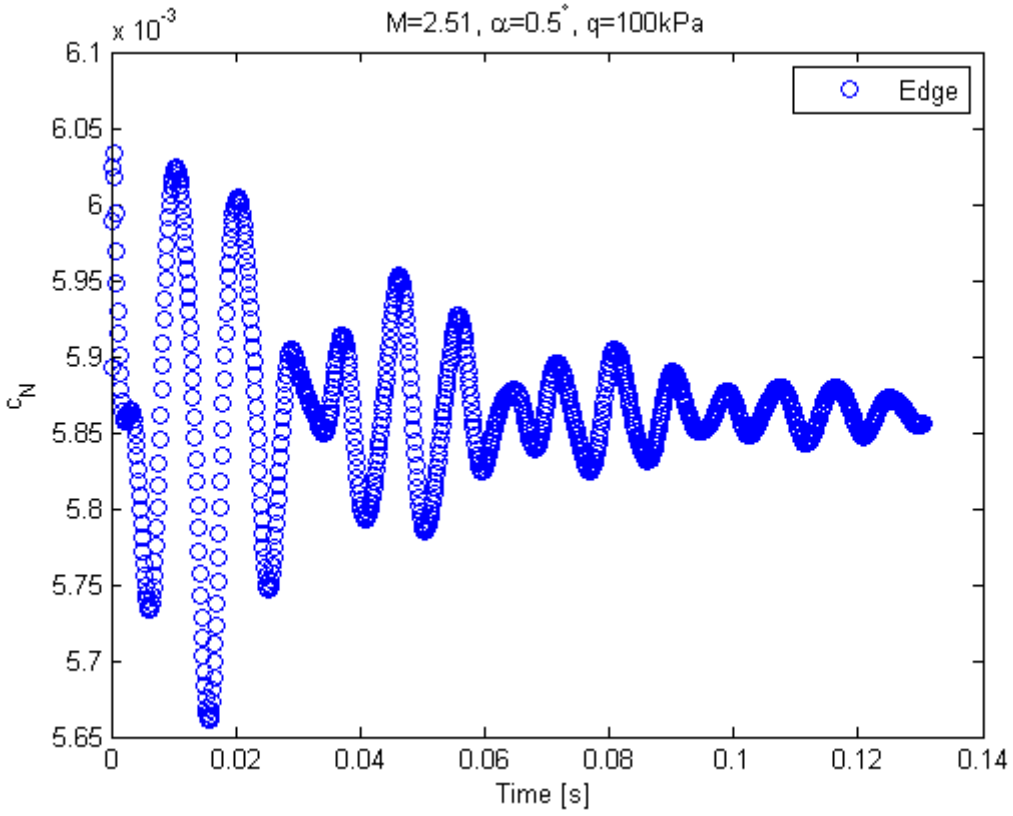


Figure 6.7: ATM-Wing Response Below Flutter Speed, cZ, Edge

The response of Mode 1 (first bending, undamped structural mode-shape) is shown in Figure 6.3 and Figure 6.4. Amongst the modal responses, Mode 1 showed the largest amplitude in response, as was expected due to the associated modal stiffness of Mode 1 being lower than that of other modes. The response is seen to decay with time (evidence of positive damping), and exhibits a periodic variation in amplitude (beating).s

The beating shown in the response of Mode 1 (first bending, undamped structural mode-shape) results due to the response being composed of two decaying sinusoids of dissimilar frequencies. It may be shown (as in Section 6.1.5) that the beat frequency suggests that the response of Mode 1 is made up of the first two aeroelastic modes. When the "spatial filter" of the undamped mode-shaped (Mode 1) is applied to the overall structural response, the response of the first two aeroelastic mode-shapes are "passed". Similar beating is shown in the response of Mode 2, as in Figure 6.5 and Figure 6.6, and in the normal-force coefficient history (which is dominated by the response of Mode 2), as in Figure 6.7.

The response of Mode 2 (first twisting, undamped structural mode-shape) is shown in Figure 6.5 and Figure 6.6. It is seen that the trends of the response are similar to those of the response of Mode 1 -- the response of Mode 2 also shows the beating of two damped sinusoids. These sinusoids, again, represent the contribution from the first two aeroelastic modes. The magnitude of the response is seen to be lower than the magnitude of Mode 1, as expected due to the higher stiffness of Mode 2.

From the phase-plane trajectory of Mode 2 in Figure 6.6, the implementation of the initial conditions in Edge is clearly shown (by the green triangle; the red square denotes the final point on the phase-plane); Mode 2 was given the initial condition of $\dot{x}_2 = 1 \text{ x } 10^{-2}$, which was modelled in Edge as a modal velocity impulse (due to the time-averaging of modal displacements and velocities).

The normal-force coefficient history is shown in Figure 6.7. It was found that the normal-force response was driven by the response of Mode 2 (first twisting mode). This was expected, as the normal-force coefficient is dominated by α-effects rather than through plunge effects; Mode 2 is predominantly a twisting mode (giving rise to a change in α down the span of the wing). The response is seen to decay with time and exhibits beating.

6.1.3.2 Pre-Flutter System Response Near Flutter Speed

The system response to the initial modal excitation at $q = 108$ kPa is shown in Figure 6.8 through Figure 6.14.

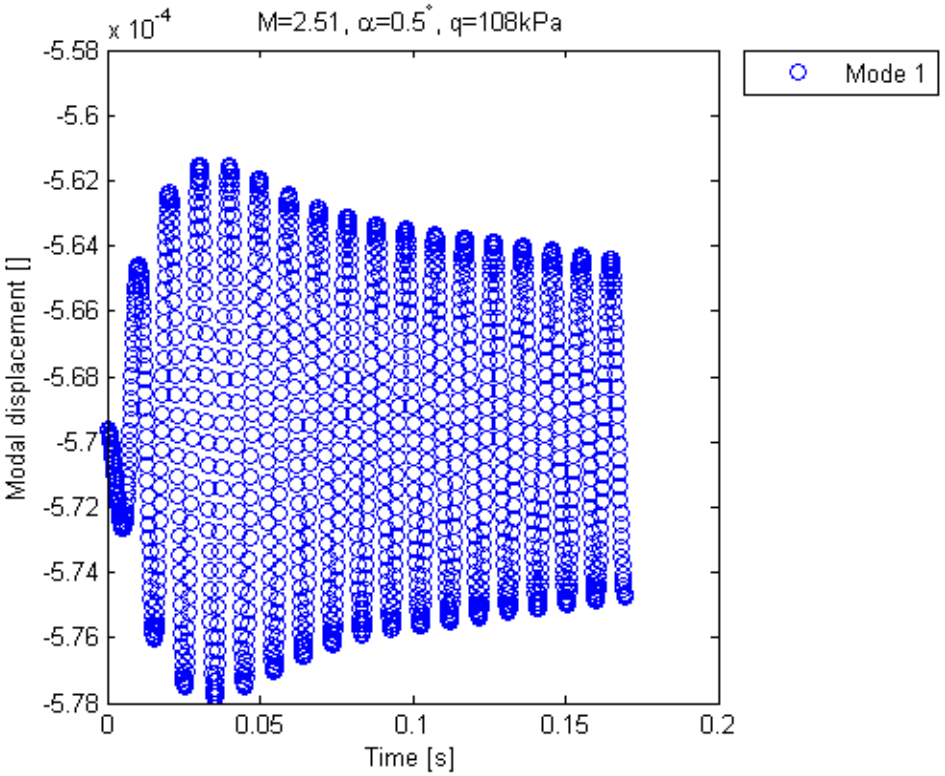


Figure 6.8: ATM-Wing Pre-Flutter Response Near Flutter Speed, Mode 1 Displacement, Edge

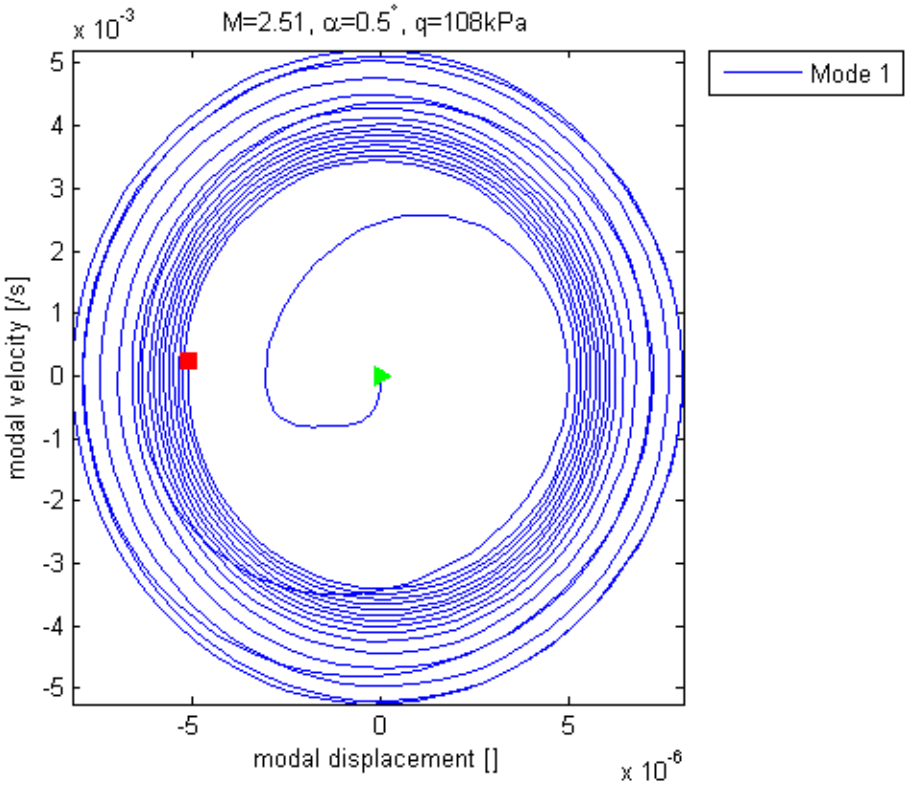


Figure 6.9: ATM-Wing Pre-Flutter Response Near Flutter Speed, Mode 1 Phase-Plane Trajectory, Edge

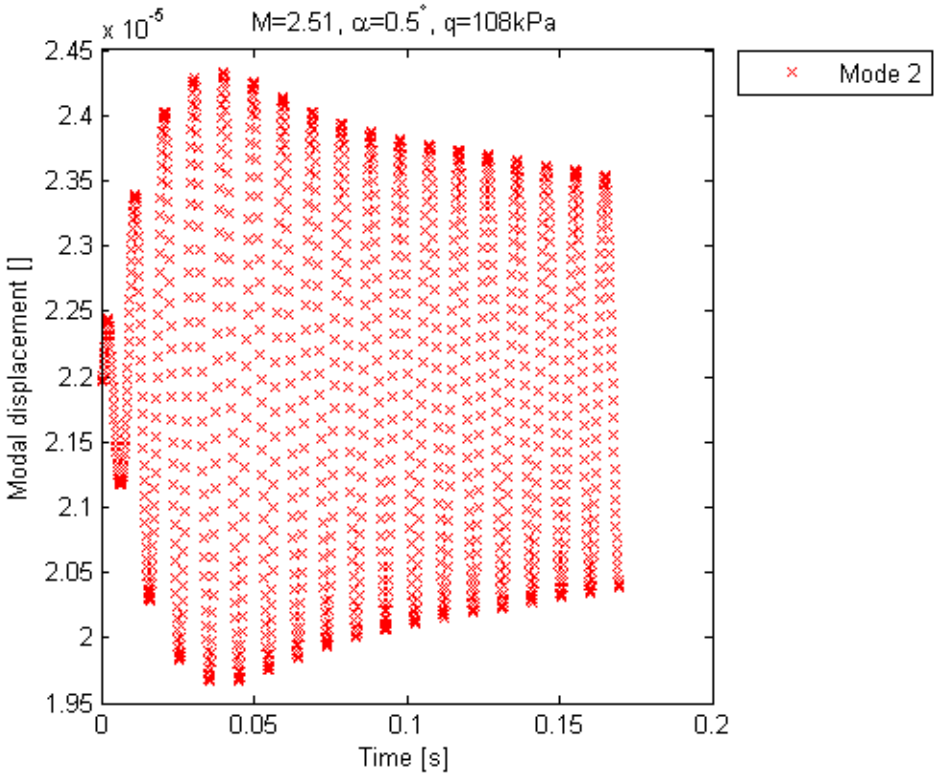


Figure 6.10: ATM-Wing Pre-Flutter Response Near Flutter Speed, Mode 2 Displacement, Edge

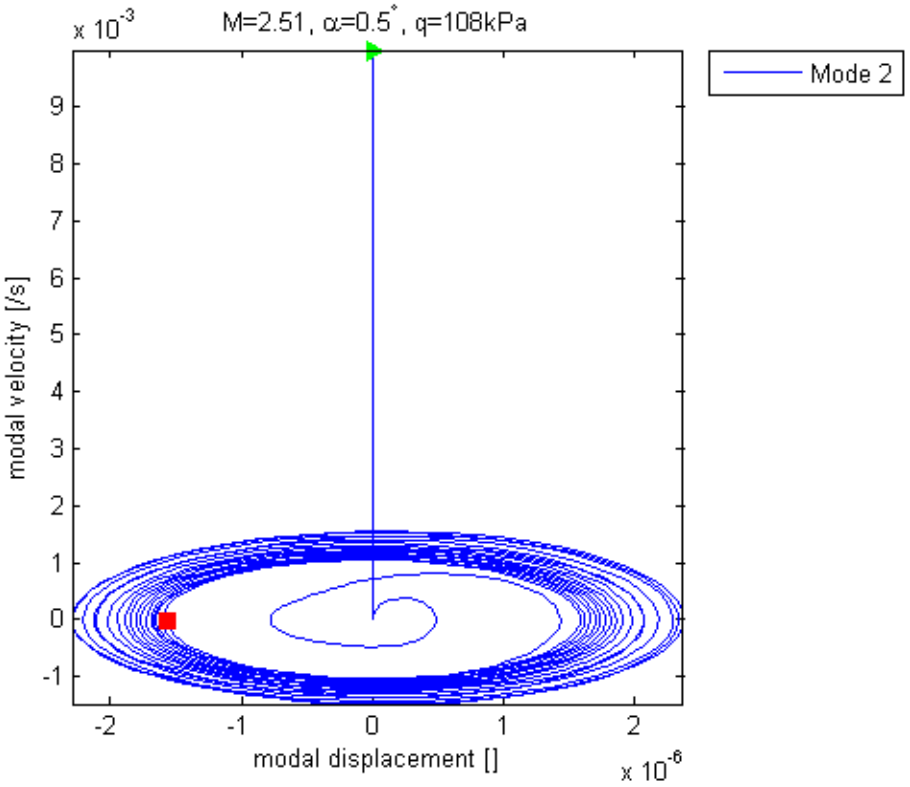


Figure 6.11: ATM-Wing Pre-Flutter Response Near Flutter Speed, Mode 2 Phase-Plane Trajectory, Edge

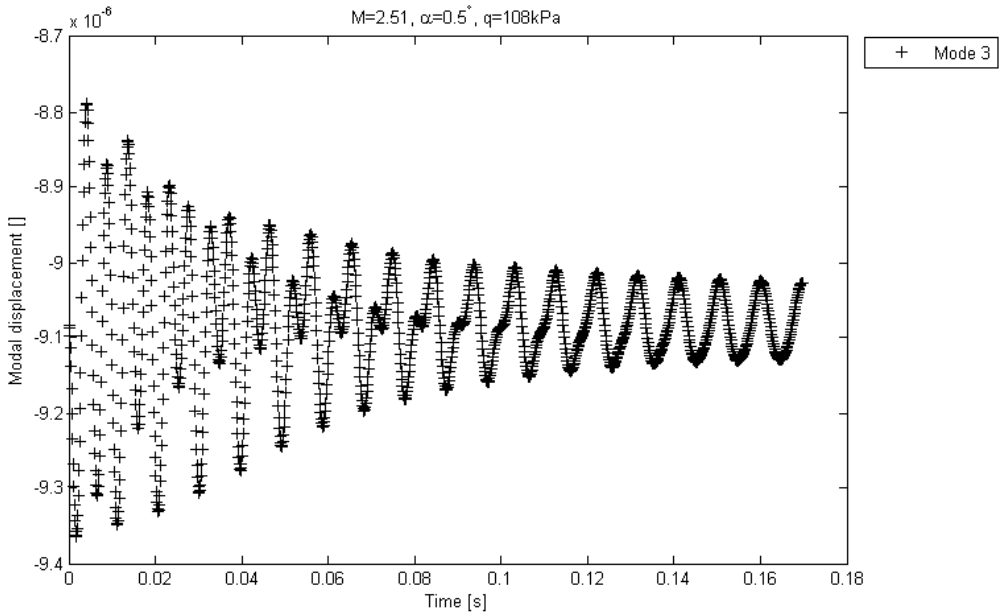


Figure 6.12: ATM-Wing Pre-Flutter Response Near Flutter Speed, Mode 3 Displacement, Edge

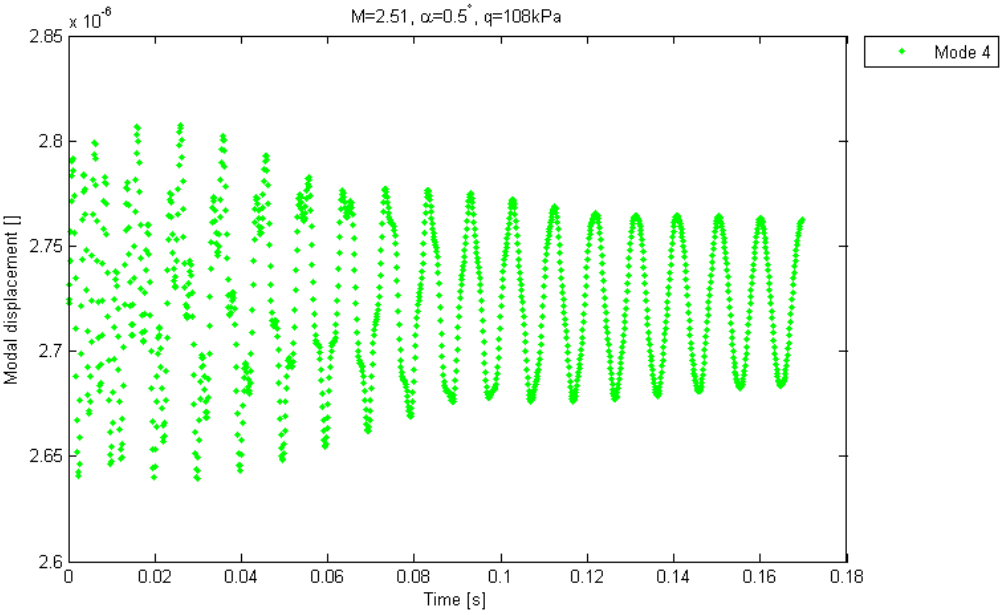


Figure 6.13: ATM-Wing Pre-Flutter Response Near Flutter Speed, Mode 4 Displacement, Edge

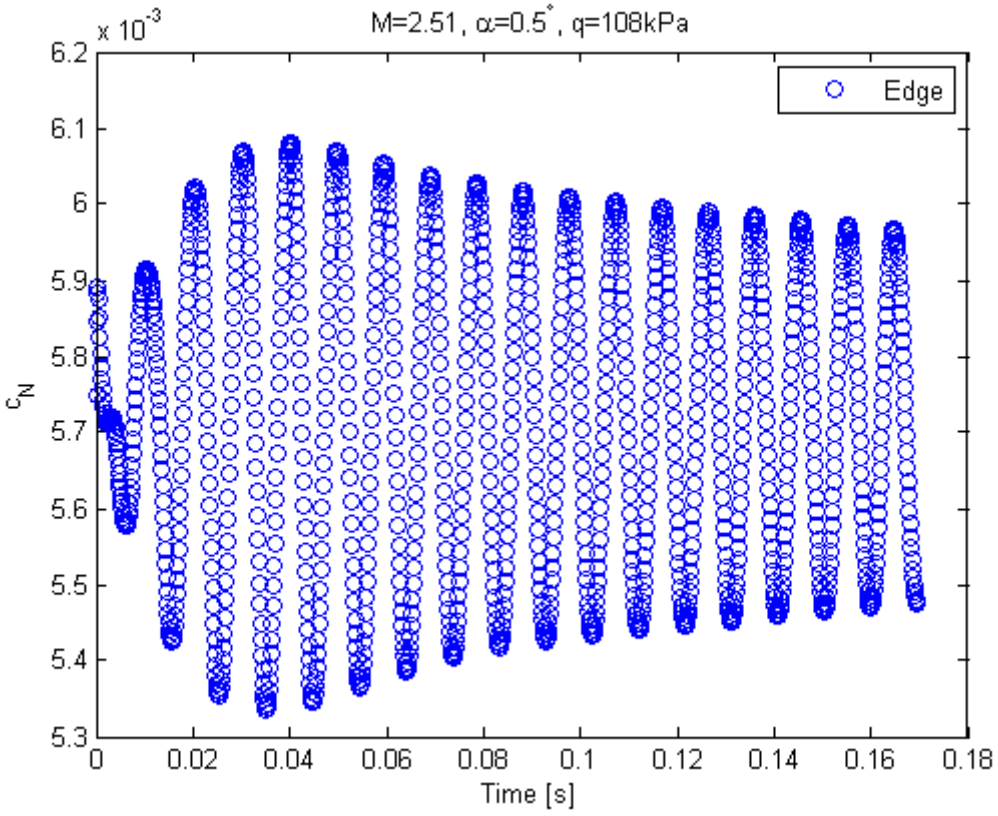


Figure 6.14: ATM-Wing Pre-Flutter Response Near Flutter Speed, cZ, Edge

The response of Mode 1 (first bending, undamped structural mode-shape) is shown in Figure 6.8 and Figure 6.9. The response shows gradual decay after an initial growth, giving evidence of the aerodynamic damping approaching zero. The beating that was present at lower dynamic pressures (e.g., $q = 100$ kPa, Figure 6.3) is no longer present. This suggests that the frequencies of the first two aeroelastic modes are close to one another (which would result in a low beat frequency).

The varying rate at which the spacing between the spirals of the phase-plane trajectory of Mode 1 in Figure 6.9 changes highlights the change in the perceived damping of the response. This is reflected in the slight change in the slope of the envelope of the response in Figure 6.8 between $t = 0.05$ s $\rightarrow t = 0.08$ s and $t = 0.08$ s $\rightarrow t = 0.15$ s. Recalling that the response of Mode 1 (and Mode 2) is the sum of the contributions of the first two aeroelastic modes, the variation in the perceived damping suggests that one of the aeroelastic modes has near-zero damping, whilst the other has higher damping which decays the contribution of the mode significantly by $t = 0.08$ s.

Similar trends are observed for the response of Mode 2 (first twisting, undamped structural mode-shape), as shown in Figure 6.10 and Figure 6.11.

From the time-history of modal response, it is evident that at $q = 108$ kPa, the ATM-wing is near flutter.

Figure 6.12 and Figure 6.13 show the modal response of Mode 3 and Mode 4, respectively. The history of displacements suggests that the response is made up of two signals: a dampened transient free response of high frequency (the natural frequency of the aeroelastic mode); and a steady-state forced response of frequency corresponding to the GAF (which is dominated by Mode 2). The transient component of the response of Mode 3 and Mode 4 suggests the modes are more heavily damped than Mode 2.

The normal-force coefficient history is shown in Figure 6.14. Once again, the response is found to be nearly identical in its trends to the modal response of Mode 1 and Mode 2.

6.1.3.3 Post-Flutter System Response Near Flutter Speed

The system response to the initial modal excitation at $q = 108.5$ kPa is shown in Figure 6.15 through Figure 6.21.

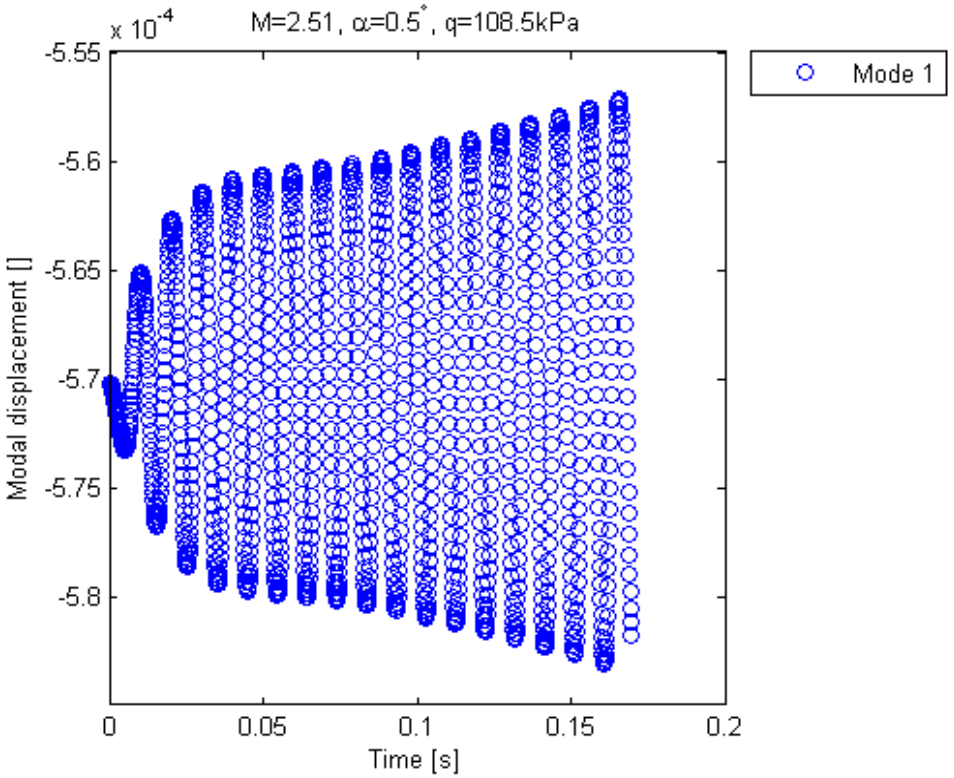


Figure 6.15: ATM-Wing Post-Flutter Response Near Flutter Speed, Mode 1 Displacement, Edge

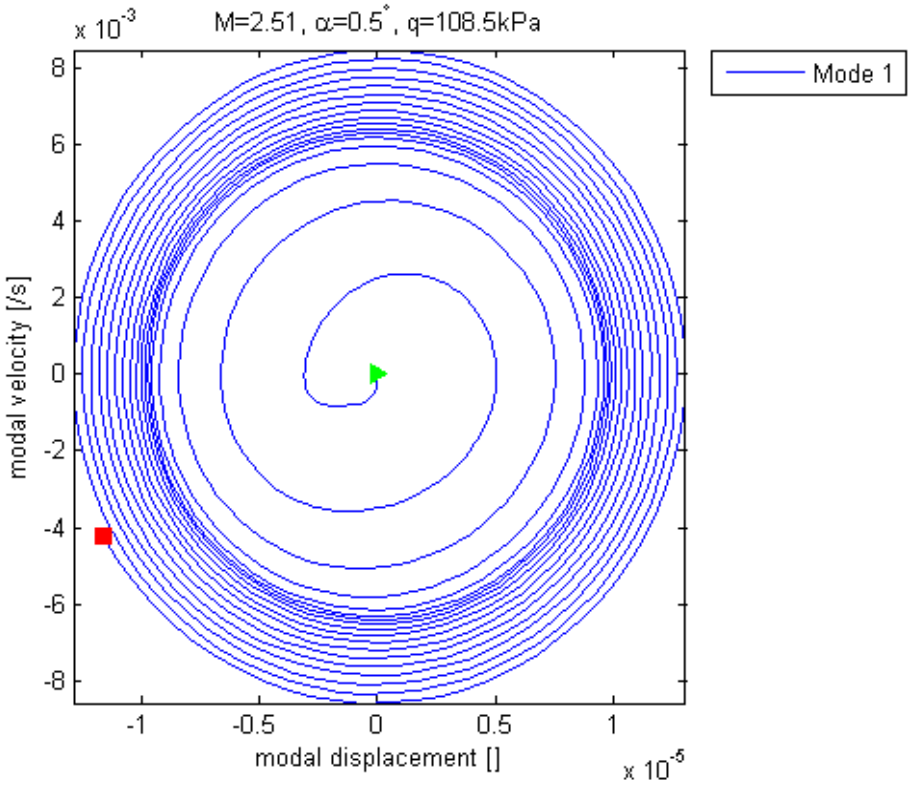


Figure 6.16: ATM-Wing Post-Flutter Response Near Flutter Speed, Mode 1 Phase-Plane Trajectory, Edge

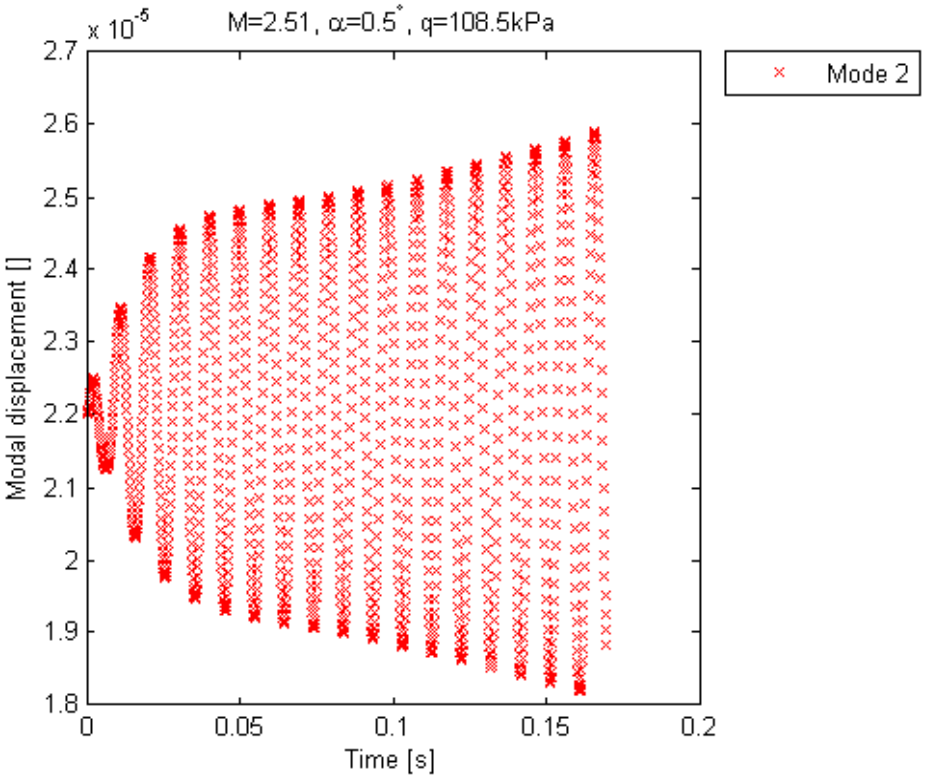


Figure 6.17: ATM-Wing Post-Flutter Response Near Flutter Speed, Mode 2 Displacement, Edge

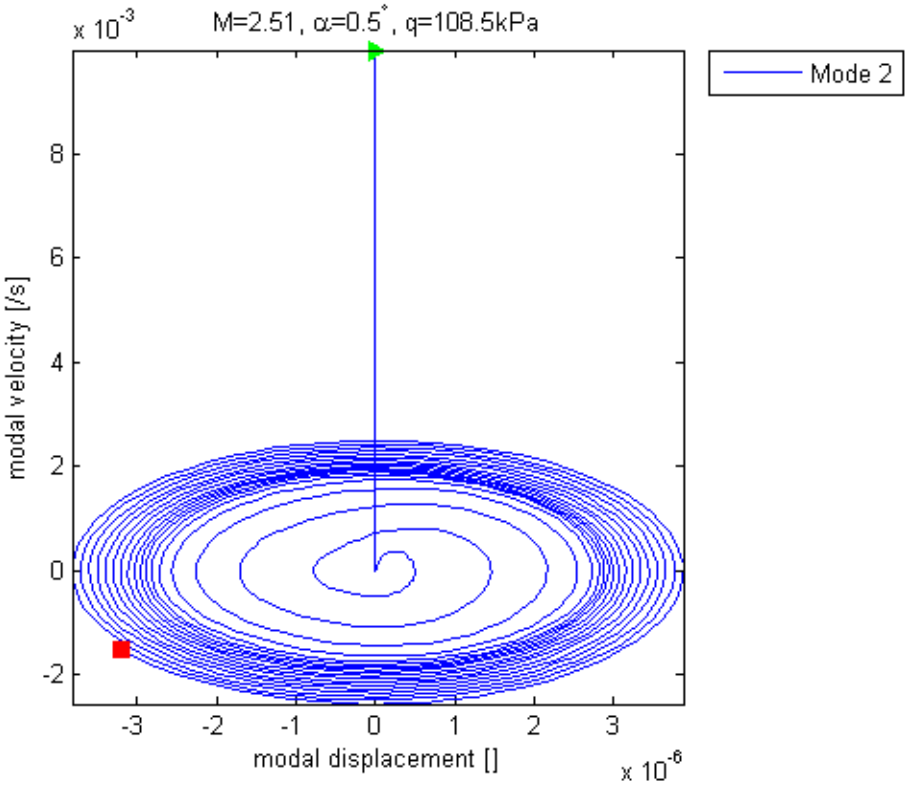


Figure 6.18: ATM-Wing Post-Flutter Response Near Flutter Speed, Mode 2 Phase-Plane Trajectory, Edge

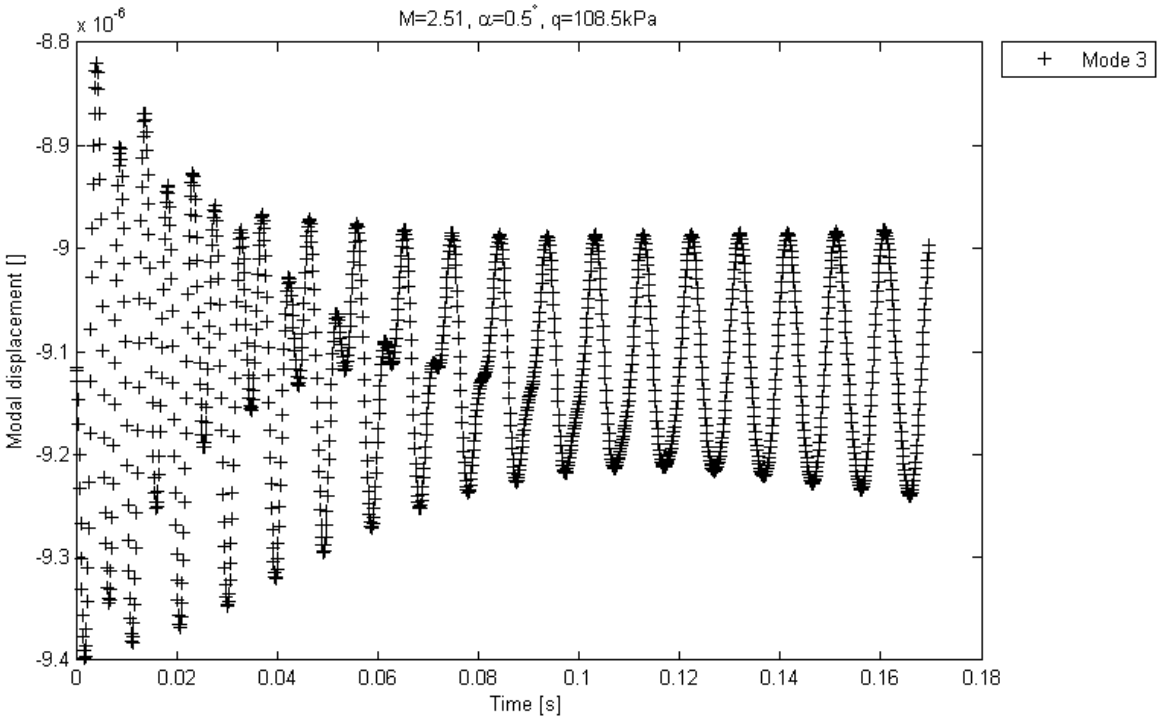


Figure 6.19: ATM-Wing Post-Flutter Response Near Flutter Speed, Mode 3 Displacement, Edge

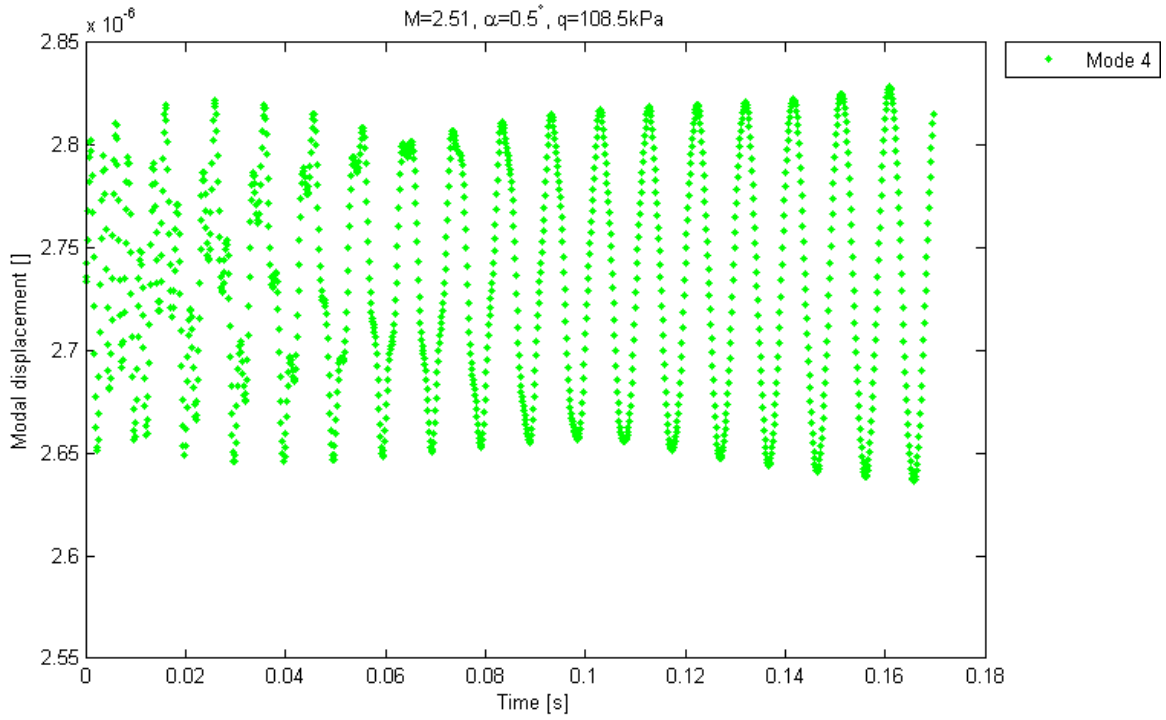


Figure 6.20: ATM-Wing Post-Flutter Response Near Flutter Speed, Mode 4 Displacement, Edge

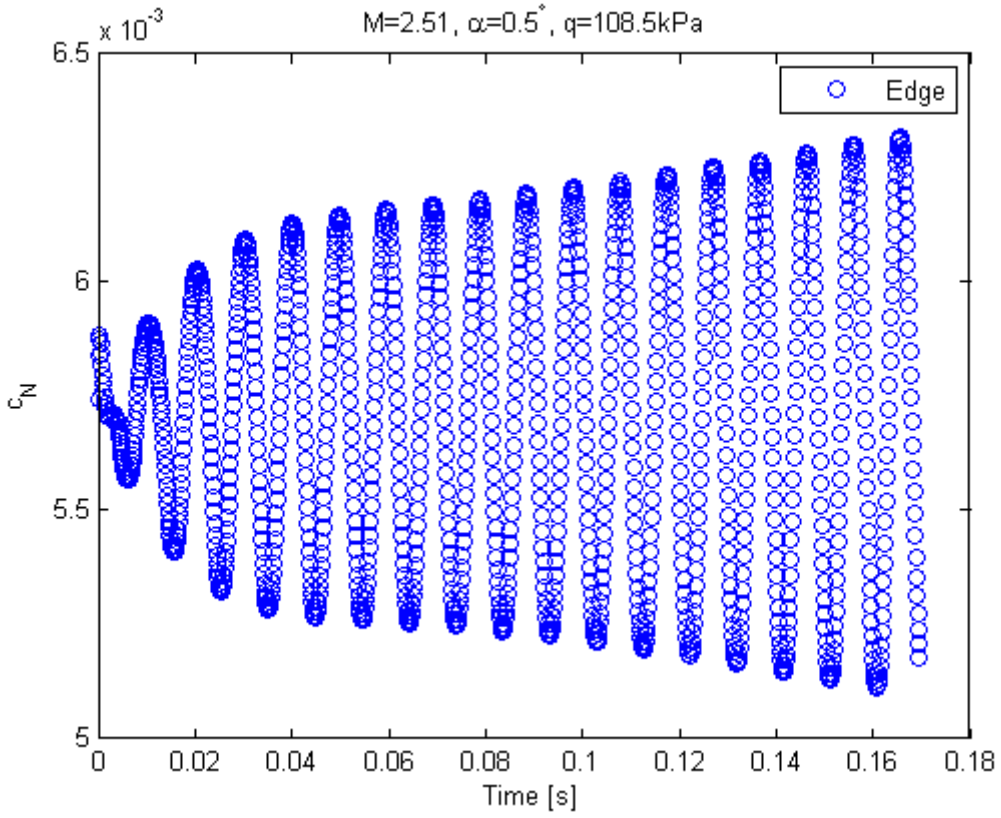


Figure 6.21: ATM-Wing Post-Flutter Response Near Flutter Speed, cZ, Edge

The response of Mode 1 (first bending, undamped structural mode-shape) is shown in Figure 6.15 and Figure 6.16. The response shows gradual further growth after an initial growth, showing that the aerodynamic damping is negative. The beating that was present at lower dynamic pressures (e.g., $q = 100$ kPa, Figure 6.3) is no longer present, suggesting that the frequencies of the first two aeroelastic modes are close to one another.

Similar trends are observed for the response of Mode 2 (first twisting, undamped structural mode-shape), as shown in Figure 6.17 and Figure 6.18.

From the time-history of modal response, it is evident that at $q = 108.5$ kPa, the ATM-wing is experiencing flutter at a speed slightly higher than the flutter speed.

Figure 6.19 and Figure 6.20 show the modal response of Mode 3 and Mode 4, respectively. Once again, the history of displacements suggests that the response is made up of two signals: a dampened transient free response of high frequency (the natural frequency of the aeroelastic mode); and a steady-state forced response of frequency corresponding to the GAF (which is

dominated by Mode 2). The transient component of the response of Mode 3 and Mode 4 suggests the modes are more heavily damped than Mode 2.

The normal-force coefficient history is shown in Figure 6.21. Once again, the response is found to be nearly identical in its trends to the modal response of Mode 1 and Mode 2.

6.1.3.4 Modal Parameter Estimation

The time-history of the total displacement from modal contributions was computed at the leading-edge and at the trailing-edge of the wing-tip for each dynamic pressure analysed. These points were chosen due to the large deflections associated with the wing-tip. The history of the displacement was pre-processed before the system identification tool was applied, with the displacement being taken about the (initial) equilibrium deflection. The subsequent time-series was then band-filtered to pass frequencies between 80 Hz and 140 Hz.

The modal parameters were obtained from the system model estimated using the `armax` system identification function in MATLAB, with order [4,1] (an ARMA model with an AR component of order 4 and a MA component of order 1). System identification was performed using the displacements at the leading-edge of the wing-tip, as the results obtained were a better representation of the time-history of response.

The estimated modal parameters are shown in Figure 6.22, with the flutter dynamic pressure as estimated from the ARMA model being shown by the solid black line ($q_F \approx 106.2$ kPa).

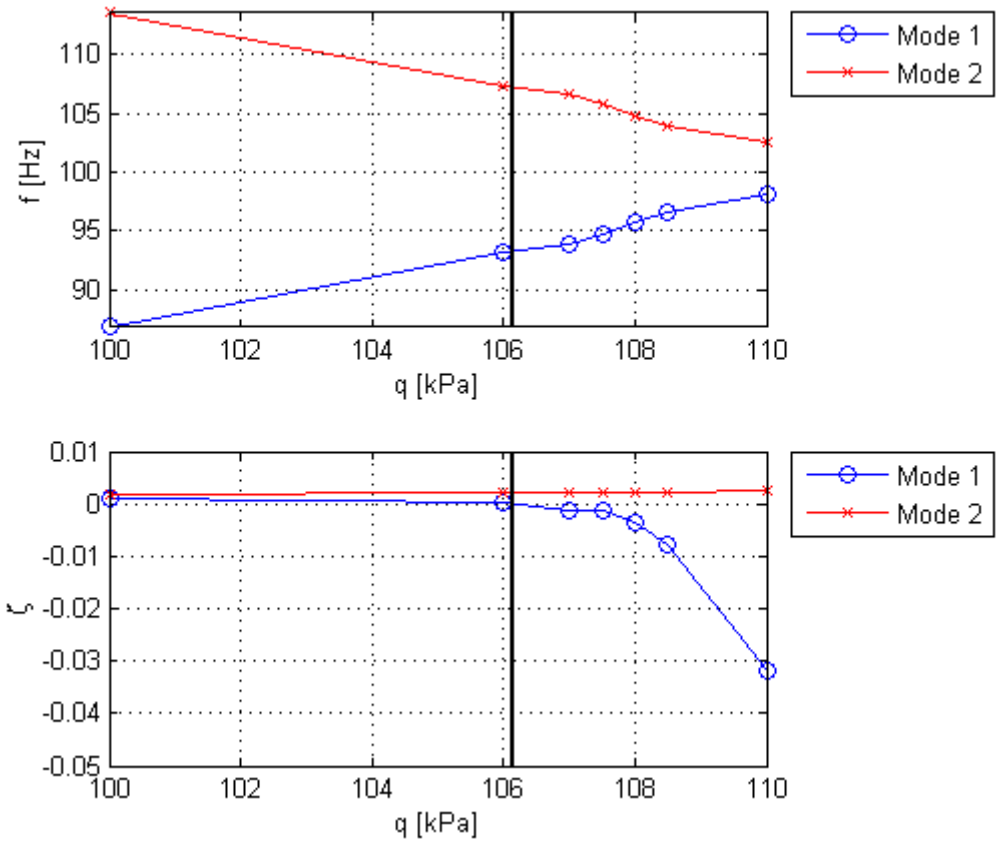


Figure 6.22: ATM-Wing Estimated Modal Parameters, Edge

The quality of the estimation of the modal frequencies obtained is relatively good, as the predicted modal frequencies at $q = 100$ kPa compare well with frequencies directly estimated from the time-history of the total displacement. The beat frequency at $q = 100$ kPa may be estimated to be approximately $f_2 - f_1 \approx 30$ Hz, which agrees well with the separation of the modal frequencies of $f_2 - f_1 \approx 27$ Hz at $q = 100$ kPa in Figure 6.22. This estimation may also be performed for the modal displacement histories in Figure 6.3 and Figure 6.5 for Mode 1 and Mode 2, respectively, with similar results being estimated.

The source of the error in the estimation of modal damping ratios using the ARMA model remained unidentified, as the use of the trailing-edge data in the system identification yielded similarly poor results. It is suggested that better estimation of the system model might be obtained through application of the ARMA model at measurement points best suited to modal measurements, as outlined by Yildiz [62]. A further possible source of error could be slight nonlinearity in the response, in which case the accuracy of the ARMA identification method (used for the identification of linear systems) would be affected.

Nonetheless, the following general trends may be observed from the estimated modal parameters in Figure 6.22. The aeroelastic frequencies coalesce as flutter is approached; the frequency of the plunge (first-bending) mode, Mode 1, is seen to increase, whilst the frequency of the pitch (first-twisting) mode, Mode 2, is seen to decrease. However, the damping of the plunge mode (Mode 1) decreases towards flutter and post-flutter, whilst the damping of the pitch mode (Mode 2) is seen to increase -- this would suggest that the plunge mode is driving the flutter, which is unlikely. The damping of Mode 1 estimated from the ARMA model is seen to decrease gradually towards flutter; this is not representative of the hard-flutter of the TM-wing in experiment, as determined by Matsuzaki [55].

The flutter dynamic pressure as estimated from the ARMA model is approximately $q_F \approx 106.2$ kPa. However, as may be seen from the time-history of modal responses in Section 6.1.3.2 and Section 6.1.3.3, the flutter dynamic pressure lies between $q = 108$ kPa and $q = 108.5$ kPa, and was consequently estimated to be $q_F \approx 108.3$ kPa. This is 4.6% lower than the experimental flutter dynamic pressure of $q_F = 113.5$ kPa. as determined by Matsuzaki [55], and represents good correlation to experiment.

6.1.4 Analysis in MATLAB (nonlinear)

The aeroelastic free response of the ATM-wing was analysed in MATLAB using the nonlinear coupled aeroelastic equations formulated from SE/LPT at dynamic pressures between 113 kPa and 121 kPa. The flutter dynamic pressure was found to lie between 120.5 kPa and 120.9 kPa, and was estimated as $q_F \approx 120.8$ kPa.

6.1.4.1 System Response Below Flutter Speed

The system response to the initial modal excitation at $q = 113$ kPa is shown in Figure 6.23 through Figure 6.27. The general trends of the system response are similar to those exhibited by the analysis in Edge, as described in Section 6.1.3.1. The reader is referred back to Section 6.1.3.1 for more detailed descriptions of the trends in the system behaviour.

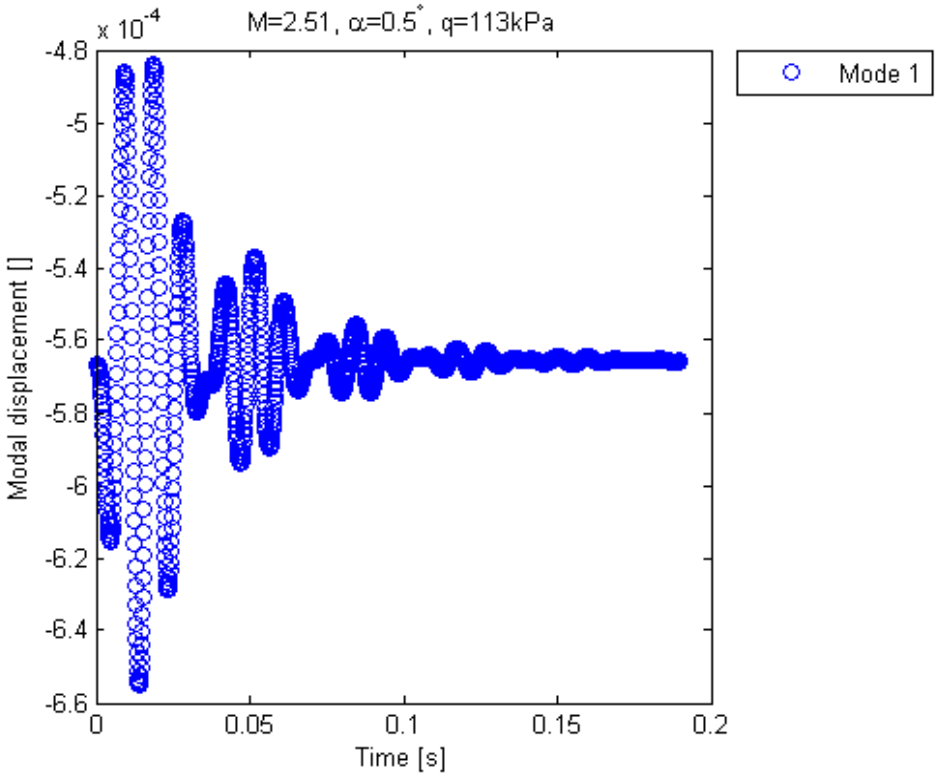


Figure 6.23: ATM-Wing Response Below Flutter Speed, Mode 1 Displacement, MATLAB (nonlinear)

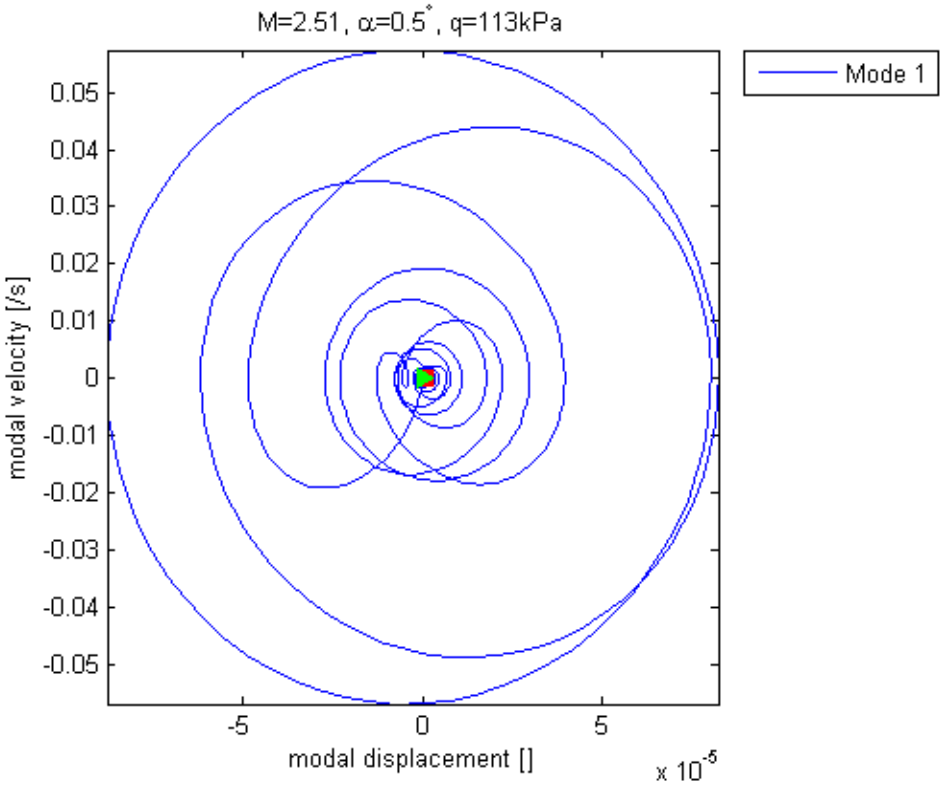


Figure 6.24: ATM-Wing Response Below Flutter Speed, Mode 1 Phase-Plane Trajectory, MATLAB (nonlinear)

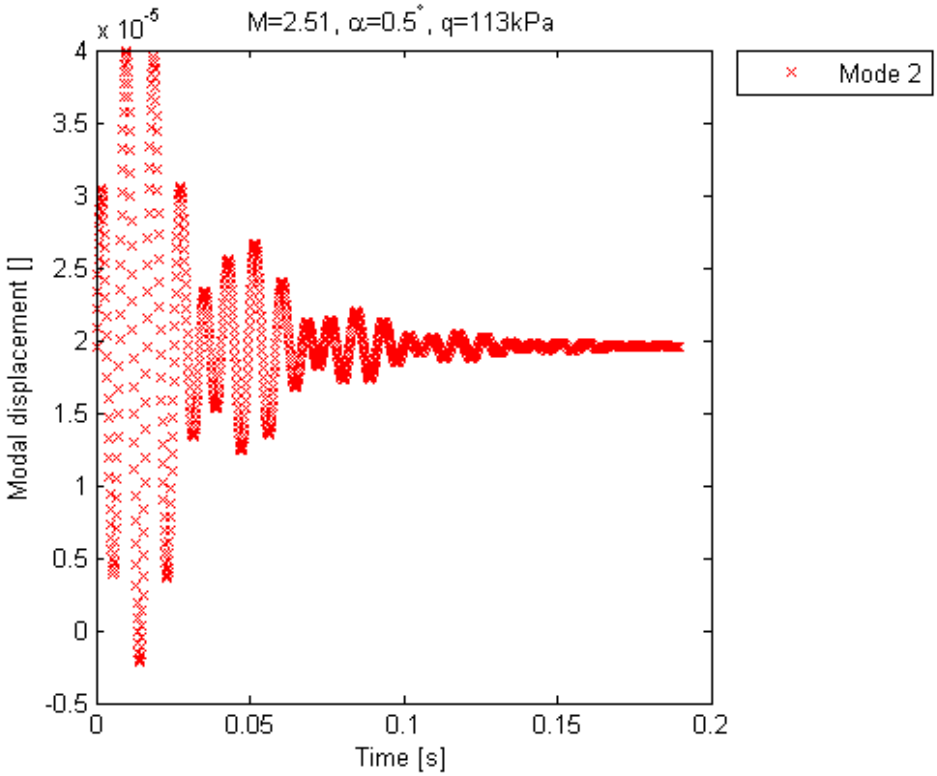


Figure 6.25: ATM-Wing Response Below Flutter Speed, Mode 2 Displacement, MATLAB (nonlinear)

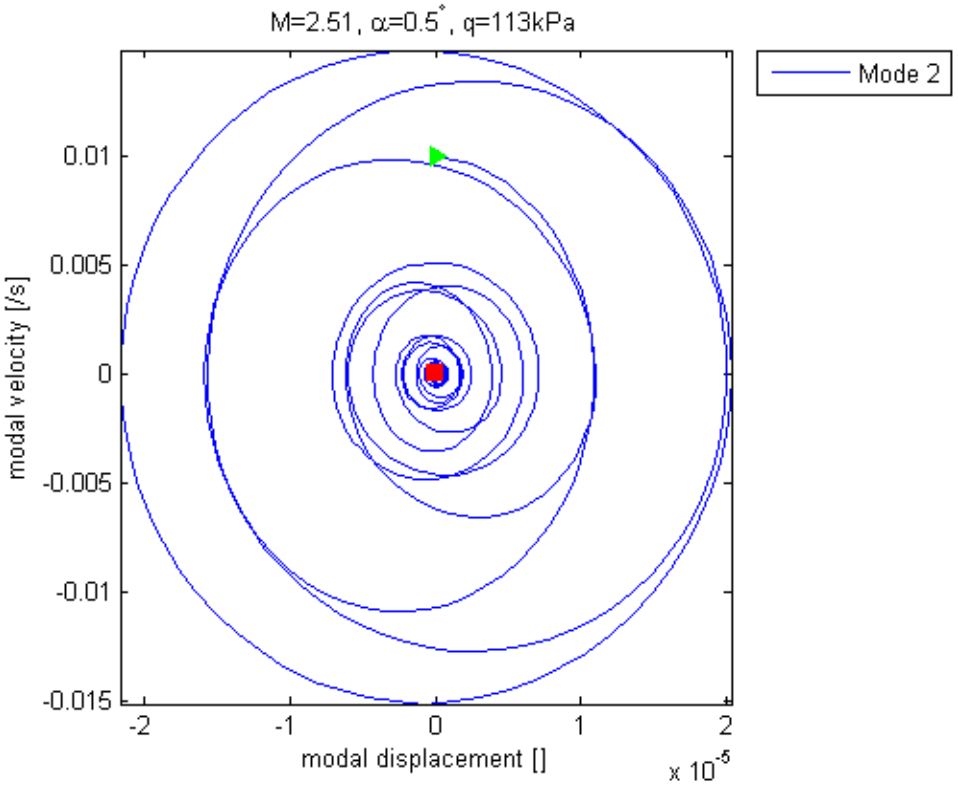


Figure 6.26: ATM-Wing Response Below Flutter Speed, Mode 2 Phase-Plane Trajectory, MATLAB (nonlinear)

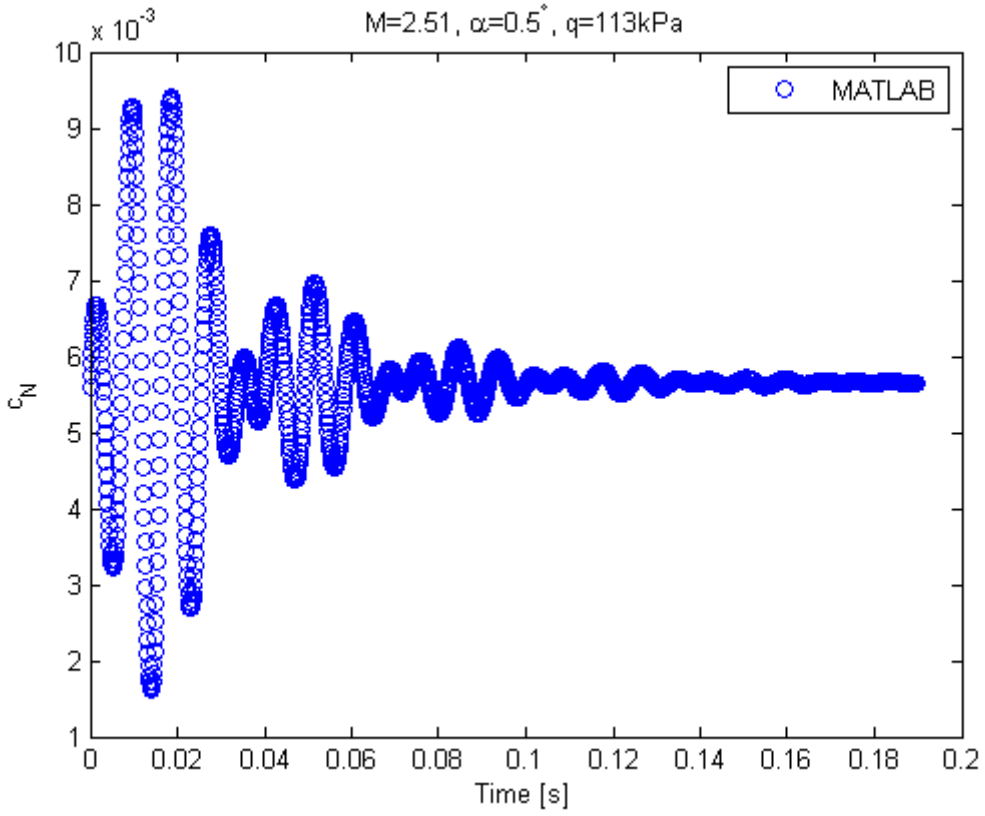


Figure 6.27: ATM-Wing Response Below Flutter Speed, cZ, MATLAB (nonlinear)

The response of Mode 1 (first bending, undamped structural mode-shape) is shown in Figure 6.23 and Figure 6.24. The modal response shows positive damping, with beating in the response. The trends are similar to those given by analysis in Edge for the response of the ATM-wing below flutter speeds.

The response of Mode 2 (first twisting, undamped structural mode-shape) is shown in Figure 6.25 and Figure 6.26. Once again, beating is present with positive damping of the response, and similar trends to those obtained in Edge are observed.

The phase-plane trajectory of Mode 2 in Figure 6.26 shows the implementation of the initial conditions in MATLAB (nonlinear) using SE/LPT. (The green triangle denotes the initial conditions, and the red square denotes the final point on the phase-plane). It is seen that the initial condition of $\dot{x}_2 = 1 \times 10^{-2}$ is properly implemented, with a smooth trajectory in the phase-plane for the subsequent motion. This is in contrast to the implementation in Edge, as seen in Figure 6.6.

The normal-force coefficient history is shown in Figure 6.27. Again, the trends of the response are similar to those seen in Edge.

6.1.4.2 Pre-Flutter System Response Near Flutter Speed

The system response to the initial modal excitation at $q = 120.5$ kPa is shown in Figure 6.28 through Figure 6.36. The system response shows similar trends to those exhibited by the analysis in Edge, as described in Section 6.1.3.2, although the system is not as near the flutter speed in the present case. The reader is referred to Section 6.1.3.2 for more detailed descriptions of the trends in the system behaviour.

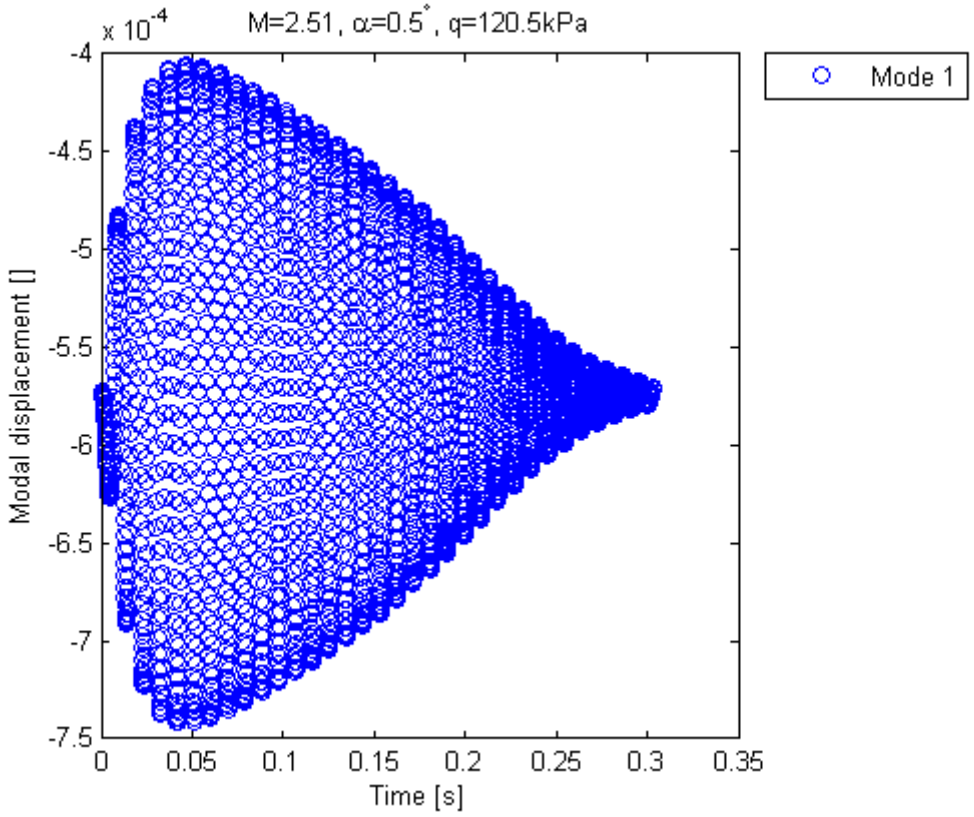


Figure 6.28: ATM-Wing Pre-Flutter Response Near Flutter Speed, Mode 1 Displacement, MATLAB (nonlinear)

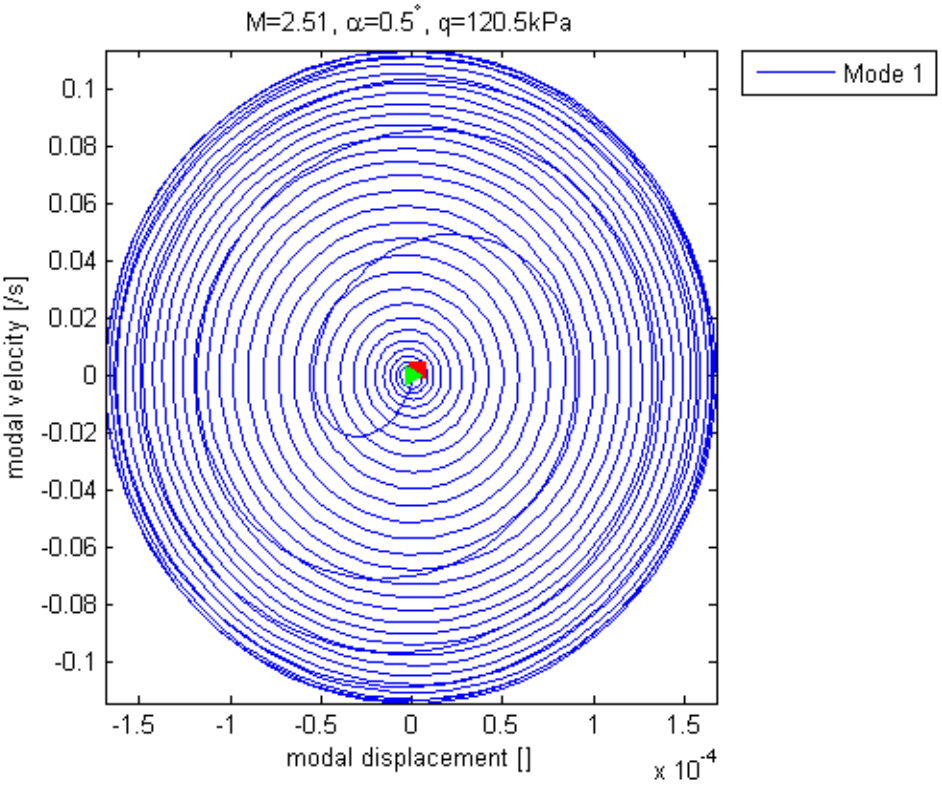


Figure 6.29: ATM-Wing Pre-Flutter Response Near Flutter Speed, Mode 1 Phase-Plane Trajectory, MATLAB (nonlinear)

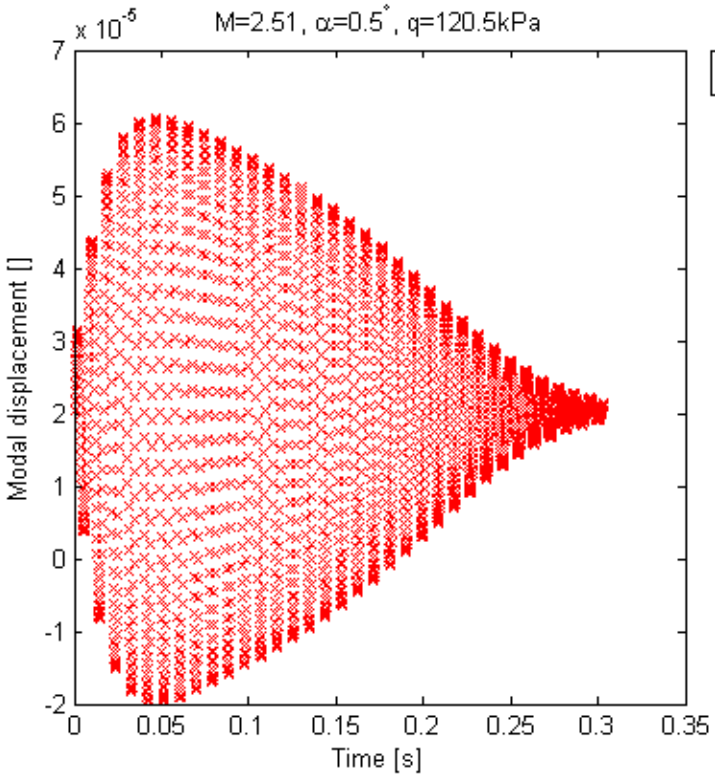


Figure 6.30: ATM-Wing Pre-Flutter Response Near Flutter Speed, Mode 2 Displacement, MATLAB (nonlinear)

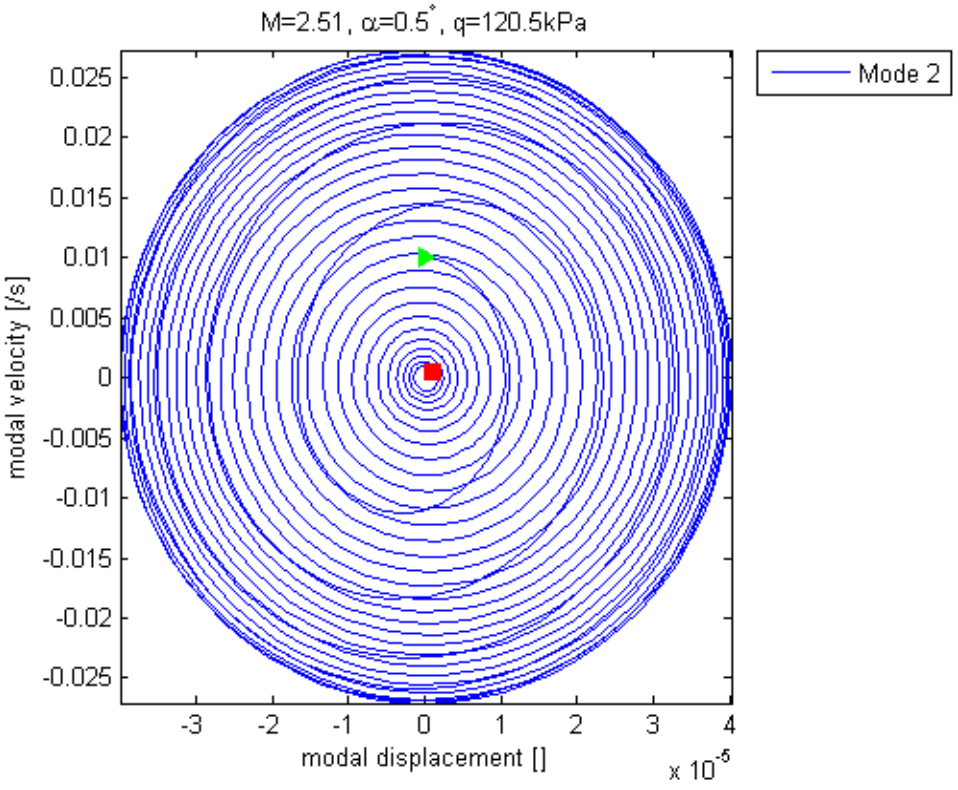


Figure 6.31: ATM-Wing Pre-Flutter Response Near Flutter Speed, Mode 2 Phase-Plane Trajectory, MATLAB (nonlinear)

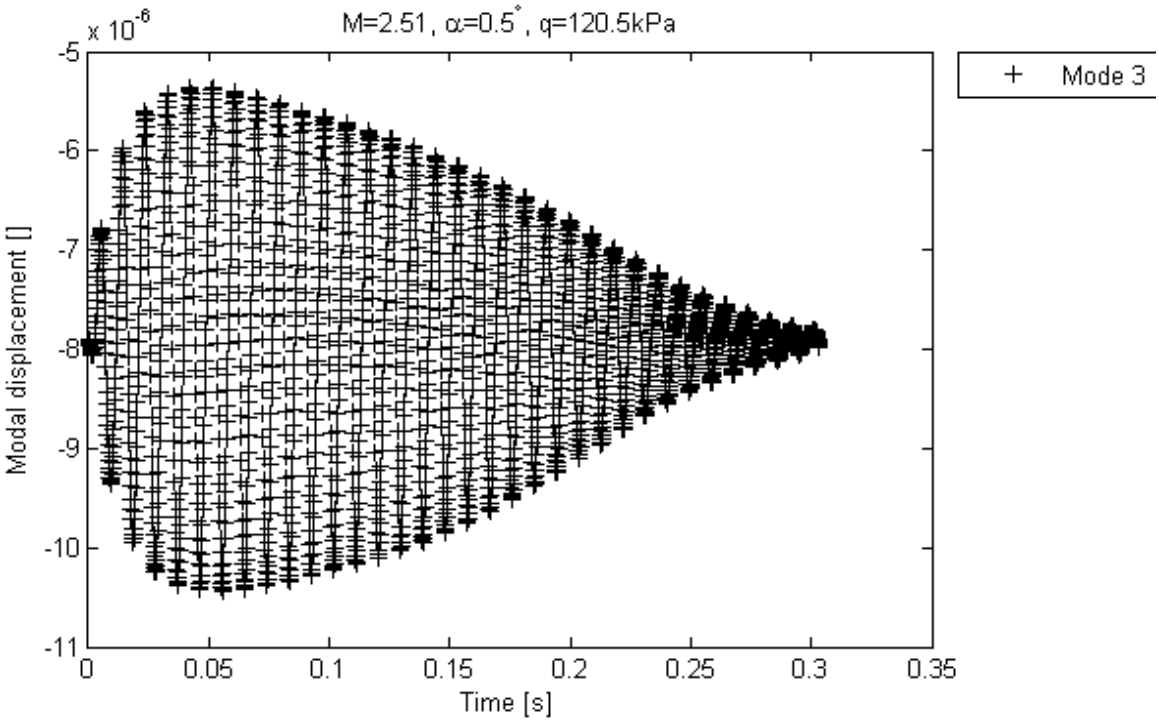


Figure 6.32: ATM-Wing Pre-Flutter Response Near Flutter Speed, Mode 3 Displacement, MATLAB (nonlinear)

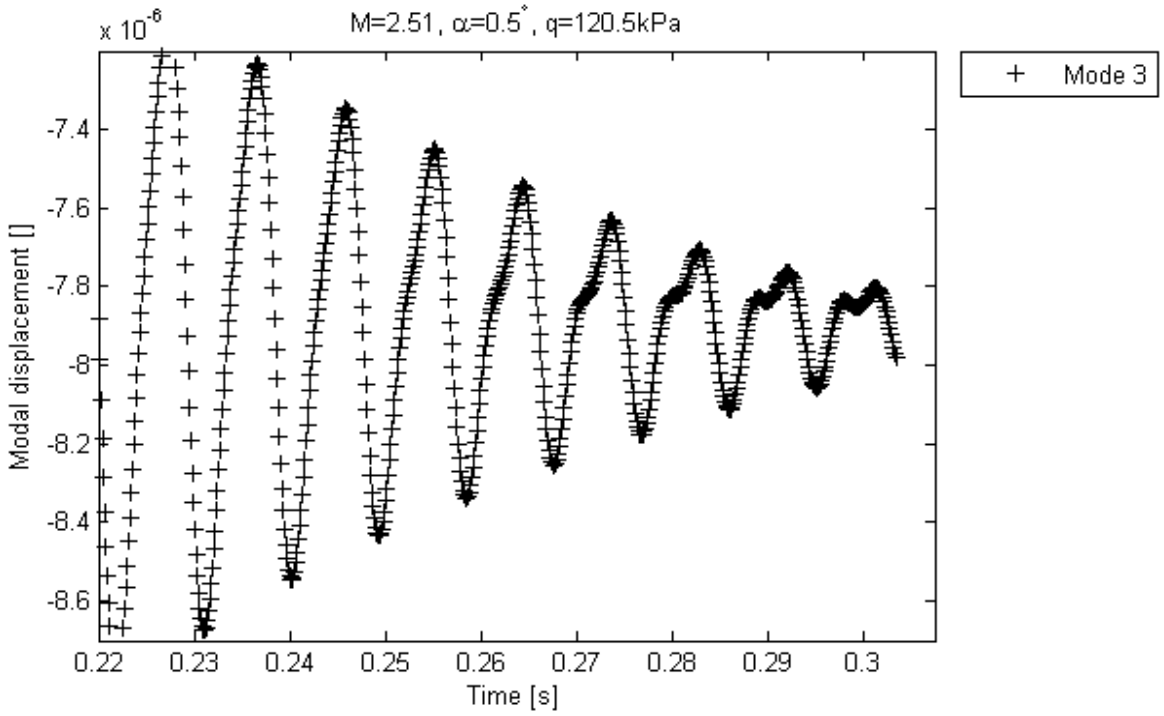


Figure 6.33: ATM-Wing Pre-Flutter Response Near Flutter Speed, Mode 3 Displacement, Transition, MATLAB (nonlinear)

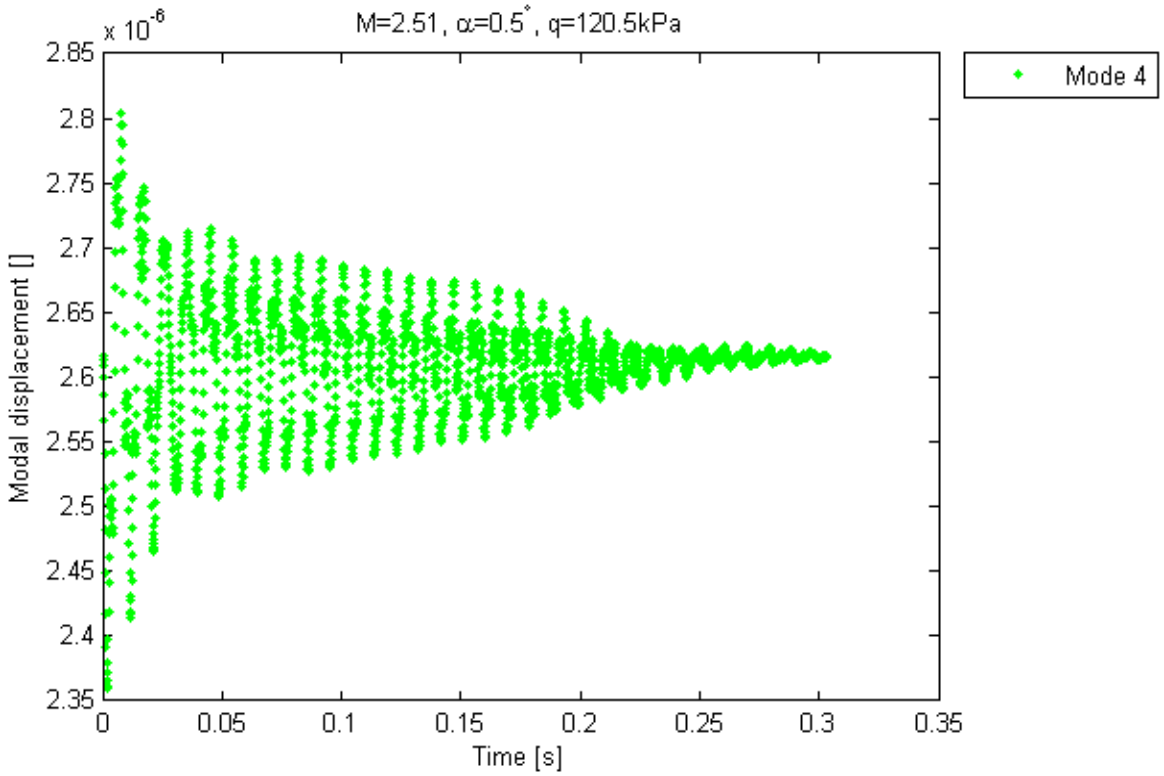


Figure 6.34: ATM-Wing Pre-Flutter Response Near Flutter Speed, Mode 4 Displacement, MATLAB (nonlinear)

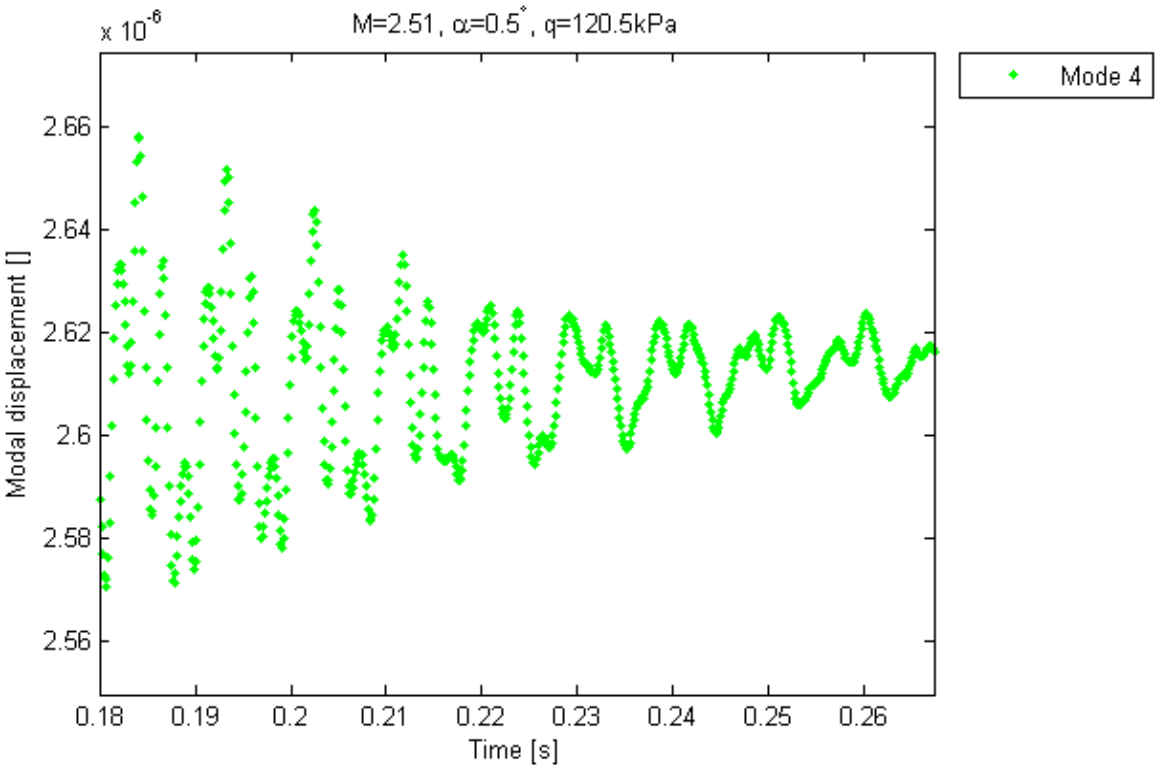


Figure 6.35: ATM-Wing Pre-Flutter Response Near Flutter Speed, Mode 4 Displacement, Transition, MATLAB (nonlinear)

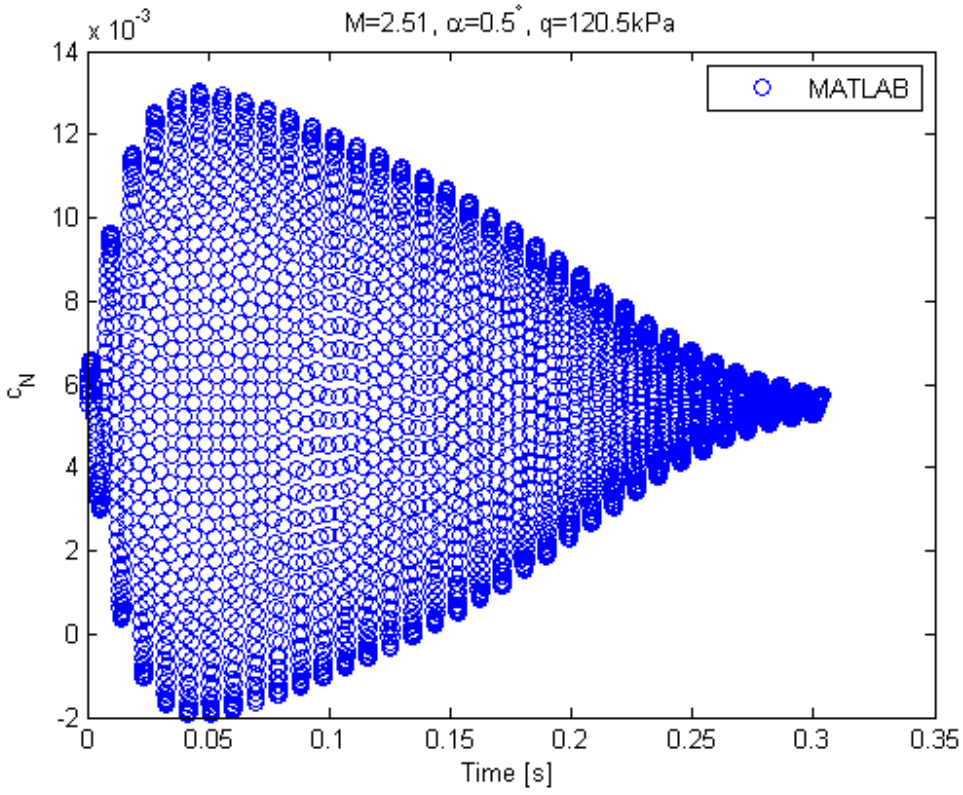


Figure 6.36: ATM-Wing Pre-Flutter Response Near Flutter Speed, cZ, MATLAB (nonlinear)

The response of Mode 1 (first bending, undamped structural mode-shape) is shown in Figure 6.28 and Figure 6.29. Positive damping of the response after an initial growth is evident; however, the sustain of the vibration in comparison to that at lower dynamic pressures (e.g., $q = 113$ kPa, Figure 6.23) shows that the system is approaching flutter speed. No beating is obvious in the response. This suggests that the frequencies of the first two aeroelastic modes are coalescing. The trends of the response are similar to those shown for the pre-flutter ATM-wing response in Edge.

The trends observed for the response of Mode 2 (first twisting, undamped structural mode-shape), as shown in Figure 6.30 and Figure 6.31, are also in agreement with those observed in the results of analysis in Edge. However, the different implementation of the initial conditions is observed in the phase-plane trajectory of Figure 6.31.

The system response at $q = 120.5$ kPa suggests the ATM-wing is near flutter.

Figure 6.32 and Figure 6.33 show the modal response of Mode 3 over two time-windows. The response suggests the presence of two signals: a dampened transient free response of high frequency (the natural frequency of the aeroelastic mode) which is evident in the tail-end of the response; and a steady-state forced response of frequency corresponding to the GAF (which is dominated by Mode 2), which dominates the initial phase of the response. No beating is evident, suggesting that (as expected), the transient natural response of Mode 3 is of significantly smaller magnitude in comparison to the forced response due to the action of the GAF.

Figure 6.34 and Figure 6.35 show the modal response of Mode 4 over two time-windows. The response of Mode 4 differs from that of Mode 3 in that the transient and forced components of the response appear to be of similar magnitude. Rather than the initial growth in response shown by Mode 3, the initial response of Mode 4 appears to be dominated by the transient component, which shows moderate damping. The transient response is seen to be of higher frequency, as expected, than the forced response.

The response of Mode 3 and Mode 4 computed in MATLAB (nonlinear) shows similar behaviour to that computed in Edge, with the transient and steady-state components being visibly distinct; however, the relative magnitudes of the components differ between the computational models used. It may also be seen that the magnitude of the response of Mode 3 in MATLAB (nonlinear) (Figure 6.32) is greater than that computed in Edge (Figure 6.12).

This suggests that the GAF associated with Mode 3 (which gives rise to the forced response) is modelled as being larger than as modelled in Edge. This is in agreement with the poor correlation of results for the response of Mode 3 and Mode 4 between SE/LPT and Edge, as seen in Section 5.8.3 and Section 5.8.4.

The normal-force coefficient history is shown in Figure 6.36. The response is again found to be similar in behaviour to the modal response of Mode 1 and Mode 2.

6.1.4.3 Post-Flutter System Response Near Flutter Speed

The system response to the initial modal excitation at $q = 120.9$ kPa is shown in Figure 6.37 through Figure 6.43. The system response shows similar trends to those exhibited by the analysis in Edge, as described in Section 6.1.3.3. The reader is referred to Section 6.1.3.3 for more detailed descriptions of the trends in the system behaviour.

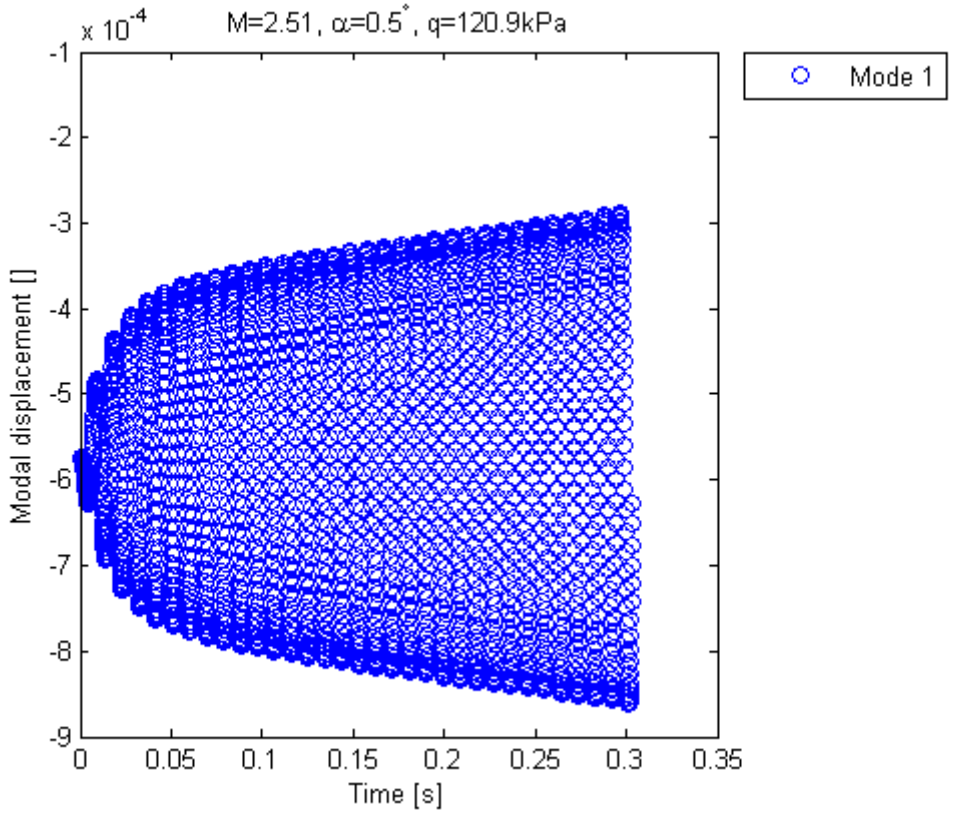


Figure 6.37: ATM-Wing Post-Flutter Response Near Flutter Speed, Mode 1 Displacement, MATLAB (nonlinear)

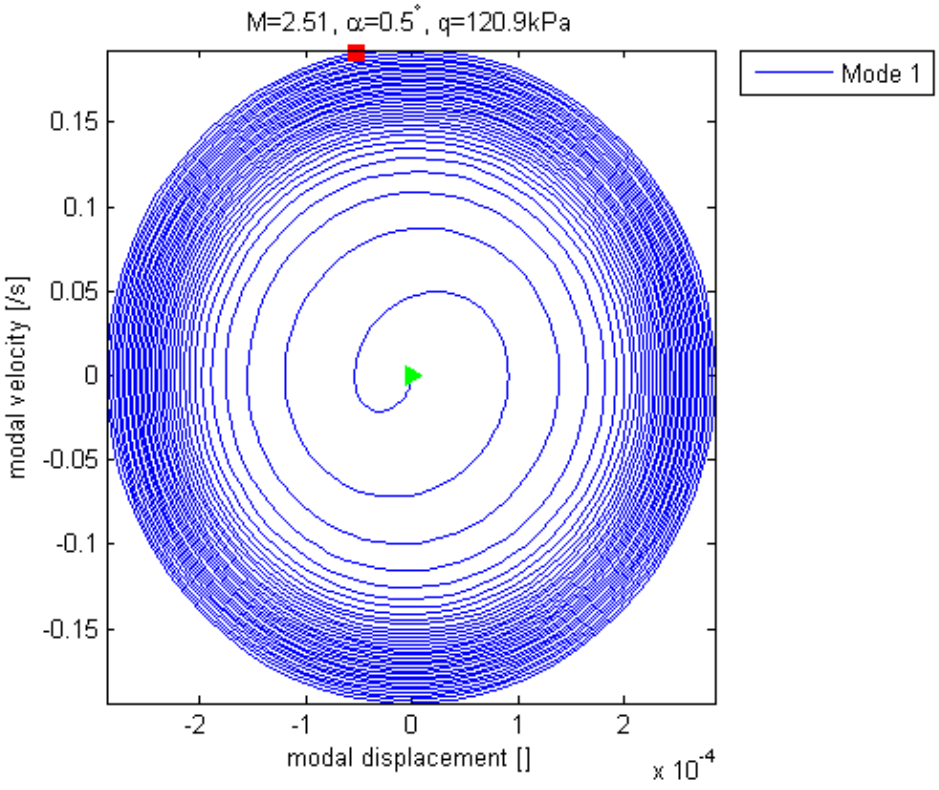


Figure 6.38: ATM-Wing Post-Flutter Response Near Flutter Speed, Mode 1 Phase-Plane Trajectory, MATLAB (nonlinear)

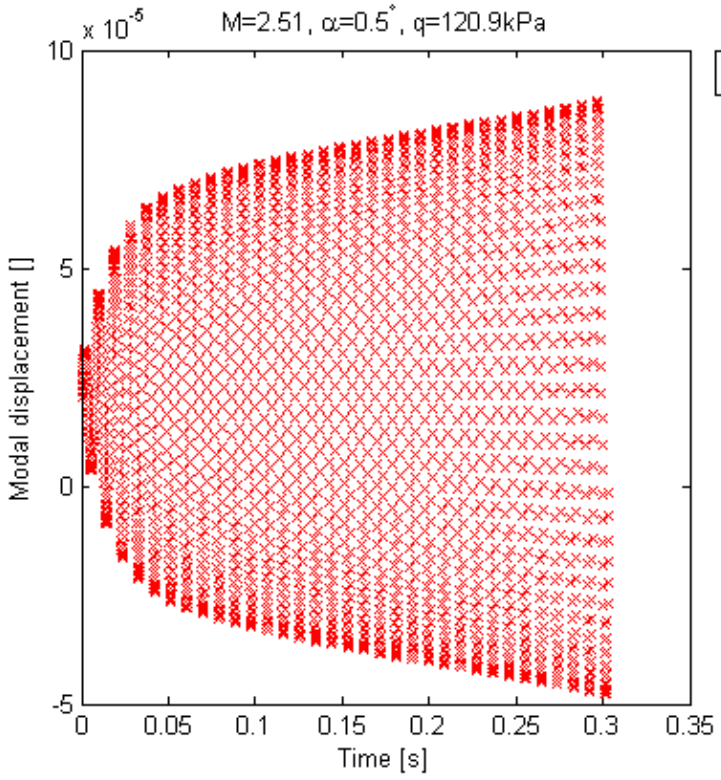


Figure 6.39: ATM-Wing Post-Flutter Response Near Flutter Speed, Mode 2 Displacement, MATLAB (nonlinear)

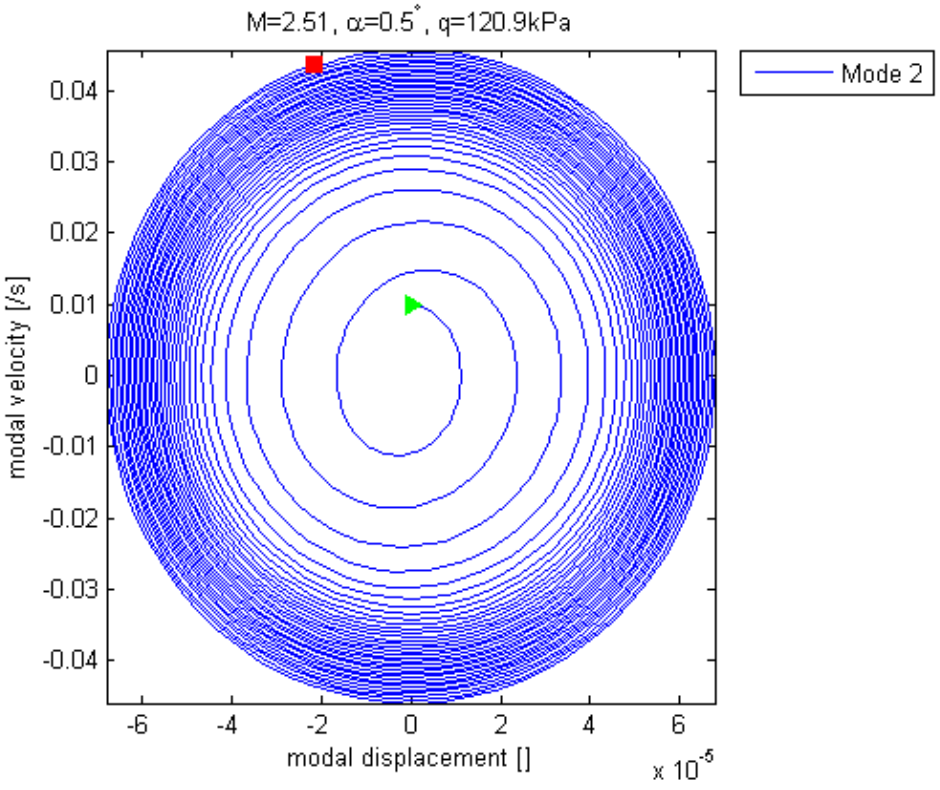


Figure 6.40: ATM-Wing Post-Flutter Response Near Flutter Speed, Mode 2 Phase-Plane Trajectory, MATLAB (nonlinear)

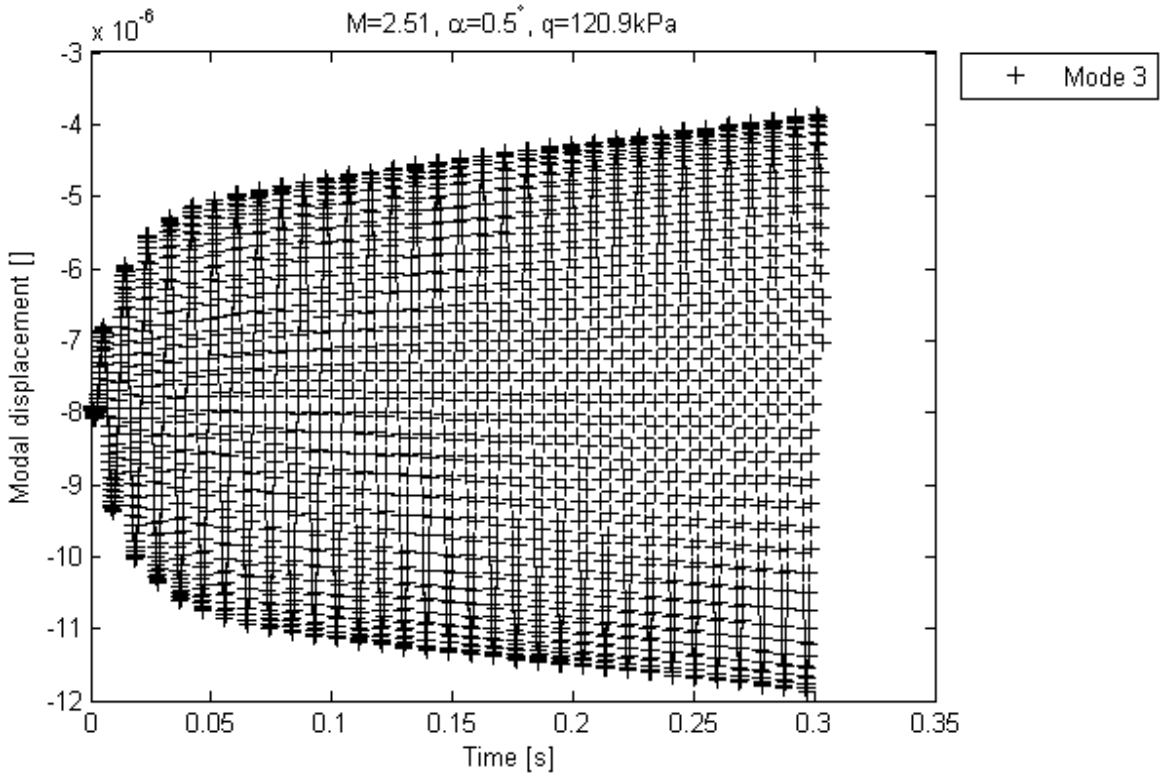


Figure 6.41: ATM-Wing Post-Flutter Response Near Flutter Speed, Mode 3 Displacement, MATLAB (nonlinear)

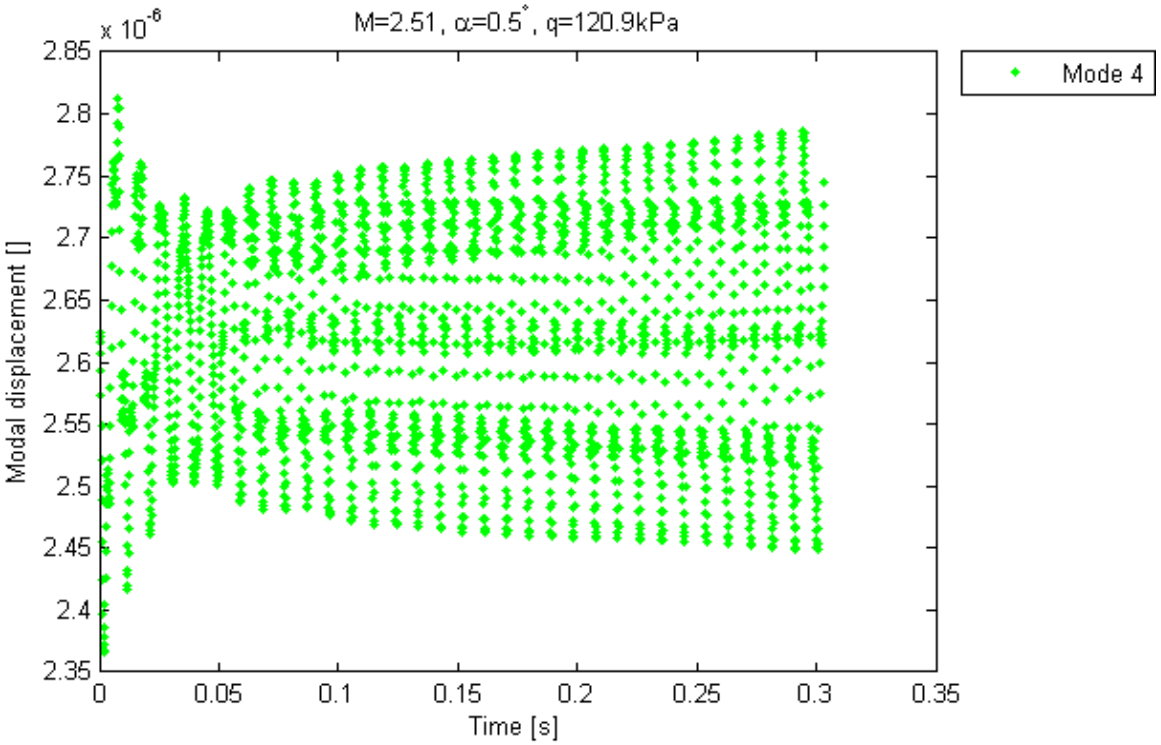


Figure 6.42: ATM-Wing Post-Flutter Response Near Flutter Speed, Mode 4 Displacement, MATLAB (nonlinear)

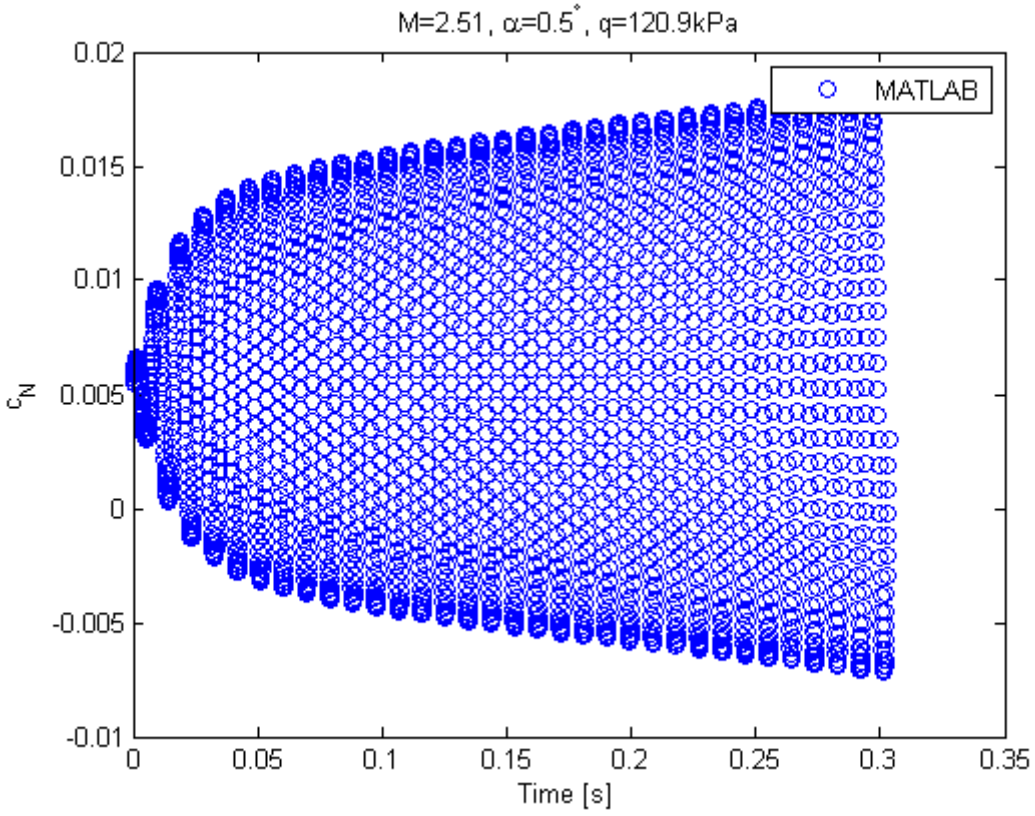


Figure 6.43: ATM-Wing Post-Flutter Response Near Flutter Speed, cZ, MATLAB

The response of Mode 1 (first bending, undamped structural mode-shape) is shown in Figure 6.37 and Figure 6.38. The response shows gradual further growth after an initial growth, showing that the aerodynamic damping is negative. Beating of the response is not evident, suggesting that the frequencies are coalescing. Similar trends are observed for the response of Mode 2 (first twisting, undamped structural mode-shape), as shown in Figure 6.39 and Figure 6.40.

The trends of the modal response of Mode 1 and Mode 2 obtained in MATLAB (nonlinear) agree with those obtained in Edge. It is evident that, for the analysis in MATLAB (nonlinear) at $\mathrm{q} = 120.9$ kPa, the ATM-wing is post-flutter, close to the flutter speed.

Figure 6.41 and Figure 6.42 show the modal response of Mode 3 and Mode 4, respectively. From the steady growth of the response of Mode 3, it is not visually obvious that the response consists of a transient component and a steady forced component; this was similarly noted at $q = 120.5$ kPa. The response of Mode 4, however, shows the two components, with an initial decay from the initially dominant transient component transitioning to the steady growth of the forced component. From the behaviour of the transient component, it is evident that Mode 4 is positively damped, although the response grows due to the growing GAF.

The normal-force coefficient history is shown in Figure 6.43 and reflects the growth in the GAF, which is dominated by the motion of Mode 2.

6.1.4.4 Modal Parameter Estimation

For the system identification of the modelling in MATLAB (nonlinear), the same pre-processing of the total displacement was used as for Edge, as outlined in Section 6.1.3.4.

The modal parameters were obtained from the system model estimated using the `armax` system identification function in MATLAB, with order [4,1] (an ARMA model with an AR component of order 4 and a MA component of order 1). System identification was performed using the displacements at the trailing-edge (as opposed to the leading-edge, for Edge) of the wing-tip, as the results obtained were a better representation of the time-history of response.

The estimated modal parameters are shown in Figure 6.44, with the flutter dynamic pressure as estimated from the ARMA model being shown by the solid black line ($q_F \approx 120.6$ kPa).

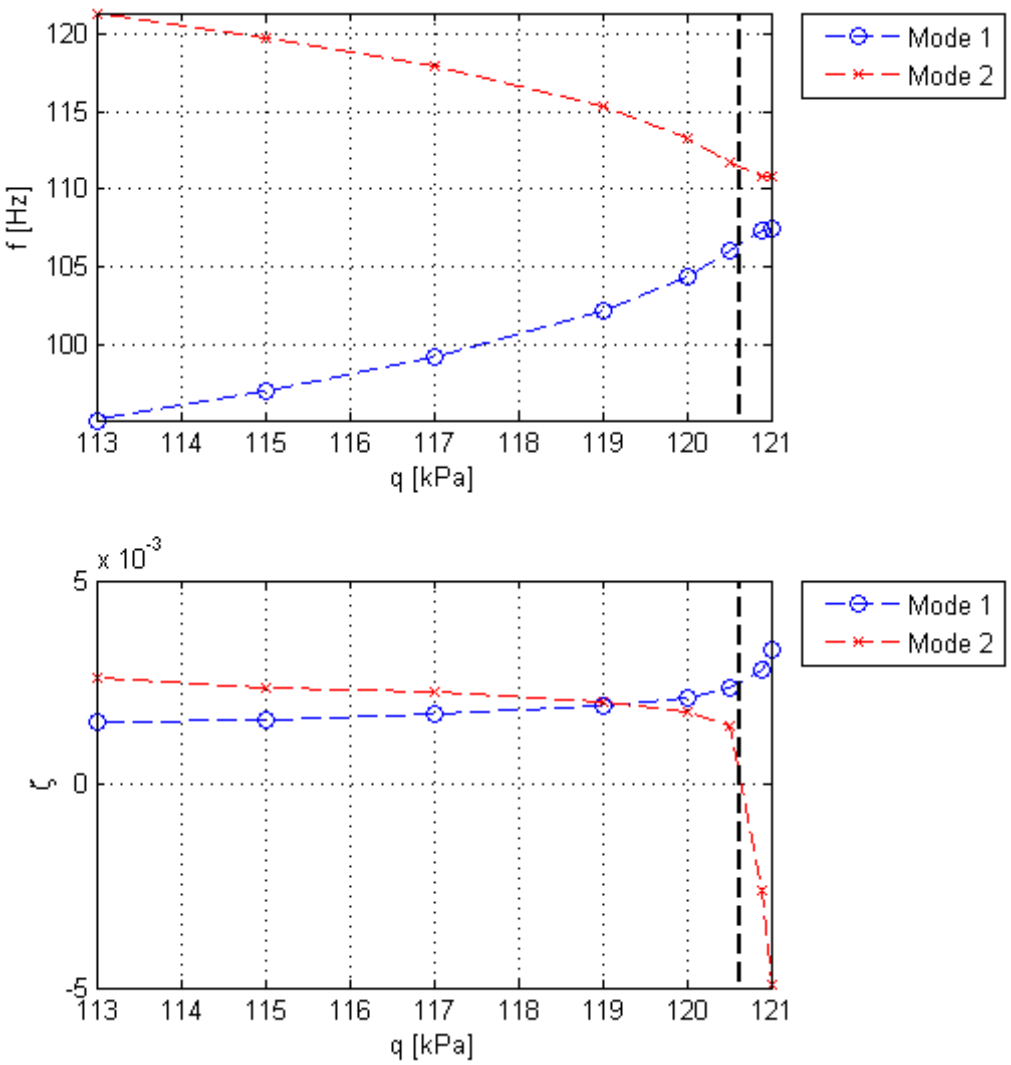


Figure 6.44: ATM-Wing Estimated Modal Parameters, MATLAB (nonlinear)

The predicted modal frequencies at $q = 113$ kPa compare well with frequencies directly estimated from the time-history of the total displacement. The beat frequency at $q = 113$ kPa may be estimated to be approximately $f_2 - f_1 \approx 28$ Hz, which agrees well with the separation of the modal frequencies of $f_2 - f_1 \approx 26$ Hz at $q = 113$ kPa in Figure 6.44. This estimation may also be performed for the modal displacement histories in Figure 6.23 and Figure 6.25 for Mode 1 and Mode 2, respectively, with similar results being estimated.

The trends in the modal damping from the identified system model compare significantly better to typical aeroelastic trends (see Section 2.7) than the trends from the system model identified for the Edge data do (see Figure 6.22). From Figure 6.44, it is seen that the pitch mode (Mode 2) experiences a very sharp drop in damping close to the flutter speed

(estimated by system identification to be $q_F \approx 120.6$ kPa). This is in good agreement with the hard-flutter of the TM-wing, as tested by Matsuzaki [55].

However, the magnitude of the damping coefficients estimated is drastically too small -- inspection of the modal response in Figure 6.23 and Figure 6.25 suggests significantly higher damping coefficients than the system-estimated values of ≈ 0.002. The source of the error in the estimation of modal damping coefficients using the ARMA model could not be identified. It is hypothesized that a refinement in the pre-processing band-pass filtering could yield improved estimation of the damping coefficients.

The flutter dynamic pressure as estimated from the ARMA model is approximately $q_F \approx 120.6$ kPa. However, the time-history of modal responses in Section 6.1.4.2 and Section 6.1.4.3, the flutter dynamic pressure is closer to $q = 120.9$ kPa, and was consequently estimated to be $q_F \approx 120.8$ kPa. This is 6.4% higher than the experimental flutter dynamic pressure of $q_F = 113.5$ kPa. as determined by Matsuzaki [55].

6.1.5 Analysis in MATLAB (linear)

The aeroelastic free response of the ATM-wing was analysed in MATLAB using the linearized coupled aeroelastic equations formulated from SE/LPT over a range of dynamic pressures. The linearization of the GAFs about the equilibrium deflection allowed for the system stability to be directly assessed using eigenanalysis. The computation time of the system response and stability for a given flight condition using MATLAB (linear) was thereby considerably shorter than the computations in MATLAB (nonlinear) and Edge. This allowed a large number of points to be analysed, and made the rapid generation of flutter envelopes feasible. A linearization step size of $\Delta x = 1 \text{ x } 10^{-4}$ was used; the recommended step-size based upon Δx_2 producing 2° twist at the wing-tip was $\Delta x_{recc} = 2.4 \text{ x } 10^{-4}$.

The flutter dynamic pressure was determined as $q_F \approx 124.5$ kPa.

6.1.5.1 Time-History of Response

Selected time-histories of modal responses at various dynamic pressures will be shown to give an example of the system behaviour. The response of Mode 2 (first twisting, undamped

structural mode-shape) will shown at dynamic pressures below flutter and near flutter. The response of Mode 3 will be shown at a selected dynamic pressures to highlight specific phenomena captured by the modelling.

Figure 6.45 shows the response of Mode 2 (first twisting, undamped structural mode-shape) at $q = 120$ kPa, which is below the flutter dynamic pressure. Beating is evident in the response, with both the contributing components being moderately damped. Thus, the beating due to the aeroelastic mode-shapes contributing to the structural modal response is captured, even with linearized GAFs.

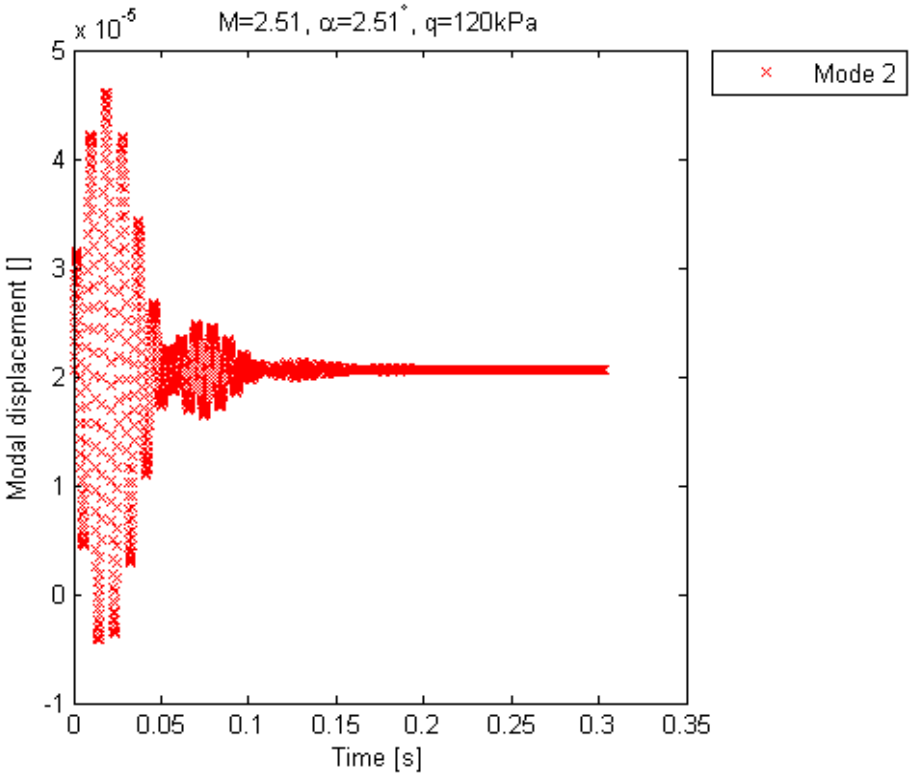


Figure 6.45: ATM-Wing Response Below Flutter Speed, Mode 2 Displacement, MATLAB (linear)

In Figure 6.46, the response of Mode 2 is shown at $q = 124$ kPa, very close to the flutter dynamic pressure. No beating is visually obvious, although the damping of the response following an initial growth is seen to be positive. The sustain of the response shows that the damping is approaching zero.

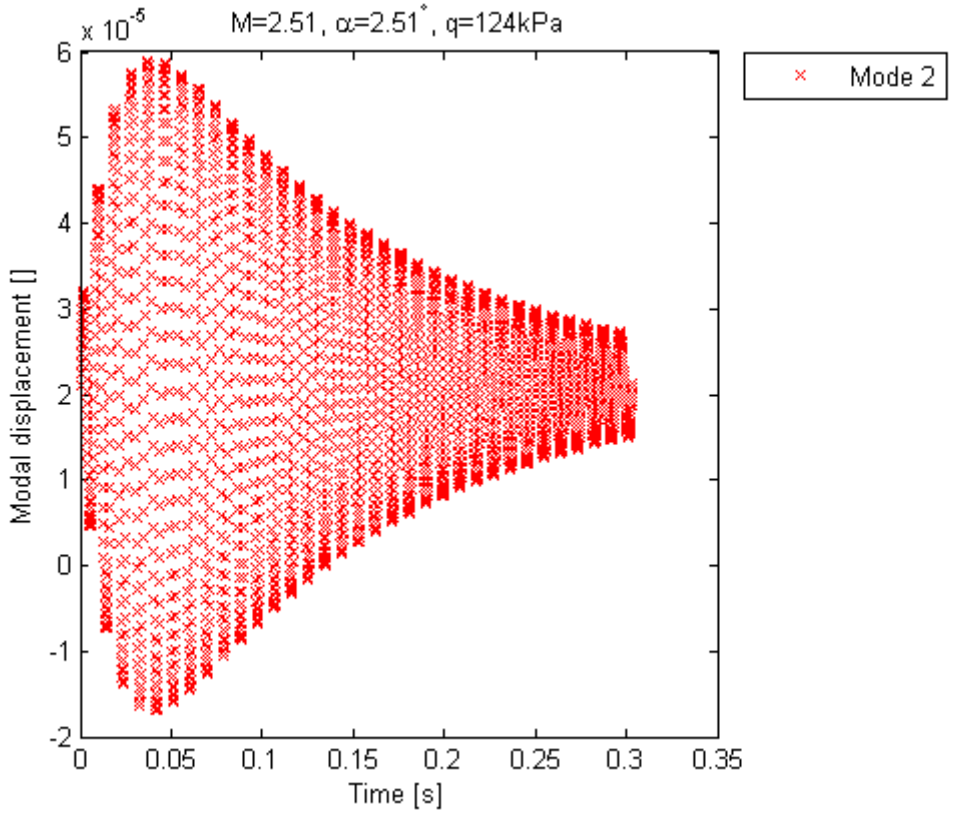


Figure 6.46: ATM-Wing Pre-Flutter Response Near Flutter Speed, Mode 2 Displacement, MATLAB (linear)

The sharp transition to flutter is evident by the change in the response of Mode to between $q = 124$ kPa and $q = 125$ kPa. The response at $q = 125$ kPa is shown in Figure 6.47 on page 183. Once again, no beating is visually evident; the damping of the forced response is clearly negative, with the continued growth of the response.

Examination of the response of Mode 3 at a dynamic pressure sufficiently below flutter conditions shows that modal response is modelled as consisting of a transient free-response component of higher frequency and of a steady forced component of lower frequency. This is shown in Figure 6.48. At higher dynamic pressures, the transient component of the response of Mode 3 is indistinguishable from the steady forced component; this was previously noted with the response as modelled in MATLAB (nonlinear), in Section 6.1.4.2.

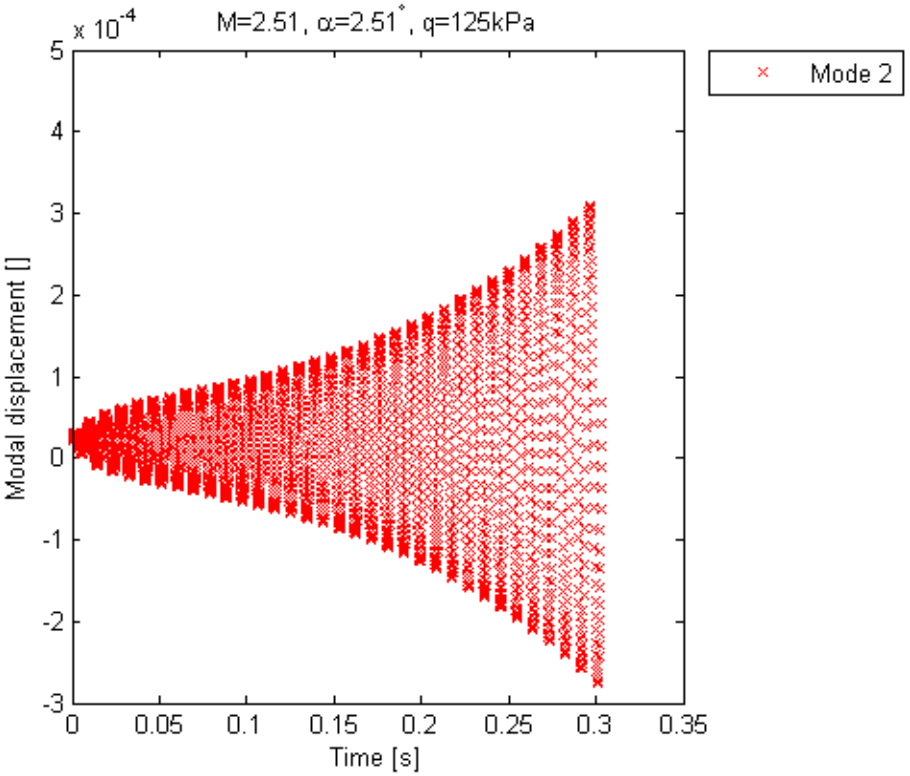


Figure 6.47: ATM-Wing Post-Flutter Response Near Flutter Speed, Mode 2 Displacement, MATLAB (linear)

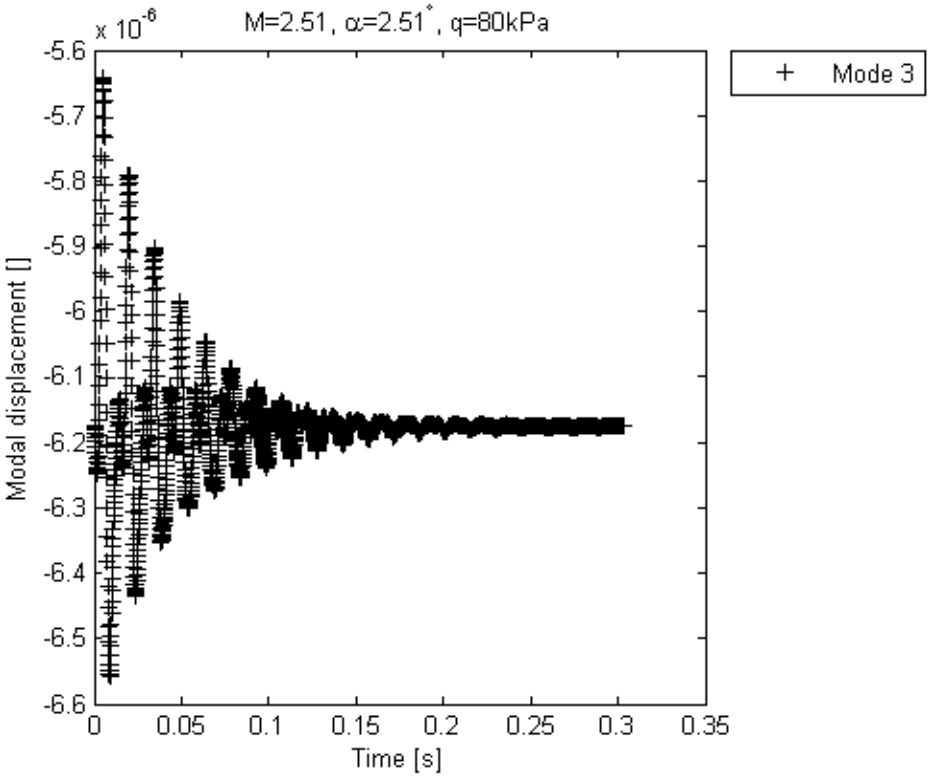


Figure 6.48: ATM-Wing Response Below Flutter Speed, Mode 3 Displacement, MATLAB (linear)

6.1.5.2 System Eigenanalysis and Modal Parameters

The stability of the system was assessed through eigenanalysis of the modal-order linearized aeroelastic system of equations. This yielded the roots of the system, from which the modal parameters could be identified as per Equation (2.50). The behaviour of the modal parameters as well as of flutter prediction metrics with dynamic pressure was investigated.

The roots of the linearized aeroelastic system of equations were determined through eigenanalysis, and the trajectory of the roots through the complex-plane is shown in Figure 6.49. Green triangles denote the location of the roots at $q = 60$ kPa, and red squares denote the location of the roots at $q = 125$ kPa. The roots associated with the first six modes are shown, with the roots associated with higher modes being located increasingly higher up on the imaginary axis (the higher modes have higher frequencies).

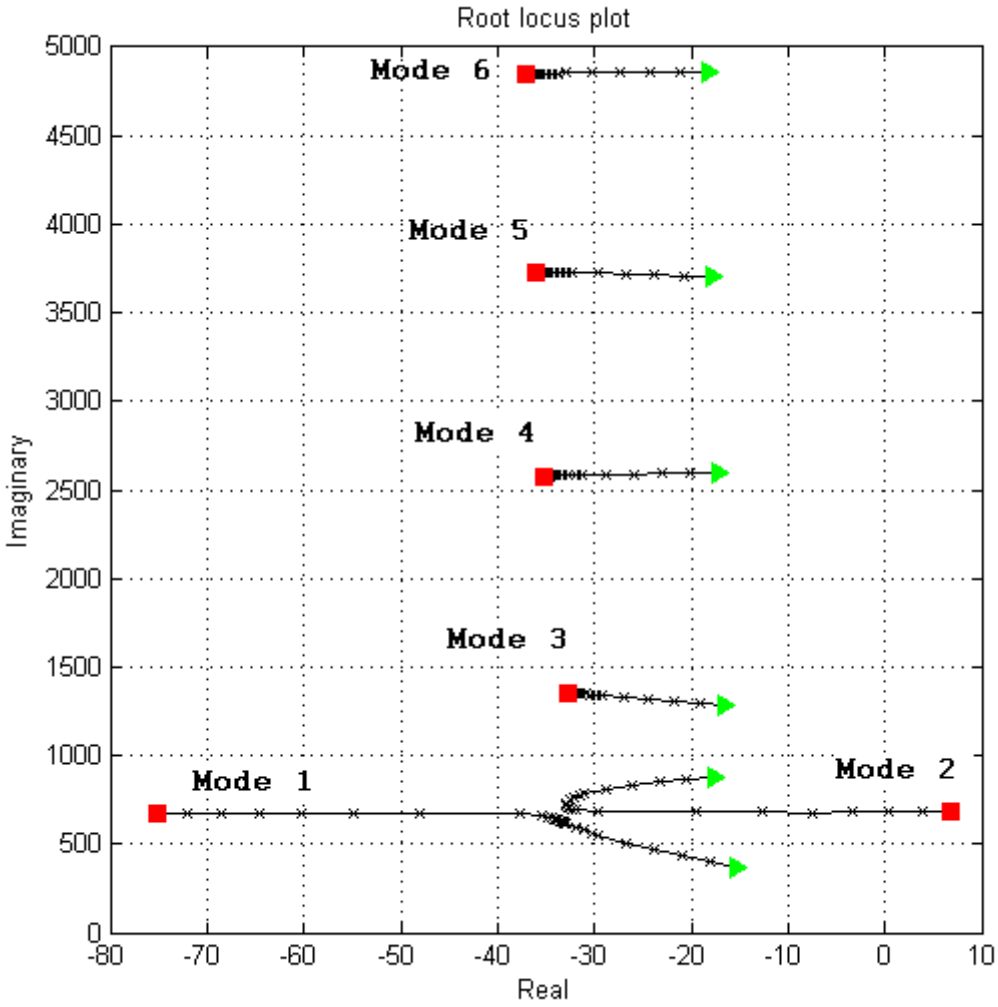


Figure 6.49: ATM-Wing System Root Locus Plot, MATLAB (linear)

Several trends may be extracted from the root locus in Figure 6.49. Firstly, it is noted that as the dynamic pressure is increased, the damping ratio (indicated by far into the left-hand plane the root is along the real axis) of all the modes initially increases. Together with this, the frequencies (indicated by the vertical location of the root on the complex-plane) of the first two modes (the lowest roots on the plane) are seen to approach one another. This initial increase in damping and coalescence of frequencies is typical of aeroelastic systems (see Section 2.7).

Secondly, as the dynamic pressure is increased further, the frequencies of the first two modes asymptotically approach one another, accompanied by a divergence of the damping ratios of Mode 1 and Mode 2; the damping ratio of Mode 1 increases, whilst the damping ratio of Mode 2 is seen to decrease and cross over into the right-hand plane -- indicating the transition to flutter. This is also typical behaviour. It is to be noted that the divergence of the damping ratios is very rapid, and the turn in the trajectory of the root associated with the flutter mode is very sharp -- this is an indicator of hard flutter occurring.

Finally, the independence of the behaviour of Mode 3 from the behaviour of Mode 1 and Mode 2 show that the flutter is 2-mode. Mode 2 is seen to be the flutter mode which couples with Mode 1.

These trends are more obviously displayed when considering the behaviour of the modal parameters, as shown in Figure 6.50 on page 186. Here, the frequency coalescence of Mode 1 and Mode 2 is clearly seen. Upon closer inspection, as per Figure 6.51 on page 187, it is seen that the frequencies are modelled as coalescing before the onset of flutter, with the frequency of Mode 2 at flutter being $f_F \approx 108$ Hz. This is in contrast to the results of the estimated system parameters from nonlinear analysis in Edge and MATLAB (nonlinear), in which flutter is reached whilst Mode 1 and Mode 2 are separated by at least 5Hz. However, the flutter frequency (frequency of Mode 2) predicted by MATLAB (linear) of $f_F \approx 108$ Hz is in good agreement with that predicted by Edge ($f_F \approx 107$ Hz) and by MATLAB (nonlinear) ($f_F \approx 112$ Hz).

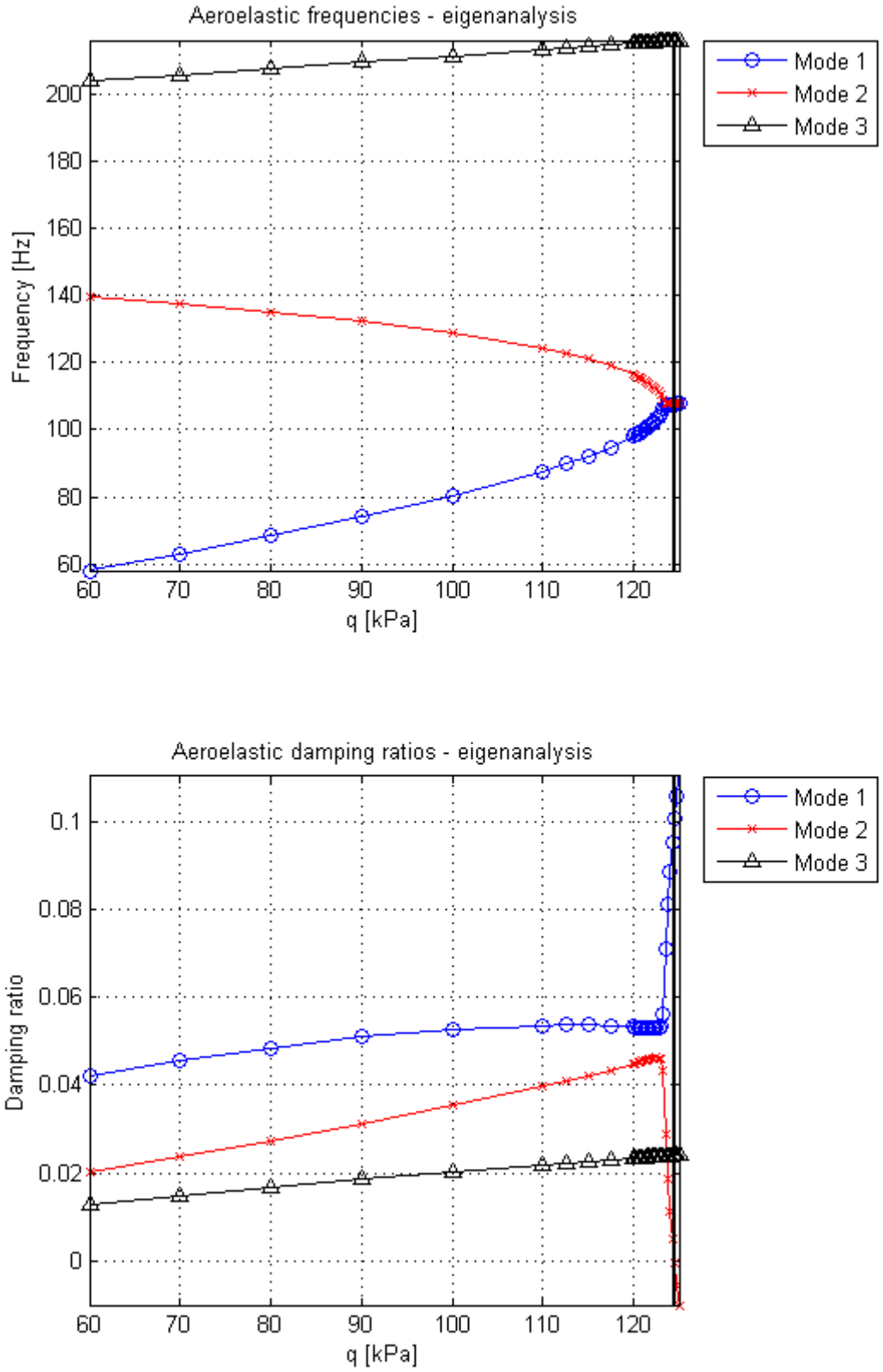


Figure 6.50: ATM-Wing Modal Parameter Variation with Dynamic Pressure, MATLAB (linear)

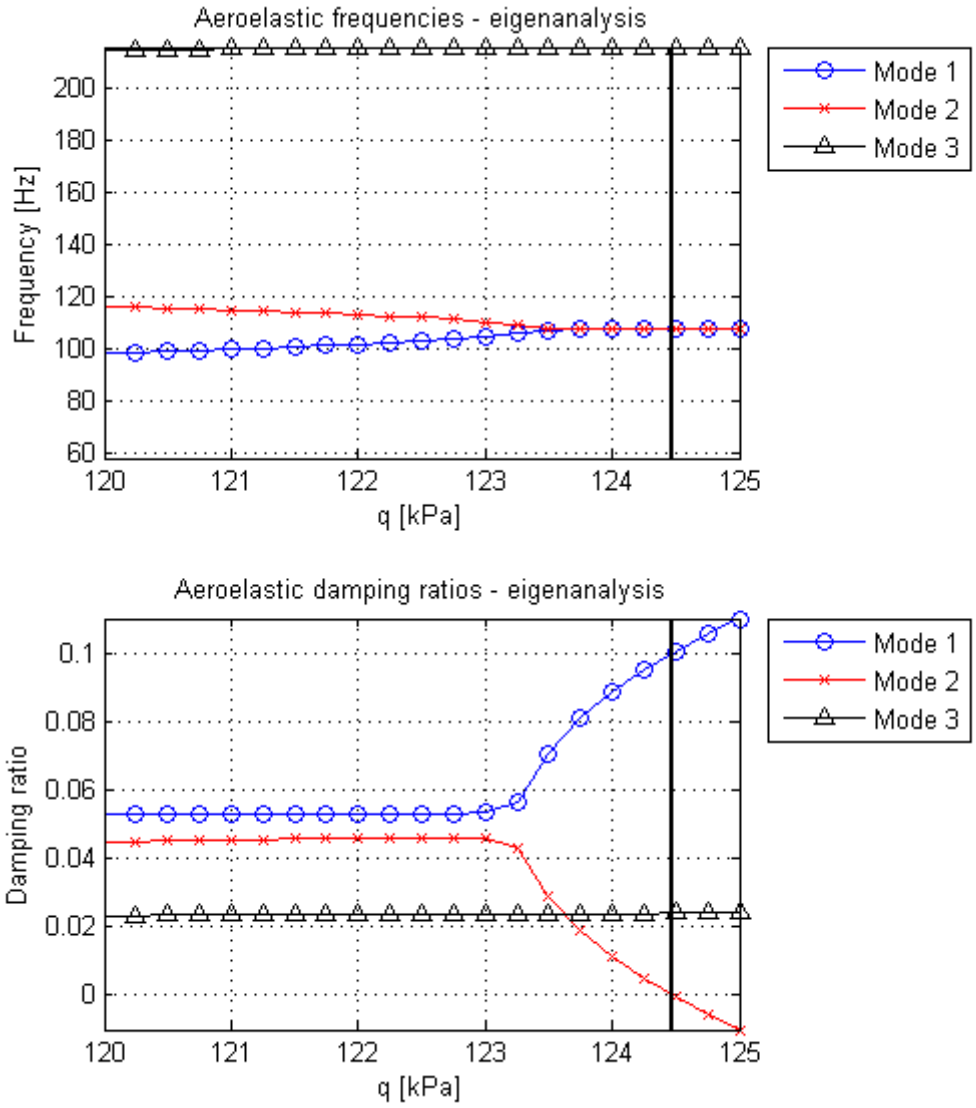


Figure 6.51: ATM-Wing Modal Parameter Variation with Dynamic Pressure Near Flutter, MATLAB (linear)

Also noted from Figure 6.50 and Figure 6.51, the drop in damping of Mode 2 is very sharp, indicating hard flutter; there is only a difference of approximately 1.2 kPa between the first sign of a decrease in damping of Mode 2 (around $q \approx 123.3$ kPa) and flutter. From the damping trend, the flutter dynamic pressure is seen to be approximately $q_F \approx 124.5$ kPa. This is 9.7% higher than the experimental flutter dynamic pressure determined by Matsuzaki [55].

The variation of the 2-mode Zimmerman-Weissenburger flutter margin (see Section 2.9.1) over the range of dynamic pressures is shown in Figure 6.52. The flutter margin was determined for coupling of different pairs of modes to investigate the behaviour of the flutter

margin if the coupling modes are incorrectly chose. It is seen that as long the flutter mode (Mode 2) is included, the flutter margin computed will become negative after flutter; however, the behaviour of the incorrectly chosen flutter margin before flutter will not follow the desired trend. The desired trend is that shown by the flutter margin based on the coupling modes - Mode 1 and Mode 2; a very nearly linear variation in the flutter margin with dynamic pressure is seen. The flutter margin crossed the x-axis at $q_F = 124.47$ kPa. The near-linear variation of the flutter margin lends itself to rapid prediction of the flutter point.

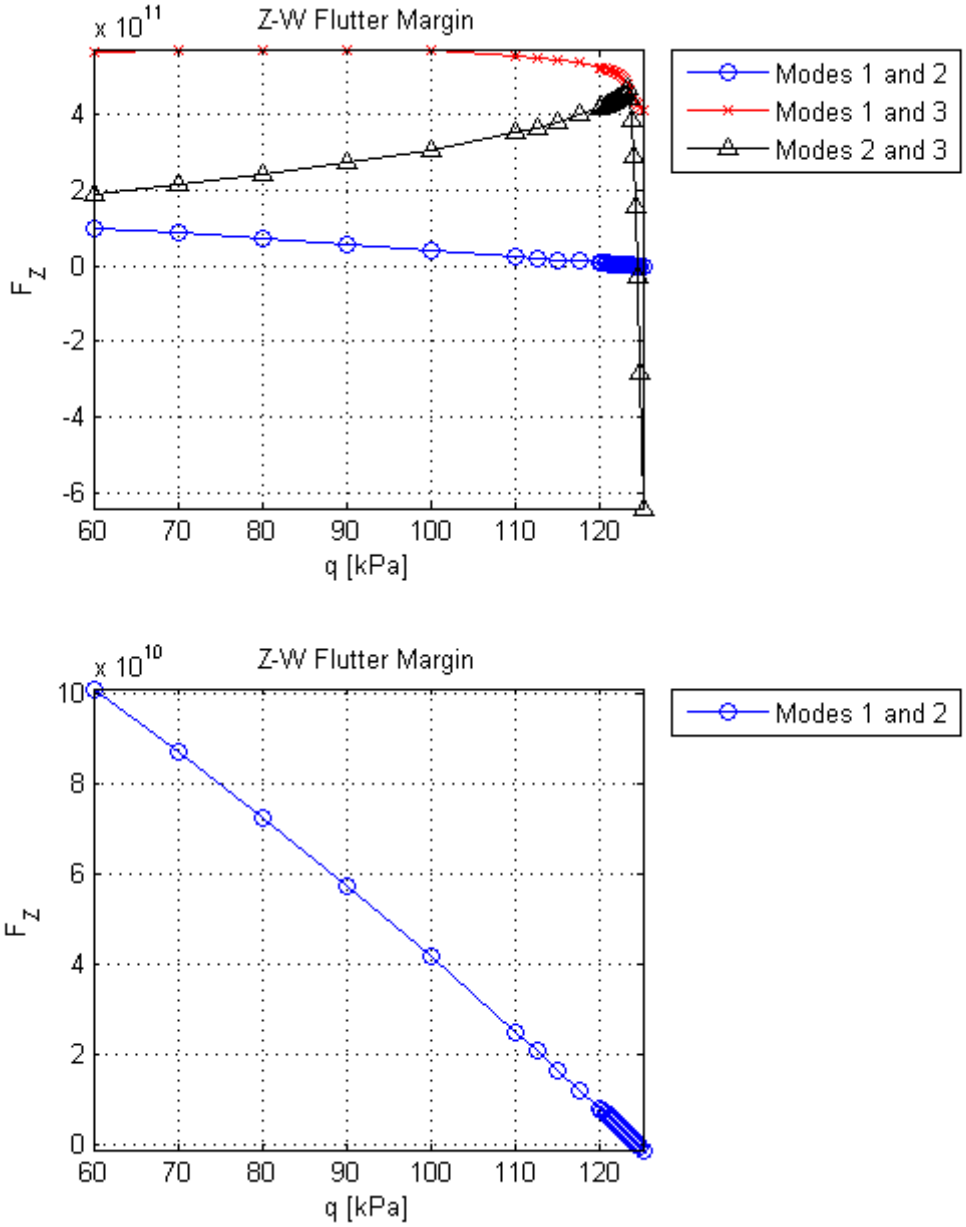


Figure 6.52: ATM-Wing Zimmerman-Weissenberger Flutter Margin Variation with Dynamic Pressure, MATLAB (linear)

The variation of the envelope function shape parameter with dynamic pressure was also investigated, as shown in Figure 6.53. The shape parameter was computed using Equation (2.62) in order that at flutter, $S^* = 0$. The shape parameter was evaluated from the modal response of Mode 1 and Mode 2. It may be seen that the behaviour of the parameter under hard flutter is not useful for flutter prediction, and will give highly non-conservative estimates of the flutter speed if extrapolated from points not very close to the flutter point. The shape parameter crossed the x-axis at $q = 124.4$ kPa for both modes analysed.

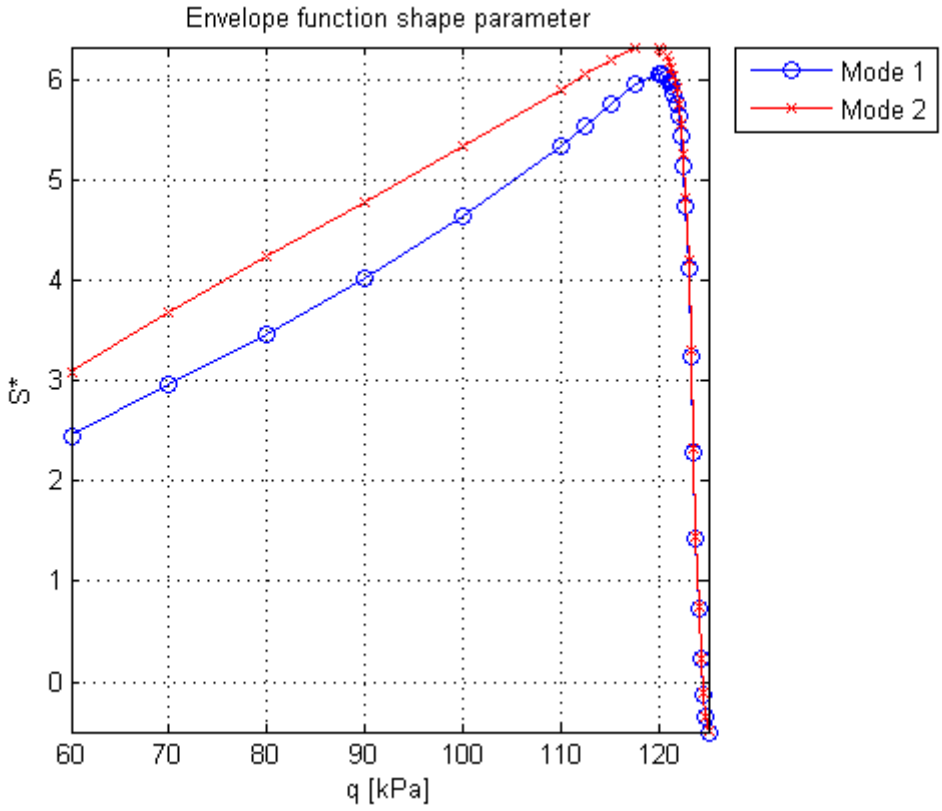


Figure 6.53: ATM-Wing Envelope Function Shape Parameter Variation with Dynamic Pressure, MATLAB (nonlinear)

6.1.6 Comparison of Analysis Results

A comparison of the variation in frequencies modelled by Edge, MATLAB (nonlinear), and MATLAB (linear) is given in Figure 6.54. The experimental flutter frequency of $q_F = 113.5$ kPa as determined by Matsuzaki [55] is included for reference.

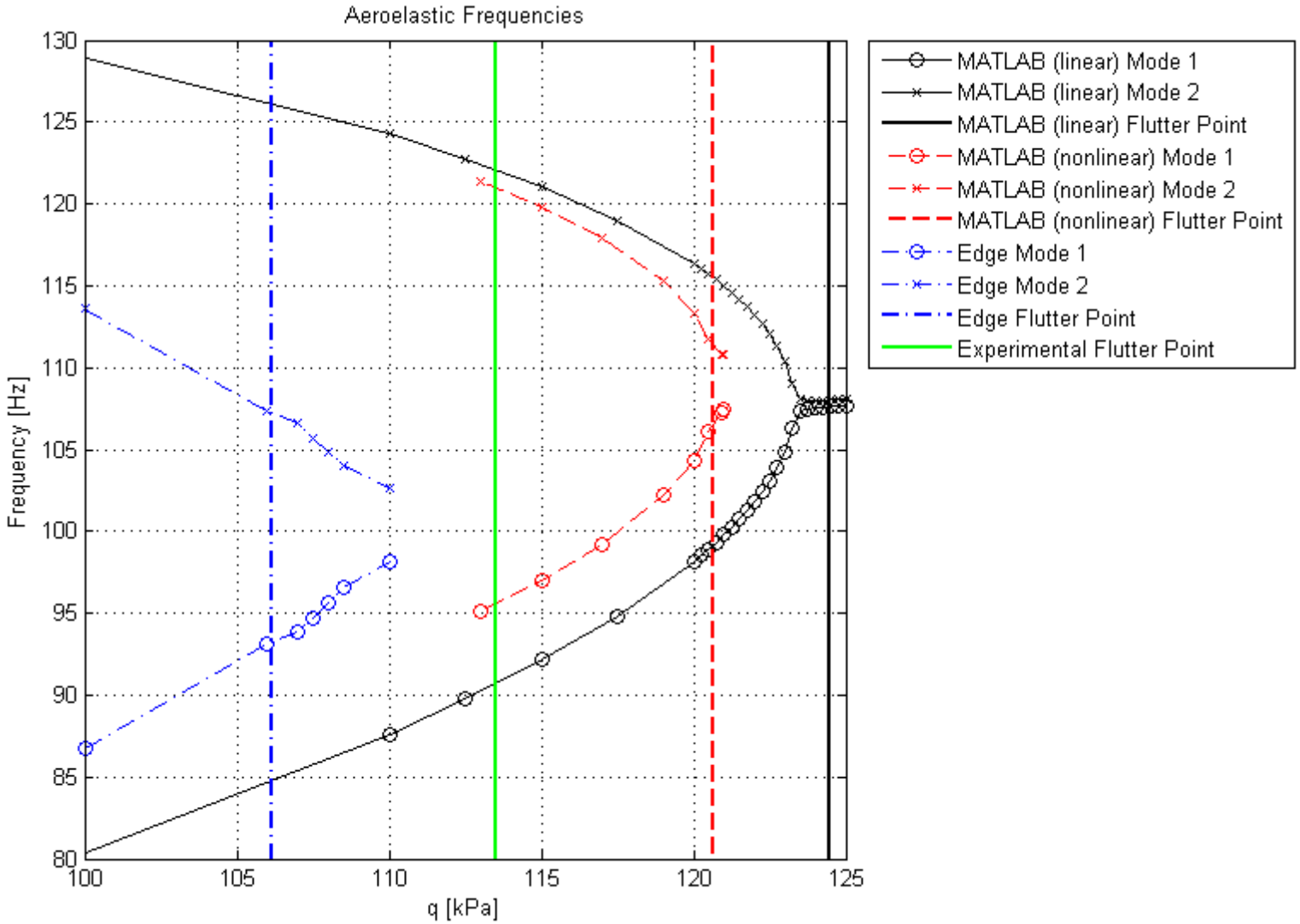


Figure 6.54: Comparison of Modal Frequencies Modelled for the ATM-Wing by Edge, MATLAB (nonlinear), and MATLAB (linear)

The flutter dynamic pressure of the ATM-Wing is bounded on either side by the simulated flutter dynamic pressures; the result from Edge is conservative, whilst the analysis using SE/LPT in MATLAB over-predicts the flutter dynamic pressure. The dynamic pressures at flutter predicted by the methods are summarized in Table 6.3. From Figure 6.54, it may be seen that there is good agreement in the trend of the aeroelastic modal frequencies; the nonlinear analysis methods both model flutter as occurring before the complete coalescence of the frequencies of Mode 1 and Mode 2. However, as was previously noted, accurate extraction of damping coefficients from the nonlinear analysis data using ARMA identification ; in contrast, the linear modelling in MATLAB provided damping trends which were representative of the response and which modelled hard flutter.

Table 6.3: Comparison of the Flutter Points Predicted by Simulation

Analysis Method	q_F [kPa]	% Error in q_F
Experiment (Matsuzaki) [55]	113.5	—
Edge	108.3	-4.6%
MATLAB (nonlinear)	120.8	6.4%
MATLAB (linear)	124.5	9.7%

It is hypothesized that the over-prediction of the flutter dynamic pressure by SE/LPT in MATLAB may be attributed to the inaccuracies in modelling the steady contribution to the aerodynamic loading (and consequently in modelling the GAFs and the aerodynamic stiffness matrix).

The importance of accurately modelling the steady contribution to the aerodynamic loading is highlighted in Figure 3.10 on page 74 from Zhang et al [11]; the main difference between the results of (1st order) local piston theory and 1st order classical piston theory given by Zhang et al lies in the use of steady Euler results to model to steady contribution to aerodynamics in LPT. The better agreement in LPT to unsteady Euler over 1st order classical PT reported by Zhang et al [11] is due to improved fidelity in the modelling of the steady aerodynamics. It is expected that the flutter speed predicted by SE/LPT is similarly over-predicted (as the results from classical PT of Zhang et al [11] are when compared to an unsteady Euler computation) due to insufficient fidelity in the computation of the steady aerodynamic contribution to the overall loading.

A comparison of the typical computation time for a given flight condition (for the given structural model described in Section5.3) required for the ≈500 time steps of the computation to steady deformation and for ≈1000 time steps for the free response computation is given in Table 6.4. The computations in Edge were performed on a different computer to those performed in MATLAB, due to limitations on licensing of software.

Table 6.4: Comparison of Typical Computation Times for the ATM-Wing

Method of Analysis	Typical computation time	Remarks
Edge	≈ 7 hours	Parallel processing on 3 processors
MATLAB (nonlinear)	≈ 9 hours	Single processor
MATLAB (linear)	≈ 3 min	Single processor

The linearization of the GAFs allowed for the holistic analysis (time-response and system stability analysis) of the aeroelastic response of the ATM-wing to be performed very rapidly in comparison to the computationally intensive time-marching of the implicit aeroelastic equations required by Edge and MATLAB (nonlinear). Through comparison of the order of computation times between Edge and MATLAB (linear) it may be seen that of the order of ∼140 flight conditions could be analysed in MATLAB (linear) in the time required for the analysis of a single flight condition in Edge. Thus, MATLAB (linear) was found to be useful as a rapid aeroelastic prediction tool, with the minimal computation time rendering it suitable to the generation of flutter envelopes and to parametric design studies.

It should be noted that Edge provides the functionality to produce a reduced-order model (ROM) of the GAFs, which would also reduce the computation time required in Edge to assess the stability and response of the wing at the specified flight condition. The ROM-generation functionality of Edge was not exploited, as this was outside the scope of the present dissertation.

In summary, the results of SE/LPT in MATLAB slightly over-predicted the flutter dynamic pressure (to within 9.7% of the experimental value), whilst the flutter point was under-predicted in Edge. The linearization of the GAFs from SE/LPT in MATLAB was shown to significantly reduce the time required to predict the flutter point of the ATM-wing at an acceptable cost in the accuracy of the prediction.

6.2 Flutter Envelope of the ATM-Wing

The flutter envelope (as based on variation of angle-of-attack) of the ATM-wing at $M = 2.51$ was determined using the linearized aeroelastic equations from SE/LPT in MATLAB (linear). The effect of the selection of the linearization step-size on the predicted flutter envelope was also investigated.

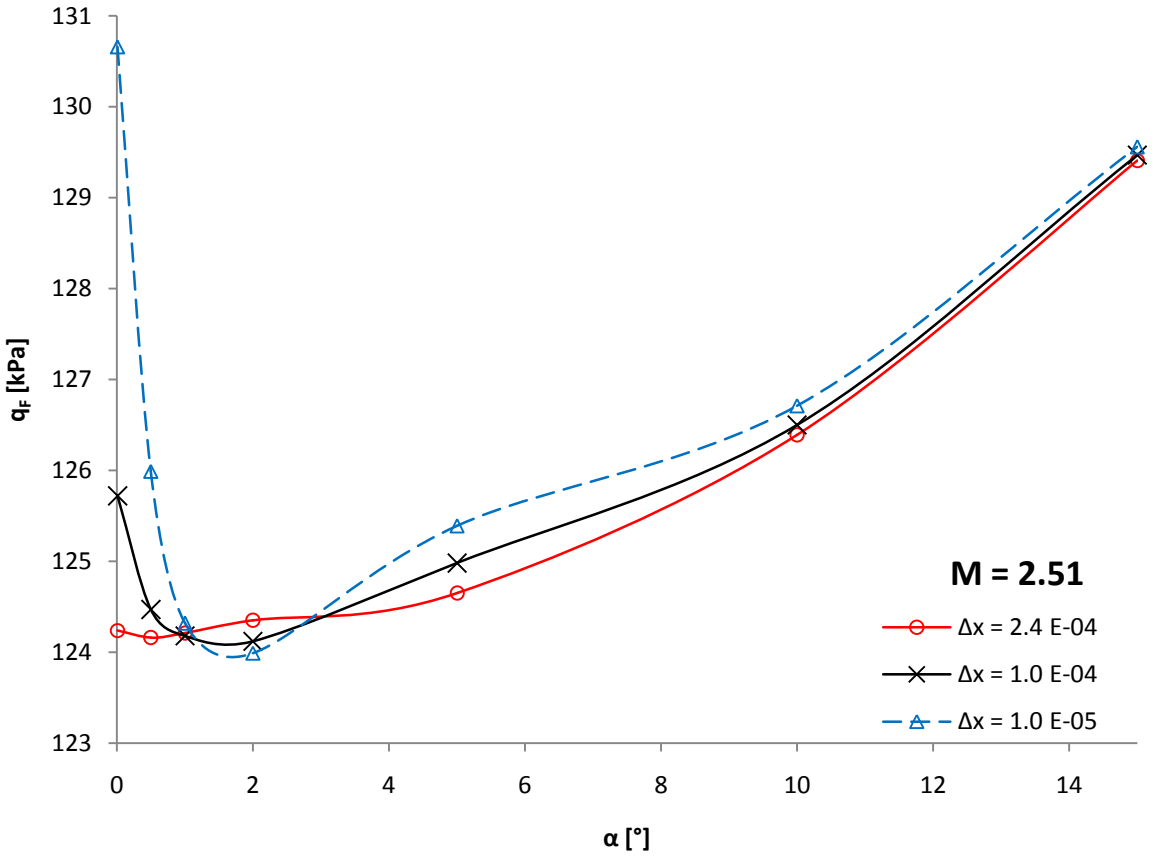


Figure 6.55: Flutter Envelope of the ATM-Wing at $\boldsymbol{M = 2.51}$*, MATLAB (linear)*

Three distinct regions are seen to exist for the predicted results: a region with high sensitivity of the results to the linearization step-size ($0° \leq \alpha \leq 1°$); an intermediate region in which a larger linearization step-size predicts a higher flutter dynamic pressure ($1° \leq \alpha \leq 3°$); and a region in which the flutter trends show consistent behaviour with linearization step-size ($\alpha > 3°$).

It is believed that the sensitivity of the predicted results to the linearization step-size as seen at low angles-of-attack ($0° \leq \alpha \leq 1°$) is due to numerical issues in either the linearization

procedure (see Section 4.5.1) (inflation of numerical error due to division by a small linearization step-size), or due to numerical issues in the implementation of shock-expansion theory in the steady-aerodynamic solver. The numerical issues result in poor prediction of the aerodynamic stiffness matrix, as was discussed in Section 5.9. Inspection of the predicted flutter envelope at higher angles-of-attack ($\alpha > 5°$) shows that the prediction becomes less sensitive to the linearization step-size. This suggests that the partial derivative of the GAFs with respect to modal displacements is largely independent of the linearization step-size at higher α.

It is concluded that at lower angles-of-attack ($\alpha \leq 3°$), numerical issues arise in the accuracy of the prediction of the steady-aerodynamic contribution to the GAFs. This is believed to arise from numerical issues in the solution of the aerodynamic forces at small angles-of-attack in the implemented solver.

A notable trend in the flutter envelope predicted for each of the linearization step-sizes is that the flutter dynamic pressure is seen to increase with angle-of-attack. Careful interpretation of the trend is required when compared to other flutter envelopes, such as those computed by Zhang et al [11] in Figure 3.10 on page 74. Comparison to the trends of Zhang et al shows that the flutter envelope predicted for the ATM-wing at $M = 2.51$ by the current work follows similar trends to the flutter enveloped computed for a (2-dimensional) 4% circular arc airfoil at $M = 6$ using 1st- and 2nd-order classical PT. Several differences exist between the two cases, such as: different Mach numbers (different flow physics), different airfoil profiles (potentially different lifting characteristics), and different structural geometries and properties (including sweep and 2D vs. 3D effects). Whilst each of these factors may be argued influence the shape of the flutter envelope, the most rigorous assessment of the validity of the flutter envelope predicted by SE/LPT in MATLAB (linear) would be comparison to a flutter envelope produced from unsteady Euler computations in Edge for the ATM-wing. If it were found that the flutter envelope from Edge followed the same trend of decreasing flutter speed with α that is observed for the geometry and flow of Zhang et al, then it would be concluded that the implementation of the shock-expansion component of SE/LPT does not describe the flow with sufficient fidelity, and another approximate aerodynamic method could be investigated for implementation with LPT for use as an aeroelastic prediction tool.

6.3 Flutter Prediction of the Tuovali-McCarty Models

6.3.1 Literature on the Experimentally Determined Flutter Conditions

Tuovali and McCarty [53] performed supersonic flutter tests on cantilevered plates of various aspect ratios, sweep angles, and taper ratios, for Mach numbers $M = 1.3$, $M = 2.0$ and $M = 3.0$ in the Langley supersonic flutter apparatus (an intermittent blow-down tunnel [53]) in 1955. Their work is a benchmark and serves for validation [52] of aeroelastic calculations by programs such as MSC NASTRAN's Aeroelastic Analysis module and ZAERO. Flutter speeds and frequencies are given for a range of wind-tunnel operating conditions.

Examination of the published [53] test conditions for the various models shows that the test conditions were tailored to produce flutter at specified Mach numbers and flow velocities. Effectively, this means that the Mach number and temperature of the flow were kept constant, and the density of the flow was varied as the control variable. This is reflected in the variation of the published results for air density at flutter between the models and tests [53].

The tests of the untapered cantilevered plates are of interest, as these were constructed from a uniform sheet of material; the centre of mass of the models that are listed in this section were also at the 50% chord position (no mass was added or removed to the baseline plate). Detailed specifications of geometry and mass were given. The test models had the same thickness; the leading- and trailing-edges were both bevelled over a length of 1/8th of the chord. A general description of the model geometries is given in Table 6.5, and the reader is referred to Appendix A for the further specifications of the model geometries. The natural frequencies of the magnesium plate series of models were experimentally determined in still air by Hanson and Tuovila [59].

Table 6.5: Summary of Planform Geometry of the Tuovali and McCarty Test Models [53]

Model	Λ_{LE} [°]	AR	$\bar{c}$ [mm]	t/c	S_{ref} [m^2]
5151	15	2.67	52.6	0.0198	0.0074
4301	30	2.08	58.7	0.0178	0.0072
3451	45	1.38	71.8	0.0145	0.0071
1601	60	0.69	101.6	0.0103	0.0072

The wind-tunnel operating conditions for the various tests are quoted in Table 6.6 through Table 6.9, together with the flutter velocity V_F, the dynamic pressure at flutter q_F, and the flutter frequency f_F. It should be noted that the "C-"series of tests were run with a plate cut from aluminium, whilst the "A-" and "B-" series of tests were run with magnesium plates.

Table 6.6: Wind-Tunnel Condition and Flutter Parameters - Model 5151 [53]

Test	M	ρ_{air} [kg/m^3]	V_F [m/s]	q_F [Pa]	f_F [Hz]
A	3.00	0.47930	618.7	91 740	146
B	2.00	0.27315	512.1	35 810	134
C	1.30	0.25254	390.1	19 220	102

Table 6.7: Wind-Tunnel Condition and Flutter Parameters - Model 4301 [53]

Test	M	ρ_{air} [kg/m^3]	V_F [m/s]	q_F [Pa]	f_F [Hz]
A	3.00	0.34530	618.7	66 100	158
B	2.00	0.22161	512.1	29 055	142
C	1.30	0.22677	390.1	17 260	94

Table 6.8: Wind-Tunnel Condition and Flutter Parameters - Model 3451 [53]

Test	M	ρ_{air} [kg/m^3]	V_F [m/s]	q_F [Pa]	f_F [Hz]
A	3.00	0.31438	618.7	60 180	170
B	2.00	0.22677	512.1	29 730	148
C	1.30	0.32469	390.1	24 710	180

Table 6.9: Wind-Tunnel Condition and Flutter Parameters - Model 1601 [53]

Test	M	ρ_{air} [kg/m^3]	V_F [m/s]	q_F [Pa]	f_F [Hz]
A	3.00	0.50917	618.7	68 070	180
B	2.00	0.53131	512.1	48 650	166
C	1.30	0.95931	390.1	50 990	174

6.3.2 Literature on Previous Computational Flutter Predictions

6.3.2.1 Results of Morgan et al

Flutter calculations based on the tests by Tuovali and McCarty for delta-wings and Model 3451 (untapered, 45° sweep, see Table 6.8) were carried out by Morgan et al [50], with second-order piston theory and Van Dyke's second order theory being used to model the aerodynamics. It was noted that for the delta-wings tested, the flutter frequencies were predicted to within 15% at all Mach numbers, and the flutter boundary using piston theory was predicted to between 23% and 14% below and above the experimentally determined values, respectively. It was noted [50] that better agreement between theory and experiment was obtained at higher Mach numbers and consequently lower reduced frequencies. This is expected, as the quasi-steady modelling is valid only for low reduced frequencies. However, the calculations for the untapered wing showed a large error (as seen in Figure 6.56) in both the calculated flutter frequency (95% higher) and the flutter boundary [50]; it was hypothesized that the error was due to the large portion of the wing that is influenced by the wingtip.

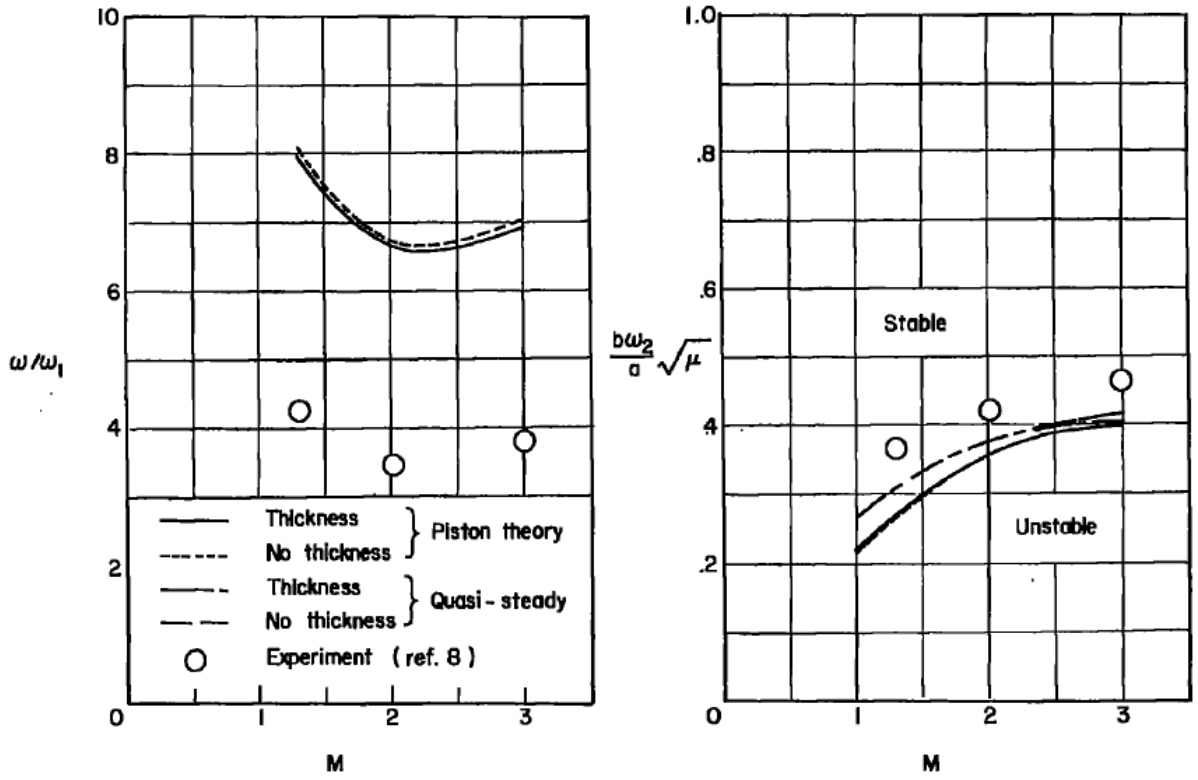


Figure 6.56: Theoretical Calculations of Morgan et al for Model 3451 of the Tuovali-McCarty Flutter Tests **[50]**

6.3.2.2 Results of Xianxin

Flutter calculations based on conical flow theory and piston theory on the plates tested by Tuovali and McCarty were performed by Xianxin [60], and are shown as adapted from Xianxin in Figure 6.57 through Figure 6.60, with comparison to the experimental results of Tuovali and McCarty [53] and the computational results of Morgan et al [50]. A significant improvement in the results can be seen over the application of piston theory alone (as done by Morgan et al [50]) through comparison of the results of Figure 6.56 and Figure 6.59. It is noted that the use of conical flow theory to account for the 3-dimensional influence of the wing yields much greater accuracy compared to strip theory [60].

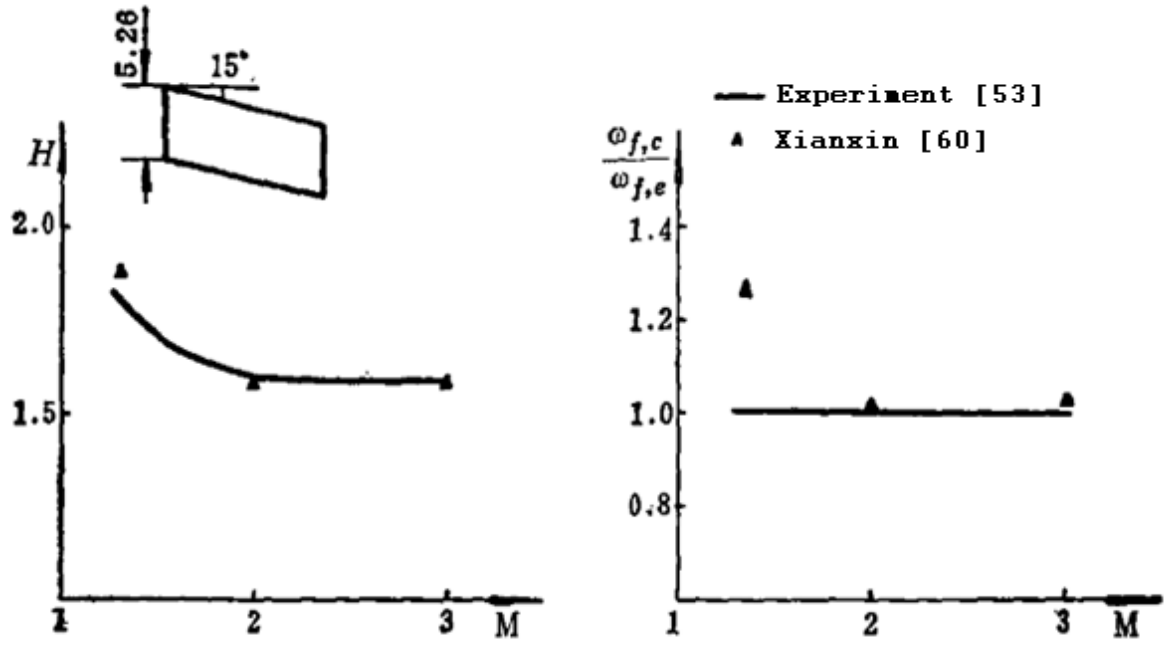


Figure 6.57: Theoretical Calculations of Xianxin for Model 5151 of the Tuovali-McCarty Flutter Tests **[60]**

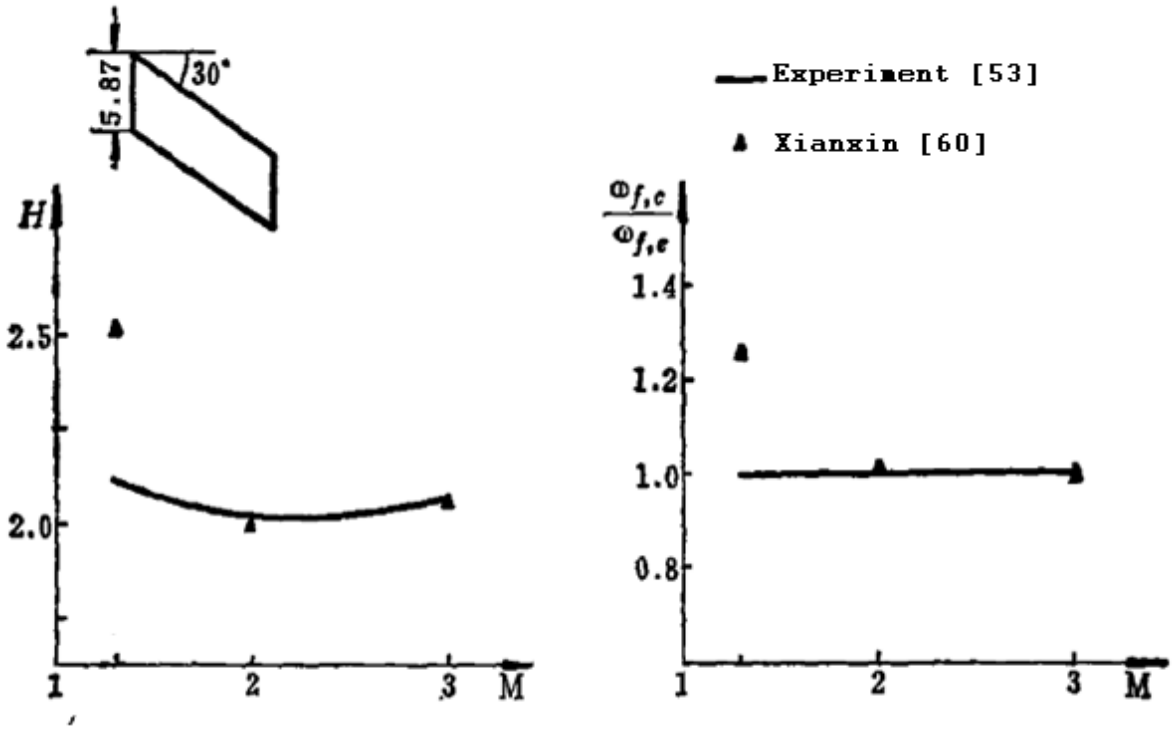


Figure 6.58: Theoretical Calculations of Xianxin for Model 4301 of the Tuovali-McCarty Flutter Tests **[60]**

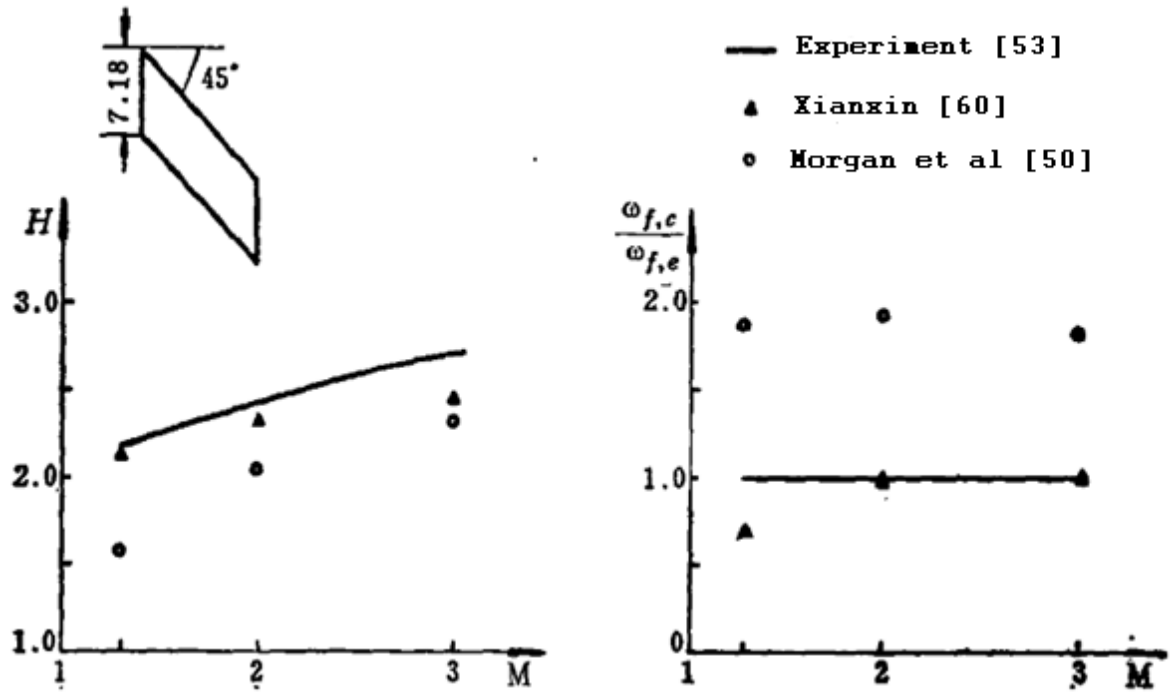


Figure 6.59: Theoretical Calculations of Xianxin for Model 3451 of the Tuovali-McCarty Flutter Tests **[60]**

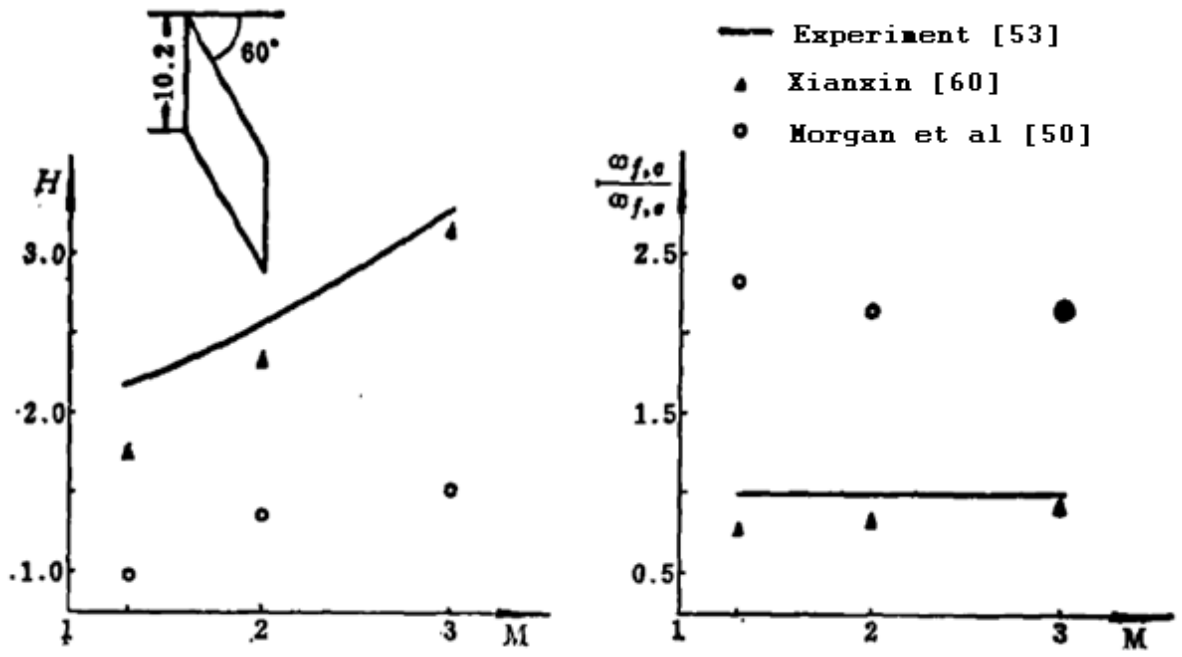


Figure 6.60: Theoretical Calculations of Xianxin for Model 1601 of the Tuovali-McCarty Flutter Tests **[60]**

6.3.2.3 Results of Chen et al

The application of the ASTROS* code (based upon the integration of ZAERO into ASTROS) and comparison of its results to the experimental data of Tuovali and McCarty was carried out by Chen et al [52]. Specifically, comparison of results was made to Test C of Model 5151 (Table 6.6), and to Test A of Model 5151. The material properties were adjusted to match experimental data [52], though it is not specified whether the modal frequencies were matched to those published by Tuovali and McCarty [53] or by Hanson and Tuovali [59].

A summary of the comparison of results of Chen et al [52] with the flutter tests of Tuovali and McCarty [53] is given in Table 6.10 and Table 6.11.

Table 6.10: Comparison of Flutter Results from ASTROS* with Experimental Data - Model 5151, Test A [52]

Method	V_F[m/s]	q_F [Pa]	f_F [Hz]
Experiment [53]	618.7	91 740	146
ASTROS*, k method / p-k method			
ZONA7 (no thickness)	722.1 / 746.2	124 960 / 133 440	158 / 154
ZONA7U (thickness effect)	578.2 / 586.1	80 120 / 82 320	154 / 152

Table 6.11: Comparison of Flutter Results from ASTROS* with Experimental Data - Model 5151, Test C [52]

Method	V_F[m/s]	q_F [Pa]	f_F [Hz]
Experiment [53]	390.1	19 220	102
MSC/NASTRAN, p-k method			
MSC/NASTRAN (ZONA51)	480.4	29 140	132
ASTROS*, k method / p-k method			
ZONA7 (no thickness)	482.5 / 488.0	29 400 / 30 070	132 / 130
ZONA7U (thickness effect)	431.3 / 434.6	23 490 / 23 850	123 / 122

6.3.3 Outline of the Computational Procedure

The untapered, sweptback cantilevered plates used in flutter testing by Tuovali and McCarty [53] were modelled in MATLAB (linear) for further validation of the developed aeroelastic prediction tool with comparison to experimental data. The comparison to the tests of Tuovali and McCarty would be of particular interest, as the tests have served as validation and benchmarking for other flutter prediction methods (see Section 6.3.2), including the use of 2nd order classical PT and 2nd order Van Dyke's by Morgan et al [50], the use of ZONA software by Chen et al [52], and the use of a hybrid of 1st order PT and conical flow theory by Xianxin [60].

The computations using SE/LPT in MATLAB (linear) were performed for $\alpha = 0.01°$ at the flight conditions specified in Table 6.6 through Table 6.9, with the dynamic pressure (q_∞) used as a control variable. The linearization step-size was chosen such that the resulting deformation of the first-torsion mode would yield a twist of 2° at the wing-tip, following the approach adopted for the ATM-wing. This was changed to produce 1° of twist at the wing-tip at $M = 1.3$ due to shock detachment at larger deflections.

The models were meshed in MATLAB (linear) using 20 chordwise elements, with the number of spanwise elements chosen such that the ratio of spanwise-to-chordwise elements matched the geometric aspect ratio of the models. The material properties were then tailored such that the frequencies of the first-torsion mode (f_2) matched the published experimental frequencies of Tuovali and McCarty [53], and that the wing mass was similarly matched.

The results for each of the models is given in Section 6.3.5; fair accuracy is obtained in the prediction of the flutter dynamic pressure through SE/LPT at $M = 3.0$ for most of the geometries considered.

6.3.4 Representation of the Flutter Prediction Results

The presentation of the results of the flutter predictions varies between authors, with the results of Chen et al [52] presented in terms of the flutter dynamic pressure (q_F) and frequency (f_F), whilst the results of Morgan et al [50], Tuovali and McCarty [53], and Xianxin [60] are presented in terms of an altitude-stiffness parameter [53]. There is some further difference in the nomenclature and definition of the parameter, which is clarified as follows, in the nomenclature of the present work:

The altitude-stiffness parameter is influenced by the mass-ratio, μ, which is defined as the ratio of the mass of the wing to the mass of air contained in a right-cylinder defined by swept wing:

$$\mu = \frac{m_{wing}}{m_{air}} \tag{6.1}$$

where m_{air} is given by:

$$m_{air} = \frac{\pi}{4}\rho_\infty b c^2 \cos\Lambda \tag{6.2}$$

leading to:

$$\mu = \left(\frac{4m_{wing}}{\pi b c^2 \cos\Lambda}\right)\frac{1}{\rho_\infty} \tag{6.3}$$

The altitude-stiffness parameter used by Tuovali and McCarty [53] (H_{TMC}) is scaled by a reference value for the mass-ratio ($\mu_0 = 50$), and is given by:

$$H_{TMC} = \frac{c\omega_\alpha}{2a_\infty}\sqrt{\frac{\mu}{\mu_0}} \quad (6.4)$$

where ω_α is the angular frequency of the first-twisting mode and a_∞ is the speed of sound in air.

The altitude-stiffness parameter used by Xianxin [60] (H_X) is not scaled, and is given by:

$$H_X = \frac{c\omega_\alpha}{2a_\infty}\sqrt{\mu} \quad (6.5)$$

Note that the altitude-stiffness parameter may be re-written in terms of the free-stream Mach number (M_∞) and the reduced frequency of the first-torsion mode (k_α) as:

$$H_X = k_\alpha M_\infty \sqrt{\mu} \quad (6.6)$$

The difference in the parameter definition is to be noted when interpreting the results of the different authors. With the altitude-stiffness parameter defined as in Equation (6.3) and Equation (6.5), the following relationship may be shown to hold between the altitude-stiffness parameter at flutter (H_F) and the dynamic pressure at flutter (q_F):

$$q_F = \left(\frac{m_{wing}\, V_F^2 \omega_\alpha^2}{2\pi b a_\infty^2 \cos\Lambda}\right)\frac{1}{H_F^2} \quad (6.7)$$

where V_F is the flutter velocity.

Equation (6.7) was used to extract results for the flutter dynamic pressure from the work of Morgan et al [50] and Xianxin [60] for comparison to the results of Chen et al [52] and the results from MATLAB (linear).

6.3.5 Analysis in MATLAB (linear)

6.3.5.1 Model 5151

The results of the flutter prediction for the 5151-series of models of Tuovali and McCarty [53] using SE/LPT in MATLAB (linear) are compared to the results of Xianxin [60], Chen et al [52], and experiment [53] in Figure 6.61 through Figure 6.65.

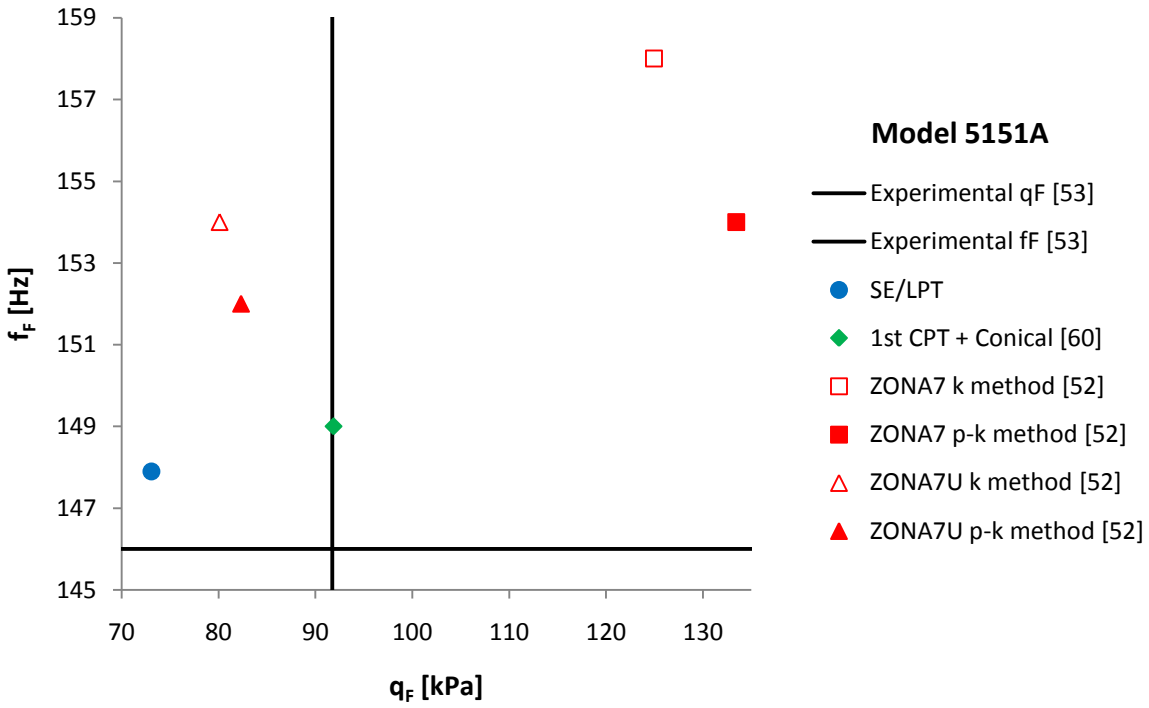


Figure 6.61: Tuovali-McCarty Model 5151A, Comparison of Flutter Predictions

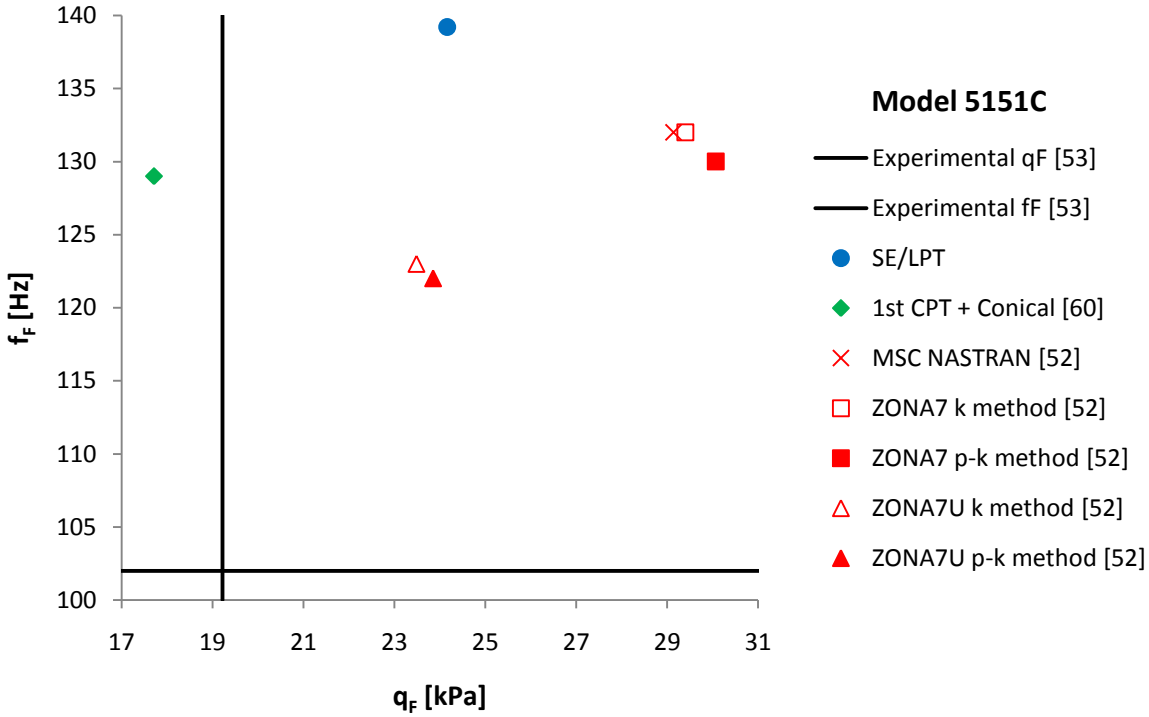


Figure 6.62: Tuovali-McCarty Model 5151C, Comparison of Flutter Predictions

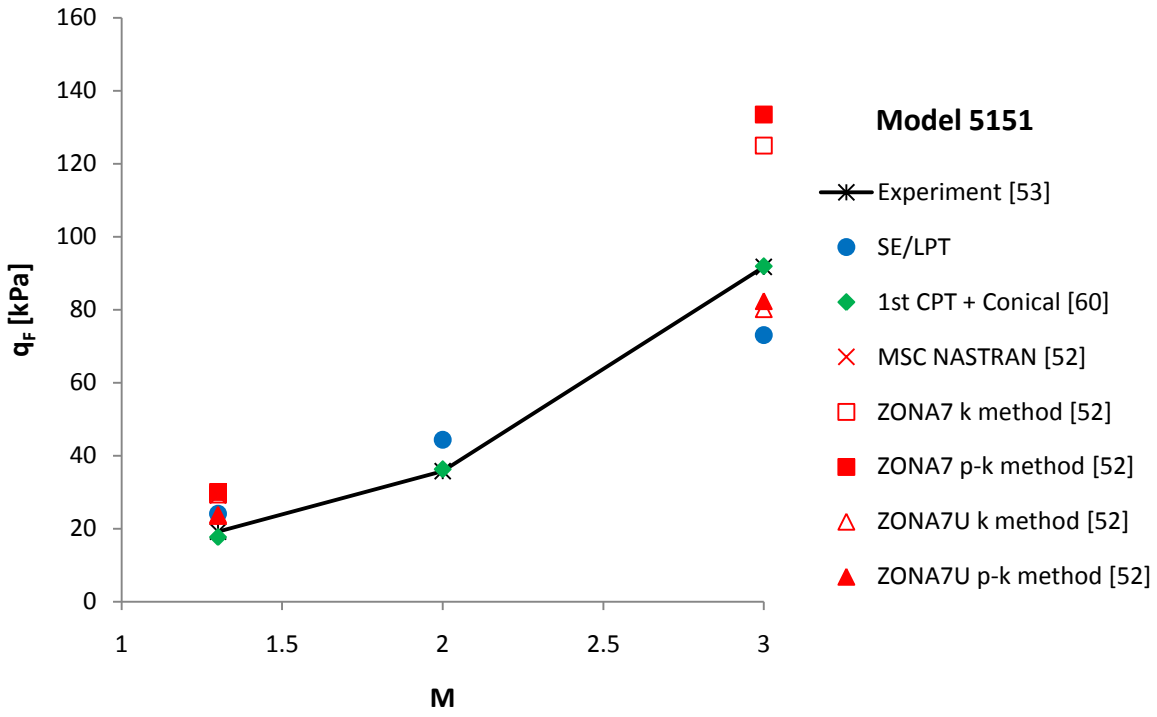


Figure 6.63: Tuovali-McCarty Model 5151, Flutter Dynamic Pressure Variation with Mach Number

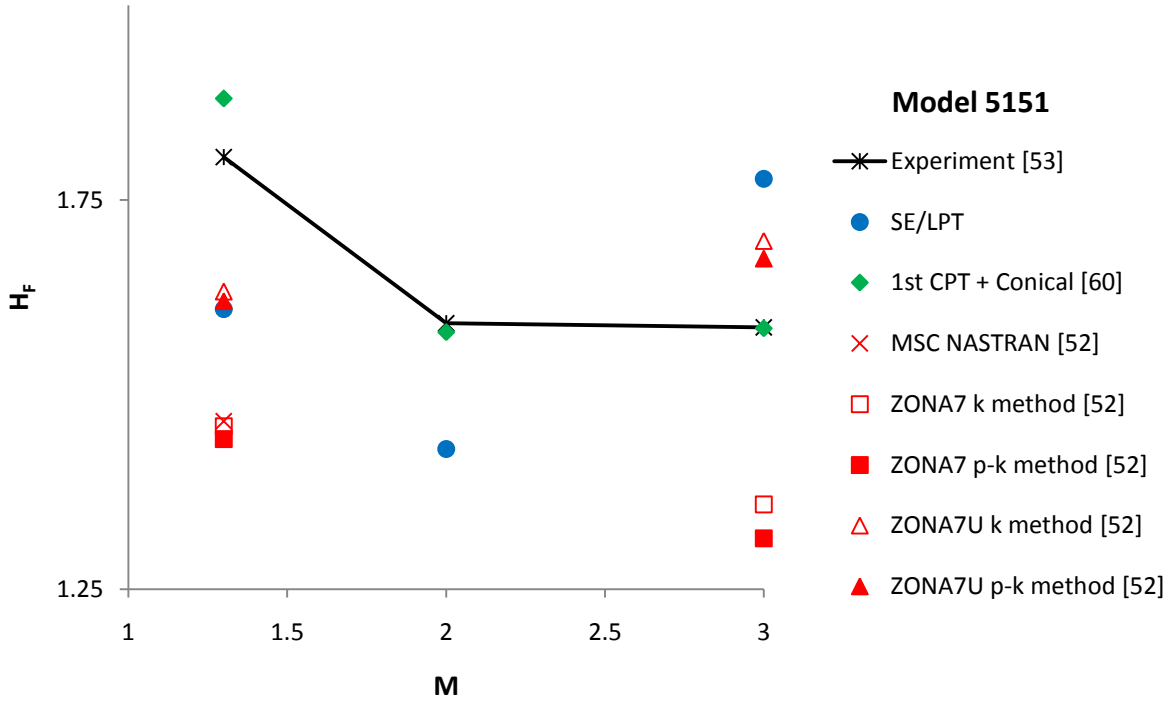


Figure 6.64: Tuovali-McCarty Model 5151, Flutter Altitude-Stiffness Parameter Variation with Mach Number

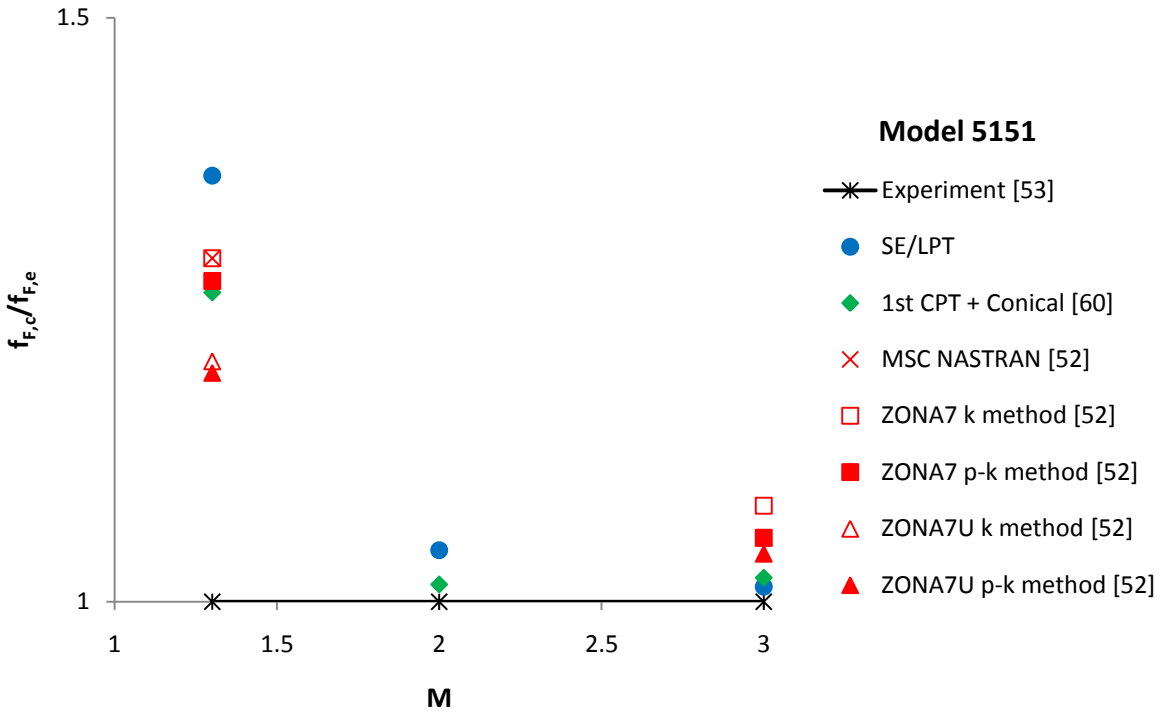


Figure 6.65: Tuovali-McCarty Model 5151, Variation of Computational-Experimental Flutter Frequency Ratio with Mach Number

The flutter trends predicted by SE/LPT show good correlation to other methods for $M = 1.3$ and $M = 2.0$, but is seen to depart from the general trends for $M = 3.0$. The flutter dynamic pressure is predicted non-conservatively, except at $M = 3.0$, as is seen from the figures. The accuracy of the flutter dynamic pressure is seen to predicted better than through ZONA7 (Figure 6.61 and Figure 6.62), whilst not as accurately as through ZONA7U; this suggests that the thickness effects (which are modelled in ZONA7U, and not in ZONA7) that are modelled by SE/LPT are of significant importance. It is also noted that for the given test case, the thickness effects have a de-stabilizing effect, resulting in a lower dynamic pressure predicted for flutter than with thickness effects ignored. Very good prediction of the flutter frequency is noted from Figure 6.65 for $M = 2.0$ and $M = 3.0$.

The hybrid of 1st classical PT and conical flow theory of Xianxin [60] is seen to give excellent agreement to experiment for $M = 2.0$ and $M = 3.0$ in both the flutter dynamic pressure and the flutter frequency. The superiority in aeroelastic modelling achieved through the improved fidelity of the steady-aerodynamic computation is clearly evident through comparison of the results of 1st CPT/conical flow (3D effects modelled) with SE/LPT (2D

strip theory). However, the 1st CPT/conical flow hybrid of Xianxin [60] is seen to give better results than the predictions of ZONA7 and ZONA7U, which also account for 3D effects. This is likely due to the suitability of the more analytical approach of conical flow theory to the given simple geometry.

Consideration of the flutter trends predicted by the ZONA7 and ZONA7U codes in Figure 6.61 and Figure 6.62 reveals that for both Mach numbers considered, the inclusion of thickness effects by ZONA7U results in a lower flutter dynamic pressure predicted; as noted earlier, the thickness effects are seen to have a de-stabilizing effect. It is further noted that better prediction of the flutter frequency is obtained by ZONA7U than with ZONA7. Furthermore, the method of flutter prediction is seen have an effect on the predicted flutter values: at both Mach numbers, the p-k method predicts lower flutter frequencies, but higher flutter dynamic pressures than the k-method.

Lastly, the similarity in the formulation of the MSC NASTRAN aeroelastic tool and of ZONA7 is seen to give rise to almost equivalent results in Figure 6.62 through Figure 6.65.

Poor prediction of the flutter frequency at $M = 1.30$ is noted in Figure 6.65 for all the methods, with improvement in the prediction achieved with increasing Mach number. It is suspected that poor modelling of the flow physics at the lower Mach number is achieved with the aerodynamic methods used.

6.3.5.2 Model 4301

The results of the flutter prediction for the 4301-series of models of Tuovali and McCarty [53] using SE/LPT in MATLAB (linear) are compared to the results of Xianxin [60] and with experiment [53] in Figure 6.66 through Figure 6.68.

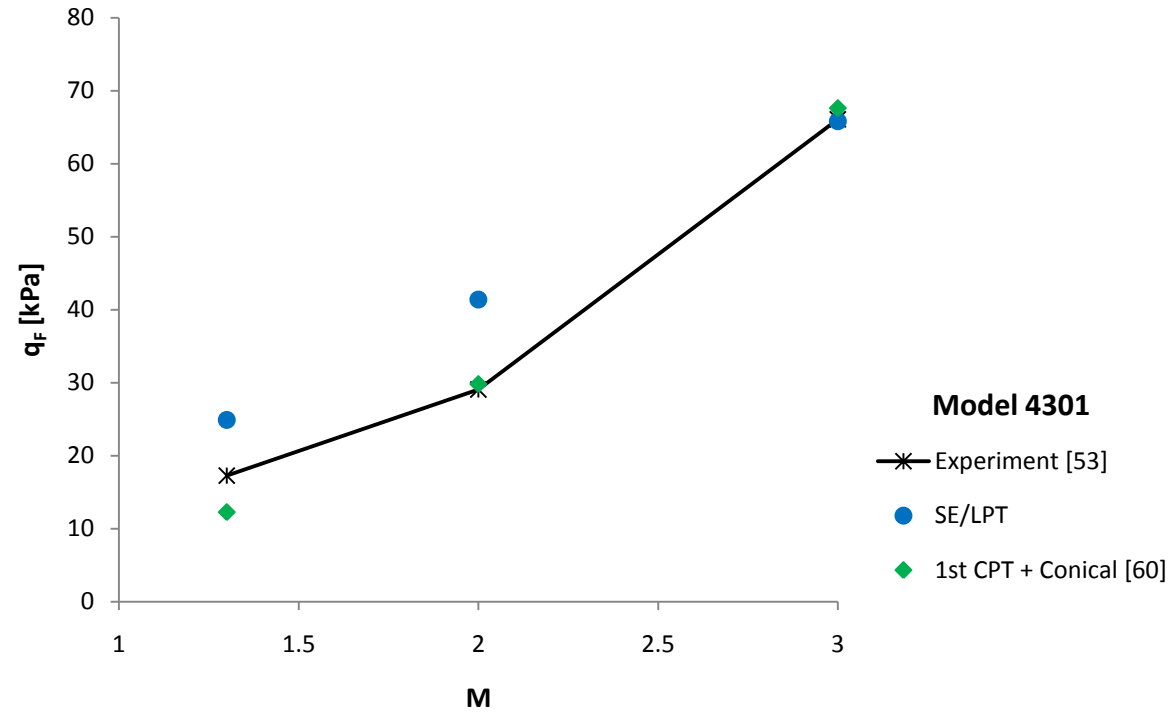


Figure 6.66: Tuovali-McCarty Model 4301, Flutter Dynamic Pressure Variation with Mach Number

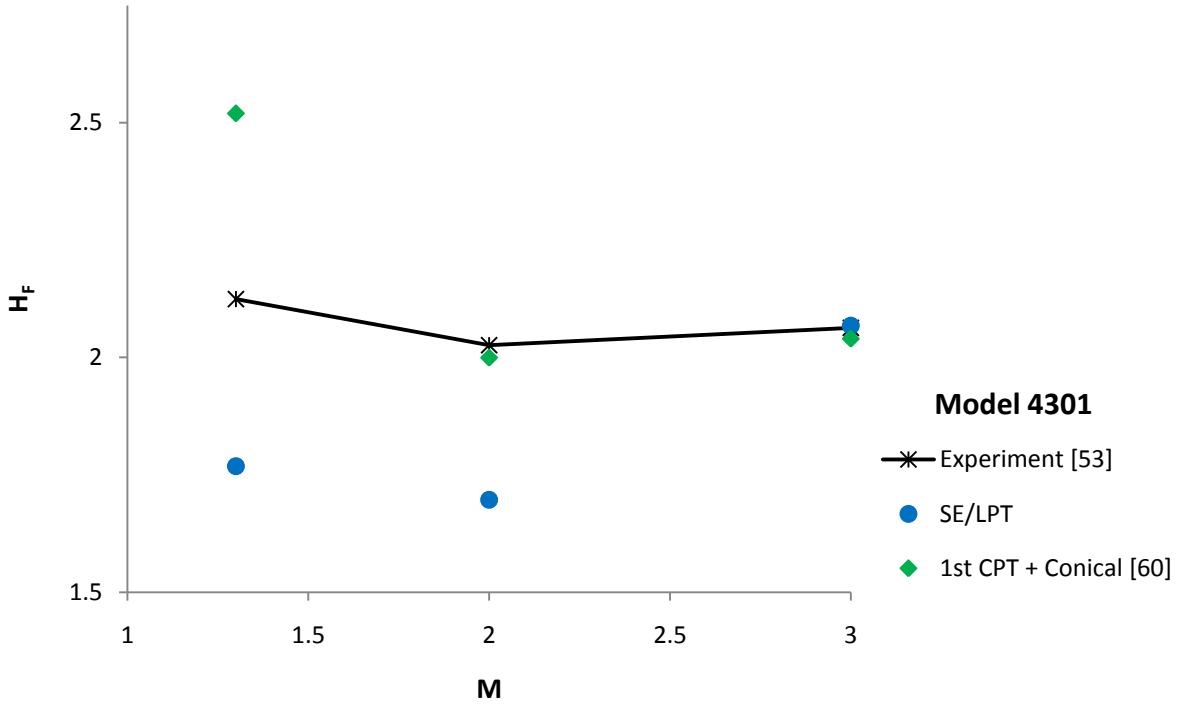


Figure 6.67: Tuovali-McCarty Model 4301, Flutter Altitude-Stiffness Parameter Variation with Mach Number

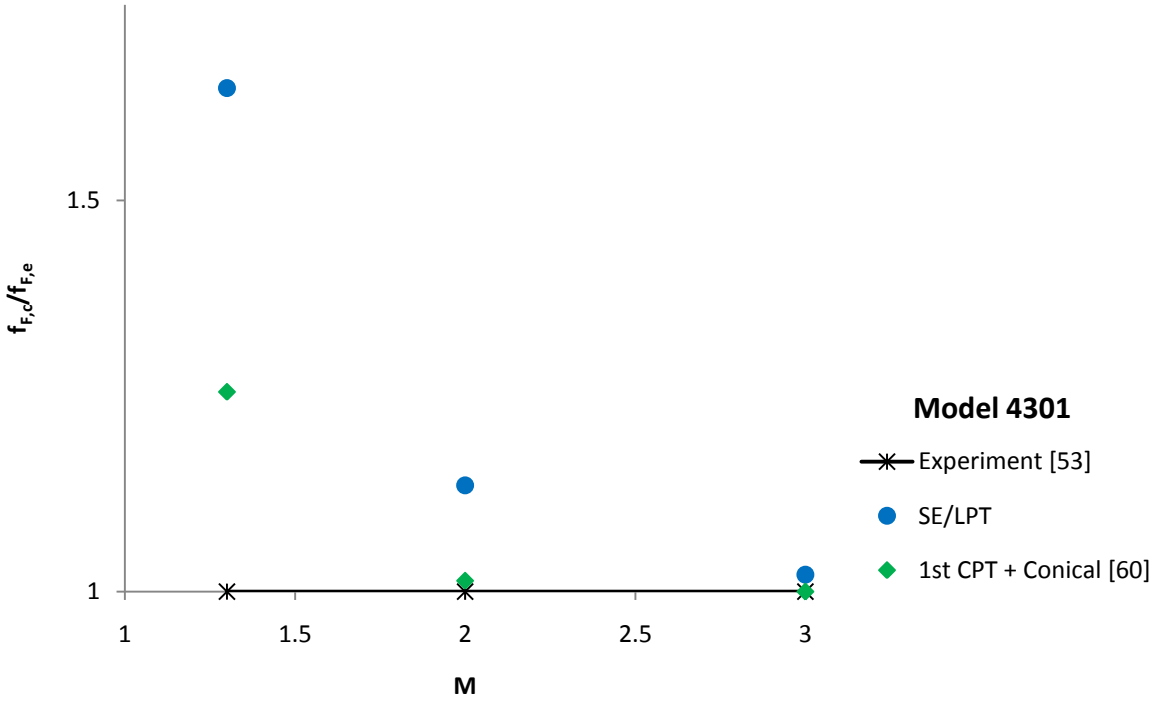


Figure 6.68: Tuovali-McCarty Model 4301, Variation of Computational-Experimental Flutter Frequency Ratio with Mach Number

The flutter trends predicted by SE/LPT show mixed correlation to experiment and to the results of Xianxin over the range of Mach numbers considered. The flutter dynamic pressure is predicted non-conservatively, except at $M = 3.0$, as is seen from Figure 6.66 and Figure 6.67. The trend in dynamic pressure seen in Figure 6.66 suggests good correlation in trends to both experiment and Xianxin's results for $M = 1.3$ and $M = 2.0$, and the trend of the altitude-stiffness parameter correlates well to experiment for the given Mach numbers. The accuracy of the flutter dynamic pressure is best predicted for $M = 3.0$. Very good prediction of the flutter frequency is noted from Figure 6.68 for $M = 3.0$, with poorer prediction at lower Mach numbers, expected to arise from insufficient fidelity in the modelling of the flow physics by the aerodynamic methods considered.

The results of Xianxin [60] are once again seen to give excellent agreement to experiment for $M = 2.0$ and $M = 3.0$ in both the flutter dynamic pressure and the flutter frequency. The superiority in aeroelastic modelling achieved through the improved fidelity of the steady-aerodynamic computation is again apparent through comparison of the results of 1st CPT/conical flow (3D effects modelled) with SE/LPT (2D strip theory).

The best agreement to experiment is obtained at $M = 3.0$ for both prediction methods.

6.3.5.3 Model 3451

The results of the flutter prediction for the 3451-series of models of Tuovali and McCarty [53] using SE/LPT in MATLAB (linear) are compared to the results of Xianxin [60], the results of Morgan et al [50], and with experiment [53] in Figure 6.69 through Figure 6.71.

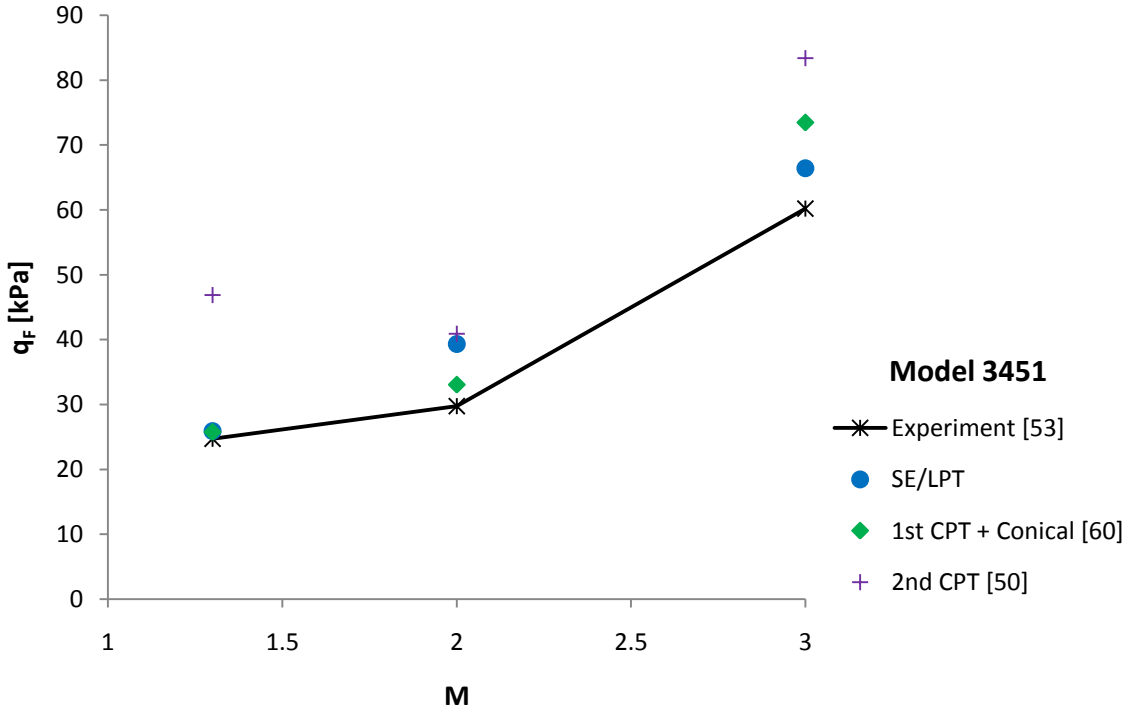


Figure 6.69: Tuovali-McCarty Model 3451, Flutter Dynamic Pressure Variation with Mach Number

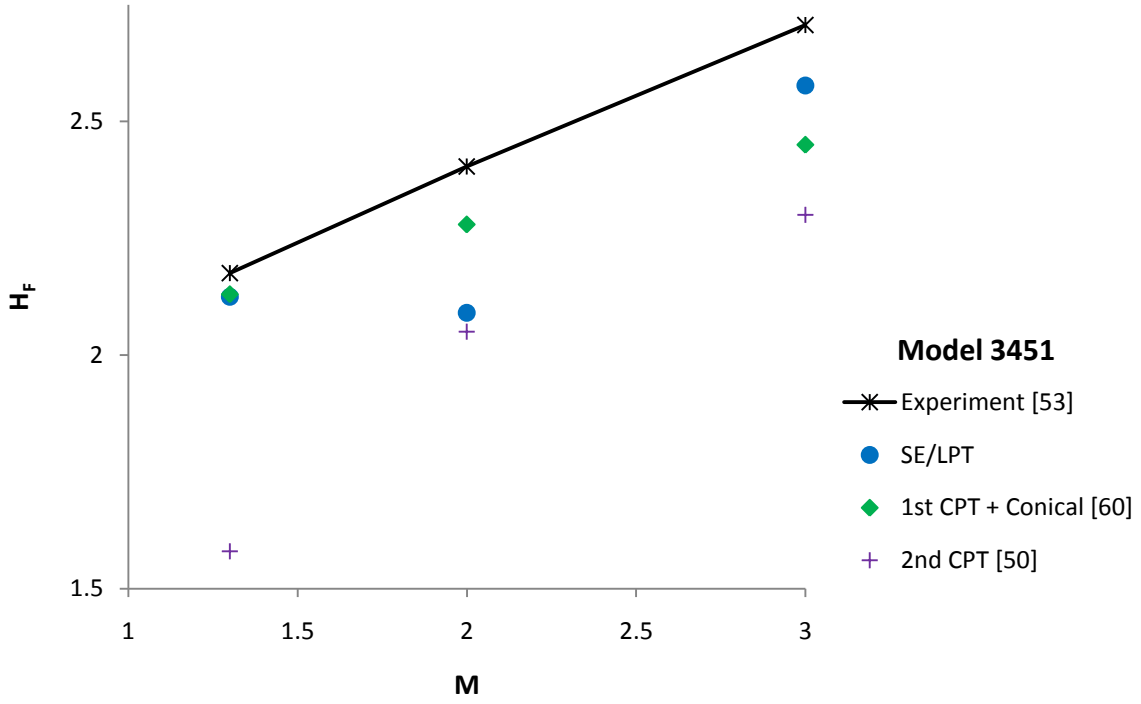


Figure 6.70: Tuovali-McCarty Model 3451, Flutter Altitude-Stiffness Parameter Variation with Mach Number

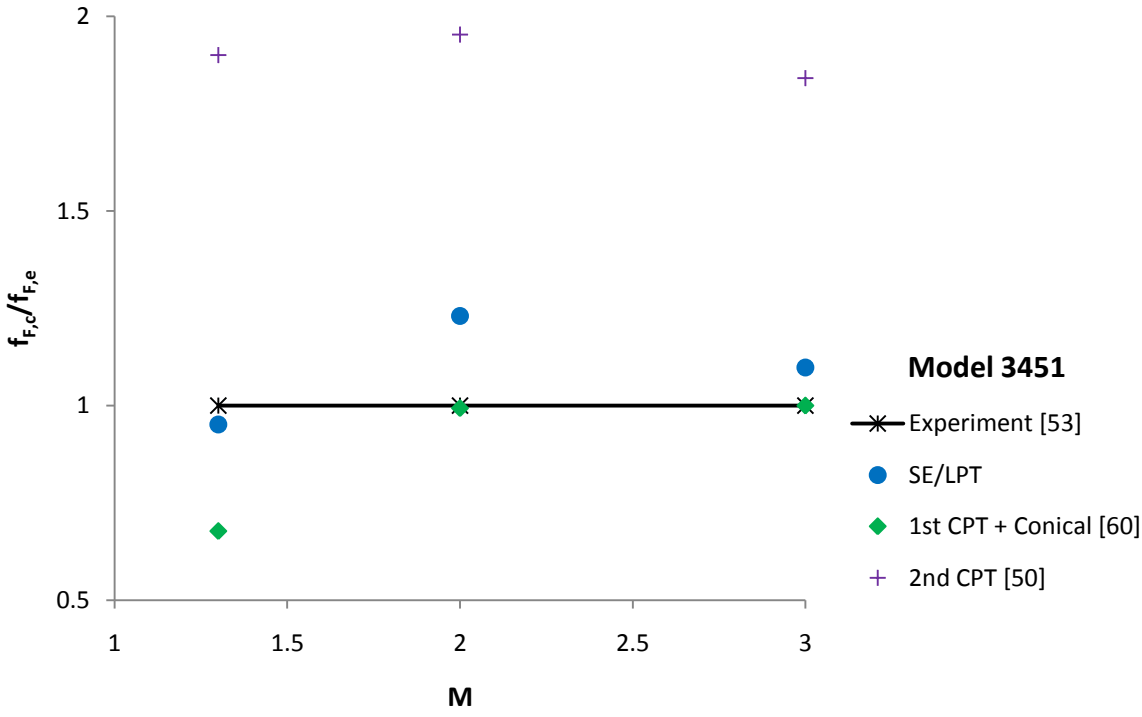


Figure 6.71: Tuovali-McCarty Model 3451, Variation of Computational-Experimental Flutter Frequency Ratio with Mach Number

The flutter trends predicted by SE/LPT show good correlation to experiment and to the results of Xianxin and of Morgan et al over the range of Mach numbers considered, with the exception of $M = 2.0$. The flutter dynamic pressure is predicted non-conservatively, as is seen from Figure 6.69 and Figure 6.70. In contrast to the trend observed for other geometries, the accuracy of the flutter dynamic pressure of Model 3451 is best predicted by SE/LPT for $M = 1.3$. Good prediction of the flutter frequency is noted from Figure 6.71 for both $M = 1.3$ and $M = 3.0$; the trend for the flutter frequency prediction correlates well to that observed for the other prediction methods.

The trends of the flutter prediction of Xianxin [60] give good agreement to experiment over the range of Mach numbers considered. Better agreement with experiment is obtained for the dynamic pressure and altitude stiffness parameter at $M = 1.3$ and $M = 2.0$, whilst excellent frequency prediction is obtained for $M = 2.0$ and $M = 3.0$. Improved prediction at higher Mach numbers is typical of the results of Xianxin for the other geometries considered; the reason for the better agreement in dynamic pressure at lower Mach numbers for the geometry of Model 3451 is unknown.

The results of Morgan et al [50] are seen to follow the experimental flutter trends well, whilst the accuracy of the predictions are generally poor. No relationship between improved accuracy of the prediction and Mach number is apparent. The flutter dynamic pressure is predicted non-conservatively, and the prediction of the flutter frequency is seen to be particularly poor, as in Figure 6.71.

Of particular interest is the general improvement of the accuracy of the prediction achieved by SE/LPT over 2nd-order classical PT. Consideration of the physical effects modelled by 2nd-order classical PT (see Section 3.6) suggests that better modelling of thickness effects is achieved by shock-expansion theory than by classical PT for the given geometry and flight conditions. This is further supported by the previous observation (Section 6.3.5.1) that inclusion (and improved modelling of) thickness effects provides a de-stabilizing effect.

6.3.5.4 Model 1601

The results of the flutter prediction for the 1601-series of models of Tuovali and McCarty [53] using SE/LPT in MATLAB (linear) are compared to the results of Xianxin [60] and with experiment [53] in Figure 6.72 through Figure 6.74.

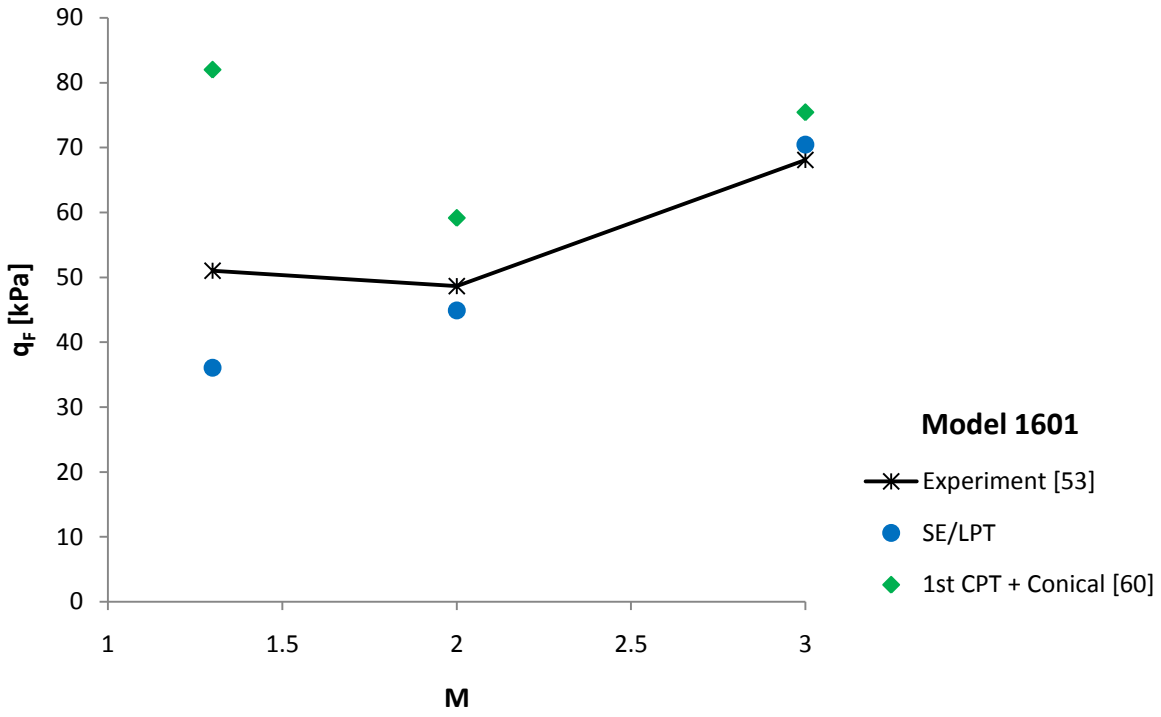


Figure 6.72: Tuovali-McCarty Model 1601, Flutter Dynamic Pressure Variation with Mach Number

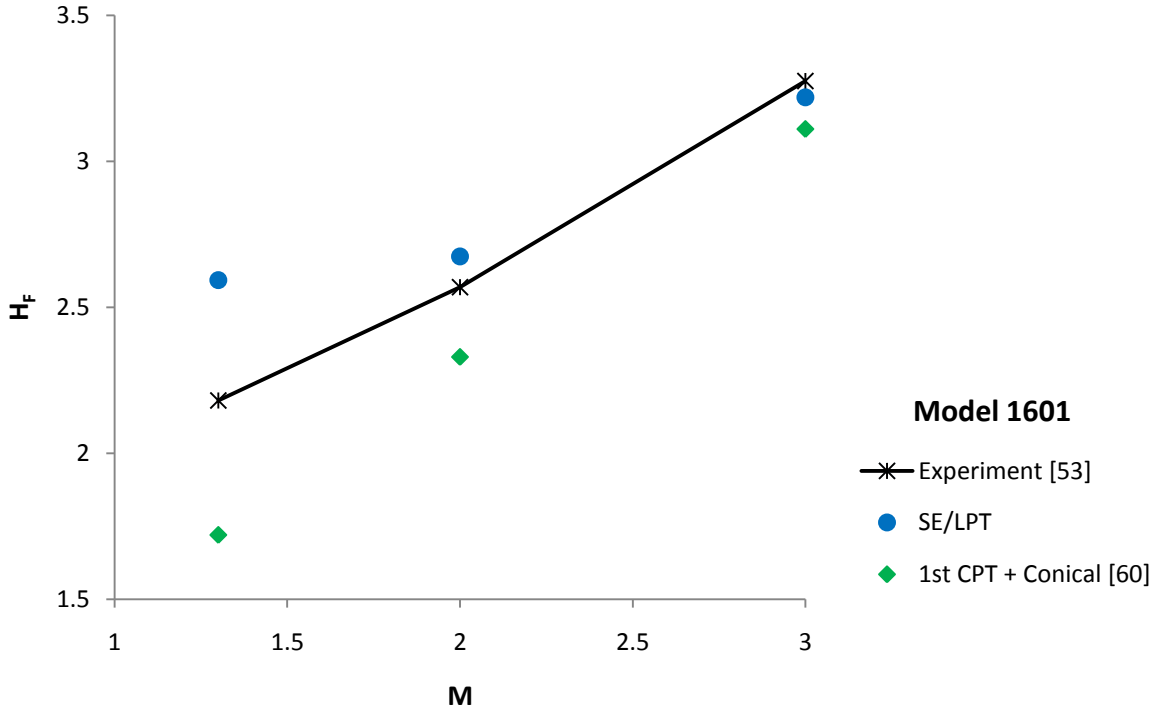


Figure 6.73: Tuovali-McCarty Model 1601, Flutter Altitude-Stiffness Parameter Variation with Mach Number

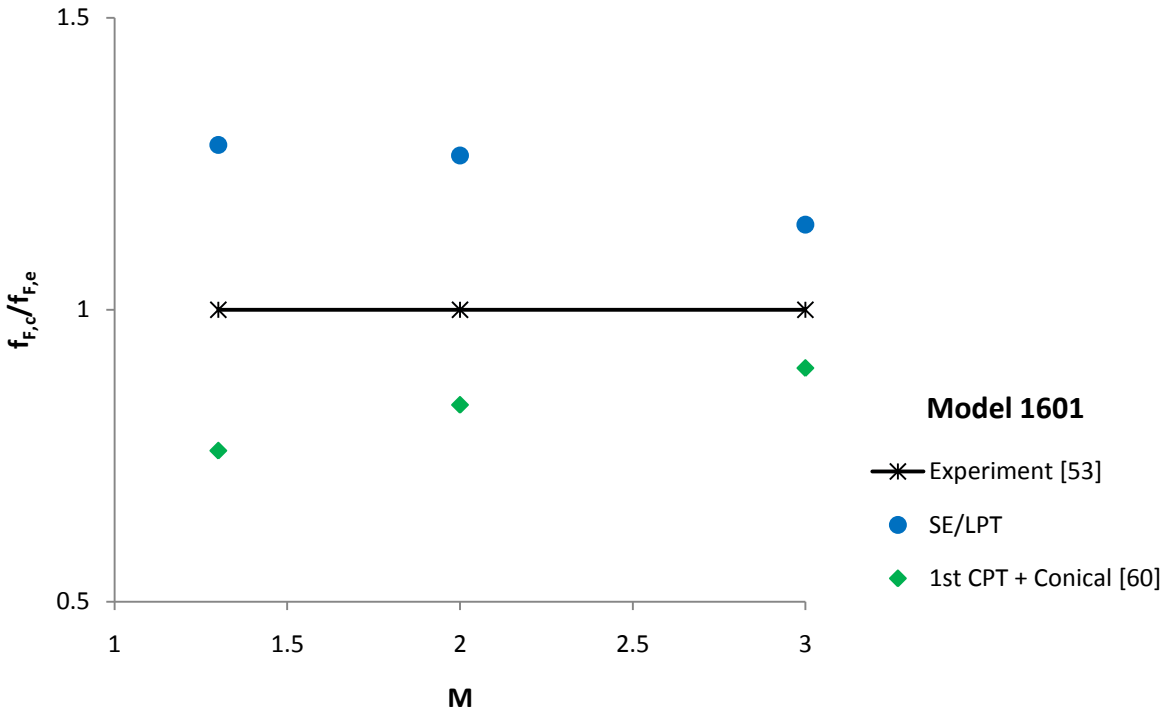


Figure 6.74: Tuovali-McCarty Model 1601, Variation of Computational-Experimental Flutter Frequency Ratio with Mach Number

The flutter trends predicted by SE/LPT show good correlation to experiment and to the results of Xianxin at higher Mach numbers ($M = 2.0$ and $M = 3.0$). The flutter dynamic pressure is predicted conservatively, as is seen from Figure 6.72 and Figure 6.73, with the exception at $M = 3.0$. The accuracy of the flutter dynamic pressure is again seen to be best predicted by SE/LPT for higher Mach numbers, with good accuracy obtained for the geometry of Model 1601. Poor prediction of the flutter frequency is noted from Figure 6.74 across the range of Mach numbers considered.

The trends of the flutter prediction of Xianxin [60] give good agreement to experiment at higher Mach numbers, with poor correlation shown between $M = 1.3$ and $M = 2.0$. The dynamic pressure and altitude stiffness parameter at flutter are predicted non-conservatively, with particularly poor prediction for $M = 1.3$. Poor agreement with experiment is also obtained for the frequency prediction for all Mach numbers considered.

The improved prediction achieved for the dynamic pressure at flutter achieved by SE/LPT over the hybrid of 1st classical PT and conical flow theory for the geometry of Model 1601 is in contrast to the trends observed for the previous geometries. Given the high sweep angle

($\Lambda = 60°$), the entire span of the wing would be affected by the shock at the leading-edge root for Mach numbers of $M \leq 2.0$; this would not be modelled by SE/LPT, but should be accounted for by conical flow theory. From this consideration, it is expected that the results of Xianxin [60] would give better flutter prediction than SE/LPT. As such, further investigation would be required for an informed observation to be made on the reason for the better prediction achieved by SE/LPT for the given geometry.

6.4 Effect of Fin Taper Ratio on the Flutter Envelope

The developed aeroelastic prediction tool based on SE/LPT in MATLAB (linear) was used to investigate the effect of fin taper ratio on the predicted flutter envelope of an un-swept cantilevered fin. The geometry and material properties of the untapered fin were chosen to be similar to those used for the experimental models of Tuovali and McCarty [53], with $c = 2"$.

In performing the preliminary parametric study, it was intended to isolate the effect of the fin taper ratio on the flutter envelope from other geometric parameters; to this end, the geometric aspect ratio of the wing, the wing span, the wing thickness, and the wing reference area were kept constant. The root chord length was then varied with the taper ratio according to the simple geometric relationship:

$$c_R = \left(\frac{2S_{ref}}{b}\right)\frac{1}{1+\lambda} \tag{6.8}$$

The tip chord was subsequently calculated based on the chosen taper ratio. The bevel on the leading- and trailing-edges was of constant length down the span of the model, and was equal to $1/8^{th}$ of the root chord length.

The general geometry of the wing is defined in Figure 6.75 and Figure 6.76, and the dimensions of the wing that were kept constant are listed in Table 6.12.

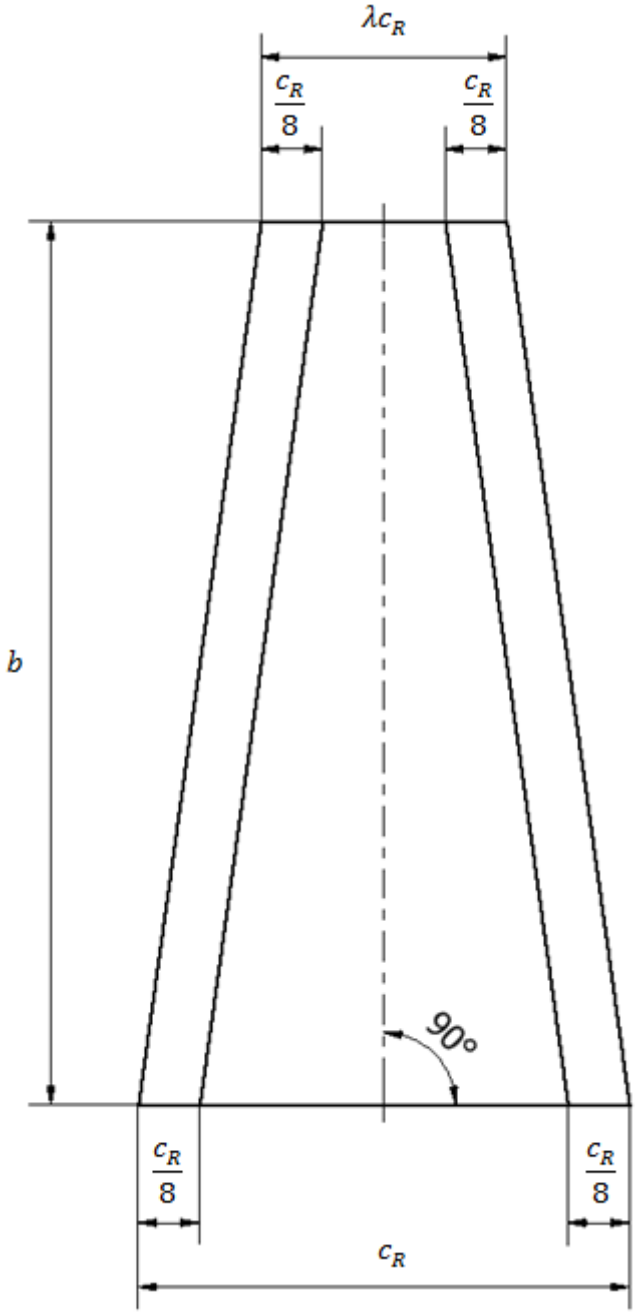


Figure 6.75: Planform of the Unswept Tapered Fins



Figure 6.76: Profile of the Unswept Tapered Fins

Table 6.12: Geometry and Material Constants for the Parametric Study

Constant	Value
b [m]	0.122
S_{ref} [m^2]	6.198 x 10^{-3}
AR	2.40
t [mm]	1.04
$\Lambda_{0.5c}$ [°]	0
E [GPa]	34.5 x 10^9
ρ_{wing} [kg.m^{-3}]	1744
Poisson's ratio υ	0.25

The computations were run using SE/LPT in MATLAB (linear) at $M_\infty = 3.0$, $T_\infty = 105.8$ K (corresponding to the test conditions of Tuovali and McCarty [53]) for a range of dynamic pressures and angles-of-attack. The linearization step-size was chosen such that the resulting deformation of the first-torsion mode would yield a twist of 2° at the wing-tip.

The models were meshed in MATLAB (linear) using 20 chordwise elements and 48 spanwise elements. The bevel lengths were modelled using 3 chordwise elements on each bevel.

The variation of the dynamic pressure at flutter is shown in Figure 6.77. The individual flutter envelopes for each of the taper ratios follow the same trend with α that was seen for the flutter envelope of the ATM-wing (see Figure 6.55). It may be argued that this further supports the hypothesis (see Section 6.2) that the trend of increasing flutter dynamic pressure with increasing α is as a result of insufficient fidelity in the modelling of the steady-contribution to the aerodynamic loading by the implementation of shock-expansion theory in SE/LPT. However, a flutter envelope determined from 3D unsteady Euler computations for either of the geometries considered (ATM-wing or the tapered geometries simulated) would serve as a more rigorous proof of this hypothesis.

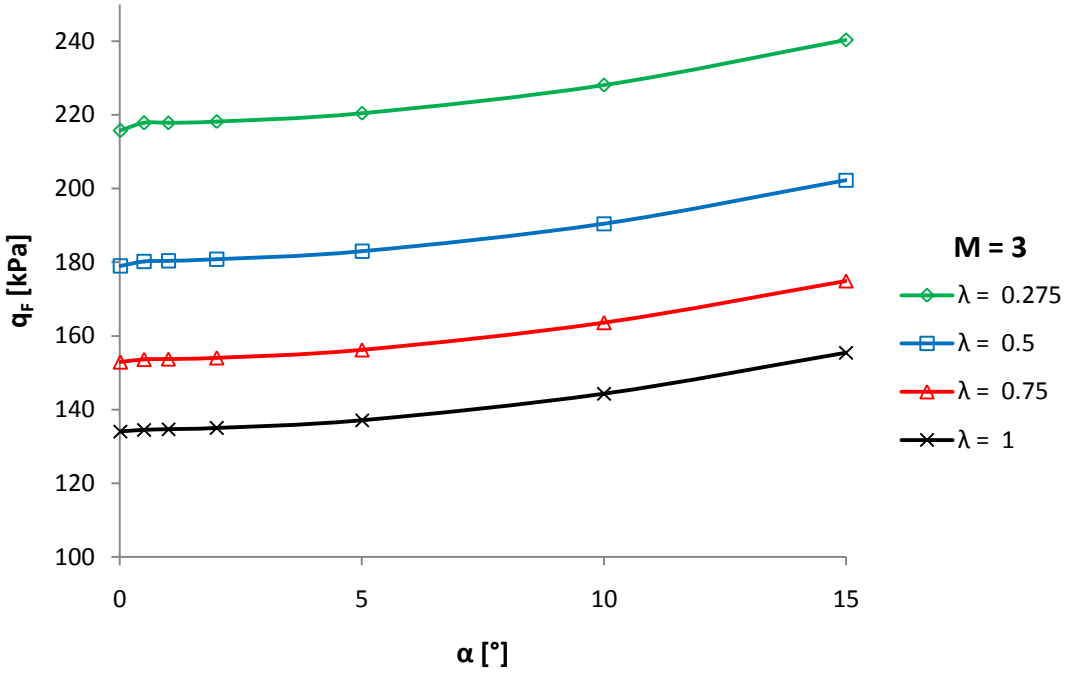


Figure 6.77: Variation of the Flutter Dynamic Pressure Envelope with Fin Taper Ratio

It is clearly seen in Figure 6.77 that the flutter envelope is shifted upward (higher flutter dynamic pressures) with decreasing taper ratio. This is to be expected, as the associated change in geometry serves to increase the natural frequencies of the fin. As the taper ratio is increased, both structural mass and aerodynamic surface area are shifted away from the wing-tip and closer to the root. This implies less inertia and greater stiffness in bending as well as in torsion. It is expected that the increase in flutter dynamic pressure is primarily due to changes to the structural characteristics of the wing, rather than due to changes in the aerodynamic characteristics.

The variation in the flutter frequency with taper ratio is shown in Figure 6.78. The flutter frequency is also seen to increase with decreasing taper ratio. This is also expected, as the higher structural natural frequencies of the wing will result in the coalescence of the aeroelastic modes (which is behaviour associated with flutter) at a higher frequency.

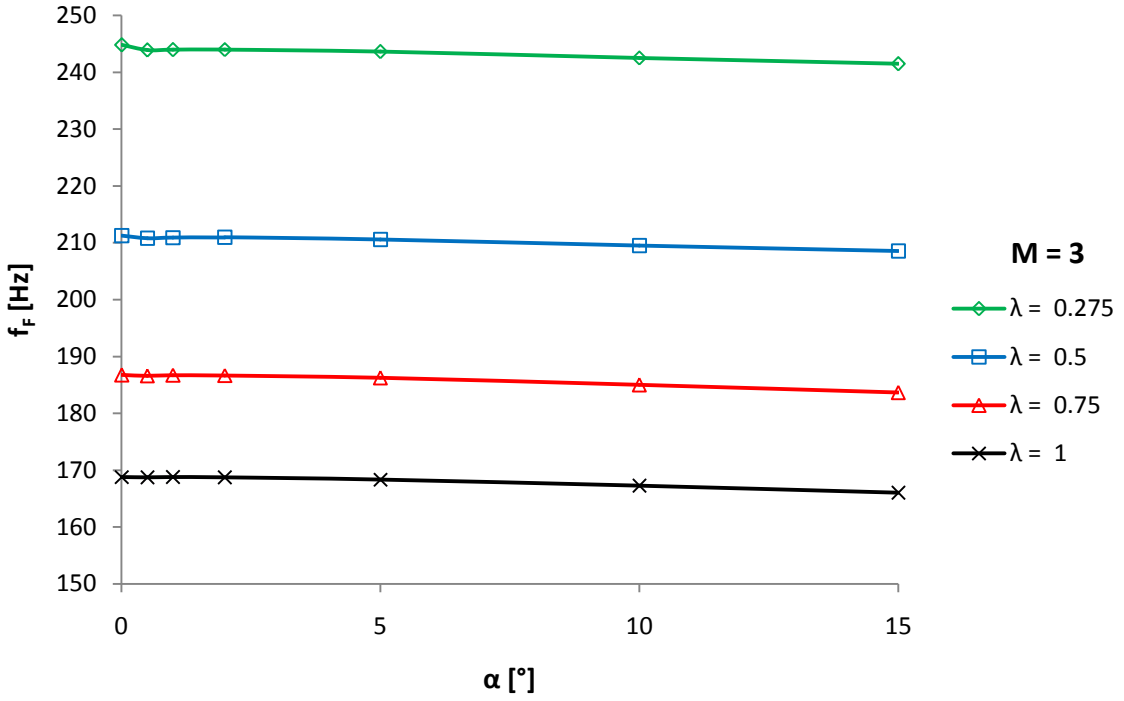


Figure 6.78: Variation of the Flutter Frequency Envelope with Fin Taper Ratio

The increased structural stiffness of the wing with increasing taper ratio is thus seen to result in higher aeroelastic modal frequencies and higher flutter dynamic pressures, effectively expanding the range of flight conditions for which the fin is free from flutter. This has been observed for the considered geometry at $M = 3.0$.

The use of SE/LPT with linearized GAFs has been shown to enable the rapid prediction of aeroelastic behaviour of a cantilevered plate, and has been demonstrated to be suitable for parametric studies.

7 CONCLUSIONS

7.1 Work Accomplished

With reference to the objectives set for this dissertation (Section 1.3), the following have been accomplished:

1. The developments in piston theory were reviewed in Chapter 3, and a consistent definition of the assumptions, nomenclature, formulation, and application of the various forms of piston theory was made. This represents a collection of existing literature on piston theory along with expansion there upon, as a rigorous treatment of the basis from which the differences between local and classical piston theory stem could not be found in literature.

   Furthermore, a computational treatment of the experimental work on the supersonic flutter testing of a cantilevered plate performed by Torii [54] and Matsuzaki [55] was performed in Chapters 5 and 6, expanding on the literature on the use of CFD to analyse supersonic aeroelasticity of cantilevered plates referenced against experimental results.

   Similarly, work on approximate aerodynamic modelling in the aeroelasticity of supersonic cantilevered plates by Morgan et al [50], Chen et al [52], and Xianxin [60] was expanded on through the combined use of shock-expansion theory and local piston theory. The results of the present work in Chapter 6 were compared to the results of the aforementioned authors and to the experimental references (as tested by Tuovali and McCarty [53]) against which the methods were validated.

2. A tool for aeroelastic analysis of cantilevered plates in supersonic tools was developed in MATLAB, with FEM structural solver and with SE/LPT used for the aerodynamic solver, as outlined in Chapter 4. Linearization of the generalized aerodynamic forces was shown to drastically reduce the computational time required for aeroelastic analysis compared to computational aeroelastic simulations requiring the implicit time-marching of the coupled aeroelastic equations. A reduction in computational time of the order of ∼140 was found, as detailed in Section 6.1.6, with an acceptable loss of accuracy (∼5%) in the prediction of the flutter dynamic pressure. The linearized tool was shown to be suitable for preliminary parametric studies of the effect of fin geometry on the flutter envelope in Section 6.4.
3. A number of flutter prediction tools were used in parallel with the assessment of the aeroelastic system stability where possible: the Zimmerman-Weissenburger flutter margin, the flutter margin for discrete systems (FMDS) of Torii [54] , the envelope function shape parameter, and extrapolation of the damping coefficient were investigated in Chapter 6.

   The implementation of an auto-regressive moving-average (ARMA) model to identify the aeroelastic system from computational modal response was successful in identifying the modal frequencies; however, anomalous identification of the modal damping coefficients was made. The incorrect identification of the damping coefficients resulted in poor pre-flutter trends of FMDS.

   The Zimmerman-Weissenburger flutter margin applied to the aeroelastic analysis using a linearized system was shown to be highly suitable for the prediction of the flutter point from a small number of simulated flight conditions in Section 6.1.5.2. Comparison to the performance of the other flutter prediction methods as implemented in the current work showed the clear superiority of the Zimmerman-Weissenburger flutter margin for linearized systems.

   The extrapolation of the envelope shape parameter and damping coefficients was found to be entirely unsuitable in Section 6.1.5.2 for the geometry of Torii and Matsuzaki [54], as the wing experienced hard flutter. The use of these metrics were also found to be unsuitable for the non-linearized systems due to the inaccuracy of the damping coefficients estimated using the ARMA model.

4. The developed tool for aeroelastic prediction was shown to be fully capable of predicting hard flutter in Section 6.1.4 and 6.1.5.

7.2 Recommendations for Future Work

Comparison of the performance of the aeroelastic prediction tool based on SE/LTP to aeroelastic analyses in which 3D effects were accounted for showed that the fidelity of the analysis of the steady contribution to the aerodynamic loading is a critical factor in the accuracy and validity of the predicted flutter trends. The use of 2D strip theory effectively limits the accuracy of aerodynamic analysis of a large range of plate geometries and flow conditions. Therefore it is recommended that future implementations of LPT with approximate analytical methods for the steady aerodynamic contributions use a method in which 3D influence (such as tip effects and wing-body interference) is accounted for. This (along with the appropriate extension of the structural solver) would potentially further extend the applicability of the analysis to the missile body, as well as accounting for the influence of the body aerodynamics on the aeroelastic behaviour of the fins.

It is further recommended that future computational work be done to determine the flutter envelope and its variation with angle-of-attack for the wing of Torii and Matsuzaki [54] using 3D unsteady Euler computations. This would serve to extend the literature on supersonic flutter computation, and the work could be used as a further benchmark for the validation of future developments in approximate aeroelastic analyses.

REFERENCES

[1] McNamara, J.J., "Aeroelastic and aerothermoelastic behaviour of two and three dimensional lifting surfaces in hypersonic flow," Ph.D. thesis, University of Michigan, 2005.

[2] Chabalko, C.C., "Identification of transient nonlinear aeroelastic phenomena," MSc thesis, Virginia Polytechnic Institute and State University, 2007.

[3] "MSC Nastran 2012: Getting Started with MSC Nastran," MSC Software

[4] Zona Technology Inc., INTERNET, http://www.zonatech.com/Products.htm, Cited 9 February 2014.

[5] Zona Technology Inc., INTERNET, http://www.zonatech.com/ZAEROInformation.htm#sec1, Cited 9 February 2014.

[6] NeoCASS Suite, INTERNET, http://www.neocass.org/?Home, Cited 9 February 2014.

[7] Nielsen Engineering and Research Inc., INTERNET, http://www.nearinc.com/index.cfm., Cited 9 February 2014.

[8] Favier, G., Kibangou, A.Y., and Bouilloc, T., " Nonlinear system modeling and identification using Volterra-PARAFAC models," *International Journal of Adaptive Control and Signal Processing*, Vol. 26, 2012.

[9] McNamara, J.J. and Friedmann, P.P., "Aeroelastic and aerothermoelastic analysis in hypersonic flow: past, present, and future," *AIAA Journal*, Vol. 49, No. 6, 2011, pp. 1089–1121.

[10] McNamara, J.J., Crowell, A.R., Friedmann, P.P., Glaz, B., and Gogulapati, A., "Approximate modelling of unsteady aerodynamics for hypersonic aeroelasticity," *Journal of Aircraft*, Vol.47, No. 10, 2009, pp. 1932–1935.

[11] Zhang, W.-W., Ye, Z.-Y, Zhang, C.-A., and Liu, F., "Supersonic flutter analysis based on a local piston theory," *AIAA Journal*, Vol. 47, No. 10, 2009, pp. 2321–2328.

[12] Liu, D.D., Yao, Z.X., Sarhaddi, D., and Chavez, F., "From piston theory to a unified hypersonic-supersonic lifting surface method," *Journal of Aircraft*, Vol. 34, No. 3, 1997, pp. 304–312.

[13] Anderson, J.D., *Hypersonic and high temperature gas dynamics*, AIAA, 2000.

[14] Gentry, A.E., Smyth, D.N., and Oliver, W.R., *The Mark IV Supersonic-Hypersonic Arbitrary-Body Program. Volume II. Program Formulation*, USAF Flight Dynamics Laboratory, AFFDL-TR-73-159, 1973.

[15] Anderson, J.D., *Fundamentals of aerodynamics*, McGraw-Hill, 3rd ed., 2001.

[16] Hayes, W.D. and Probstein, R.F., *Hypersonic flow theory. Volume I. Inviscid Flows*, Academic Press, New York, 2nd ed., 1966.

[17] Eggers, A.J., Syverston, C.A. and Kraus, S., "A study of inviscid flow about airfoils at high supersonic speeds," Report 1123, NACA, 1953.

[18] Savin, R.C., "Application of the generalized shock-expansion method to inclined bodies of revolution traveling at high supersonic airspeeds," NACA TN-3349, 1955.

[19] Syverston, C.A. and Dennis, D.H., "A second-order shock expansion method applicable to bodies of revolution near zero lift," Report 1328, NACA, 1957.

[20] Munk, M.M. "The aerodynamic forces on airship hulls," Report 184, NACA, 1924.

[21] Gülçat, Ü. *Fundamentals of modern unsteady aerodynamics*, Springer, 2010.

[22] Ashley, H. and Landhal, M. *Aerodynamics of wings and bodies*, Addison-Wesley Publishing Company Inc., 1965.

[23] Van Dyke, M.D., "Second-order slender body theory - axisymmetric flow,". NASA TR R-47, 1959.

[24] Pivko, S., "On nonlinear effects in slender body theory," *Publications de L'Institut Mathematique*, Vol. 9, No. 23, 1969, pp. 75–83.

[25] Moore, F.G. and Moore, L.Y., "2009 Version of the Aeroprediction code," *Journal of Spacecraft and Rockets*, 2008, Vol. 45, No. 4, 2008, pp. 667–690.

[26] Rosema, C., Doyle, J., Auman, L., Underwood, M., nad Blake, W., "MISSILE DATCOM: User's Manual -- 2011 Revision," AFRL-RB-WP-TR-2011-3071, 2011.

[27] Van Dyke, M.D., "A study of hypersonic small-disturbance theory," Report 1194, NACA, 1954.

[28] Ashley, H. and Zartarian, G., "Piston theory - a new aerodynamic tool for the aeroelastician," *Journal of the Aeronautical Sciences*, Vol. 23, No.12, 1956, pp. 1109–1118.

[29] McNamara, J.J. and Friedmann, P.P., "Flutter boundary identification for time-domain computational aeroelasticity," *AIAA Journal*, 2007, Vol. 45, No. 7, 2007, pp. 1546–1555.

[30] unkown, INTERNET, http://soliton.ae.gatech.edu/labs/windtunl/classes/unstaero/wing2/wingflo2.html, Cited 14 February 2014.

[31] Olsen, J., "Demonstration of a supersonic box method for unsteady aerodynamics of nonplanar wings," AFFDL-TR67-104 Part II, 1967.

[32] Ehlers, F.E. and Rubbert, P.E., "A Mach line panel method for computing the linearized supersonic flow over planar wings," NASA CR-152126, 1978.

[33] Ehlers, F.E., Epton, M.A., Johnson, F.T., Magnus, A.E., and Rubbert, P.E., "A higher order panel method for linearized supersonic flow," NASA CR-3062, 1979.

[34] Chen, P.C. and Liu, D.D., "Unified hypersonic/supersonic panel method for aeroelastic applications to arbitrary bodies," *Journal of Aircraft*, Vol. 39, No. 3, 2002, pp. 499–506.

[35] Scanlan, R.H., "Dynamic similitude in models," *Aero-hydroelasticité*, Eyrolles, Ermenonville, 1972.

[36] Ashley, H., "Principles of aero-hydroelasticity," *Aero-hydroelasticité*, Eyrolles, Ermenonville, 1972.

[37] Amsallem, D., "Interpolation on manifolds of CFD-based fluid and finite-element-based structural reduced order models for on-line aeroelastic predictions," Ph.D. thesis, Stanford University, 2010.

[38] Sarigul-Klijn, N., "Efficient interfacing of fluid and structure for aeroelastic instability predictions," *Internation Journal for Numerical Methods in Engineering*, 2000, Vol. 47, pp. 705–728.

[39] Rao, S.S., *Mechanical vibrations*, Pearson Prentice Hall, 4th ed., 2004.

[40] Katona, M.G., Thompson, R. and Smith, J., "Efficiency study of implicit and explicit time integration operators for finite element applications," TR-856, Civil Engineering Laboratory, AD-A043968, 1977.

[41] Dowell, E.H. and Tang, D., "Nonlinear aeroelasticity and unsteady aerodynamics," *AIAA Journal*, Vol. 40, No. 9, 2002, pp. 1697–1707.

[42] Dowell, E.H., Peters, D.A., Clark, R., Scanlan, R., et. al., *A modern course in aeroelasticity*, Kluwer Academic Publishers, 2005.

[43] Thomas, J.P., Dowell, E.H. and Hall, K.C., "Nonlinear inviscid aerodynamic effects on transonic divergence, flutter, and limit-cycle oscillations," *AIAA Journal*, Vol. 40, No. 4, 2002, pp. 638–646.

[44] Dotson, K.W., Baker, R.L. and Sako, B.H., "Limit-cycle oscillation induced by nonlinear aerodynamic forces," *AIAA Journal*, Vol. 40, No. 11, 2002, pp. 2197–2205.

[45] Lee, I.-W., "Chapter 16A Direct Integration Methods," *CE514 lecture notes*, Korea Advanced Institute of Science & Technology, 2013, INTERNET, http://sdvc.kaist.ac.kr/lecture/CE514_2013Fall/ch16A-Direct%20Integration%20Mehods.pdf, Cited 14 February 2014.

[46] Farhat, C., "Chapter 7 Direct Time-Integration Methods," *AA242B lecture notes*, Stanford University, 2012, INTERNET, http://www.stanford.edu/group/frg/course_work/AA242B/CA-AA242B-Ch7.pdf, Cited 14 February 2014.

[47] Kukreja, S.L., "Non-linear system identification for aeroelastic systems with application to experimental data,". NASA TM-2008-214641, 2008.

[48] Dimitriadis, G., "Lecture 7: Supersonic Aeroelasticity," Universite de Liege, INTERNET, http://www.ltas-aea.ulg.ac.be/cms/index.php?page=aeroelasticity-course, Cited 15 February 2014.

[49] Ashley, H., "Analytical Methods in Aero-Hydroelasticity," *Aero-hydroelasticité*, Eyrolles, Ermenonville, 1972.

[50] Morgan, H.G., Huckel, V. and Runyan, H.L., "Procedure for calculating flutter at high supersonic speed including camber deflections, and comparison with experimental results," NACA TN-4335, 1958.

[51] Dimitriadis, G., "Lecture 6: Flight Flutter Testing," Universite de Liege, INTERNET, http://www.ltas-aea.ulg.ac.be/cms/index.php?page=aeroelasticity-course, Cited 15 February 2014.

[52] Chen, P.C., Sarhaddi, D., Liu, D.D., and Striz, A.G., "Development of the aerodynamic/aeroservoelastic modules in ASTROS," Air Force Research Laboratory, AFRL-VA-WP-TR-1999-3051, 1999.

[53] Tuovila, W.J. and McCarty, J.L., "Experimental flutter results for cantilever-wing models of Mach numbers up to 3.0," NACA-RM-L55E11, 1955.

[54] Torii, H., "The extension of discrete-time flutter margin," *28th International Congress of the Aeronautical Sciences*, Brisbane, 2012.

[55] Matsuzaki, Y., "An overview of flutter prediction in tests based on stability criteria in discrete-time domain," *International Journal of Aeronautical and Space Sciences,* Vol. 12, No. 4, 2011, pp. 305–317.

[56] Allen, C.B., Jones, D., Taylor, N.V., Badcock, K.J., Woodgate, M.A., et al., "A comparison of linear and nonlinear flutter prediction methods: A summary of PUMA DARP aeroelastic results," *Aeronautical Journal*, Vol. 110, Issue 1107, 2006, pp. 333–343.

[57] Lind, R., "Flight-test evaluation of flutter prediction methods," *Journal of Aircraft*, Vol. 40, No. 5, 2003, pp. 964–970.

[58] Zhang, W.-W., Ye, Z.-Y, Zhang, C.-A., and Liu, F., "Prediction of flutter and LCO by an Euler method on non-moving Cartesian grids with boundary-layer corrections," *43rd AIAA Aerospace Sciences Meeting and Exhibit*, Reno, Nevada, AIAA 2005-0833, 2005.

[59] Hanson, P.W. and Tuovila, W.J., "Experimentally determined natural vibration modes of some cantilever-wing flutter models by using an acceleration method," NACA TN-4010, 1957.

[60] Xianxin, W., "A new method for calculating supersonic unsteady aerodynamic forces and its application," *Acta Aeronautica et Astronautica Sinica*, 1983, Vol. 4, No. 3, 1983, pp.9–18.

[61] Dimitriadis, G., "Investigation of nonlinear aeroelastic systems," Ph.D. thesis, University of Manchester, 2001.

[62] Yildiz, E.N., "Aeroelastic stability prediction using flutter flight test data," Ph.D. thesis, Middle East Technical University, 2007.

[63] unknown., The Faculty of Aerospace Engineering. Israel Institute of Technology, INTERNET, http://ae-www.technion.ac.il/admin/serve.php?id=15345, Cited 16 February 2014.

[64] Weisshaar, T.A., "AAE556 Lecture 32: The V-g method," Purdue University, INTERNET, https://engineering.purdue.edu/AAE/Academics/Courses/aae556/2011, Cited 16 February 2014.

[65] Weisshaar, T.A., "AAE556 Lectures 34, 35: The p-k method, a modern alternative to V-g," Purdue University, INTERNET, https://engineering.purdue.edu/AAE/Academics/Courses/aae556/2011, Cited 16 February 2014.

[66] Lighthill, M.J., "Oscillating airfoils at high Mach numbers," *Journal of the Aeronautical Sciences*, Vol. 20, No. 6, 1953, pp. 402–406.

[67] Van Dyke, M.D., "A study of second-order supersonic flow theory," NACA TN-2200, 1951.

[68] Donov, A.E., "A flat wing with sharp edges in a supersonic stream," NACA TM-1394, 1956.

[69] Houghton, E.L. and Carpenter, P.W., *Aerodynamics for engineering students*, Butterworth-Heinemann, 5th ed., 2003.

[70] The MathWorks Inc., *MATLAB Product Help*, 2009.

[71] FOI., "Edge - Theoretical Formulation," INTERNET, http://www.foi.se/edge, March 2007, Cited 16 February 2014.

[72] Kwon, Y.W. and Bang, H., *The finite element method using MATLAB*, CRC Press, 1997.

[73] Aalami, B. and Williams, D.G., *Thin plate design for transverse loading*, Crosby Lockwood Staples, 1975.

[74] Hughes, T.J.R., *The finite element method: linear static and dynamic finite element analysis*, Dover Publications, New York, 2000.

[75] Chia, C.-Y., *Nonlinear analysis of plates*, McGraw-Hill, New York,1980.

[76] Liu, G.R. and Quek, S.S., *The finite element method: a practical course*, Butterworth-Heinemann, 2003.

[77] Hughes, T.J.R. and Tezduyar, T.E., "Finite elements based upon Mindlin plate theory with particular reference to the four-node bilinear isoparametric element," *Journal of Applied Mechanics*, Vol. 48, No. 3, 1981, pp. 587–596.

[78] Przemieniecki, J.S., *Finite element structural analysis: new concepts*, AIAA, 2009.

[79] Ferreira, A.J.M., *MATLAB codes for finite element analysis*, Springer, 2009.

[80] Komzsik, L., *What every engineer should know about computational techniques of finite element analysis*, CRC Press, 2009.

[81] Faber, M.H. and Mojsilovic, N., "The finite element method for the analysis of non-linear and dynamic systems," Swiss Federal Institute of Technology, INTERNET, http://www.ibk.ethz.ch/emeritus/fa/education/FE_II/FEII_07/Lecture_10.pdf, Cited 29 September 2013.

APPENDICES

A. GEOMETRY OF THE TUOVALI AND McCARTY TEST MODELS

The data quoted in this section are from the reports by Tuovali and McCarty [53], and Hanson and Tuovali [59]. The models considered are untapered, backward-swept trapezoidal wings with constant thickness. The leading- and trailing-edges are sharpened, with a constant bevel length of $1/8$th of the chord-length. The cross-section of the models were the same when taken perpendicular to the leading-edge of each model.

The dimensions of the models are given in Table A.1, with the nomenclature defined in Figure A.1 and Figure A.2.

Table A.1: Dimensions of the Tuovali and McCarty Models

Model	Λ [°]	AR	b [mm]	c [mm]	t [mm]
5151	15	2.67	140	52.6	1.04
4301	30	2.08	122	58.7	1.04
3451	45	1.38	99.0	71.8	1.04
1601	60	0.69	70.5	101.6	1.04

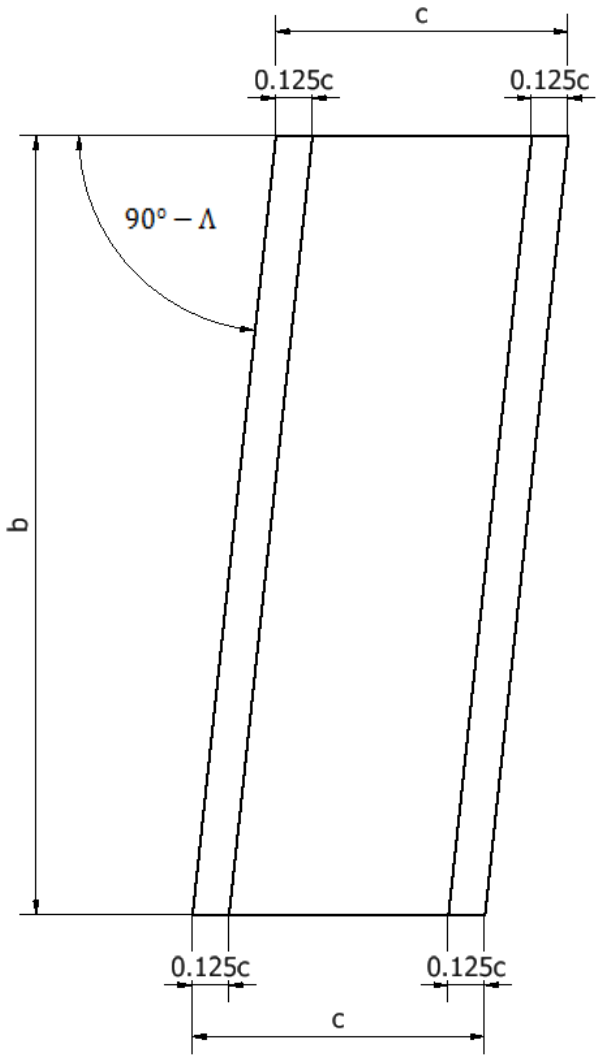


Figure A.1: Typical Planform of the Tuovali and McCarty Models

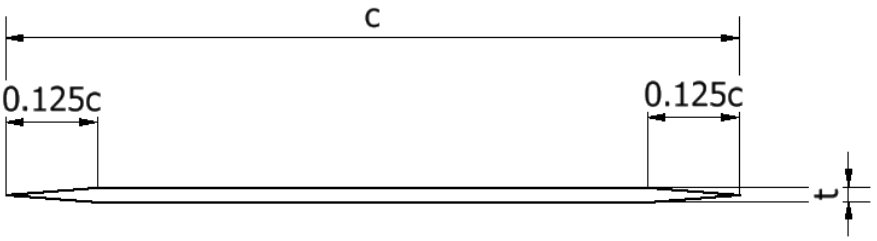


Figure A.2: Typical Profile of the Tuovali and McCarty Models

B. FINITE ELEMENT FORMULATION

Nomenclature

The following nomenclature is adopted for this appendix; previous nomenclature does not apply.

A^e	element area
B	strain-displacement matrix
b	plate span
C^m	continuity of the m-th derivative
D	constitutive matrix
d	element displacement vector
E	young's modulus
f	element distributed loading vector
I	inertial matrix
J	Jacobian
j	Jacobian determinant
K	global stiffness matrix
k	element stiffness matrix
M	global mass matrix
m	element mass matrix
N	shape function
n_{el}	number of elements
n_{nodes}	number of nodes
P	global unsmoothed nodal strain vector
S	global strain-smoothing matrix
s	element strain-smoothing matrix
t	plate thickness

u, v, w	displacements in x, y, and z, respectively
x, y, z	physical coordinates
γ	shear strain
ε	strain
ϵ	element unsmoothed nodal strain vector
θ	fibre rotation
κ	shear stress factor
ρ	material density
σ	stress
τ	shear stress
υ	Poisson's ratio
χ	curvature
ξ, η	natural coordinates (corresponding to x and y) in the computational plane

Subscripts

$cent$	centroid
i, j	node number
$x, y, z,$	component in the respective direction
ξ, η	component in the respective direction

Superscripts

b	bending
e	element
s	shear

Finally, comma notation is used to denote partial differentiation, for example:

$$\xi_{,x} \equiv \frac{\partial \xi}{\partial x}$$

Plate Mechanics

In the analysis of a beam in twisting and bending, the sectional properties are generally treated as remaining constant. Specifically, in the aeroelastic analysis of wings, the sectional shape (airfoil) of the wing is generally assumed to remain constant, and the wing is generally analysed as a beam. The description of the bending behaviour of plates is somewhat more complex than that of simple beams. In considering the deformation undergone by a cantilevered plate, the applicability of terms such as "bending" and "twist" becomes strained, as the local sectional shape of the plate is no longer constant. The complexity of plate mechanics precludes the use of a purely analytical description of the plate behaviour, and lends itself to finite element analysis. The description of plate mechanics is generally divided into two categories: thin-plate theory, and plate theory taking into account thickness effects.

Linear Thin-Plate Theory

In classical plate theory (Kirchhoff plate theory), transverse deformations in the plate are neglected, and the plate is assumed to be in plane stress [72]. Plates may be modelled to undergo only flexural action (bending), or to only undergo membrane action (in-plane tension), and the resulting thin-plate theories are linear; however, a plate undergoing membrane action only does not deform out of plane [73]. Aalami and Williams [73] describe how classical thin-plate theory (CPT) is applicable only to plates undergoing small deflections, due to a nonlinearity developing between displacements and transverse loading as the plate deforms out of plane.

Hughes [74] notes that Kirchhoff plate theory requires C^1-continuity (continuity of the 1st-derivatives) across boundaries of displacements. Hughes [74] remarks the development of C^1-interpolation schemes for two-dimensional plate elements based on classical theory results in interpolation schemes which are extremely complicated.

Non-Linear Thin-Plate Theory

Non-linearity in thin-plate theory may enters through the material non-linearity, finite (nonlinear) strains, and geometric non-linearity. For a thin isotropic plate undergoing large deflections, non-linearity enters through the use of Von Karman's nonlinear strain-displacement relations in the formulation of mid-plane strains [75]. Chia [75] recommends that linear thin-plate theory be used with plates that have a thickness-to-span ratio of $\frac{t}{b} \leq \frac{1}{15}$ (≈ 0.067), with a maximum transverse deflection of less than twice the plate thickness (for clamped plates) $\frac{w_{max}}{t} < 2$; thereafter, nonlinear effects become important.

Aalami and Williams [73] give empirical guidelines for the design of plates for transverse loading, and describe the large-deflection behaviour of plates as resulting from the interaction between the flexural (small-deflection) and membrane actions in the plate.

The definition of what magnitude of deflection constitutes "large deflections" varies between authors and the applied constraints. Typically, though, nonlinearity is seen to occur once the transverse displacement of the plate is of the order of the plate thickness.

Mindlin-Reissner Plate Theory

Mindlin-Reissner plate theory accounts for transverse shear deformations in the plate, and is consequently applicable to thicker plates than CPT is. Slightly larger displacements are achieved for thin plates in comparison to CPT [74].

The equations of Mindlin-Reissner plate theory involve the rotations of fibres in the plate; two sign conventions exist for these rotations. The sign convention adopted here follows the "right-hand rule".

The main assumptions, as given by Hughes [74], are repeated here:

1. The domain Ω is of the following special form:

$$\Omega = \left\{(x, y, z) \in R^3 \middle| z \in \left[\frac{-t}{2}, \frac{t}{2}\right], (x, y) \in A \subset R^2\right\}$$

where t is the plate thickness and A is its area.

2. $\sigma_{zz} = 0$ [plane stress]

3. $u(x, y, z) = z\theta_y(x, y)$ [plane sections remain plane]
   $v(x, y, z) = -z\theta_x(x, y)$

4. $w(x, y, z) = w(x, y)$ [transverse displacement does not vary through the thickness]

The derivation of the equations in Mindlin-Reissner theory is widely published in literature (see Kwon and Bang [72], Hughes [74], and Liu and Quek [76]), and only the main results will be repeated here.

Finite Element Analysis

Variational methods are used to discretize the continuous system physics into a set of simpler discrete equations. The weak form of the system equations are used, and trial solutions to the system are computed. For more information on variational methods and the weak and strong formulations in plate mechanics, the reader is referred to texts on the finite element method such as those by Hughes [74], Chia [75], Kwon and Bang [72], and Liu and Quek [76].

Bilinear Quadrilateral Elements

Bilinear (4-node) quadrilateral elements (the formulation of which is covered by Hughes [74], Hughes and Tezduyar [77], Przemieniecki [78], Liu and Quek [76], and Ferreira [79]) are C^0 elements (continuity of the 0-th derivative). This implies that whilst interpolated displacements are continuous across element boundaries, terms depending on the derivatives of the shape functions (e.g., strains) are not.

The displacements w, θ_x, and θ_y are assumed and are interpolated by bilinear shape functions (see page 239).

Bilinear quadrilateral elements offer the advantage of being simple in their formulation and coding, and have been broadly covered in literature -- this makes the elements a good choice for a first-development of finite-element code. Other low-order quadrilateral elements exist

which give better performance for a wide range of parameters, and which have correct rank for bending elements. Hughes [74] discusses the differences in formulation of these elements and their performance, considering elements such as McNeal's QUAD4, as well as the heterosis and T1 elements developed in part by Hughes. Some differences between the basic bilinear quadrilateral elements and other bilinear elements, such as T1, lies in the use of an assumed shear-strain field which is interpolated bilinearly, as well as various "tuning parameters" [74].

Higher order elements, as well as triangular elements, may also be used. In some cases, better results may be obtained using higher-order elements, however, they are computationally more complex and expensive. Under certain conditions, lower-order elements may perform better than higher-order elements (CQUAD4 is better for doubly curved surfaces than CQUAD8)[3].

Meshing

The reader is referred to the MSC Nastran Guide [3] and to other texts on FEA on good meshing procedures.

The following element distortions are considered acceptable [3] for the CQUAD4 element of Nastran, and are quoted here as a guideline:

Table B.1: Acceptable QUAD4 Element Distortions

Distortion Type	Acceptable Limits
Aspect Ratio	< 4
Warp	$< 5\%$
Skewing	$< 60°$
Taper Angle	$< 30°$
Taper Ratio	$> \frac{1}{3}$

Shape Functions

The use of shape functions allows variables at any point on the interior of an element to be described in terms of (or interpolated from) the values those variables take at the nodes of the element. In displacement-type element formulations, shape functions are used to describe displacements and coordinates; however, element thicknesses, as well as applied pressures, may also be described by shape functions.

Liu and Quek [76] explain the various properties that shape functions are required to satisfy; one such property is referred to as the property of unity. This requires that the value of the shape function of a node be equal to 1 at the node, and be equal to 0 at all other nodes. Such functions are often described as "tent-functions" [74]. The sum of the nodal shape functions at any point within the element boundary is necessarily equal to 1. This allows the shape functions to describe the value of a variable inside the element in terms of the value of the variable at the element nodes.

Hughes [74] states that the basic conditions shape functions must satisfy to ensure convergence of the finite element solution are:

1. smoothness (at least C^1 continuity) on each element interior,
2. continuity (at least C^0) across each element boundary,
3. completeness.

The degree of smoothness is determined by the level of continuity of derivatives of the shape-function. A shape function possessing C^m-continuity has continuity of the m-th derivative of the shape function. Elements constructed from shape functions that have C^1-continuity on the element interior and have C^0-continuity across element boundaries are referred to as C^0-elements [74].

Hughes [74] remarks that conditions 1 and 2 ensure that all integrals necessary for the computation of element arrays are well-defined.

It is noteworthy that condition 2 relates to C^0-continuity across the element boundary -- the value of the shape function must be continuous. Recall that in displacement-type elements, shape functions are used to describe the displacements on an element interior. Thus, condition 2 requires that displacements be continuous across the element boundary; however,

terms dependent on derivatives of the displacements (i.e., strains), need not be continuous across the boundary.

Regarding condition 3, Hughes [74] notes that completeness refers to the ability of the shape functions to represent rigid-body motions and constant strains. In 2-dimensional problems, the appropriate selection of basis functions (monomials) to include the linear terms leads to completeness for elements with 3 or more nodes [74].

Shape functions for bilinear quadrilateral elements are described in the natural coordinates (see page 240for the equations of the shape functions and their derivatives). The following shape functions have been used in the formulation of a variable-thickness, bilinear quadrilateral displacement-type element subjected to a non-uniform transverse pressure:

$$w(\xi,\eta) = \sum_{i=1}^{4} N_i(\xi,\eta) w_i \qquad (B.1)$$

$$\theta_x(\xi,\eta) = \sum_{i=1}^{4} N_i(\xi,\eta) \theta_{x_i} \qquad (B.2)$$

$$\theta_y(\xi,\eta) = \sum_{i=1}^{4} N_i(\xi,\eta) \theta_{y_i} \qquad (B.3)$$

$$t(\xi,\eta) = \sum_{i=1}^{4} N_i(\xi,\eta) t_i \qquad (B.4)$$

$$f_z(\xi,\eta) = \sum_{i=1}^{4} N_i(\xi,\eta) f_{z_i} \qquad (B.5)$$

Smoothing (see page 246) will be applied to the Von Mises stress in the element, and the smoothed stress will be interpolated by shape functions.

Coordinate Transformation

In computing the shape functions and their derivatives, the quadrilateral element domain in the physical plane (described by physical coordinates (x, y)) is transformed into a square in the computational plane (described by natural coordinates (ξ, η)). This mapping, shown in Figure B.1, allows for simpler expressions to be developed for the shape functions, and also

lends itself directly to Gaussian quadrature, as the domain is the appropriate size and shape. Field variables may be interpolated using shape functions in the natural coordinates [76].

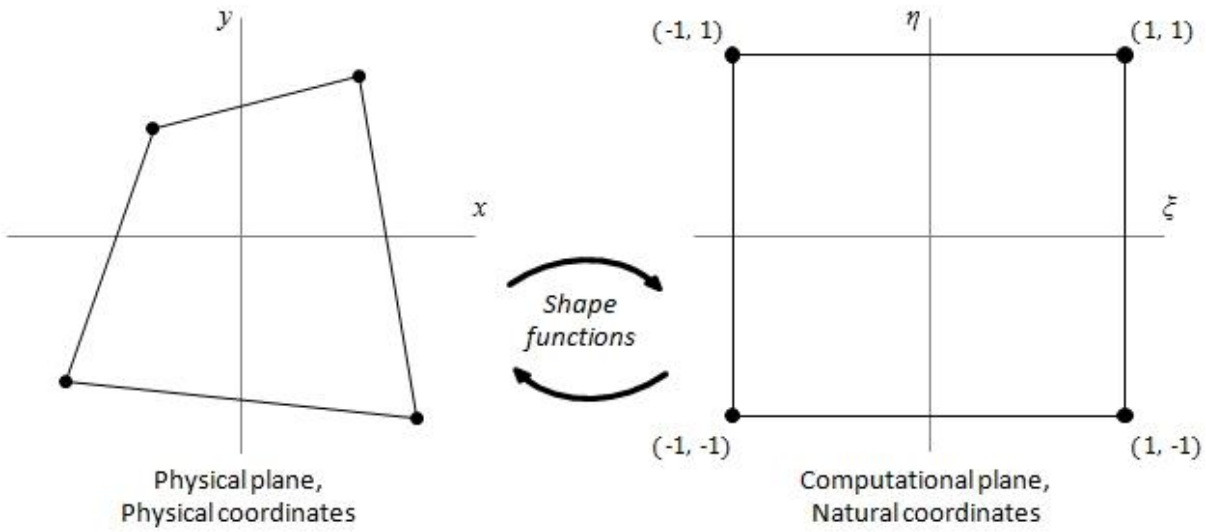


Figure B.1: Coordinate Transformation in the Finite Element Method

Following the standard FEM numbering convention for nodes, the coordinates of the transformed quadrilateral in the natural space are:

Node 1 (x_1, y_1), $(i = 1)$: $(\xi_1, \eta_1) = (-1, -1)$ (B.6)

Node 2 (x_2, y_2), $(i = 2)$: $(\xi_2, \eta_2) = (1, -1)$ (B.7)

Node 3 (x_3, y_3), $(i = 3)$: $(\xi_3, \eta_3) = (1,1)$ (B.8)

Node 4 (x_4, y_4), $(i = 4)$: $(\xi_4, \eta_4) = (-1,1)$ (B.9)

The equations that follow are cited from Hughes [74]. The shape functions are given by:

$$N_i(\xi, \eta) = \frac{1}{4}(1 + \xi_i \xi)(1 + \eta_i \eta) \quad \text{(B.10)}$$

and hence the natural derivatives are given by:

$$N_{i,\xi} = \frac{1}{4}(1 + \eta_i \eta)(\xi_i) \quad \text{(B.11)}$$

$$N_{i,\eta} = \frac{1}{4}(1 + \xi_i \xi)(\eta_i) \quad \text{(B.12)}$$

The physical coordinates of a point on the interior of an element are described in terms of the nodal coordinates (x_i, y_i) and the nodal shape functions N_i evaluated at the point:

$$x(\xi,\eta) = \sum_{i=1}^{4} N_i(\xi,\eta)\, x_i \qquad \text{(B.13)}$$

$$y(\xi,\eta) = \sum_{i=1}^{4} N_i(\xi,\eta)\, y_i \qquad \text{(B.14)}$$

The following derivatives then follow from the previous equations:

$$x_{,\xi} = \sum_{i=1}^{4} \frac{1}{4}(1+\eta_i\eta)\xi_i\, x_i \qquad \text{(B.15)}$$

$$x_{,\eta} = \sum_{i=1}^{4} \frac{1}{4}(1+\xi_i\xi)\eta_i\, x_i \qquad \text{(B.16)}$$

$$y_{,\xi} = \sum_{i=1}^{4} \frac{1}{4}(1+\eta_i\eta)\xi_i\, y_i \qquad \text{(B.17)}$$

$$y_{,\eta} = \sum_{i=1}^{4} \frac{1}{4}(1+\xi_i\xi)\eta_i\, y_i \qquad \text{(B.18)}$$

These may be collected into the Jacobian matrix:

$$J = \begin{bmatrix} x_{,\xi} & x_{,\eta} \\ y_{,\xi} & y_{,\eta} \end{bmatrix} \qquad \text{(B.19)}$$

$$j = det(J) \qquad \text{(B.20)}$$

which is used to find the physical derivatives:

$$\begin{bmatrix} \xi_{,x} & \xi_{,y} \\ \eta_{,x} & \eta_{,y} \end{bmatrix} = \begin{bmatrix} x_{,\xi} & x_{,\eta} \\ y_{,\xi} & y_{,\eta} \end{bmatrix}^{-1} \{N_{i,x}, N_{i,y}\} = \{N_{i,\xi}, N_{i,\eta}\}(J) \qquad \text{(B.21)}$$

whence:

$$N_{i,x} = N_{i,\xi}\xi_{,x} + N_{i,\eta}\eta_{,x} \qquad \text{(B.22)}$$

$$N_{i,y} = N_{i,\xi}\xi_{,y} + N_{i,\eta}\eta_{,y} \qquad \text{(B.23)}$$

Element Matrices

The following matrices and vectors are applicable to a 4-node, bilinear quadrilateral plate element, and have been collected from Hughes [74] and Liu and Quek [76]:

Displacements: $$d^e = \{d_1; d_2; d_3; d_4\} \quad \text{(B.24)}$$

$$d_i = \{w_i, \theta_{x_i}, \theta_{y_i}\} \quad \text{(B.25)}$$

Shape-function matrix: $$N = [N_1, N_2, N_3, N_4] \quad \text{(B.26)}$$

$$N_i = \begin{bmatrix} N_i & 0 & 0 \\ 0 & N_i & 0 \\ 0 & 0 & N_i \end{bmatrix} \quad \text{(B.27)}$$

B-matrix: (bending) $$B^b = \left[B_1^b, B_2^b, B_3^b, B_4^b\right] \quad \text{(B.28)}$$

$$B_i^b = \begin{bmatrix} 0 & 0 & -N_{i,x} \\ 0 & N_{i,y} & 0 \\ 0 & N_{i,x} & -N_{i,y} \end{bmatrix} \quad \text{(B.29)}$$

B-matrix: (shear) $$B^s = [B_1^s, B_2^s, B_3^s, B_4^s] \quad \text{(B.30)}$$

$$B_i^s = \begin{bmatrix} N_{i,x} & 0 & N_i \\ N_{i,y} & -N_i & 0 \end{bmatrix} \quad \text{(B.31)}$$

Curvatures: $$\chi = B^b d^e \quad \text{(B.32)}$$

Strain: (in-plane) $$\varepsilon = -z\chi \quad \text{(B.33)}$$

Strain: (shear) $$\gamma = B^s d^e \quad \text{(B.34)}$$

Constitutive matrix: (bending) $$D^b = \frac{E}{1-\nu^2}\begin{bmatrix} 1 & \nu & 0 \\ \nu & 1 & 0 \\ 0 & 0 & \dfrac{(1-\nu)}{2} \end{bmatrix} \quad \text{(B.35)}$$

Constitutive matrix: (shear) $$D^s = \frac{E}{1-\nu^2}\begin{bmatrix} \dfrac{(1-\nu)}{2} & 0 \\ 0 & \dfrac{(1-\nu)}{2} \end{bmatrix} \quad \text{(B.36)}$$

Stress: (in-plane) $$\sigma = \{\sigma_{xx}; \sigma_{yy}; \tau_{xy}\} \quad \text{(B.37)}$$

$$\sigma = D^b \varepsilon \quad \text{(B.38)}$$

Stress: (off-plane) $$\tau = \{\tau_{xz}; \tau_{yz}\} \quad \text{(B.39)}$$

$$\tau = \kappa D^s \gamma \quad \text{(B.40)}$$

Inertial matrix: $$I = \begin{bmatrix} \rho z & 0 & 0 \\ 0 & \frac{\rho z^3}{12} & 0 \\ 0 & 0 & \frac{\rho z^3}{12} \end{bmatrix} \quad \text{(B.41)}$$

Element mass matrix: $$m^e = \iint_{A^e} N^T I N dA^e \quad \text{(B.42)}$$

Stiffness matrix: (bending) $$k_b^e = \iint_{A^e} \frac{z^3}{12} [B^b]^T D^b B^b dA^e \quad \text{(B.43)}$$

Stiffness matrix: (shear) $$k_s^e = \iint_{A^e} \kappa z [B^s]^T D^s B^s dA^e \quad \text{(B.44)}$$

Element stiffness matrix: $$k^e = k_b^e + k_s^e \quad \text{(B.45)}$$

Element loading vector: $$f^e = \iint_{A^e} N^T \begin{Bmatrix} f_z \\ 0 \\ 0 \end{Bmatrix} dA^e \quad \text{(B.46)}$$

Gaussian Quadrature

Gaussian quadrature may be used to numerically integrate a function through a weighted summation of the value of the function at specific integration points. For a detailed discussion on Gaussian quadrature, the reader is referred to texts on numerical methods; for the application of Gaussian quadrature to problems in FEA, the reader is referred to Hughes [74] and Kwon and Bang [72]. The use of higher-order Gaussian quadrature may yield exact results for polynomial functions.

For Mindlin-Reissner bilinear quadrilateral elements, selective integration involves 2x2 Gaussian quadrature on the bending-stiffness and one-point Gaussian quadrature on the shear-stiffness term[74; 76; 79]. Hughes [74] elaborates on the equivalence of certain mixed-formulation (assumed displacements and assumed pressure fields are solved for) elements and of selectively reduced integration elements. In particular, the displacements between the different element formulations are identical [74]; the strain at the centroid [74] of the element as obtained from selectively reduced integration agrees with that given by the strain field of the mixed-formulation element [74].

Shear Locking and Rank Deficiency

Correct rank in an element stiffness matrix is achieved [74] when the rank of the matrix is equal the number of degrees of freedom in the element minus the number of rigid-body modes. Rank deficiency refers to the case in which an element stiffness matrix as a lower rank than which correctly represents the element mechanics. This may arise from using an integration rule which is of too low an order [74]. As a result, the element is modelled as having additional (spurious) zero-energy modes, referred to as hourglass modes or mechanisms [74; 80]. These modes incorrectly represent the mechanics of the system, and can lead to a singular global stiffness matrix, rendering a solution of the system impossible.

In using Mindlin-Reissner plate-bending elements, a phenomenon known as "shear locking" may occur, in which an element is over-constrained in shear. A detailed look into the existence of a meaningful solution to a system and the effect of the number of constraints imposed is given by Hughes [74]. In summary, shear locking may be avoided through the use of selectively reduced integration of the shear stiffness matrix. However, Hughes [74] notes: that selectively reduced integration may result in rank deficiency, which may lead to a singular global stiffness matrix. The application of boundary conditions, however, generally renders the global stiffness matrix positive-definite [74]. Hughes [74] remarks that if the zero-energy modes are prevented in one element, they will be prevented in the remainder of the mesh; this may be achieved through the specification of w (transverse displacement) at two adjacent nodes [74]. Considering the boundary conditions applied to a cantilevered plate, the global stiffness matrix will be free of zero-energy modes.

Global Matrices

The discretization of a system into elements in FEA essentially allows the global system equations to be discretized into a set of simpler simultaneous equations per element. These equations may then be formulated on a per-element basis, and the formulated equations may then be re-assembled into a global set of equations for the entire system.

In the description of the geometry or displacements of the elements, a local coordinate system may be used. When element matrices are formulated based on a local coordinate system, as opposed to from the global coordinate system, they must be reformulated in terms of the

global coordinate system (through means of coordinate transformation) before they can be assembled into the global matrices. However, if the element matrices are formulated based on the global coordinate system, no subsequent coordinate transformation is necessary, and the element matrices may be directly assembled into the global matrices.

Boundary Conditions

The assembled global system equations (matrices) describe the physics of each degree of freedom in the system. The unconstrained system is free to undergo rigid body motions, and a solution of the equations is not possible, as the matrix equations are singular [72].

Two classes of boundary conditions exist for problems in plate mechanics, namely essential boundary conditions and natural boundary conditions. Hughes [74] provides a mathematical treatment of the boundary conditions with reference to the variational equation (equation of virtual work), and remarks that trial solutions to the variational equation are explicitly required to satisfy the essential boundary conditions; satisfaction of the variational equation in turn implies satisfaction of the natural boundary conditions. Ferreira [79] offers the alternative description of the boundary conditions as displacement (essential) and force (natural) boundary conditions. Essential boundary conditions are Dirichlet boundary conditions, in which the displacement is specified; natural boundary conditions are Neumann boundary conditions, in which the derivative of the displacement is specified.

In applying the essential (displacement) boundary conditions, the rows and columns of the mass- and stiffness-matrices corresponding to the prescribed (constrained) degrees of freedom are removed; similarly, the rows of the displacement, acceleration, and force vectors corresponding to prescribed degrees of freedom are removed. The reduced system of equations may then be solved to find the displacements of the unconstrained degrees of freedom. These may then be substituted into the full system equations to calculate the constraint forces.

Strain Smoothing

The shape function formulation of displacement-type bilinear quadrilateral elements results in C^0-continuity of displacements across element boundaries; however, derivatives of displacements have a finite discontinuity across element boundaries. A node that is shared between elements will consequentially show the same displacements immediately adjacent to the node on either element interior; however, strains (dependent on first-derivatives of displacements) evaluated at the node on each element interior will not have the same value contributed from neighbouring elements at the node. This results in a discontinuous strain (and hence, stress) field for pure displacement-type elements. This is shown in the Figure B.2 below, in which the strains at the central node (ε_a, ε_b, ε_c, and ε_d) are discontinuous:

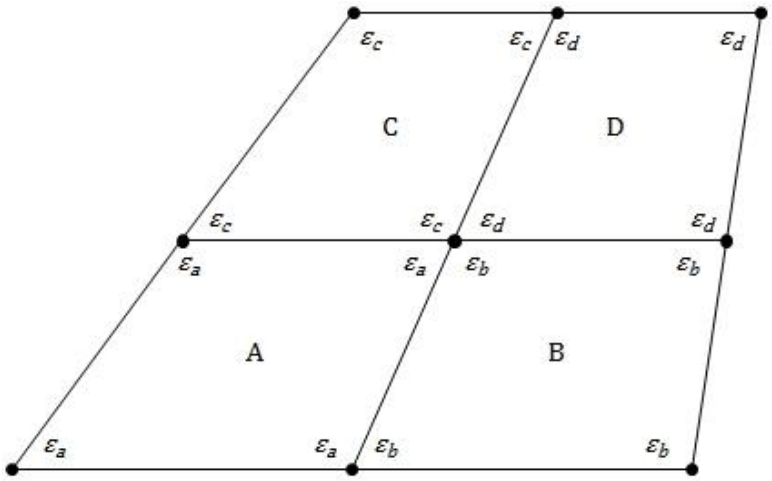


Figure B.2: Discontinuity in Strain at Nodes

Hughes [74] notes that generally, all displacement derivatives for C^0 isoparametric elements are discontinuous across element boundaries. If the strains are smoothed across elements by describing the strain in each element with shape functions, the strains/stresses will then also exhibit C^0 continuity across element boundaries, and the discrepancy in stresses at nodes will be eliminated.

Hughes [74] outlines the following smoothing procedure for constant-strain elements:

The smoothed strain is written as $\varepsilon_{smoot\,h}$, where

$$\boldsymbol{S}\varepsilon_{smoot\,h} = P \qquad (B.47)$$

in which

$$size(\boldsymbol{S}) = n_{nodes} \times n_{nodes}$$

$$size(\varepsilon_{smoot\,h}) = n_{nodes} \times 1$$

$$size(P) = n_{nodes} \times 1$$

$\boldsymbol{S}$ and P are constructed in the element-by-element fashion through the global assembly operators, similar to the assembly of the global stiffness- and mass-matrices (however, there is only one DOF (pressure) per node, and no boundary conditions are imposed):

$$\boldsymbol{S} = \bigwedge_{e=1}^{n_{el}} \boldsymbol{s}^e \tag{B.48}$$

$$P = \bigwedge_{e=1}^{n_{el}} \epsilon^e \tag{B.49}$$

where $\bigwedge_{e=1}^{n_{el}}$ denotes the FEM assembly operations, and in which

$$\boldsymbol{s}^e = \begin{bmatrix} s_{11}^e & s_{12}^e & s_{13}^e & s_{14}^e \\ s_{21}^e & s_{22}^e & s_{23}^e & s_{24}^e \\ s_{31}^e & s_{32}^e & s_{33}^e & s_{34}^e \\ s_{41}^e & s_{42}^e & s_{43}^e & s_{44}^e \end{bmatrix} \tag{B.50}$$

$$\epsilon^e = \begin{Bmatrix} \epsilon_1^e \\ \epsilon_2^e \\ \epsilon_3^e \\ \epsilon_4^e \end{Bmatrix} \tag{B.51}$$

where $\boldsymbol{s}^e$ and ε^e denote the element-matrices, with the nodal terms given by

$$s_{ij}^e = \iint_{\Omega^e} N_i^e N_j^e \, dA^e \tag{B.52}$$

$$\epsilon_i^e = \varepsilon_{cent}^e \iint_{\Omega^e} N_i^e \, dA^e \tag{B.53}$$

for $1 \leq i, j \leq 4$, and with e denoting the element number.

The matrix $\boldsymbol{s}^e$ may be replaced by an associated diagonal matrix, by approximating:

$$s_{ij}^e = \delta_{ij} j^e(\xi_i, \eta_i) \tag{B.54}$$

where δ_{ij} is the Kronecker delta, and

$$j^e = det \begin{bmatrix} x,_\xi^e & x,_\eta^e \\ y,_\xi^e & y,_\eta^e \end{bmatrix} \quad \text{(B.55)}$$

leading to

$$\epsilon_i^e = \varepsilon_{cent}^e j^e(\xi_i, \eta_i) \quad \text{(B.56)}$$

Nonlinear Structures

Structural nonlinearity may arise from geometric nonlinearities (such as play in joints and connections), from nonlinearities associated with large deflections, and from nonlinear material properties [3]. Nonlinearity may also arise from a nonlinear dependence of the forcing function on the system state. The solution of nonlinear systems is not trivial, and is computationally expensive as the system equations are solved iteratively [3]. The reader is referred to Komzsik [80] for a review of common solution methods used in nonlinear analysis. The Komzsik remarks that in the methods presented for nonlinear dynamics, the external load is considered to be explicit and time-variant, without dependence on the resulting structural displacements. This is typical of solution methods treated in literature, where the forcing function is assumed to be know a-priori; this, however, is not the case in aeroelastic analysis.

Solution Methods

Modal analysis

In modal analysis, the total response of the structure is modelled through the superposition of the mode-shapes of the undamped structure. Modal analysis is only applicable to linear structures with constant structural matrices. The reader is referred to Komzsik's [80] text on computational techniques in FEA for a comprehensive review of the solution methods associated with modal analysis and frequency response.

In normal modes analysis, the free vibration of the system is considered (eigenanalysis is performed) and the natural frequencies and mode shapes of the structure are found. The

response of the system to a particular forcing frequency may then be obtained through the summation of the individual modal responses [3]. Modal analysis may also be used in the analysis of damped systems, in which complex eigenanalysis is used to compute the damped modes of structures and to assess the structural stability [3].

One important advantage realized by modal analysis is the reduction of the order of the system to be solved, as is covered in detail by Komzsik [80]. The order of the system is reduced from being equal to the number of unconstrained degrees of freedom to being equal to the number of eigenmodes considered. The system response is described in terms of modal displacements, which may be related to the system displacements through the associated eigenvectors. Computation is performed on the system in terms of modal displacements, rendering the reduction in order of the system.

For a modal system with time-invariant coefficients, the solution of the system in time is straight forward. Various time-integration schemes may be employed that take full advantage of the time-invariance of the coefficient matrices.

Direct analysis

In direct analysis, which is applicable to both linear and nonlinear systems, the structural response is solved for directly, as formulated in terms of the full-order degrees of freedom. No reduction in the number of degrees of freedom analysed is made. The solution of the system response in time requires the use of appropriate time-integration schemes that account for the time-variance of the system coefficient matrices; these matrices must be recomputed after each iteration. A number of suitable time-integration schemes are mentioned below.

The central, backward, and forward finite differencing schemes are all explicit methods, making their solution relatively straight-forward. A distinct disadvantage of the central-difference scheme is that it is conditionally stable [74; 80], and the time-step must be suitably small for stability of the scheme. In particular, the time-step should be approximately $\Delta t \leq 0.1 T_n$ where T_n is the smallest period in the system [40; 81].

Many other time-marching schemes may be used, many of which are implicit and unconditionally stable, including the Newmark-β scheme [74; 80], Houbolt's Method [74], Park's Method [74], Wilson-θ Method [74], and others. The reader is referred to Hughes [74] for a comprehensive discussion on the merits and details of the various methods.

The afore-mentioned methods generally require the forcing function to be know at the time under consideration. However, in the aeroelastic problem, the forcing function at that time is a function of the displacements and rates that are being solved for; it is an inherently implicit system. Thus, the solution must be arrived at iteratively

C. SET-UP PROCEDURE FOR AEROELASTIC COMPUTATIONS IN EDGE

The procedure followed here is largely based on instructions for running an aeroelastic computation as provided by Dr. Louw van Zyl. The author expresses his thanks to Dr. van Zyl for his assistance in the author's familiarization with the aeroelastic options Edge.

The selection of the time-marching methodology in the Edge input file requires consideration of the formulation of the aeroelastic equations in time if a coupled modal solution (*ISOOPT=102* under the *AEROELASTICS* section) is to be run. The modal equations of motion in Edge are discretized in time with using a central differences scheme being used for time-derivatives [71], and with the modal displacements and modal forces being computed from three-point time-averaging [71] (see Section 6).

The resulting modal equations are implicit in the modal displacement at the next physical-time (the outer loop of the dual time-stepping iteration) step (unless the time-averaging weights, ETA, for the modal forces are chosen such that ETA=0). The solution for the modal displacement and modal force at the next physical-time step is progressively reached through successive iterations in pseudo-time (the inner loop of the dual time-stepping iteration).

Thus, the solution of the aeroelastic equations of motion requires implicit time-accurate integration, as the converged pair of modal displacements and modal forces at the next physical time step is required to be solved iteratively (due to the implicit formulation in modal displacements). Thus, the parameter *ITIMAQ* must be set to *ITIMAQ=1*. The specified *DELTAT* is then equal to the global step in physical-time. The number of inner-iterations performed is driven by the convergence criterion *RESTAQ* for the pseudo-time (inner-loop) iterations, with limits enforced by the parameters *ITMNAQ* and *ITMXAQ*. The Edge manual [71] recommends that *ITMXAQ* should be between 30 - 100 for full viscous computations; it is expected that for inviscid computations with slightly-unsteady effects (e.g. low reduced frequencies for small aeroelastic motions), a number of *ITMXAQ* below 30 should be sufficient.

Steady computation – static mesh

The general set-up procedure in Edge for a steady computation is as follows:

1. Copy the mesh file *your_mesh.bmsh* into the working directory,
2. Copy the solution input file *default.ainp* and edit it to reflect the desired solver specifications (flow conditions, solver options, filenames, etc.). Rename the file to *your_job.ainp*,
3. Run *bound* and generate the boundary conditions,

   ```
   bound your_job.ainp
   ```

4. Run preprocessor

   ```
   preprocessor your_job.ainp
   ```

5. Run the solver using the number of processors required (in this instance, *NPART=3*)

   ```
   edge_mpi_run your_job.ainp 3
   ```

6. Monitor convergence by running *plotres*:

   ```
   plotres your_job.bres -n
   ```

Steady computation – deformable mesh

When running an aeroelastic simulation in Edge, the aerodynamics may be calculated for the "jig shape" of the structure or for the "design shape" [71]. The methodology for the "jig shape" approach involves the transient computation to steady-state (with heavy artificial structural damping) of the geometry, starting from an initially undeformed shape in steady flow. Once convergence to the steady deformed (aeroelastically static) shape is reached, the solution is restarted with new modal parameters – the artificial structural damping is removed, and initial modal velocities are assigned to perturb the structure.

The set-up procedure in Edge for the initial steady computation with a mesh that will deform in subsequent computations is as follows:

1. Copy the mesh file *your_mesh.bmsh* into the working directory,
2. Copy the solution input file *default.ainp* and edit it to reflect the desired solver specifications (flow conditions, solver options, filenames, etc.). Rename the file to *your_job_und.ainp*,

It is recommended to set the filenames to reflect the type of computation run.

3. Run *bound* and generate the boundary conditions:

   bound your_job_und.ainp (follow Edge instructions)

   The boundary-condition file *your_mesh.aboc* is generated.

4. Run preprocessor with *NPART=1* in *your_job_und.ainp*:

   preprocessor your_job_und.ainp

   The following file is generated: *your_job_und.bedg*

5. Extract the moving boundaries from the mesh:

   aexbset (follow Edge instructions)

   The file with the moving boundaries *your_mesh.bset* is generated

6. Generate the boundary displacement files for each mode:

   Note: Edge aeroelastic utilities and helper programs are available to import a MSC Nastran modal structural model (*SOL=103* in MSC Nastran) into Edge, and to extract surface nodes from the model.

   The approach outlined here does not utilize these programs, but utilizes a MATLAB script to extract the surface nodes on the moving boundaries from the fluid mesh. The node displacements for each structural mode are written into the required FFA-format for the *.bdis* files. The aforementioned script, *getbdis.m*, was provided by Dr. van Zyl, and was modified by the author to extract the structural mode shapes from the author's MATLAB FEM code and to interpolate the modal displacements onto the surface nodes of the fluid mesh.

   NB: the mode shapes written into the *.bdis* files were scaled by a factor of 10^{-3} to in order that the deformed meshes that would be generated would not undergo large deformations.

   The following files are written: *mode_1.bdis*, *mode_2.bdis*, etc.

7. Generate the deformed mesh for each mode:

```
meshdeform -mth 2 your_job_und.bedg your_job.bmsh mode_1.bdis mode_1.bmsh
```

The deformed mesh files are *mode_1.bmsh*, *mode_2.bmsh*, etc.

Note: the deformed mesh is calculated based on the boundary displacements in the files *mode_1.bdis*, *mode_2.bdis*, etc. The boundary displacements have been scaled by 10^{-3} and thus the deformed mesh reflects the scaled mode shapes.

8. Generate the perturbation field for each mode:

```
aeputpert your_mesh.bmsh mode_1.bmsh your_mesh.bmos -scale 1.0e+03
```

This writes the perturbation field for each mode into the *your_mesh.bmos* file. Here, the physical displacements of the fluid nodes on the moving boundary into the volume mesh have been rescaled by 10^{3}. This is done so that the perturbation field reflects the mass-normalized mode shapes. Modal responses computed in Edge are then computed based on the mass-normalized mode shapes.

9. Change *NPART* in *your_job_und.ainp* to the number of processors required (in this instance, *NPART=3*) and run the preprocessor again:

```
preprocessor your_job_und.ainp
```

The following files are generated for the parallel-processing job: *your_job_und.bedg_p1*, *your_job_und.bedg_p2*, etc.

10. Run the solver using the number of processors required (in this instance, *NPART=3*)

```
edge_mpi_run your_job_und.ainp 3
```

11. Monitor convergence by running *plotres*:

```
plotres your_job_und.bres -n
```

The results files generated include *your_job_und.bres* and *your_job_und.bout*. For the "jig shape" procedure of aeroelastic computation, the following step is to use the results of the undeformed steady solution (now obtained) as an initial solution for a transient computation.

Transient computation – coupled modal solution – undeformed to steady-state

The set-up procedure in Edge for the transient coupled modal computation from an initially undeformed structure to the steady-state (static aeroelastic) deformed structure is as follows:

1. Copy the following files from the undeformed steady computation folder into the folder for the undeformed-to-steady-state folder:

   your_mesh.bmsh

   your_mesh.aboc

   your_mesh.bmos

   mode_1.bdis, *mode_2.bdis*, etc.

   mode_1.bmsh, *mode_2.bmsh*, etc.

   your_job_und.bout

   your_job_und.ainp

2. Copy the example modal parameters (*.amop*) file from the Edge directory and edit the parameters to reflect the modal parameters of the system being analysed. Rename the modal parameters file to *your_job_ae_ss.amop*, and rename the input file to *your_job_ss.ainp*.
3. Rename the output file from the undeformed steady computation (*your_job_und.bout*) to *your_job_ss.bini*.
4. Edit the solution input file *your_job_ss.ainp* to reflect the desired solver specifications. In particular:

   Under *Initialization*:

   - change *INPRES* from *0* to *1* (available),

   Under *Multigrid options*:

   - change *IFULMG* from *1* to *0*,

   Under *Time accurate options*:

   - change *ITIMAQ* from *0* to *1* (implicit time accurate),

- change *DELTAT* to the time-step required
- change *RESTAQ* from *1.0* to *0.0* (convergence criterion)
- change *ITMXAQ* from *100* to *15* (maximum number of implicit iterations per physical-time step)

Under the *Aeroelastics and related options*:

- change *ISOOPT* from *0* to *102* (coupled modal solution),
- change *MODOPT* from *0* to *1* (volume grid perturbation),
- change *POFFSET* from *0* to the value used for *PFREE* (equal to the static pressure at the conditions for the computation),
- change *CFIMOP* to *'your_job_ae_ss.amop'*,
- change *CFIMOS* to *'your_mesh.bmos'*,

Under *Number of iterations, CFL, etc.*:

- change *ITMAX* to the desired number of time steps,

Under *Miscellaneous options*:

- change *IWRSOL* to *25* (write solution every 25 time steps),

Under *File names*:

- change *CFIRES* to *'your_job_ss.bres'*,
- change *CFIOUT* to *'your_job_ss.bout'*,
- change *CFIINI* to *'your_job_ss.bini'*,

5. Run the preprocessor again:

   ```
   preprocessor your_job_ss.ainp
   ```

   The following files are generated for the parallel-processing job: *your_job_ss.bedg_p1*, *your_job_ss.bedg_p2*, etc.

6. Run the solver using the number of processors required (in this instance, *NPART=3*)

   ```
   edge_mpi_run your_job_ss.ainp 3
   ```

7. Monitor convergence by running *plotres*:

```
plotres your_job_ss.bres -n
```

The results files generated include *your_job_ss.bres* and *your_job_ss.bout*. For an elastic wing with heavy artificial structural damping operating below divergence speed, the modal displacements (and aerodynamic coefficients) of the transient computation should converge in time to a steady value. For the "jig shape" procedure of aeroelastic computation, the following step is to use the results for the elastic steady-state obtained from the transient solution (now obtained) as an initial solution for a transient restart to model free response to a disturbance.

Transient computation – coupled modal solution – steady-state to free response

The set-up procedure in Edge for the transient coupled modal computation for the free aeroelastic response of the structure to a disturbance from an initially steady-state (static aeroelastic) deformed structure is as follows:

1. In the undeformed-to-steady-state folder, create a copy of the modal parameters file and rename it to *your_job_ae_free.amop*. Edit the parameters to reflect the desired system state. In particular:
   - Remove artificial structural damping from the modes (set the value of *damping_ratio* to *0* for each mode),
   - Set the initial modal velocity of mode 2 to the desired value (for mode identifier 2, set *init_velocity* to *1.0E-02*).
2. Update the solution input file *your_job_ss.ainp* to reflect the desired solver specifications. In particular:

   Under *Initialization*:

   - change *INPRES* from *1* to *2* (restart of previous run),

   Under the *Aeroelastics and related options*:

   - change *CFIMOP* to *'your_job_ae_free.amop'*,

   Under *Number of iterations, CFL, etc.*:

   - change *ITMAX* to the desired number of time steps,

3. Run the solver using the number of processors required (in this instance, *NPART=3*)

```
edge_mpi_run your_job_ss.ainp 3
```

4. Monitor convergence by running *plotres*:

```
plotres your_job_ss.bres -n
```

The transient computation run for the "undeforned to steady-state" case is continued with the new modal parameters and with an initial modal velocity for mode 2. The results files are updated and include the free response as a continuation of the previous results.

D. FURTHER RESULTS OF THE VALIDATION OF SHOCK-EXPANSION THEORY

The following figures are further results of the parameter sweep for determining grid independence and the accuracy of the MATLAB shock-expansion computations for the undeformed ATM-wing, as outlined in Section 5.4.3.

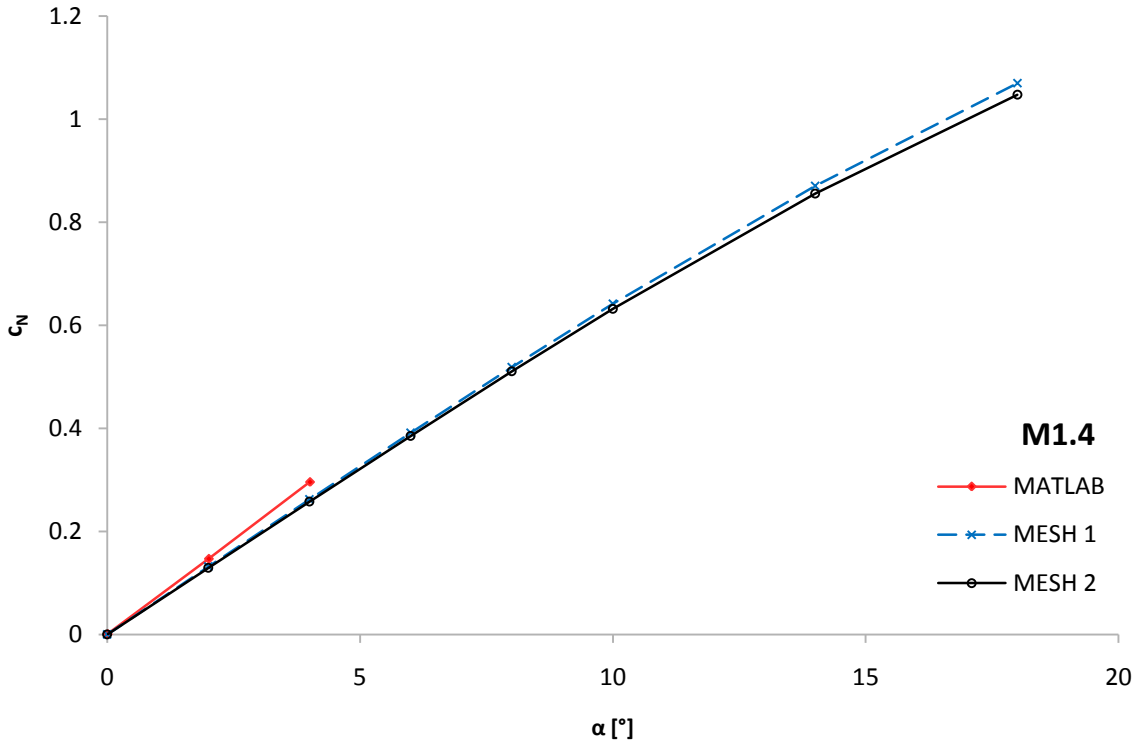


Figure D.1: Normal Force Coefficient vs Angle-of-Attack, Undeformed ATM-Wing, Mach 1.4

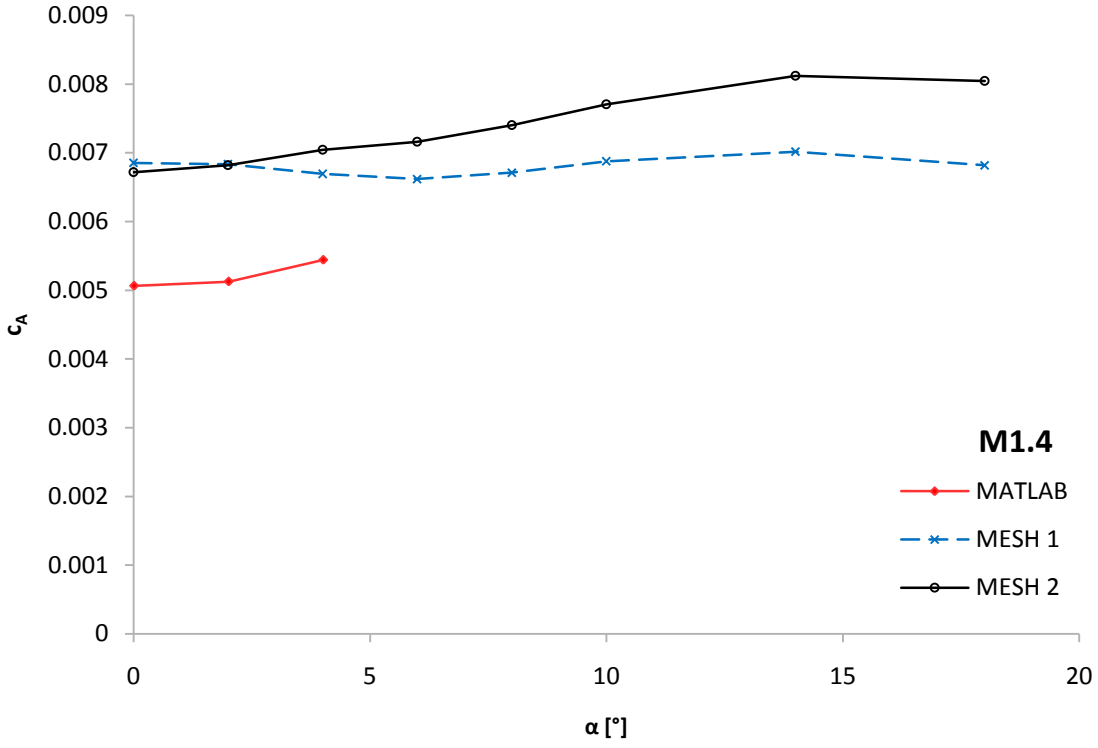


Figure D.2: Axial Force Coefficient vs Angle-of-Attack, Undeformed ATM-Wing, Mach 1.4

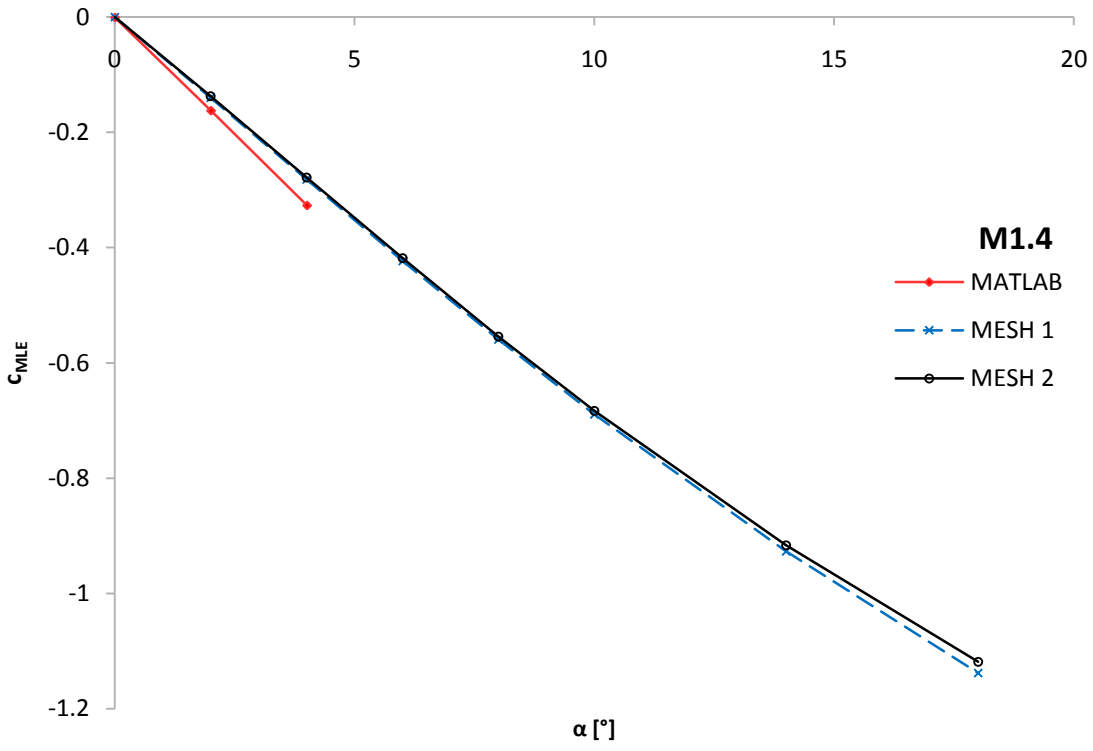


Figure D.3: Pitching Moment Coefficient (LE root) vs Angle-of-Attack, Undeformed ATM-Wing, Mach 1.4

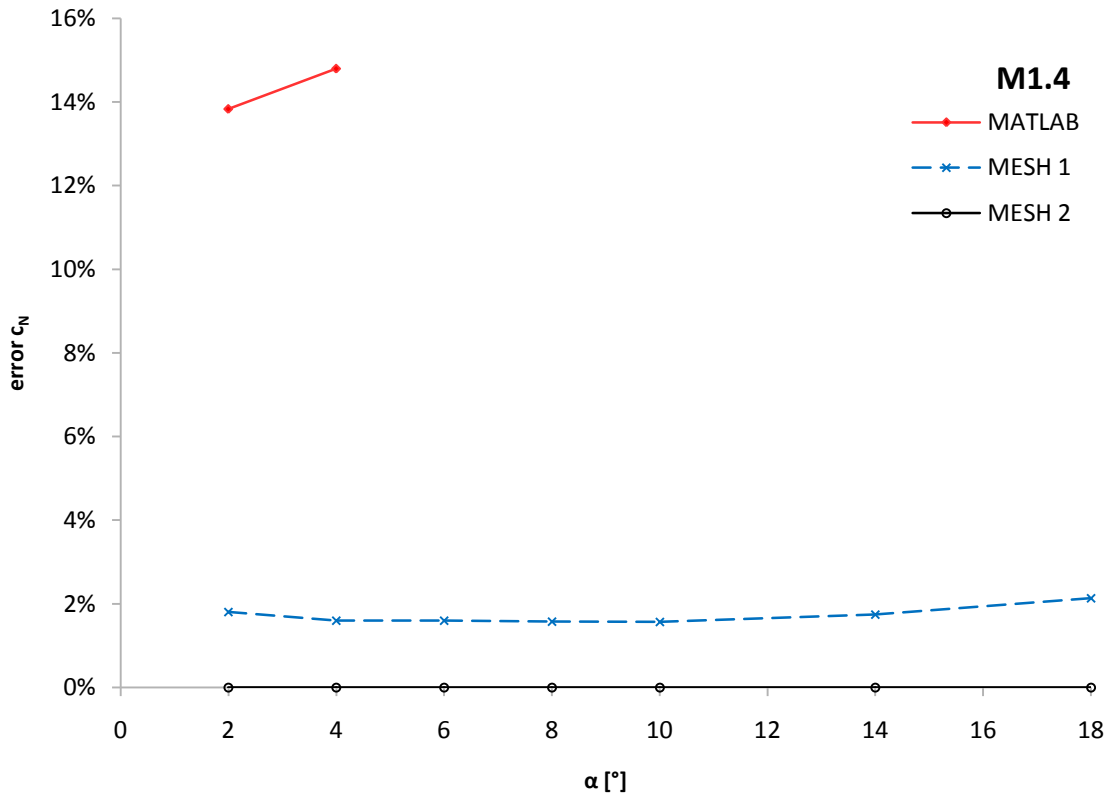


Figure D.4: Comparison of Normal Force Coefficients, Undeformed A TM-Wing, Mach 1.4

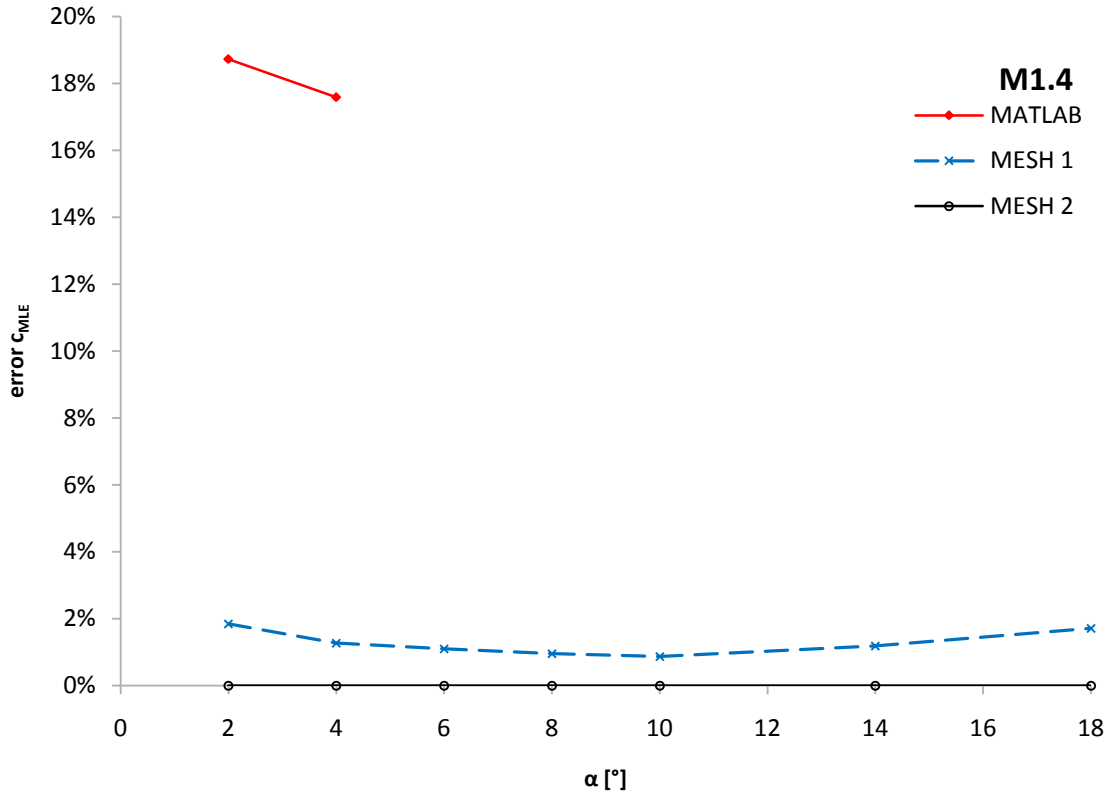


Figure D.5: Comparison of Pitching Moment Coefficients, Undeformed ATM-Wing, Mach 1.4

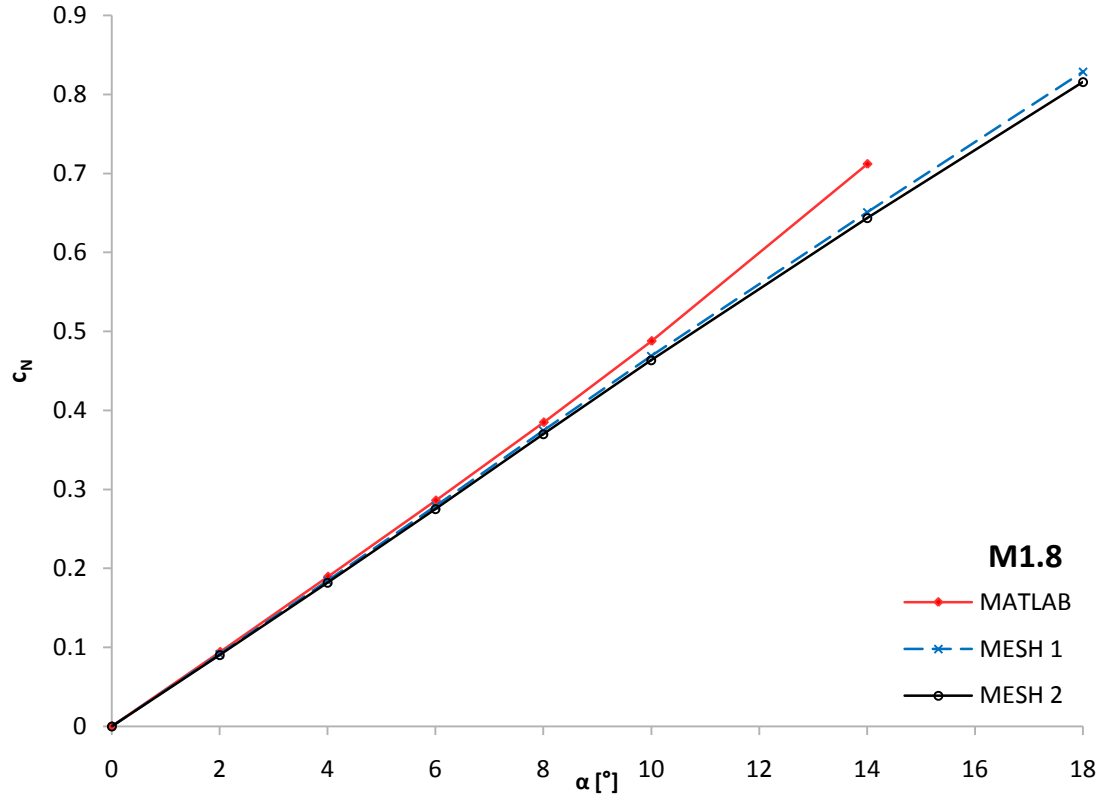


Figure D.6: Normal Force Coefficient vs Angle-of-Attack, Undeformed ATM-Wing, Mach 1.8

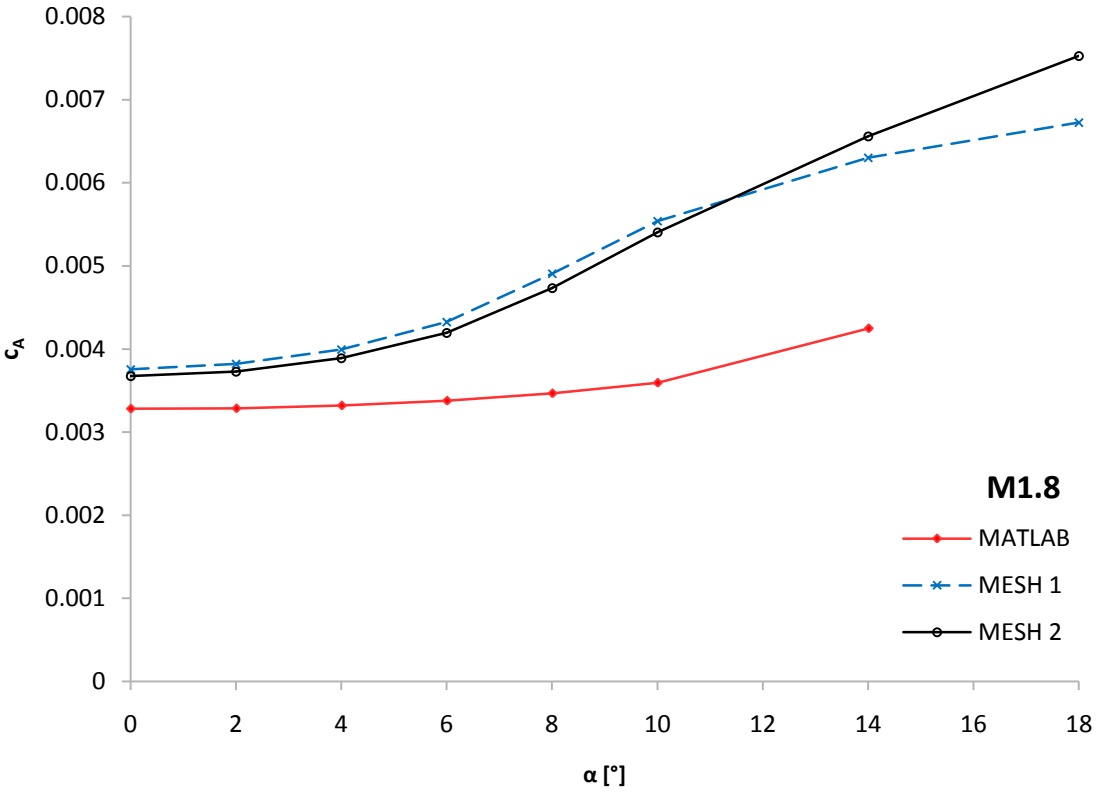


Figure D.7: Axial Force Coefficient vs Angle-of-Attack, Undeformed ATM-Wing, Mach 1.8

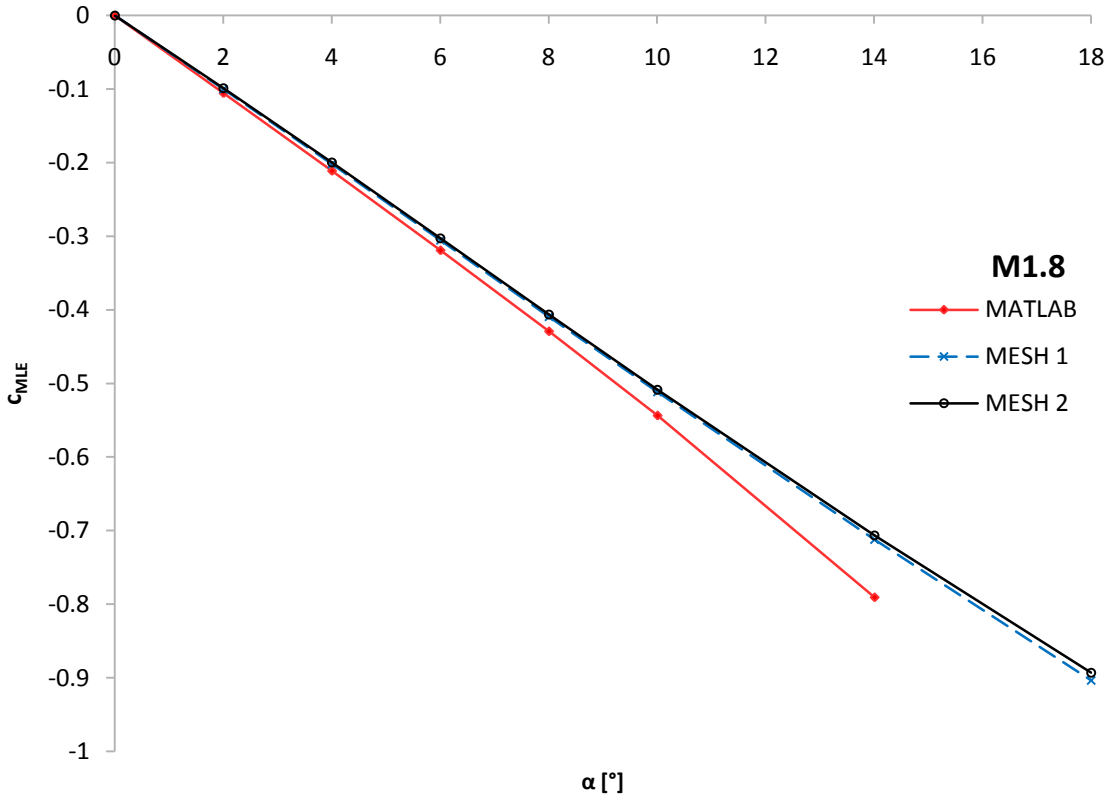


Figure D.8: Pitching Moment Coefficient (LE root) vs Angle-of-Attack, Undeformed ATM-Wing, Mach 1.8

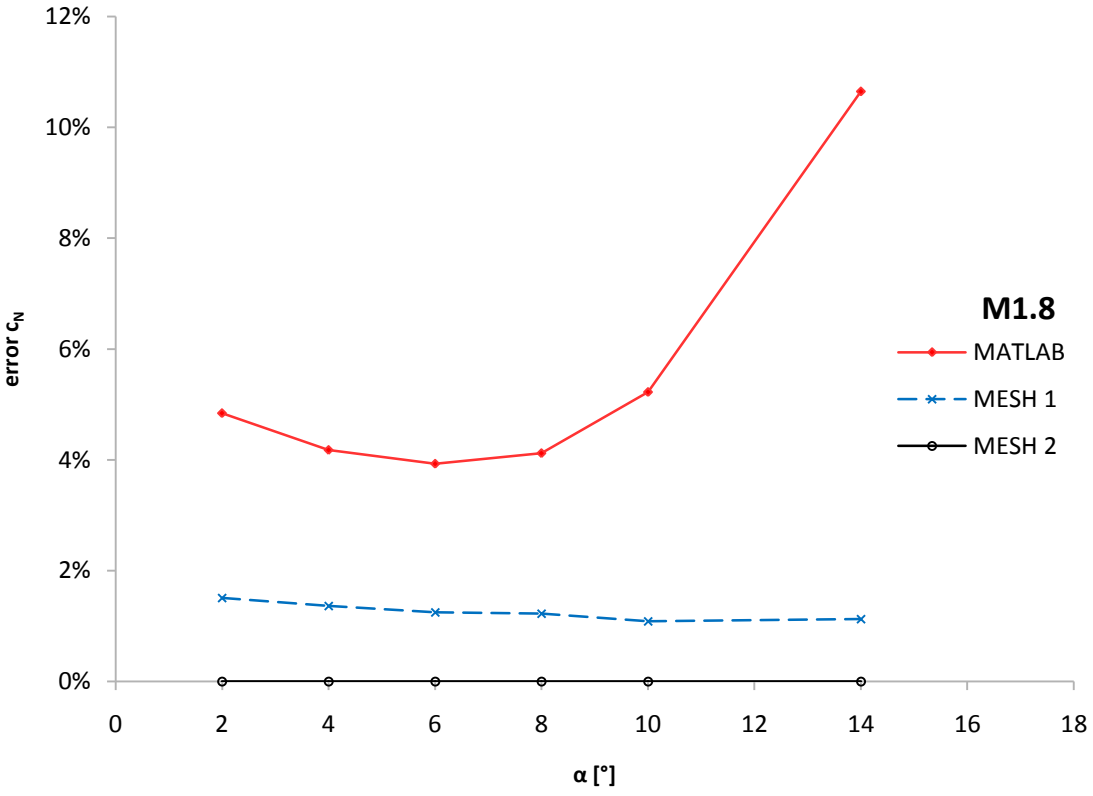


Figure D.9: Comparison of Normal Force Coefficients, Undeformed A TM-Wing, Mach 1.8

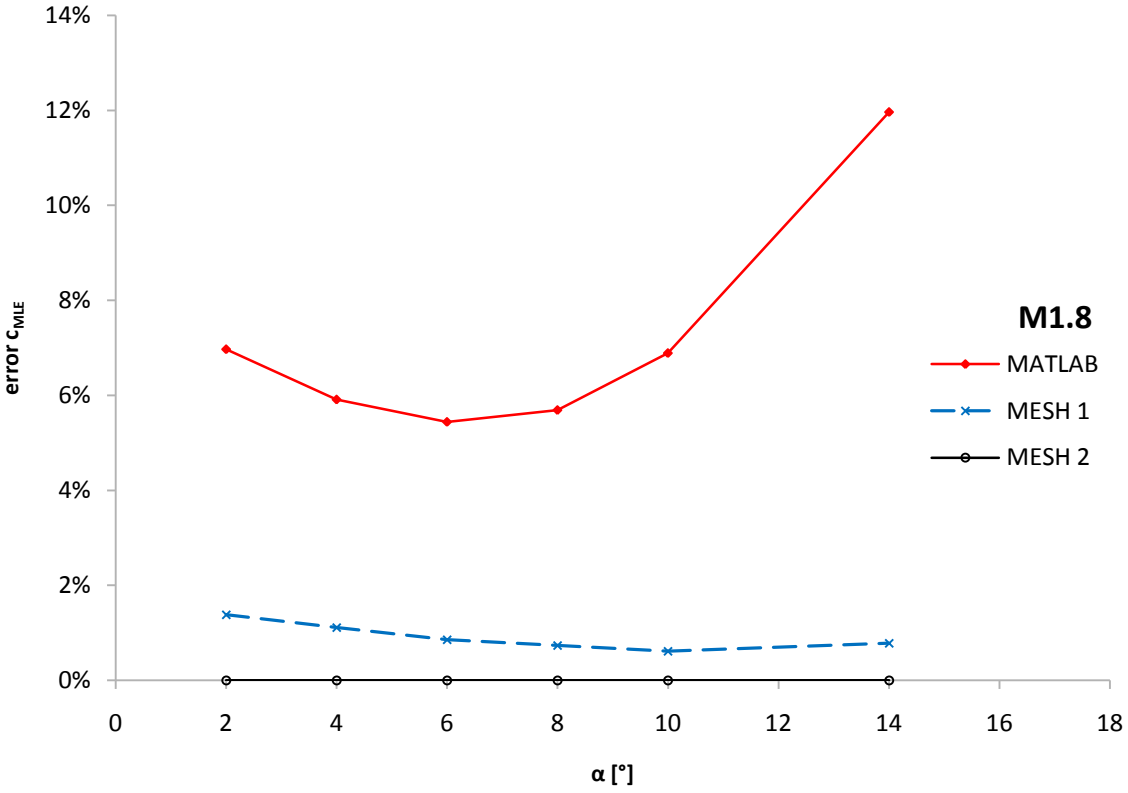


Figure D.10: Comparison of Pitching Moment Coefficients, Undeformed ATM-Wing, Mach 1.8

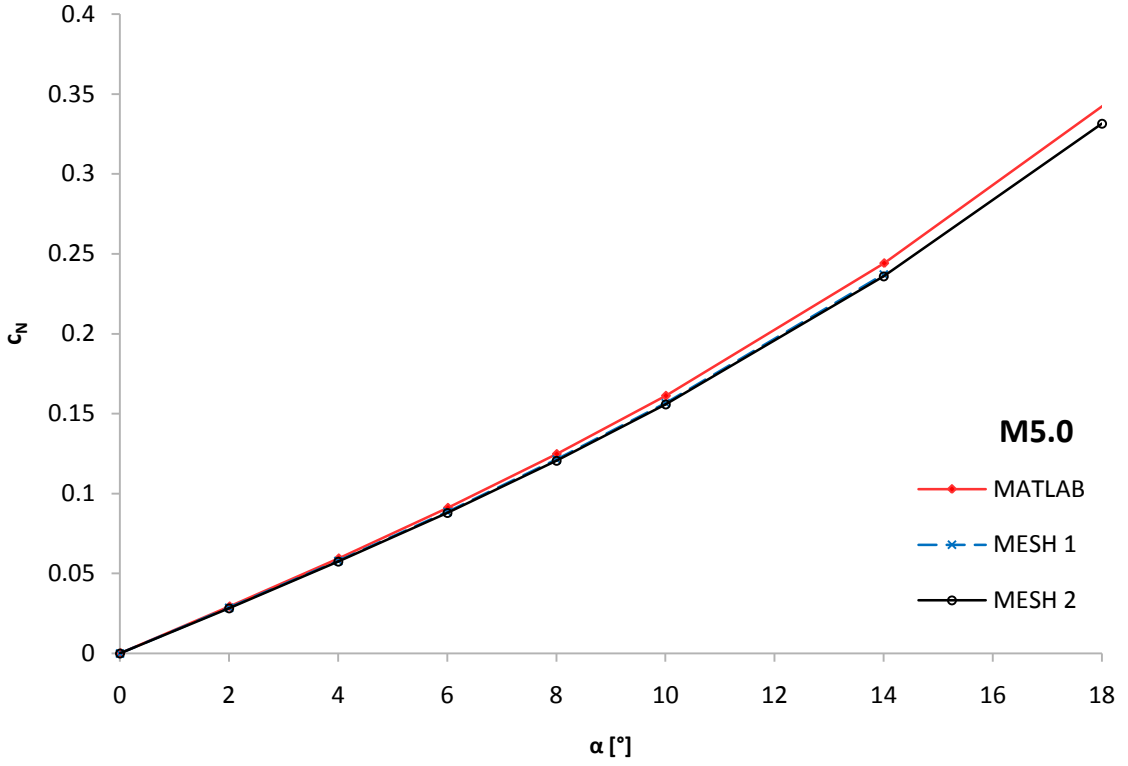


Figure D.11: Normal Force Coefficient vs Angle-of-Attack, Undeformed ATM-Wing, Mach 5

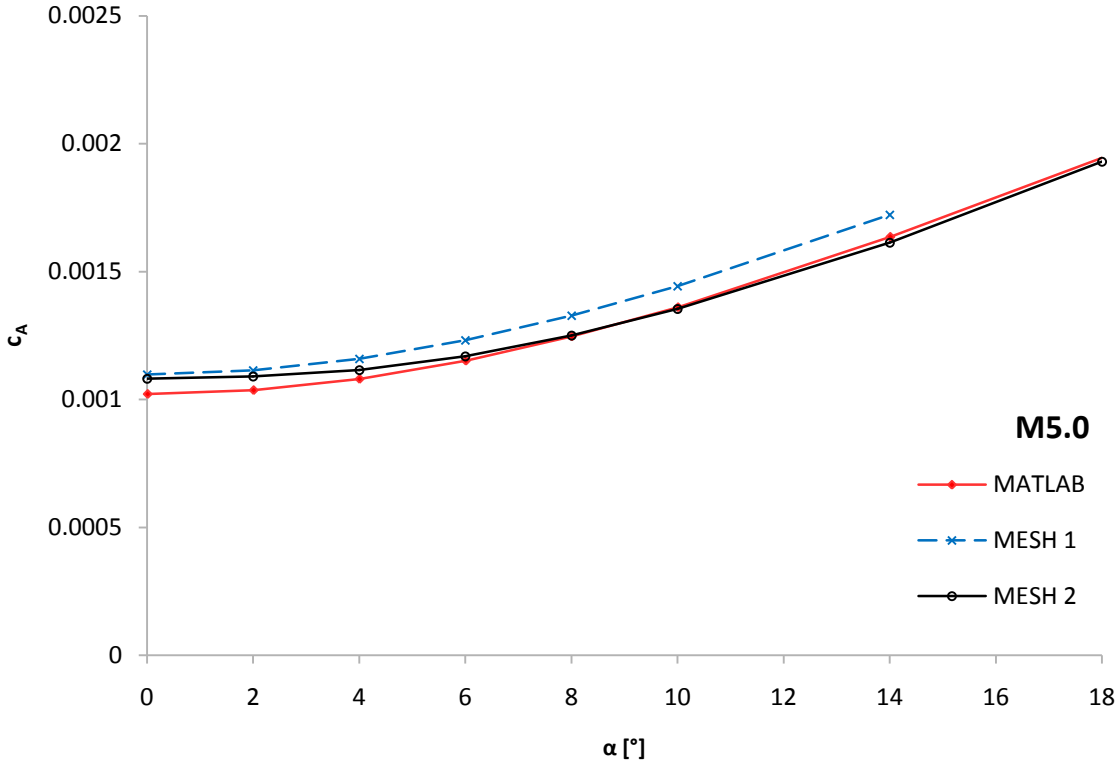


Figure D.12: Axial Force Coefficient vs Angle-of-Attack, Undeformed ATM-Wing, Mach 5

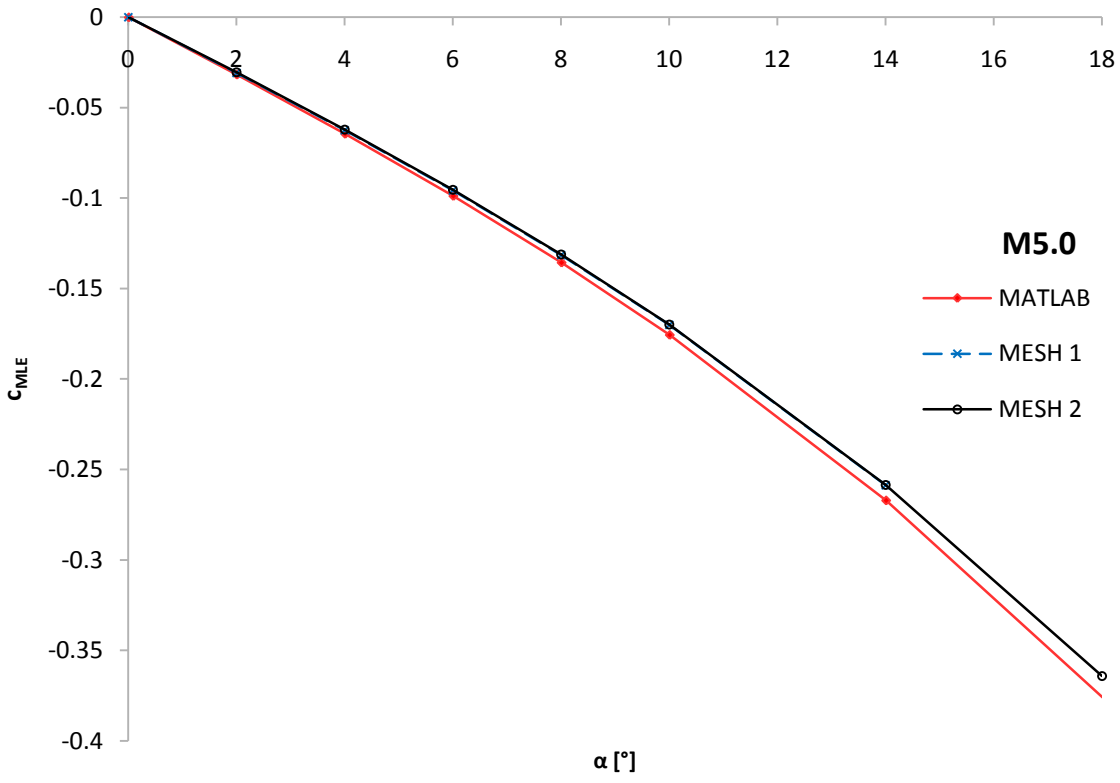


Figure D.13: Pitching Moment Coefficient (LE root) vs Angle-of-Attack, Undeformed ATM-Wing, Mach 5

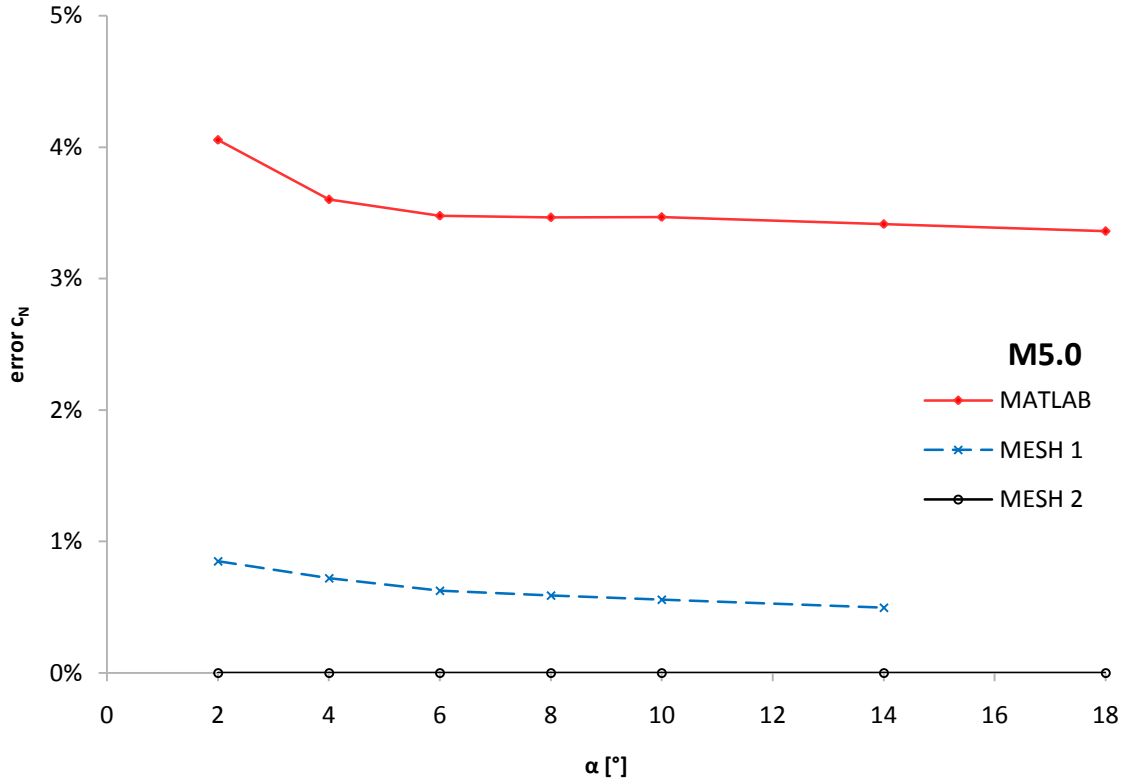


Figure D.14: Comparison of Normal Force Coefficients, Undeformed A TM-Wing, Mach 5

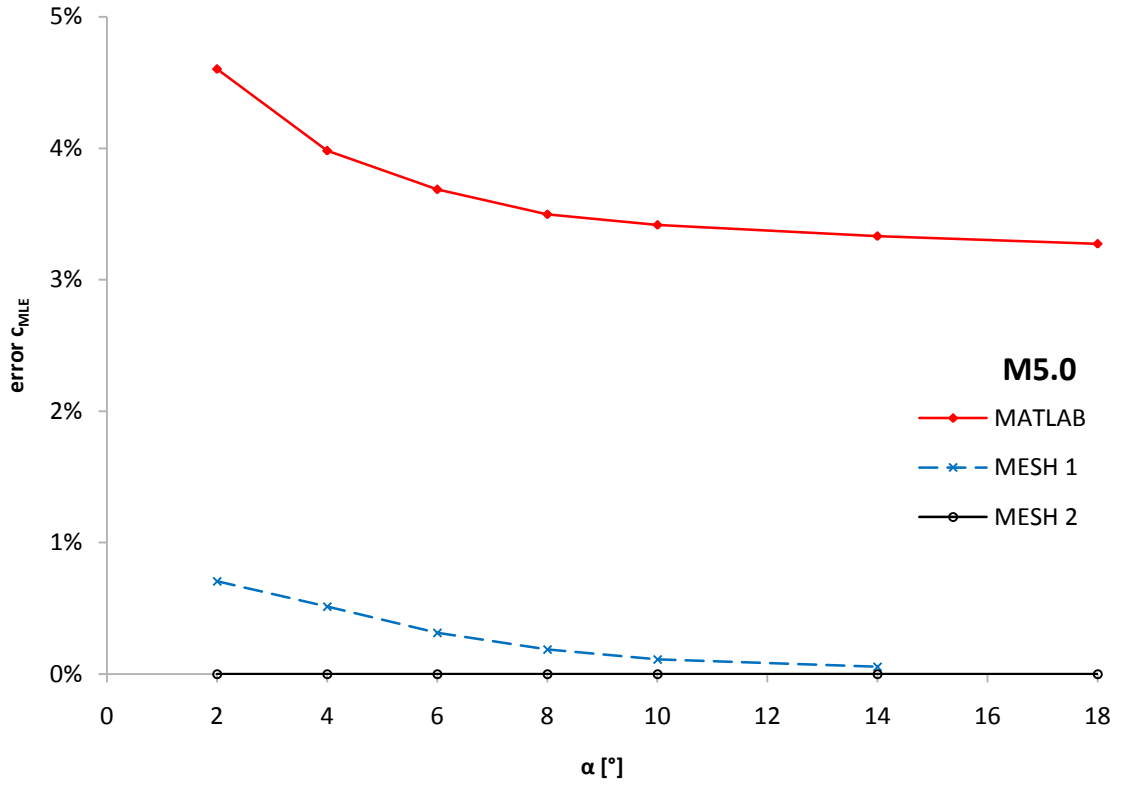


Figure D.15: Comparison of Pitching Moment Coefficients, Undeformed ATM-Wing, Mach 5

E. DEFORMED GEOMETRIES USED FOR MESH DEFORMATION COMPUTATIONS IN EDGE

The following figures show the deformed geometries of the ATM-wing which were used to generate the deformed meshes for the perturbation fields in Edge, as outlined in Section 5.4.4.

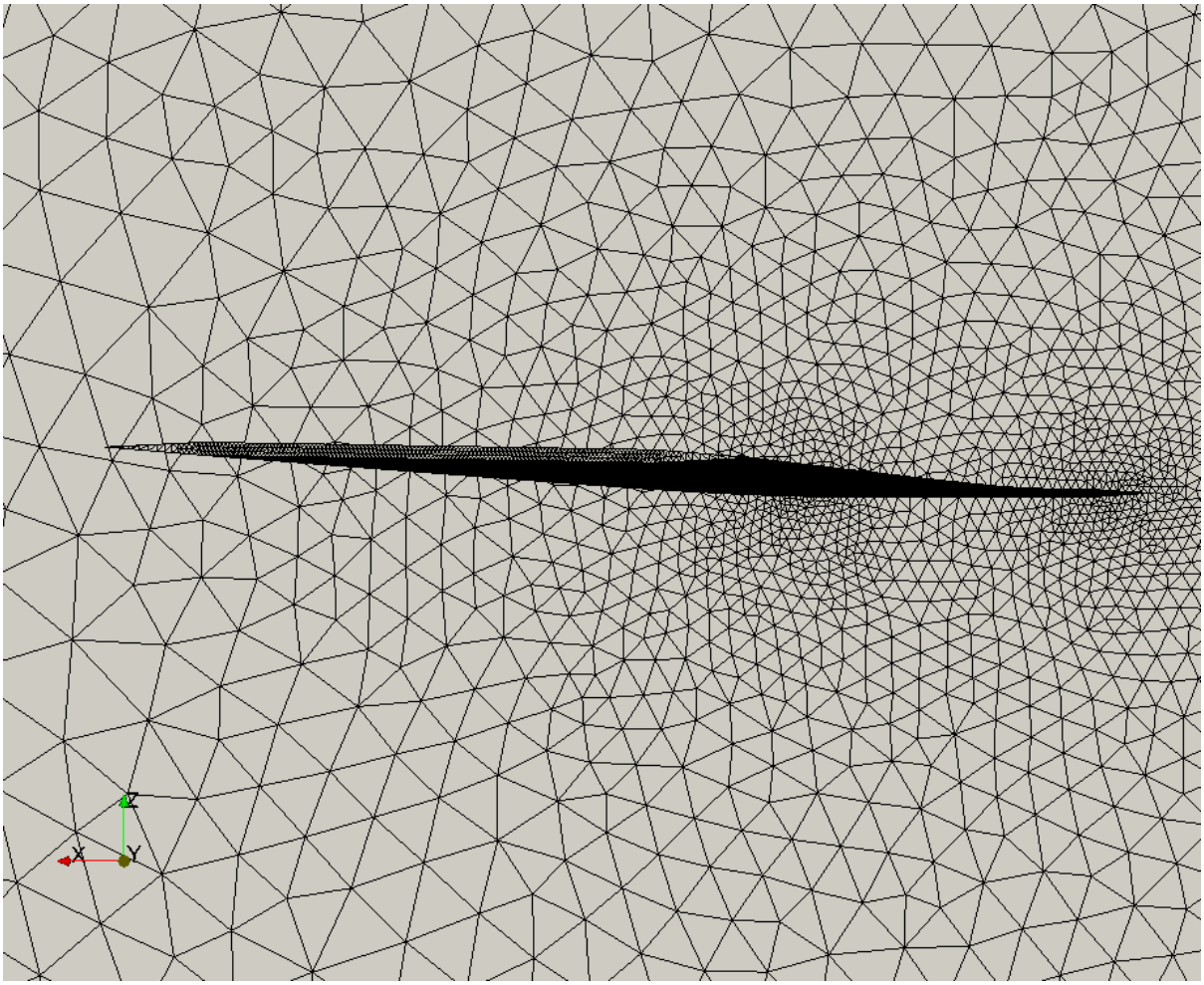


Figure E.1: ATM-Wing Deformed Mesh, Mode 1, Wing Tip

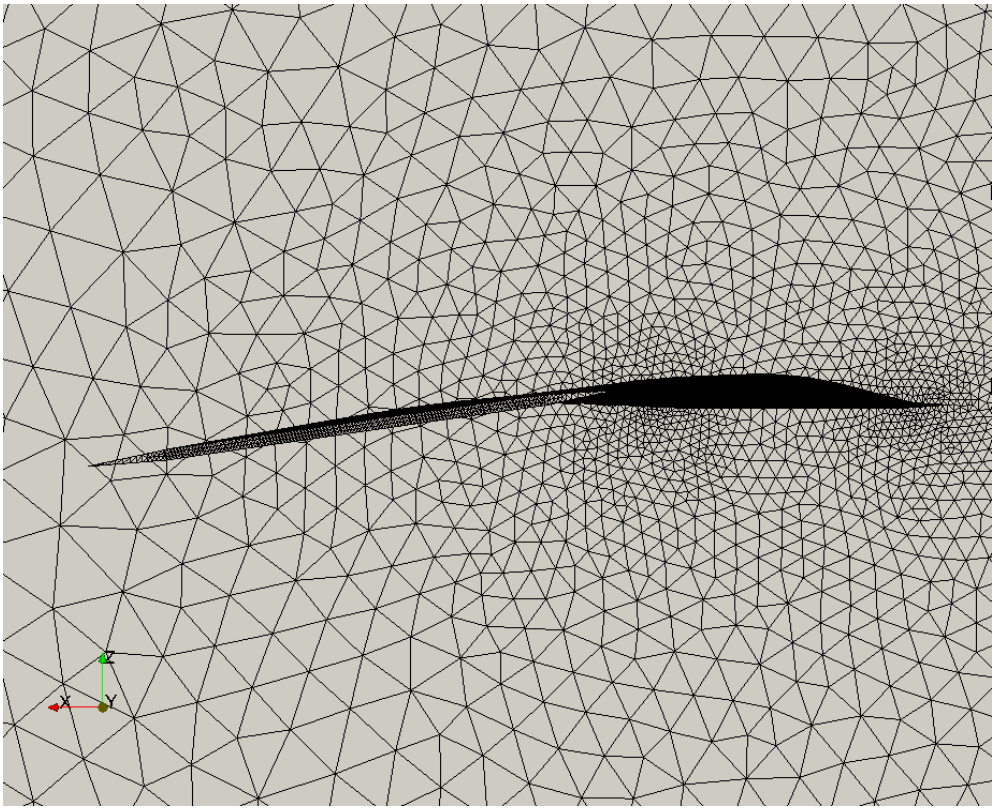


Figure E.2: ATM-Wing Deformed Mesh, Mode 2, Wing Tip

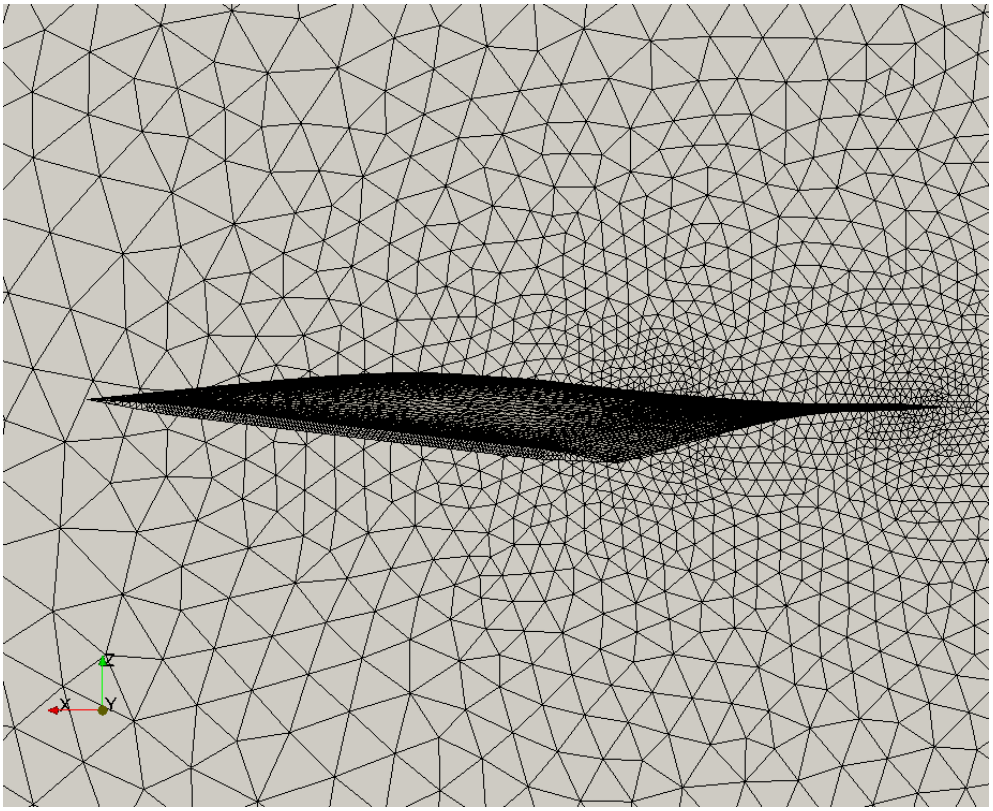


Figure E.3: ATM-Wing Deformed Mesh, Mode 3, Wing Tip

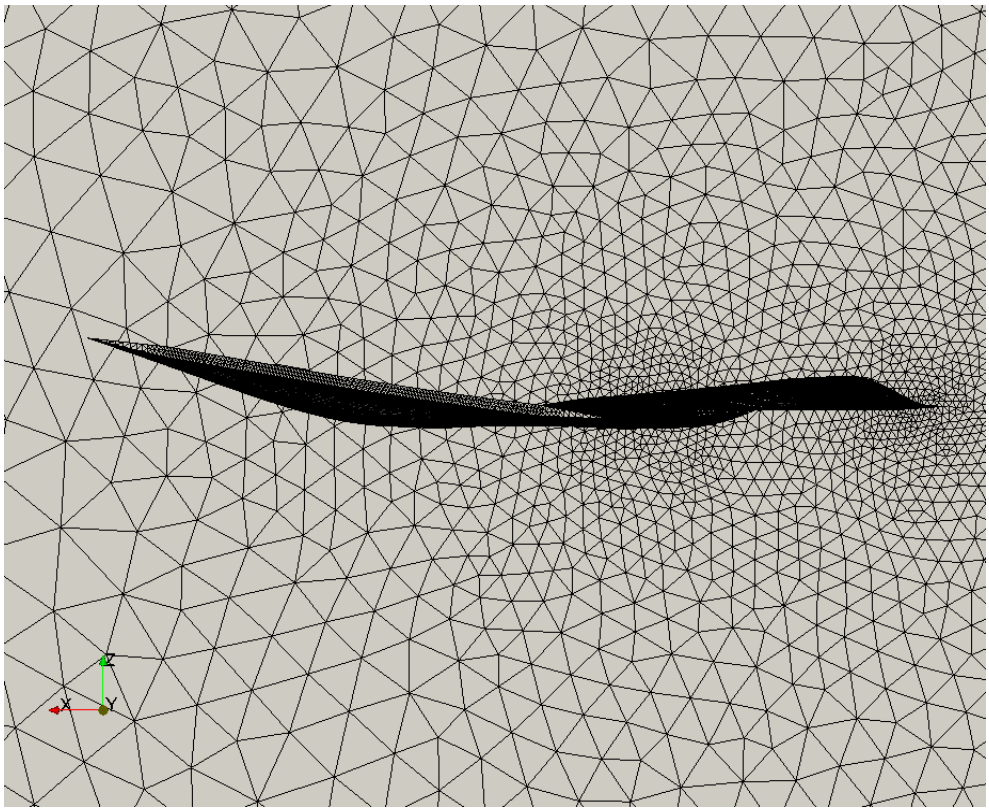


Figure E.4: ATM-Wing Deformed Mesh, Mode 4, Wing Tip

F. FURTHER RESULTS OF THE PRESCRIBED MODAL DISPLACEMENTS

The results given below are a for the prescribed step modal displacements for the ATM-wing at $M = 2.51, \alpha = 0.5°, q = 108$ kPa as described in Section 5.8.

Table F.1: Prescribed Motion Results for Mode 1, Step Size 1 x 10^{-5}

	$\Delta x_1 = 0$		$\Delta x_1 = 5$ x 10^{-5}		$\Delta x_1 = -5$ x 10^{-5}	
	Edge	MATLAB	Edge	MATLAB	Edge	MATLAB
c_N	1.476 x 10^{-2}	1.529 x 10^{-2}	1.556 x 10^{-2}	1.627 x 10^{-2}	1.387 x 10^{-2}	1.433 x 10^{-2}
c_A	2.285 x 10^{-3}	2.137 x 10^{-3}	2.294 x 10^{-3}	2.145 x 10^{-3}	2.278 x 10^{-3}	2.128 x 10^{-3}
c_M	-1.609 x 10^{-2}	-1.697 x 10^{-2}	-1.722 x 10^{-2}	-1.823 x 10^{-2}	-1.496 x 10^{-2}	-1.573 x 10^{-2}
Q_1	-79.46	-85.56	-86.07	-92.98	-72.85	-78.27
Q_2	53.49	46.12	56.83	48.83	50.15	43.40
Q_3	-22.59	-20.82	-23.27	-21.76	-21.91	-20.00
Q_4	24.86	30.78	25.15	31.73	24.57	29.86

Table F.2: Prescribed Motion Results for Mode 1, Step Size 1 x 10^{-6}

	$\Delta x_1 = 0$		$\Delta x_1 = 5$ x 10^{-6}		$\Delta x_1 = -5$ x 10^{-6}	
	Edge	MATLAB	Edge	MATLAB	Edge	MATLAB
c_N	1.476 x 10^{-2}	1.529 x 10^{-2}	1.485 x 10^{-2}	1.540 x 10^{-2}	1.467 x 10^{-2}	1.520 x 10^{-2}
c_A	2.285 x 10^{-3}	2.137 x 10^{-3}	2.286 x 10^{-3}	2.137 x 10^{-3}	2.285 x 10^{-3}	2.136 x 10^{-3}
c_M	-1.609 x 10^{-2}	-1.697 x 10^{-2}	-1.621 x 10^{-2}	-1.710 x 10^{-2}	-1.598 x 10^{-2}	-1.686 x 10^{-2}
Q_1	-79.46	-85.56	-80.12	-86.27	-78.80	-84.98
Q_2	53.49	46.12	53.83	46.36	53.16	45.87
Q_3	-22.59	-20.82	-22.66	-21.02	-22.52	-20.74
Q_4	24.86	30.78	24.89	30.94	24.83	30.65

Table F.3: Prescribed Motion Results for Mode 2, Step Size 1 x 10^{-5}

	$\Delta x_2 = 0$		$\Delta x_2 = 1$ x 10^{-5}		$\Delta x_2 = -1$ x 10^{-5}	
	Edge	MATLAB	Edge	MATLAB	Edge	MATLAB
c_N	1.476 x 10^{-2}	1.529 x 10^{-2}	1.579 x 10^{-2}	1.650 x 10^{-2}	1.373 x 10^{-2}	1.410 x 10^{-2}
c_A	2.285 x 10^{-3}	2.137 x 10^{-3}	2.296 x 10^{-3}	2.146 x 10^{-3}	2.277 x 10^{-3}	2.126 x 10^{-3}
c_M	-1.609 x 10^{-2}	-1.697 x 10^{-2}	-1.754 x 10^{-2}	-1.872 x 10^{-2}	-1.465 x 10^{-2}	-1.525 x 10^{-2}
Q_1	-79.46	-85.56	-88.71	-96.79	-70.22	-74.45
Q_2	53.49	46.12	55.93	47.33	51.05	44.91
Q_3	-22.59	-20.82	-22.66	-21.27	-22.52	-20.48
Q_4	24.86	30.78	23.15	30.04	26.57	31.54

Table F.4: Prescribed Motion Results for Mode 2, Step Size 1 x 10^{-6}

	$\Delta x_2 = 0$		$\Delta x_2 = 1$ x 10^{-6}		$\Delta x_2 = -1$ x 10^{-6}	
	Edge	MATLAB	Edge	MATLAB	Edge	MATLAB
c_N	1.476 x 10^{-2}	1.529 x 10^{-2}	1.487 x 10^{-2}	1.547 x 10^{-2}	1.466 x 10^{-2}	1.513 x 10^{-2}
c_A	2.285 x 10^{-3}	2.137 x 10^{-3}	2.286 x 10^{-3}	2.137 x 10^{-3}	2.285 x 10^{-3}	2.135 x 10^{-3}
c_M	-1.609 x 10^{-2}	-1.697 x 10^{-2}	-1.624 x 10^{-2}	-1.722 x 10^{-2}	-1.595 x 10^{-2}	-1.675 x 10^{-2}
Q_1	-79.46	-85.56	-80.38	-87.04	-78.53	-84.20
Q_2	53.49	46.12	53.74	46.24	53.25	45.99
Q_3	-22.59	-20.82	-22.60	-21.16	-22.58	-20.60
Q_4	24.86	30.78	24.69	30.78	25.03	30.81

Table F.5: Prescribed Motion Results for Mode 3, Step Size 1 x 10^{-5}

	$\Delta x_3 = 0$		$\Delta x_3 = 1 \text{ x } 10^{-5}$		$\Delta x_3 = -1 \text{ x } 10^{-5}$	
	Edge	MATLAB	Edge	MATLAB	Edge	MATLAB
c_N	1.476 x 10^{-2}	1.529 x 10^{-2}	1.611 x 10^{-2}	1.679 x 10^{-2}	1.342 x 10^{-2}	1.381 x 10^{-2}
c_A	2.285 x 10^{-3}	2.137 x 10^{-3}	2.299 x 10^{-3}	2.149 x 10^{-3}	2.275 x 10^{-3}	2.125 x 10^{-3}
c_M	-1.609 x 10^{-2}	-1.697 x 10^{-2}	-1.783 x 10^{-2}	-1.896 x 10^{-2}	-1.436 x 10^{-2}	-1.500 x 10^{-2}
Q_1	-79.46	-85.56	-89.09	-96.73	-69.83	-74.51
Q_2	53.49	46.12	57.62	49.36	49.36	42.88
Q_3	-22.59	-20.82	-25.61	-24.32	-19.57	-17.43
Q_4	24.86	30.78	24.87	31.72	24.85	29.87

Table F.6: Prescribed Motion Results for Mode 3, Step Size 1 x 10^{-6}

	$\Delta x_3 = 0$		$\Delta x_3 = 1 \text{ x } 10^{-6}$		$\Delta x_3 = -1 \text{ x } 10^{-6}$	
	Edge	MATLAB	Edge	MATLAB	Edge	MATLAB
c_N	1.476 x 10^{-2}	1.529 x 10^{-2}	1.490 x 10^{-2}	1.550 x 10^{-2}	1.463 x 10^{-2}	1.510 x 10^{-2}
c_A	2.285 x 10^{-3}	2.137 x 10^{-3}	2.287 x 10^{-3}	2.137 x 10^{-3}	2.284 x 10^{-3}	2.135 x 10^{-3}
c_M	-1.609 x 10^{-2}	-1.697 x 10^{-2}	-1.627 x 10^{-2}	-1.724 x 10^{-2}	-1.592 x 10^{-2}	-1.672 x 10^{-2}
Q_1	-79.46	-85.56	-80.42	-87.04	-78.50	-84.21
Q_2	53.49	46.12	53.91	46.45	53.08	45.78
Q_3	-22.59	-20.82	-22.89	-21.47	-22.29	-20.29
Q_4	24.86	30.78	24.86	30.95	24.86	30.64

Table F.7: Prescribed Motion Results for Mode 4, Step Size 1 x 10^{-5}

	$\Delta x_4 = 0$		$\Delta x_4 = 1 \text{ x } 10^{-5}$		$\Delta x_4 = -1 \text{ x } 10^{-5}$	
	Edge	MATLAB	Edge	MATLAB	Edge	MATLAB
c_N	1.476 x 10^{-2}	1.529 x 10^{-2}	1.519 x 10^{-2}	1.562 x 10^{-2}	1.434 x 10^{-2}	1.498 x 10^{-2}
c_A	2.285 x 10^{-3}	2.137 x 10^{-3}	2.290 x 10^{-3}	2.140 x 10^{-3}	2.283 x 10^{-3}	2.134 x 10^{-3}
c_M	-1.609 x 10^{-2}	-1.697 x 10^{-2}	-1.637 x 10^{-2}	-1.702 x 10^{-2}	-1.582 x 10^{-2}	-1.694 x 10^{-2}
Q_1	-79.46	-85.56	-79.05	-83.14	-79.87	-88.09
Q_2	53.49	46.12	60.53	55.33	46.45	36.90
Q_3	-22.59	-20.82	-26.39	-25.62	-18.79	-16.12
Q_4	24.86	30.78	27.51	32.10	22.20	29.49

Table F.8: Prescribed Motion Results for Mode 4, Step Size 1 x 10^{-6}

	$\Delta x_4 = 0$		$\Delta x_4 = 1 \text{ x } 10^{-6}$		$\Delta x_4 = -1 \text{ x } 10^{-6}$	
	Edge	MATLAB	Edge	MATLAB	Edge	MATLAB
c_N	1.476 x 10^{-2}	1.529 x 10^{-2}	1.480 x 10^{-2}	1.532 x 10^{-2}	1.472 x 10^{-2}	1.528 x 10^{-2}
c_A	2.285 x 10^{-3}	2.137 x 10^{-3}	2.286 x 10^{-3}	2.137 x 10^{-3}	2.285 x 10^{-3}	2.136 x 10^{-3}
c_M	-1.609 x 10^{-2}	-1.697 x 10^{-2}	-1.612 x 10^{-2}	-1.696 x 10^{-2}	-1.607 x 10^{-2}	-1.701 x 10^{-2}
Q_1	-79.46	-85.56	-79.42	-85.13	-79.50	-86.12
Q_2	53.49	46.12	54.20	47.15	52.79	45.09
Q_3	-22.59	-20.82	-22.97	-21.31	-22.21	-20.46
Q_4	24.86	30.78	25.12	31.03	24.59	30.56